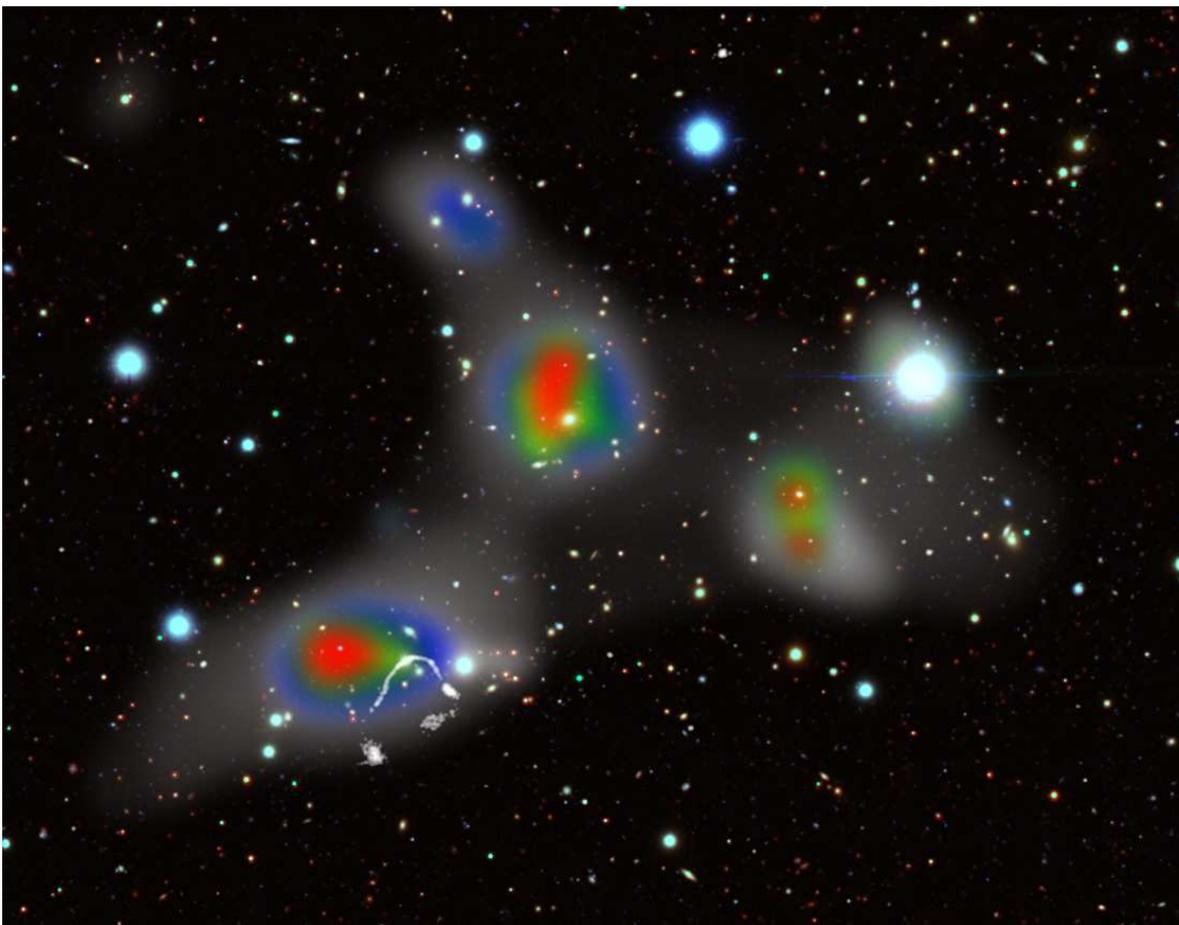# THE FAINT RADIO POPULATION IN THE VLA-COSMOS SURVEY: STAR FORMING GALAXIES AND ACTIVE GALCTIC NUCLEI

Vernesa Smolčić

Max–Planck–Institut für Astronomie

Heidelberg 2007

Dissertation in Astronomy
submitted to the
Combined Faculties for the Natural Sciences and for Mathematics
of the Ruperto–Carola University of Heidelberg, Germany
for the degree of
Doctor of Natural Sciences

presented by
Dipl. Ing. Phys. *Vernesa Smolčić*
born in Zagreb, Croatia

Oral examination: **19.12.2007, 2:00 pm**

The Faint Radio Population in the VLA-COSMOS Survey: Star Forming Galaxies and Active Galctic Nuclei

Zusammenfassung (German)

Die Zusammensetzung der lichtschwachen – submillijansky – Radiopopulation, die in der Vergangenheit ein Gegenstand heißer Debatten war und immer noch ist, wird erforscht: durch Beobachtungen des 1.4 GHz (20 cm) Radiokontinuums des 2□° COSMOS-Feldes, die eine grosse statistisch signifikante Stichprobe ergeben, und der Entwicklung einer Methode, die eine minimale Parameteranzahl zur effizienten Unterscheidung zwischen den beiden Hauptpopulationen in extragalaktischen Radio-Durchmusterungen – aktive galaktische Kerne (AGN) und sternbildende Galaxien – nutzt. Diese Methode hat das Potential auch erfolgreich auf Stichproben, die bei anderen Wellenlängen selektiert wurden, angewendet zu werden. Eines der Hauptergebnisse dieser Arbeit ist, dass sternbildende Galaxien nicht die submillijansky Radiopopulation dominieren, wie oft angenommen wurde, sondern nur ungefähr $30 - 40\%$ beitragen, während der Rest aus AGN und Quasaren besteht. Diese gut definierte Stichprobe von sternbildenden Galaxien im Radiobereich bei 1.4 GHz wurde benutzt, um die kosmische Sternentstehungsgeschichte aus Radiodaten zu bestimmen. Insbesondere wurde zum ersten Mal die staub-unabhängige kosmische Entwicklung der Sternentstehungsrate der intensivsten sternbildenen Galaxien ($\gtrsim 100$ M$_\odot$ yr^{-1}) seit ~ 5 Gyr nach dem 'Big Bang' mit hoher Präzision bestimmt. Zusätzlich bestägtigt die, aus den Radiodaten abgeleitete, kosmische Sternentstehungsgeschichte die Gültigkeit der großen Korrekturen für Staub, die bei anderen Wellenlängen angebracht werden.

Abstract (English)

The composition of the faint – submillijansky – radio population, that has been a matter of strong debate in the past, is explored by performing observations at 1.4 GHz (20 cm) radio continuum of the 2□° COSMOS field providing a large statistically significant sample, and by developing a method that uses a minimal number of parameters to efficiently discriminate between the two main populations in extragalactic radio surveys: active galactic nuclei (AGN) and star forming galaxies. This method bears the potential to be successfully applied to similar samples selected at other wavelengths. One of the main findings is that star forming galaxies do not dominate the submillijansky radio population, as often assumed, but form only about $30-40\%$ of it, while the remainder is composed of AGN and quasars. Using this well defined sample of radio-selected star forming galaxies at 1.4 GHz, the cosmic star formation history is derived using radio data, for the first time constraining the dust-unbiased cosmic evolution of star formation rate in the most intensively star forming galaxies ($\gtrsim 100$ M$_\odot$ yr^{-1}) since ~ 5 Gyr after the Big Bang with high precision. In addition, the radio derived cosmic star formation history confirms the validity of the large dust corrections applied at other wavelengths.

Contents

List of Figures

List of Tables

Chapter 1

Introduction

One of the fundamental aims of astrophysics is understanding the formation and evolution of galaxies, trying to reveal when the first galaxies formed and how they changed through cosmic times. Answering these questions can, and needs to, be approached in numerous different ways, each providing a little piece to the overall big puzzle. This thesis, in particular, focuses on a radio-based view of the sky, and aims to shed light on the above challenges using panchromatic (X-ray to radio) data for a large number of galaxies. This chapter provides an introduction to the broad scientific context and topics relevant for this thesis.

1.1 The evolution of galaxies and their panchromatic properties

The most successful paradigm for understanding the distribution of matter in the universe is 'hierarchical galaxy formation' (White & Rees 1978) within a Λ cold dark matter (ΛCDM) cosmology. The success of the ΛCDM model in describing the universe, when compared to observations, has been tremendous, ranging from the anisotropies of the cosmic microwave background at high redshifts (e.g. Spergel et al. 2007) to the clustering properties of galaxies in the local universe (e.g. Peacock et al. 2001; Weinberg et al. 2004; Springel et al. 2005). In this model, structure in the universe is formed via gravitational instabilities arising from small perturbations seeded during the inflationary epoch in the early universe (e.g. Pen 1999; Springel et al. 2005). The dominant mass component in the universe is collisionless cold dark matter, which is the main driver of the dynamics and structure of baryons on large scales. Both the visible and invisible matter on these large scales, once they have formed, continue to grow 'violently' in a hierarchical fashion: large features grow through mergers of smaller precursors. In such a universe strong evolution of galaxies through cosmic times is expected (and observed). In the following, average properties of galaxies in a ΛCDM universe, and their evolution, relevant to the content of this thesis, are discussed.

1.1.1 Global properties of galaxies in the near-ultraviolet to near-infrared range

For many years observed galaxy properties, and correlations between them, have been known to trace the underlying physics of these galaxies. This implies that observed properties of galaxies are valuable tools for studying internal physical mechanisms. For example, one of the well known astronomical relations for elliptical (pressure supported) galaxies is the 'Faber – Jackson' relation (Faber & Jackson 1976), which represents a correlation between the galaxy's central velocity dispersion and optical luminosity. This relation is a consequence of the virial theorem and correlates two, out of the three, fundamental parameters that appear to represent the *entire* family of elliptical galaxies (the so called 'fundamental plane'). This 'fundamental plane' combines the contributions of a galaxy's gravitational potential with its radius and luminosity (hence its surface brightness). On the other hand, for spiral galaxies, which are rotationally supported systems, a tight correlation between the galaxy's optical luminosity and its maximum rotational velocity exists. This relation again reflects the underlying galaxy's gravitational well and it is known as the 'Tully – Fisher' relation (Tully & Fisher 1977). It is noteworthy that the 'Tully – Fisher' relation was originally obtained via radio observations of the 21 cm neutral hydrogen (electron spin-flip) spectral line for a sample of spiral galaxies. One other, observationally extremely useful, relation is the correlation between the galaxy's morphology and its color indices.

All of the above mentioned relations have significantly contributed to the advance of our understanding of galaxies. However, as astronomy advanced (e.g. in instrumentation, observing strategies) our knowledge of galaxy properties and their interdependence has been put on stronger footing thanks to the recent advent of multi-wavelength all-sky surveys (e.g. Strateva et al. 2001; Ivezić et al. 2002; Blanton et al. 2001, 2003, 2005; Hogg et al. 2003; Kauffmann et al. 2003a,b,c; Brinchmann et al. 2004; Baldry et al. 2004; Balogh et al. 2004; Yip et al. 2004; Smolčić et al. 2004, 2006, 2007b; Obrić et al. 2006). This is in particular true for the interplay between galaxy properties in the near ultraviolet (NUV) to near infrared (NIR) wavelength range, extensively used in latter chapters, that is discussed below.

The NUV – NIR properties of galaxies in the local ($z < 0.3$) universe have been extensively studied using multi-wavelength data obtained by various all-sky surveys (SDSS, NVSS, FIRST, IRAS, ROSAT; see Appendix A for details on these surveys; Strateva et al. 2001; Kauffmann et al. 2003a; Brinchmann et al. 2004; Yip et al. 2004; Obrić et al. 2006; Smolčić et al. 2006). The results have strongly converged towards a *simple parameterization of the NUV – NIR spectral energy distribution (SED)*, as well as its correlation to spectroscopic features, of the overall population of galaxies. In general, colors of galaxies reflect their dominant stellar populations and thus correlate with morphology (Humason 1936; Hubble 1936). A strong bimodality in the distribution of local galaxies has been shown to exist in NUV – NIR color space (Strateva et al. 2001; Baldry et al. 2004; Balogh et al. 2004), with the two peaks of the bimodal distribution corresponding roughly to early- (E, S0 and Sa), and late- (Sb, Sc and Irr) type galaxies (see Fig. 1.1; Strateva et al.

2001). A similar distribution has been found extending to at least $z \sim 1$ (Lin et al. 1999; Im et al. 2002; Bell et al. 2004; Weiner et al. 2005; Willmer et al. 2006) and possibly beyond (Giallongo et al. 2005).

This 'simplicity' in the NUV – NIR properties of the overall galaxy population has been confirmed in numerous other studies, using different approaches. For example, analyzing 170,000 SDSS local galaxy spectra using the principal component analysis (Karhunen-Loéve transform) Yip et al. (2004) have found that more than 99% of the galaxies can be fully described using a two-dimensional locus in the space spanned by the ratios of *only* the first three eigencoefficients. Further, using UV (GALEX), optical (SDSS) and IR (2MASS) data to construct the NUV – NIR broad-band SEDs for various types of galaxies (selected based on their spectroscopic properties; Baldwin, Phillips, & Terlevich 1981) Obrić et al. (2006) have demonstrated that the overall NUV – NIR SED is a nearly one-parameter family. In addition, Smolčić et al. (2006) have shown that *rest-frame* optical colors, constructed using the $3,500 - 5,800$ Å wavelength range, strongly correlate with spectroscopic properties, such as emission-line flux ratios commonly used to trace the hardness of the ionization potential in a galaxy, which discriminates between emission from starbursts and accretion onto supermassive black holes (Baldwin, Phillips, & Terlevich 1981).
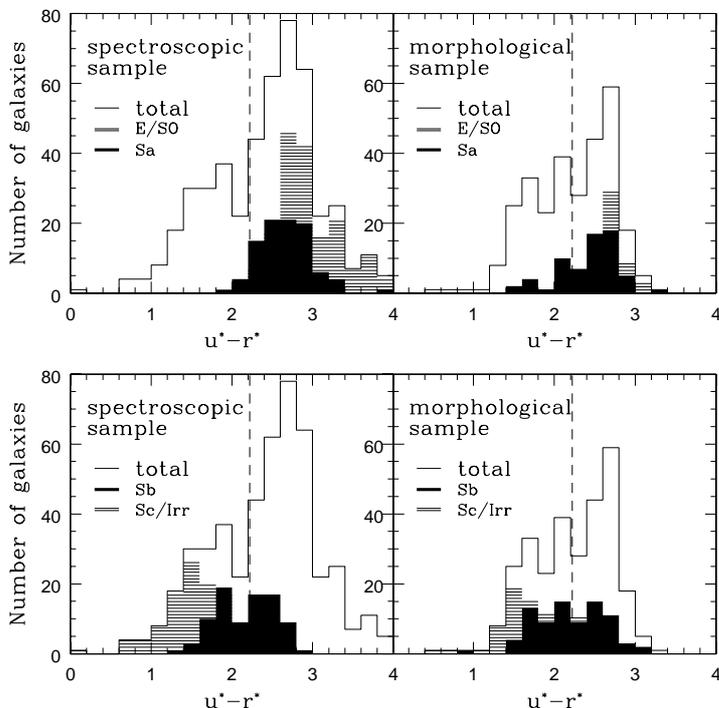
Figure 1.1 $u - r$ color distributions for the spectroscopically (left panels) and morphologically (right panels) classified SDSS galaxies, adopted from Strateva et al. (2001). The bimodal distribution of the overall population of galaxies is obvious. The division between red and blue types of galaxies proposed by Strateva et al. (2001) is indicated by the vertical dashed line in each panel ($u - r = 2.22$). There is also a clear sub-division in color for different types of galaxies (indicated in each panel).

1.1.2   About the evolution of galaxies

The idea that the two dominant types of galaxies in the universe, the 'blue' (star forming) and 'red' (non-star forming) galaxies, do not represent two completely independent channels of galaxy formation, but rather different stages of the galaxy formation process itself,
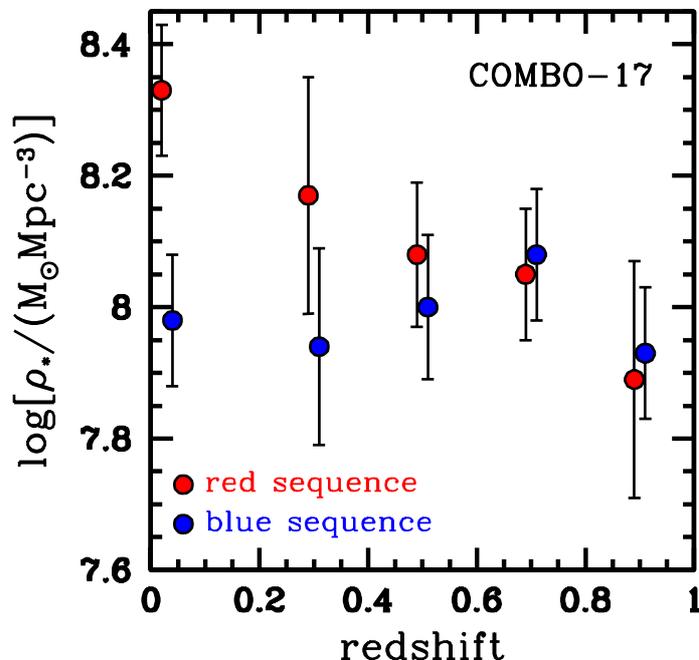
Figure 1.2 Evolution of the stellar mass density of red and blue sequence galaxies since $z \sim 1$. The diagram was obtained using the COMBO-17 data from Borch et al. (2006, courtesy of Frank C. van den Bosch). Note that the stellar mass density of blue galaxies is roughly constant with redshift, while it substantially increases for red galaxies from high to low redshift. Given that relatively few stars form in red sequence galaxies this implies that suppression of star formation in a fraction of previously blue, star forming, galaxies is responsible for the stellar mass growth of galaxies in the red sequence (see text for details).

has already been proposed by Hubble (1936). Recently it has been observationally demonstrated that the stellar mass on the red sequence has increased by a substantial amount ($\sim 50\%$) since $z \sim 1$, (Bell et al. 2004; Borch et al. 2006; Faber et al. 2007; Brown et al. 2007), while it stays roughly constant for blue cloud galaxies (see Fig. 1.2). Given that relatively few stars form in red sequence galaxies (Bell et al. 2004) this buildup has been argued to be driven by quenching of star formation in a fraction of previously blue, star forming, galaxies. A schematic outline (Faber et al. 2007) of the buildup of the red sequence is shown in Fig. 1.3. In this scenario, proposed by Faber et al. (2007), the quenching of the star formation in a blue cloud galaxy moves the galaxy to the red sequence by the ageing of its stellar population which turns redder with time. Although the physical mechanism of the star formation quenching process is not understood, it is assumed that star formation is suppressed by a *major merger* event between two gas-rich blue galaxies (this is referred to as 'wet' merger) which doubles the mass of the initial merger constituents. However, processes that do not include major mergers, such as ram pressure stripping and galaxy harassment, may also cause the fuel for star formation to be removed from the galaxy and thereby quench star formation. Once on the red sequence, the mass of the object may grow further (although more slowly) through a sequence of dissipationless mergers with gas-poor red galaxies (hence such mergers are called 'dry' mergers).

1.1.3 Major mergers as the main drivers for galaxy evolution

Galaxy evolution through the process of wet (gas rich) mergers has been initially proposed by Sanders & Mirabel (1996) in the context of a special class of local galaxies usually referred to as 'infrared galaxies'. One of the most striking results of the Infrared Astron-
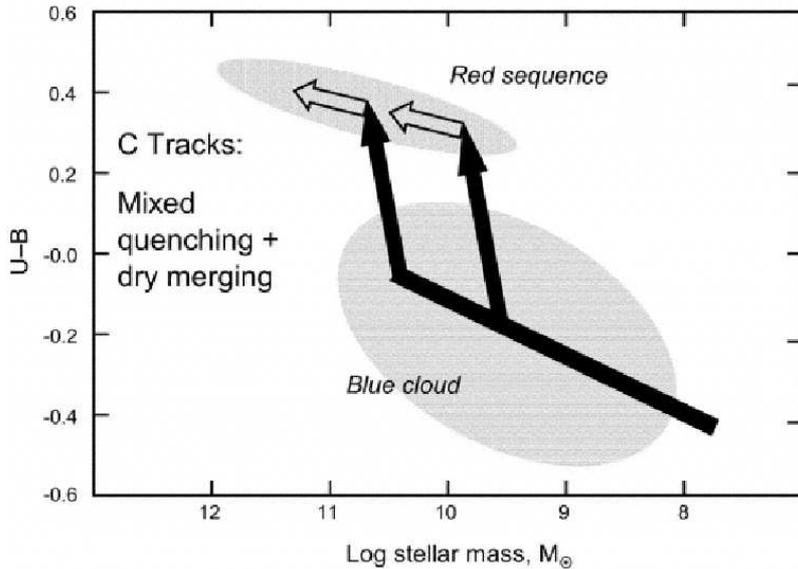
Figure 1.3 Illustration of the evolutionary scenario proposed for the build-up of the red sequence (adopted from Faber et al. 2007). In this picture, major mergers between gas-rich star forming galaxies located in the blue cloud lead towards the suppression of star formation and double the mass of the initial merging constituent. After star formation is quenched the stellar population ages, and therefore reddens and migrates to the red sequence. Once on the red sequence, the object's mass can further grow through gas-poor mergers with other 'red and dead' galaxies.

omy Satellite (IRAS; Neugebauer et al. 1984) All-sky Survey has been the existence of a substantial population of, previously unknown, 'infrared galaxies' that may emit more than 99% of their bolometric luminosity at IR wavelengths (see Sanders & Mirabel 1996 for a review). [The most extreme example of such galaxies is Arp 220 (Soifer et al. 1984).] Sanders & Mirabel (1996) have postulated that these ultra-luminous IR galaxies (ULIRGs, $L_{IR} > 10^{12}L_\odot$) represent an important intermediate stage in the formation of massively accreting black holes in the form of quasi stellar objects (QSO) and powerful radio galaxies, suggesting further that wet mergers may be the major process driving their evolution. In the context of the above described 'blue' to 'red' galaxy evolution scenario (Faber et al. 2007), (U)LIRGs would be placed roughly in the evolutionary transitional region between the initially blue - pre-merger - star forming galaxies and the finally red, dead and gas-poor galaxies.

Studies of ULIRGs based on the IRAS Bright Galaxy Sample (Sanders et al. 1988a,b; Kim et al. 2002; Veilleux et al. 2002) have indicated that the ULIRG phase occurs near the end of the merger between two gas-rich disk galaxies, when the disks overlap. The upcoming merger of the nuclei of the two galaxies is followed by a transition to an optically active, quasi stellar object, phase. In particular, a five stage sequence was proposed for the evolution of luminous IR galaxies (LIRGs; $L_{IR} = 10^{11-12}L_\odot$) to QSOs (e.g. Sanders & Mirabel 1996; Sanders 2003). First, LIRGs, which are dominated by merging pairs of gas rich spirals, evolve to "cool ULIRGs" ($T_{dust} \sim 30 - 60$ K). In the latter systems the bulk of their molecular gas, which fuels both star formation and black hole accretion, that was originally distributed throughout the disk, is funneled into the inner few kpc of the merging system. These "cool ULIRGs" tend to show HII-like emission in their optical spectra, and may be considered to be powerful starbursts. As the merger advances, the "cool ULIRGs" transform into "warm ULIRGs" ($T_{dust} \sim 150 - 250$ K), which are post-starburst systems and have Seyfert like optical spectra, hence they are dominated by the emission of the accretion onto the central supermassive black hole. These then fade into IR-excess QSOs which eventually turn into "IR normal QSOs" (see Sanders 2003 for details and references

therein).

The above proposed picture has grown stronger with the advent of new studies using statistically significant samples of galaxies in, and beyond, the local universe. For example, there is observational evidence in the local universe that the active galaxy phase, dominated by the emission from the central supermassive black hole accretion, may be an intermediate evolutionary phase: AGN (active galactic nuclei) largely tend to occupy the 'green valley', i.e. the sparsely populated region in NUV – NIR space between the blue cloud and red sequence (see Fig. 1.4; Smolčić et al. 2006). The lower galaxy density in the 'green valley' implies a much shorter life-time for these (compared to red/blue) galaxies yielding a fairly rapid transition from the blue cloud into the red sequence (assuming the validity of the blue-to-red galaxy evolutionary scenario). Further, using a compilation of observationally
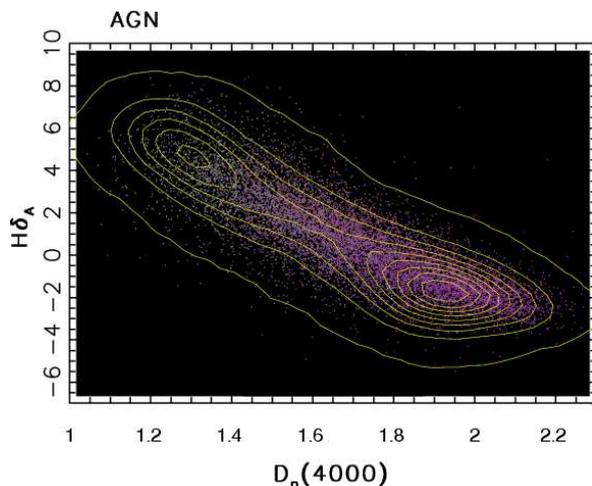
Figure 1.4 The distribution of spectroscopically selected (Baldwin, Phillips, & Terlevich 1981) AGN (dots) compared to the overall galaxy distribution (contours) drawn from the SDSS (DR1) 'main' spectroscopic sample (see Smolčić et al. 2006 for details) in the space spanned by the Hδ absorption line and the 4000 Å break. The strength of Hδ and $D_n(4000)$ are tracers of a galaxy's young stellar population, and the galaxy's age, respectively (see Kauffmann et al. 2003a for a comprehensive discussion of this point). This plane clearly shows the observed galaxy bimodality; 'blue' (star forming) galaxies are located in the top-left peak, and 'red' (non-star forming) comprise the bottom-right peak of the bimodal distribution (shown in contours). Note that the active galaxies (dots) preferentially occupy the interspace between the 'blue' and 'red' maxima, consistent with the so called 'green valley', implying that AGN may be an intermediate evolutionary phase in the build-up of the red sequence (see text for details).

determined red galaxy mass functions to study the rate of the buildup of the red sequence as a function of mass and redshift Hopkins et al. (2007) have found that dissipationless (gas-poor, dry) mergers account for the buildup of the red sequence at only the largest masses ($\gtrsim 10^{11} M_\odot$) and low redshifts ($z \lesssim 0.3$). However, at higher redshifts ($z \gtrsim 0.5$) the buildup is dominated *at all masses* by gas-rich (wet) mergers. Overall, their observational data support the hypothesis that *mergers drive the transition from blue and star forming, to red and 'dead' galaxies, through massive starburst and active, AGN, phases, and that gas-rich, wet, mergers are the dominating evolutionary process.*

1.1.4 The advantage of using panchromatic properties

An important ingredient of the structure of galaxies is their *interstellar medium* comprised of gas and dust. The effective absorption of photons by dust is inversely proportional to wavelength. For example, Charlot & Fall 2000 find that the optical depth, τ_λ, may roughly be approximated as a function of wavelength by $\tau_\lambda \propto \lambda^{-0.7}$ (note that the attenuation due to dust is then $\propto e^{-\tau_\lambda}$; see also Mathis et al. 1977). However, explaining the exact behavior of dust is non-trivial and subject of many studies (e.g. Mathis et al. 1977; Charlot & Fall 2000; Calzetti 2001; Fischera et al. 2003). Due to this inverse wavelength dependence dust-obscuration in galaxies substantially complicates the interpretation of short-wavelength,

e.g. UV/optical, observations, while long-wavelength radiation, such as FIR to radio, stays essentially unaffected by dust. This is of particular importance for both AGN (un-obscured Type-I and obscured Type-II AGN in the context of the AGN unification theory; see e.g. Padovani & Urry 1992) and intensely star forming galaxies that have been demonstrated to contain larger dust reservoirs than modestly star forming galaxies (e.g. Bell 2003; Hopkins 2004). Further, the IR emission of a galaxy, thermal in origin, arises from the galaxy's interstellar dust heated by shorter wavelength radiation, such as e.g. by young hot stars being formed in dust enshrouded regions or by the radiation from the accretion disk of the AGN. For these reasons it is essential to observe the entire SED of galaxies in order to fully understand their properties.

Since observations started being performed in different wavelength windows (tracing different physical types of radiation), numerous 'unexpected' correlations have been found. To date, many of these relations are not fully understood giving rise to a new challenging field of astrophysics: the panchromatic view on galaxy properties and evolution. In particular, tight correlations between IR and radio emission (e.g. Helou et al. 1985; Condon 1992; Obrić et al. 2006), as well as X-ray and radio emission (e.g. Brinkmann et al. 2000; Ranalli et al. 2003), have been found separately for AGN and star forming galaxies. For illustration, the IR – radio correlation is outlined below.

The IR – radio correlation

In extragalactic radio surveys two main galaxy populations are found: AGN and star forming galaxies. The radio emission observed at 20 cm predominantly traces synchrotron emission from electrons, accelerated to relativistic speeds, spiraling through magnetic fields (see Chap. 1.2.2 for details). On the other hand, observed IR emission traces the thermal radiation of the galaxy's dust component. Since the early days of observations at IR wavelengths, it has been realized that, for an IR selected sample of local galaxies, the far and total IR emission tightly correlate with radio emission at 20 cm (Helou et al. 1985; Condon 1992). This implies that for the characteristic population of IR selected galaxies, knowing the far or total IR luminosities, the radio luminosities can be predicted with a scatter of only a factor of ~ 2 (Condon 1992; Bell 2003; Obrić et al. 2006). Impressively, this correlation, basically unchanged, has been shown to hold out to high redshifts ($z \sim 2$, Garrett 2002; Appleton et al. 2004; see also Chap. 3). Given that the two observational windows, IR and radio, trace completely independent and different intrinsic physical mechanisms – thermal vs. non-thermal radiation – the existence of such a tight correspondence is remarkable, and has been argued to arise from the same radiation sources within the galaxies, implying that both IR and radio emission trace the same physical state in galaxies, such as the emission from star forming regions or the central supermassive black hole accretion. It is noteworthy that historically it has been suggested that the IR – radio correlation only holds for star forming galaxies, while 'monsters', such as AGN or QSOs, significantly deviate from it (e.g. Condon 1992). However, recently it has been demonstrated that a very similar correlation (different by only $\sim 20\%$) also holds for 'modest' monsters, i.e. low luminosity AGN such as Seyfert and LINER galaxies (Obrić et al. 2006, see also Ch. 3). While there has been

attempts to explain the origin of the IR – radio correlation for star forming galaxies (see also Sec. 1.2.2), the origin of the correlation for AGN galaxies is still not understood.

1.2 The radio sky

There are many different (mainly wavelength dependent) approaches towards our full understanding of galaxy evolution, each one being equally important for building up the full picture of the history of the universe. This thesis is focused on a radio view of the universe, and in this section the history of radio astronomy, the origin of radio emission, the major results of radio surveys and the remaining challenges are discussed.

1.2.1 A brief history of radio astronomy

The field of radio astronomy came to existence with Karl Jansky's serendipitous discovery (1933) of strong radio emission originating from the center of our galaxy. At that time optical astronomy has already been well established. For example, Edwin Hubble first proposed the now called 'Hubble law', based on radial velocity and distance measurements of 22 galaxies, four years earlier (Hubble 1929). Nonetheless, by the late 1950's radio observations have taken a key role in astronomy. Namely, they have led to the discovery of a mysterious new class of objects: the quasi-stellar radio sources or shortened 'quasars' (e.g. 3C273 from the Third Cambridge catalog; see below).

The most important early radio surveys were led by Cambridge and were performed at 158 MHz and 178 MHz with interferometers located at the outskirts of Cambridge, and built by the Cambridge Radio Astronomy Group led by Martin Ryle and Antony Hewish (Nobel prize winners for Physics in 1974). It is worth noting that the third Cambridge catalog (3C; Edge et al. 1959; Bennett & Smith 1961) reached down to a limiting flux of 9 Jy beam^{-1}, while the 4C catalog (Pilkington & Scott 1965; Gower et al. 1967) shifted this limit to 2 Jy beam^{-1}. Given the sensitivities of these surveys, their mainly observed radio populations were quasars and radio galaxies.

Striking results have arisen from the first radio surveys. In particular, radio observations by Ryle & Clarke (1961) have provided evidence against the, at that time adopted, Steady State model of the universe (opposing the 'Big Bang' theory). They have found a substantial discrepancy between the Steady State model prediction and the observed radio source counts of extragalactic sources. The development of new powerful radio interferometers, the best example of which is the Very Large Array (VLA) located in New Mexico (USA), allowed to study the radio sky in its full extent and to, at that time, unprecedented depth. The FIRST (Becker et al. 1995) and NVSS (Condon et al. 1998) all-sky surveys (see Appendix A) at 1.4 GHz were performed with the VLA to limiting fluxes of 0.15 and 0.35 mJy beam^{-1}, respectively, reaching about four orders of magnitude deeper than e.g. the 4C catalog. More recently deep pencil-beam ($\sim 100\ \square'$) surveys have also been performed in the radio regime, reaching now as deep as $\sim 5\ \mu$Jy beam^{-1} (SSA 13, Fomalont et al. 2006; see also Tab. 2.1).

One relevant finding of past deep radio surveys (Condon 1984a,b; Windhorst et al. 1985a) is that extragalactic radio sources consist of two main populations: AGN and star forming galaxies. The origin of the observed radio emission is described below.

1.2.2   The origin of radio emission in extragalactic sources

Radio emission observed from the two main extragalactic populations found in radio surveys, AGN and star forming galaxies, arises predominantly from synchrotron radiation of relativistic electrons in magnetic fields (free-free emission starts dominating below ~ 1 cm in star forming galaxies; see below). In this section the mechanism of synchrotron radiation is briefly outlined, and the origin of radio emission from AGN and star forming galaxies is discussed separately.

A brief outline of synchrotron radiation

Nearly all of the radio emission from extragalactic radio sources at 1.4 GHz is synchrotron radiation arising from relativistic electrons gyrating in a magnetic field. The observed radio (1 cm – 100 m) spectrum of extragalactic sources is well described with a power law: $F_\nu \propto \nu^{-\alpha}$, where F_ν is the observed monochromatic energy flux at the specific frequency ν, and α is the spectral index. A pure power-law spectrum is a clear signature of synchrotron radiation. As illustrated in Fig. 1.5 the synchrotron spectrum is produced by the combined radiation emitted by individual electrons as they helically orbit around the magnetic field lines. For a homogeneous radiation source with a constant magnetic field B, a power law continuum spectrum can be generated by an initial power law distribution of electron energies E: $N(E)dE = N_0 E^{-s}dE$, where $\alpha = 0.5 \cdot (s - 1)$. Typically, the median observed spectral index is 0.7 to 0.8 implying $s \approx 2.4$. This however applies to frequencies higher than the 'turn-over' frequency, where synchrotron self-absorption is not important. At frequencies lower than the 'turn-over' frequency, the emitting gas becomes optically thick, i.e. opaque to its own synchrotron radiation (this is known as the *synchrotron self-absorption*) and the spectrum turns over and starts decreasing with decreasing frequency following $F_\nu \propto \nu^{5/2}$. At the highest frequencies on the other hand, observed radio spectra sometimes curve downwards (i.e. α increases with ν). This is explained by the synchrotron energy loss rate, which is proportional to E^2, and implies that the highest-energy electrons radiate away their energy most rapidly, thus depleting the high-energy end of the emitted spectrum. For a comprehensive description of synchrotron radiation see e.g. Shu (1991, Chapters 18 & 19).

Origin of radio emission in AGN galaxies

The radio morphology of radio luminous (not necessarily radio-loud) AGN can broadly be described in terms of 'extended' (i.e. spatially resolved) and/or 'compact' (unresolved at $\sim 1''$ angular resolution) structures, both caused by synchrotron radiation. The extended component generally appears as a double jet, originating from the optical counterpart, that
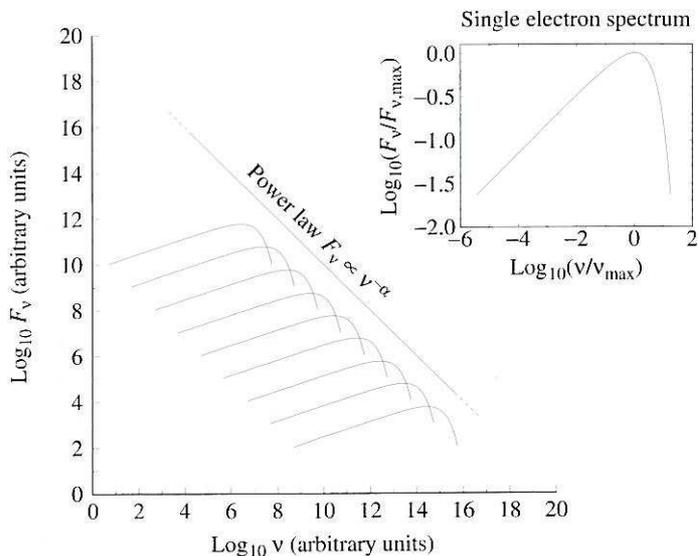
Figure 1.5   The radio (synchrotron) spectrum in terms of flux density vs. frequency $F_\nu \propto \nu^{-\alpha}$, as observed in radio surveys, is shown in the large panel. Synchrotron radiation arises from charged relativistic particles gyrating in a magnetic field, and the observed synchrotron spectrum is a superposition of single-electron synchrotron spectra (shown separately in the inset on the top-right). Note that the slope of the spectrum may change at low/high frequencies: at low frequencies, where synchrotron self-absorption becomes important the spectrum flattens, and turns over, and at the largest frequencies it curves downward (this is indicated by the dots in the spectrum, but not explicitly shown). See text for more details.

ends in lobe-like features. The linear extent of the jets may be as large as megaparsecs. The position of the optical counterpart is usually coincident with the compact radio source; however, compact radio sources are often observed without large scale radio jets (e.g. radio-quiet quasars; e.g. Kukula et al. 1998). The major difference between compact and extended radio structures is that the extended component is optically thin to its own synchrotron emission, whereas this is not true for the compact structures. The radio synchrotron spectra of the compact sources are generally flat ($\alpha \sim 0.2$), while the extended components have steep spectra ($\alpha \sim 0.7$). The accepted explanation for the flatness of the synchrotron spectrum in compact radio sources is that the observed radio emission arises from a superposition of many synchrotron spectra caused by different unresolved synchrotron spectrum radiators, each of which having a different 'turn-over' frequency (see Sec. 1.2.2).

The radio synchrotron spectrum in AGN is believed to arise from processes related to the accretion of material onto the galaxy's central supermassive black hole. The accretion process may be quantified by the accretion rate, $\dot{M}$, relative to the Eddington accretion rate, $\dot{M}_E$. The latter is defined as the maximum possible accretion rate for a spherically symmetric accreting black hole of mass M. Although the processes leading to radio synchrotron emission in AGN are not fully understood, theoretically the most promising generators are black holes that accrete at very low rates ($\dot{M}/\dot{M}_E \lesssim 0.1$) and consequently form the, so called, 'ion' accretion torus. Such mechanisms may cause a strong magnetic field anchored in the vicinity of the black hole (see Peterson 1997 for a detailed description). Within this scenario, at such low accretion rates the accretion disk becomes optically thin, and it is possible for a stable two-temperature structure, the 'ion torus', to develop as the inner regions of the disk cannot efficiently cool if the electrons and ions are thermally decoupled. The magnetic field of the central source will then be frozen into the ionized torus, creating a rapidly rotating field with an axis parallel to the angular momentum vector of the accretion disk. Ion tori are suspected of playing a major role in producing jets as this strong field could collimate the outflow of charged particles. It is believed that radio

galaxies are low accretion mode AGN. It is worth noting though that it is believed that for example radio-quiet quasars (that usually have compact radio morphologies; Kukula et al. 1998) are high accretion rate systems (see e.g. Jarvis & Rawlings 2004). However, it has also been observationally shown that both accretion rate classes can produce similar radio luminosities and structures (e.g. Blundell & Rawlings 2001).

Radio galaxies, i.e. extended radio sources that consist of a compact core and double jets extending from the core out to Mpc scales, can be divided into two separate morphology and luminosity categories, FR I & II Classes (Fanaroff & Riley 1974). FR I sources are weaker radio galaxies, and are the brightest in the center with decreasing surface brightness towards the edges of the radio structure. FR II galaxies are more luminous, limb-brightened radio sources, often showing enhanced emission in so called 'hot spots' at the edge of the radio structure or embedded within the radio jets. The transition luminosity between the two radio galaxy classes at 1.4 GHz may be considered to be 10^{25} W Hz^{-1} (Bridle & Perley 1984).

Origin of radio emission in star forming galaxies

Radio emission from star forming galaxies arises from a combination of non-thermal synchrotron radiation from relativistic electrons and free-free emission from HII regions (see Condon 1992 for a review). Thermal reradiation of starlight by dust overtakes at frequencies above ~ 200 GHz (~ 1.5 mm), defining a practical upper bound for the 'radio' regime. The relative intensities of radio and dust radiation for the typical starburst galaxy M82 are shown in Fig. 1.6. The radio continuum accounts for less than 10^{-4} of the bolometric luminosity. Note also that at 1.4 GHz observing frequency, the radio emission from star forming galaxies is clearly dominated by synchrotron radiation, even out to the highest redshifts.

The radio emission originating from star forming galaxies is thought to be caused by Type II and Types Ib supernovae[1] whose remnants are believed to accelerate most of the relativistic electrons in these galaxies.[2] The same supernovae ionize the HII regions as well. Only stars more massive than ~ 8 M$_\odot$ produce Type II and Ib supernovae, and these have lifetimes of $\lesssim 3 \times 10^7$ yr, while the relativistic electrons probably live $\sim 10^8$ yr. Radio observations therefore probe very recent star formation in galaxies, and have several

---

[1]Supernovae are classified into two main classes based on the presence of hydrogen spectral lines: SN I, with no hydrogen lines, and SN II with hydrogen lines in their early spectra. Subclasses determined by spectral (He, Si) evidence are denoted by lower-case letter suffixes. In particular Supernovae type II and Ib are believed to be a stage of massive (> 8 $M_\odot$) star evolution, while e.g. type Ia are thought to be binary systems containing a white dwarf that accretes matter from the companion star. Radio emission has not been observed from type Ia (Weiler et al. 1986).

[2]A supernova explosion may be described as a sudden release of very hot gas into the inter stellar medium (ISM) acting as a massive piston which moves supersonically through the ISM, and therefore causes a shock front to develop ahead of the ejected material (e.g. Gull 1973). Supernovae become radio sources about 50 yr after the explosion as Rayleigh-Taylor instabilities develop at the boundary between the shock and ambient ISM, and thereby accelerate the charged particles (most probably via Fermi acceleration; e.g. Blandford & Cowie 1982).
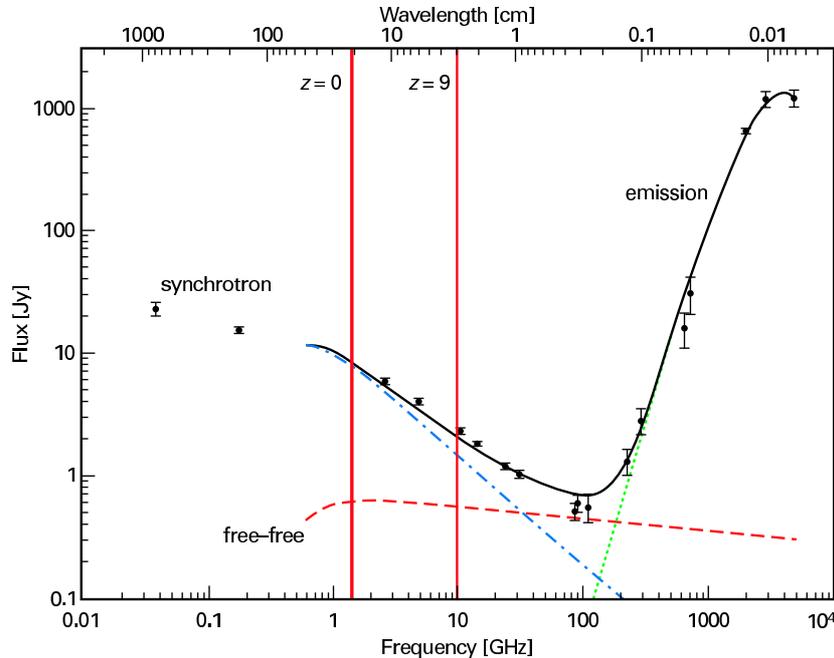
Figure 1.6 The observed radio to FIR SED of the typical starburst galaxy M 82 (symbols) modeled as the sum (black solid line) of synchrotron (blue dot-dashed line), free-free (red dashed line), and dust (green dotted line) components. Note that at an observed frequency of 1.4 GHz the observed emission is dominated by synchrotron radiation even at the highest redshifts ($z = 9$ for illustration).

advantages. First, the contribution to radio emission of stellar populations older than $\sim 10^8$ yr is insignificant. Second, the high (subarcsecond) positional accuracy of radio observations allows unambiguous panchromatic cross-identifications, and third, only radio and IR wavelengths directly trace the most intense starbursts, in such a way that the observed flux densities are accurately proportional to intrinsic luminosities (as they are not attenuated by dust).

A first sight drawback of radio emission as a star formation tracer is that radio data alone would provide a poor quantitative constraint of star formation models. The free-free radio emission emerges directly from HII regions containing the ionizing stars, and therefore the intensity of this emission is proportional to the production of Lyman continuum (UV regime) photons which directly trace the young stars. However, isolating the free-free from synchrotron emission in radio observations is technically difficult given that the flat spectrum free-free emission is usually weaker than the steeper spectrum synchrotron emission (see Fig. 1.6). On the other hand, most of the observed synchrotron radiation in star forming galaxies arises from $\gtrsim 10^7$ yr old relativistic electrons that have propagated significant distances from their parent supernovae remnants, in addition erasing any spatial information of the origin of the star formation progenitor, and therefore not providing a direct tracer of the galaxy's star formation rate. However, the tight (F)IR – radio correlation, already described in Sec. 1.1.4, provides a strong constraint of models relating radio emission to star formation. As a significant fraction of the bolometric luminosity of a galaxy is absorbed by interstellar dust and re-emitted in the thermal IR regime, the FIR luminosity provides a solid measure of the bolometric luminosity produced by young stars (see e.g. Kennicutt 1998; Bell 2003). The (F)IR – radio correlation implies that a one-parameter model specifying the (F)IR and radio luminosities in terms of recent star

formation rate can describe star forming galaxies.

Two calibrations of 1.4 GHz radio luminosity to star formation rate, developed by Condon (1992) and Bell (2003), are commonly adopted (see also Sec. 1.2.3 for the latter; see Appendix B.2 for details about the calibrations). The model developed by Condon (1992) has originally been tuned to trace the high-mass ($5 - 100$ M$_\odot$) star formation. However, it has been generalized by Haarsma et al. (2000) to a broader stellar mass range ($0.1 - 100$ M$_\odot$) and to the commonly used Salpeter initial mass function (IMF; $\psi(M) \propto M^{-2.35}$). While Condon (1992) has based his model on the Milky Way supernovae frequency in such a way that the reproduction of the FIR – radio correlation is the model's output (not input), Bell (2003) has based his radio SFR calibration on the total IR – radio correlation (also using the Salpeter IMF and the $0.1 - 100$ M$_\odot$ mass range). The difference between the two calibrations implies a factor of two uncertainty in the overall star formation rate scale based on radio.

For comparison, the UV (1250 - 2500 Å) based star formation proxy directly traces the integrated spectrum of the young stellar population (that is not dust attenuated) longward of the Lyα limit, but short enough to minimize the spectral contribution of the old stellar populations. Given different calibrations, the overall UV derived star formation rates are uncertain to a factor of 2 (see Kennicutt 1998 for a review), comparable to radio. However, an additional substantial uncertainty arises due to the significant obscuration of the UV photons by dust (see e.g. Hopkins 2004 for a summary of dust-obscuration correction methods). This is a significant uncertainty that does not affect the radio regime (as well as IR). Further, for example the tracers based on recombination lines (e.g. Hα, Hβ, Pα, Pβ), which track the re-emitted stellar luminosity shortward of the Lyman limit, and therefore directly probe young massive stellar populations, have a scatter of $\sim 30\%$ given different calibrations; while the IR star formation proxy, which traces the bolometric luminosity produced by young stars, has an intrinsic scatter of $\sim 50\%$ (Bell 2003; see also Kennicutt 1998).

1.2.3 The properties of radio sources in the local universe

In this section the major past results about the properties of radio sources in the local universe are discussed. These are mainly based on all-sky radio surveys combined with surveys at other wavelengths.

The local radio luminosity functions

The FIRST and NVSS sky surveys have significantly expanded our knowledge of properties of extragalactic radio sources in the local universe. A tremendous amount of results has emerged by combining these radio data with optical SDSS and 2dF spectroscopy (obtained over 1000's of square degrees of the sky; Ivezić et al. 2002; Sadler et al. 2002a; Best 2004; Best et al. 2005), as well as the IR IRAS (e.g. Obrić et al. 2006) and X-ray ROSAT (e.g. Brinkmann et al. 2000) all-sky surveys (see Appendix A for details about all-sky surveys). For example, the local 1.4 GHz radio luminosity function was constructed with high preci-

sion for spectroscopically identified star forming and AGN galaxies over a broad range of radio luminosities (ranging from the faintest to the brightest end; $\sim 10^{20} - 10^{26}$ W Hz^{-1}), finding a steeper slope for star forming than for AGN galaxies (Condon 1984a; Sadler et al. 1999; Jackson & Londish 2000; Chan et al. 2004; Best et al. 2005). This implies that star forming galaxies dominate the local comoving number density of radio-selected sources at low 1.4 GHz luminosity, while AGN dominate the high end; however there is no clear division in luminosity between the two.

The 1.4 GHz luminosity function for star forming galaxies was shown to agree well with the 60 μm luminosity function for star forming galaxies (see Best et al. 2005 and references therein), however seemingly deviating at the low luminosity end. This was interpreted as an indication that the radio – FIR correlation becomes non-linear at low luminosities ($< 10^{22}$ W Hz^{-1}; see also Yun et al. 2001) implying that either radio or FIR luminosity is not directly proportional to star formation. However, based on a compilation of ~ 250 local galaxies observed from UV through IR to radio, Bell (2003) has not detected such a curvature in the IR – radio correlation at low luminosities. He further showed that the IR traces most of the star formation in luminous galaxies but it traces only a small fraction of the star formation in faint galaxies. Inverting the above argument, Bell (2003) argued that the linearity of the IR – radio correlation implies that both indicators underestimate the star formation rate at low luminosities, and proposed revised star formation rate calibrations taking this effect into account. These calibrations of total IR luminosity to star formation rate, and 1.4 GHz radio luminosity to star formation rate will be used in latter sections.

Environmental dependence of star forming and AGN radio sources

The dependence on environment of radio luminous star forming and AGN galaxies has been studied in full detail in the local ($z \lesssim 0.3$) universe (Best 2004). It was demonstrated that the fraction of radio-selected star forming galaxies is lower in high-density environments ($\gtrsim 10$ Mpc^{-1}). This is consistent with the results from optical studies known for many years: star formation rates are strongly suppressed in central regions of galaxy clusters (e.g. Dressler et al. 1985; Balogh et al. 1998; Hashimoto et al. 1998; Carter et al. 2001; Lewis et al. 2002; Martini et al. 2002). On the other hand, radio luminous AGN are preferentially located in galaxy groups and poor-to-moderate richness galaxy clusters, avoiding the lowest density regions ($\lesssim 0.2$ Mpc^{-1}). Strikingly, Best (2004) has found that the ratio of *absorption-line* to *emission-line* AGN[3] dramatically changes with environment: essentially all radio luminous AGN in rich environments contain no spectral lines in emission (in the $3700 - 7900$ Å range). This result was interpreted as a consequence of i) the boosting of the AGN radio jet power (which correlates with emission line luminosity;

---

[3]These two types of radio luminous AGN, emission- and absorption-line AGN, are simply distinguished by the presence of emission lines in their optical spectra (see Chap. 3 for further discrimination of emission-line AGN from star forming galaxies which also contain emission lines in their spectra). Otherwise absorption- and emission-line AGN have comparable host galaxy properties and cover a similar range of radio luminosities.

Rawlings & Saunders 1991) due to the reduced adiabatic expansion losses caused by the jet confining effect by the intra-cluster medium (Barthel & Arnaud 1996), and ii) the lack of cold gas close to the AGN (that produces the emission lines) due to physical processes such as tidal interaction, galaxy harassment, ram pressure stripping, that may remove the gas out of galaxies, and preferentially happen in dense environments.

1.2.4 Challenges in studying evolution of the radio population

To study the evolution of the radio population, first its composition needs to be known as it consists of physically distinct types of sources (e.g. starbursts and AGN), each possibly having a different evolutionary path. The main difficulty with the interpretation of radio continuum observations (i.e. non-optical observations in general) is the immediate need for panchromatic, in particular optical, data in order to obtain i) the cosmological distance (redshift) of the observed source, and ii) the dominating origin of its radio emission. As the radio SED itself is a featureless power law (synchrotron spectrum; see Sec. 1.2.2), source redshifts cannot be determined from radio observations alone. In addition, the discrimination of the origin of radio emission requires panchromatic data. These challenges have been overcome by a large amount in the local universe due to various all-sky surveys at different wavelengths. However, panchromatic observations of the more distant universe are essential to tackle the *evolution* of radio sources.

Over the course of time the sensitivity of radio surveys has been significantly lowered allowing a better insight into the entire extragalactic radio population. However, for a long time radio sources detected in the distant universe were AGN, rather than star forming galaxies for reasons outlined below. In general, due to the difficulty in the past of obtaining panchromatic data for the observed radio sources, and therefore not being able to probe the third spatial dimension – the cosmological distance, radio astronomy diverted to modeling the 'radio source counts'.

The differential radio source counts

The most straight-forward information that can be extracted from a radio survey, without the need for panchromatic data, are the radio source counts. The slope of the counts is essentially dictated by the relative contribution of different source populations (AGN vs. star forming galaxies) at certain fluxes, which is the result of (possible) evolution of their luminosity functions with redshift. Therefore, the source counts represent a first-order observational constraint for evolutionary models of radio sources. The classical tool to test for a constant space density of sources is the '$\log N - \log S$' test (where N stands for the source space density, and S for the total flux density). The major advantage of this test is that it does not require knowledge of the cosmological distance of individual sources. [Note, however, that no information about evolution in luminosity, which has been generally found to be stronger than density evolution (e.g. Hopkins 2004; Le Floc'h et al. 2005), can be extracted using this test.] If space was Euclidian, and the space density of sources constant, then the differential radio source counts (N) would follow a power law

with an exponent of -2.5. A generalization to non-Euclidian space implies a power law with a higher exponent (i.e flatter slope in $\log N - \log S$; see e.g. Peterson 1997, Chapters 10 and 11).
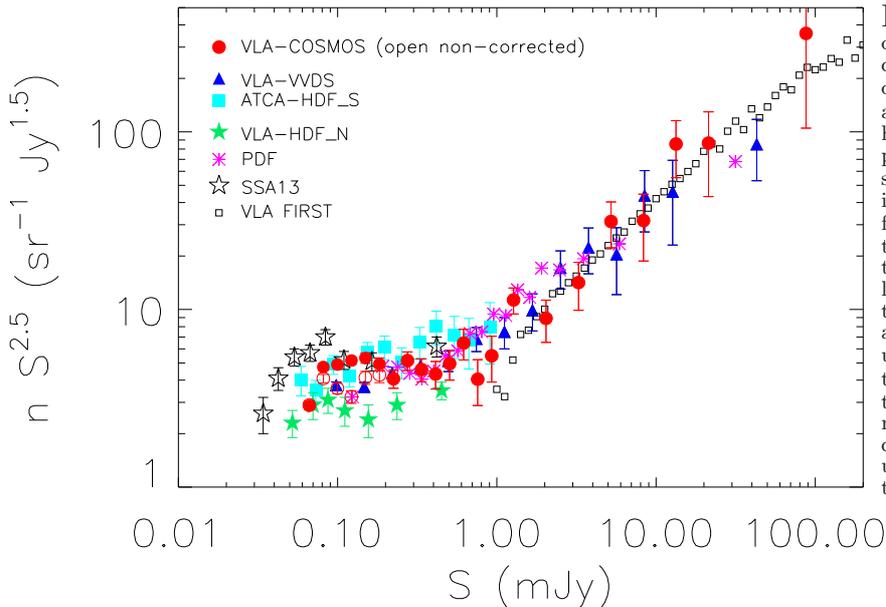
Figure 1.7 The differential radio source counts, normalized to Euclidian space, shown for various radio surveys at 1.4 GHz (indicated at the top left). The radio counts have extensively been used in the past to get an insight into the density evolution of radio sources (using the $\log N - \log S$ test; see text for details). It was shown that down to ~ 1 mJy from the highest fluxes, the counts are dominated by radio-loud FR II and FR I galaxies, while the upturn below ~ 1 mJy has been attributed to the rise of a 'new' population of objects (see text for details). However, the composition of these submillijansky radio sources is not well understood. Explaining the composition of this faint radio population is one of the major topics of this thesis.

The differential radio source counts derived by various surveys at 20 cm are shown in Fig. 1.7. At the brightest end ($\gtrsim 100$ mJy) the counts have been observed to be steeper than predicted by the $\log N - \log S$ model (i.e. at fainter fluxes more sources are observed than predicted) implying a strong positive evolution (increasing number density with increasing redshift; see also Dunlop & Peacock 1990). Based on a spectroscopically complete sample of these bright radio sources Willott et al. (2002) have shown that they are dominated by 'radio loud' objects with powerful radio-emitting jets, consistent with the Fanaroff & Riley (FR) Class II objects (see Sec. 1.2.2).

At fainter flux levels, down to ~ 1 mJy, the differential source counts follow a power law consistent with the $\log N - \log S$ model prediction, immediately excluding strong density evolution (see also Clewley & Jarvis 2004). Based on panchromatic data it has been shown that at these radio flux levels the dominant population still consists of 'radio loud' AGN, given their radio to optical flux ratios, however these objects are mainly FR I galaxies (e.g. Windhorst et al. 1993; Waddington et al. 2001). If the same population of objects would continue to dominate the differential source counts at fainter fluxes ($\lesssim 1$ mJy), they would continue to monotonically decrease following a power law (see e.g. Jarvis & Rawlings 2004). However, below ~ 1 mJy there is a significant upturn in the slope (when normalized to Euclidian space; see Fig. 1.7), and this has been attributed to the rise of a 'new' population of objects that does not significantly contribute at brighter flux levels (e.g. Condon 1984a; Windhorst et al. 1985a; Seymour et al. 2004). This population of objects is often referred to in literature as the 'submillijansky' or 'microjansky' radio population, where the first is used in the remainder of this thesis.

The 'submillijansky' radio population: controversy about its composition

Using optical spectroscopy for a fraction of sources in observed radio samples reaching to submillijansky levels (see Chap. 3 for full details) this faint radio population has been associated predominantly with spiral galaxies (Condon 1984a; Windhorst et al. 1985a; Benn et al. 1993). Although already Benn et al. (1993) pointed out that spiral galaxies may be Seyferts (therefore AGN) or star forming galaxies, in later years it has often been assumed that the submillijansky population is dominated only by star forming galaxies (e.g. Seymour et al. 2004), completely neglecting the contribution of AGN (especially radio-quiet ones). Such a simple assumption, however, is not necessarily correct for the following reasons. As stated above, past studies have well determined that *radio-loud* AGN dominate the source counts above 1 mJy. However, radio-loud AGN form *only* 10% of the overall AGN population, implying that 90% of (optically selected) AGN in the universe remain radio-quiet (e.g. Goldschmidt et al. 1999; Ivezić et al. 2002). Jarvis & Rawlings (2004) have first suggested that radio-quiet AGN may form a significant contribution to the radio population at the submillijansky flux levels, and circumstantial observational evidence verifying this has been found by Simpson et al. (2006).

To date studies of the faint radio population have not reached a concensus on the exact composition of the submillijansky radio population for several reasons that have seriously conspired. Namely, to reveal the nature of this population it is essential to characterize the physical origin of the radio emission, i.e. accurately subdivide the sources into distinct populations such as AGN- or star formation- dominated galaxies. However, the discrimination between these two types of objects is technically extremely challenging (especially beyond the local universe). The only way this can reliably be done is to assemble a wealth of panchromatic data, which is in itself a non-trivial and time consuming process. In this thesis a new deep radio survey of a large area on the sky (VLA-COSMOS - Schinnerer et al. 2007; Chap. 2), observed over the entire electromagnetic spectrum (X-ray to radio; COS-MOS - Scoville et al. 2007a), is presented (for its description see Sec. 1.3). This survey allows for the first time a full-depth analysis using to date largest, and statistically complete sample of the submillijansky radio population revealing its true nature (see Chap. 3).

The cosmic star formation history based on radio data

In the past decade the construction of large galaxy redshift surveys has allowed to estimate the evolution of the cosmic star formation rate density ('cosmic star formation history' – CSFH hereafter; e.g. Madau et al. 1996; Lilly et al. 1996; Steidel et al. 1999a; Flores et al. 1999; Haarsma et al. 2000; Hopkins 2004; Le Floc'h et al. 2005; Caputi et al. 2007), which can be interpreted as evolution of the total stellar mass in the universe generated through star formation.

Initially, a large discrepancy has been found between the CSFH derived using different, short- vs. long- wavelength, star formation tracers such as e.g. UV/optical vs. IR (e.g. Sanders 2003) or UV/optical vs. radio (Haarsma et al. 2000). This has been attributed to dust reservoirs within galaxies that attenuate large fractions of short-wavelength light

produced by young stars (see also Sec. 1.1.4). Dust obscuration has been shown to be most severe in the most intensely star forming galaxies (with high IR/radio luminosities and already assembled high stellar masses; e.g. Bell 2003) implying that UV/optical star formation tracers are most affected by attenuation in the most efficient generators of stellar mass. This precisely illustrates the already mentioned need for panchromatic observations in terms of understanding galaxy evolution. In particular, the CSFH derived using radio data is an important independent complement to the IR regime as both are dust-unbiased star formation tracers. An important prerequisite, however, for the usage of any of these two proxies is a robust discriminator between star forming and AGN galaxies in the observed monochromatic sample as both synchrotron emission and heated dust may have their origin in both, star formation and AGN related processes. This has been often neglected in the IR regime (e.g. Le Floc'h et al. 2005) for reasons such as lack of panchromatic data and commonly low angular resolution of IR observations ($\gtrsim 5$") disabling an insight into the IR morphology (e.g. nucleus vs. disk dominated radiation). On the other hand, to date the radio-based CSFH has been derived using only an extremely small sample of ~ 40 (spectroscopically selected) star forming galaxies out to high redshifts $z \sim 2$ (Haarsma et al. 2000). Obviously, large uncertainties are associated with this estimate carrying the potential for significant improvements (see Chap. 4).

Accounting for dust obscuration affecting short-wavelength star formation tracers using luminosity dependent corrections, the different wavelength based CSFHs have been put into agreement within a factor of ~ 3 scatter (out to $z \sim 1$; see Hopkins 2004) demonstrating that the cosmic (volume normalized) star formation rate has declined by an order of magnitude since $z \sim 1$. IR studies have shown that LIRGs account for the majority of the cosmic star formation rate density at $z \sim 1$ (e.g. Le Floc'h et al. 2005; Zheng et al. 2006; Caputi et al. 2007). With no attempt made to separate star forming from AGN ULIRGs Le Floc'h et al. (2005) have suggested that at ~ 2 the population dominating the cosmic star formation rate density consists of ULIRGs. However, using only two narrow redshift ranges centered at $z \sim 1$ and $z \sim 2$ Caputi et al. (2007) have cautioned that the fraction of AGN dominated ULIRGs seems to increase with redshift, and that therefore the cosmic star formation rate density is *not* dominated by *star forming* ULIRGs at $z \sim 2$. Further, only recently Daddi et al. (2007) have demonstrated that, at least at $z \sim 2$, the AGN fraction in MIR selected samples is a function of stellar mass and reaches $50 - 60\%$ at the high mass end ($> 4 \times 10^{10} \, M_{\odot}$). Overall, it remains unknown how exactly the stellar mass assembly in these most intensely star forming galaxies ($\gtrsim 100 M_{\odot} \, \mathrm{yr}^{-1}$), rarely found in space, evolves. More detailed studies of this subject have mostly been hampered by practical challenges related to observations of large comoving volumes out to high redshifts (needed to obtain statistically large enough samples of both star forming and AGN ULIRGs), and simultaneously performing panchromatic observations with comparable sensitivity (in order to efficiently separate the two classes of objects at all redshifts). In Chap. 4 of this thesis the evolution of the stellar mass generation in the most intensively star forming galaxies since ~ 5 Gyr ($\sim 1/3$ of the age of the universe) after the Big Bang ($z = 1.3$) is derived for the first time using a large sample of *star forming* ULIRGs identified in the VLA-COSMOS survey.

1.3   Studying galaxy evolution via (panchromatic) look-back surveys

1.3.1   Selection of sky area and wavelength range surveyed

Deep field surveys are the optimal tool for studying co-evolution of galaxies, such as starbursts and AGN. Because of their high sensitivity they allow constructing samples (using certain selection criteria) at different redshifts and studying how their properties evolve with cosmic time. As the ultimate goal of studying the universe via sky-surveys is to understand galaxy formation and evolution, a full panchromatic (X-ray to radio) coverage is necessary for a unified picture.

In practice, sky surveys are always a compromise between area size and sensitivity. A small-area implies possible 'cosmic variance' difficulties, and low chances of observing objects in rare phases. On the other hand, a larger area yields lower sensitivity, but gains in sampling representative large scale structure (LSS) as well as rare objects. A complex strategy is therefore required for mapping galaxy formation and evolution (i.e. the 'wedding-cake' approach). The deepest, pencil-beam surveys [HDF - Hubble Deep Field (Williams et al. 1996) and UDF – Ultra Deep Field (Beckwith et al. 2006)] are necessary to probe the galaxy inventory to the faintest levels and greatest distance. However, field of views of $2' - 3'$ correspond only to $4 - 6$ comoving Mpc at $z = 3$. For example, large differences, due to 'cosmic variance', are seen between HDF-North and HDF-South in the radio number counts (Dickinson et al. 2002; see Fig. 1.7). Simulations of LSS (ΛCDM) show that the typical scale-length of the LSS bubbles and voids is $\sim 20 - 40$ comoving Mpc (see Scoville et al. 2007a and references therein). Therefore, the minimum scale that must be covered in order to fairly sample the *full* range of environments at $z \sim 1$ is ~ 40 comoving Mpc at this redshift. This roughly corresponds to an angular field size of $1.4°$ in a ΛCDM universe.

Surveys in the past have mainly been wavelength-driven allowing for studies of specific kinds of galaxy populations. For example, optical surveys sample 'normal' galaxies and 'monsters'; IR surveys have been specialized for trying to understand the broad galaxy population called 'infrared galaxies'; surveys performed in the X-ray regime study the AGN population (and galaxy clusters). However, to reach a full consensus of galaxy properties and their evolution, understanding of the full galaxy SED is needed. Therefore, the optimal survey strategy, based on physical ground, is panchromatism, i.e. observations of a sky-area over the full electromagnetic spectrum.

1.3.2   The COSMOS and VLA-COSMOS surveys

The panchromatic (X-ray to radio) COSMOS survey (Scoville et al. 2007a) of an equatorial $1.4° \times 1.4°$ field on the sky has been optimally constructed to encompass a large enough area for sampling the full range of environments at $z \sim 1$, as well as statistically complete samples of objects in rare phases, to unprecedented sensitivity over the full electromagnetic

spectrum. This panchromatic data-set is used as the basis of this thesis. A detailed description of all aspects of this project can be found in the COSMOS ApJS special issue (September 2007, Volume 172).

COSMOS stands out among other multi-wavelength surveys (see Fig. 1.8) because of two major advantages: i) the large area provides enough sources to enable robust statistical analyses, even of low density objects in rare phases and ii) the entire field has been observed to an unprecedented depth over the full wavelength range, allowing for detailed in-depth panchromatic studies. The COSMOS field has been observed to date by the major space- (Hubble, Spitzer, GALEX, XMM, Chandra) and ground-based observatories (see Scoville et al. 2007a for details).
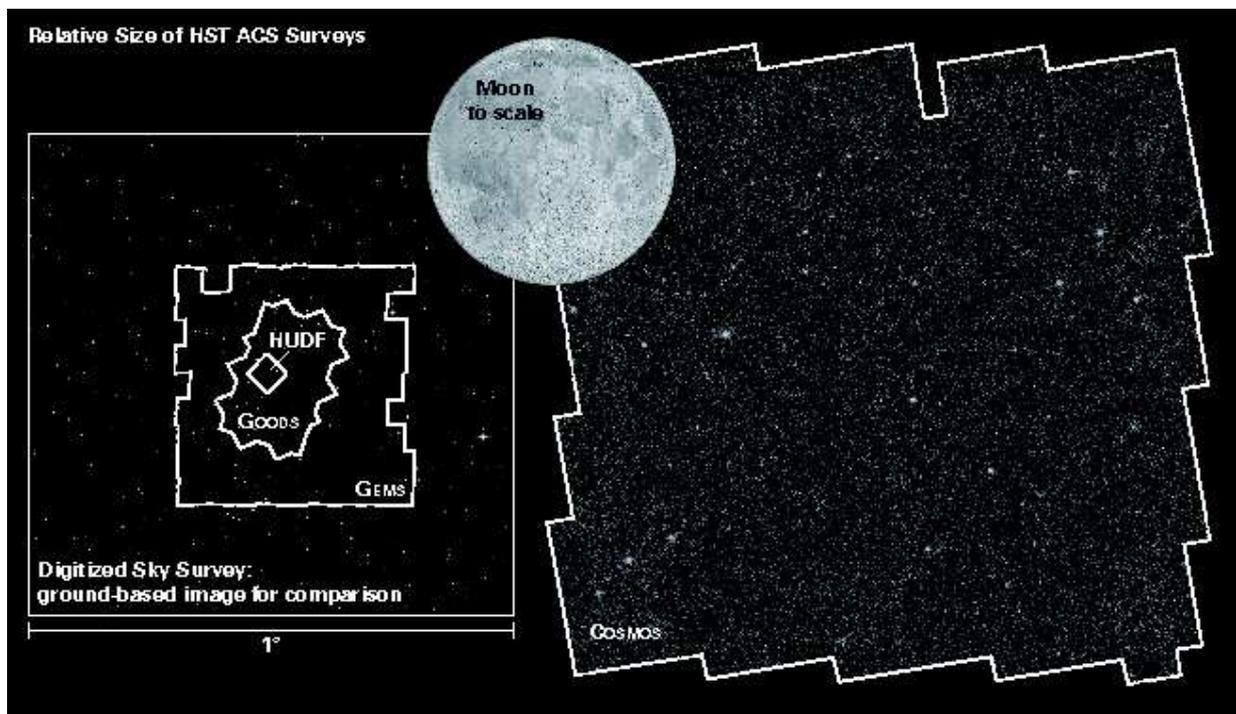
Figure 1.8   Comparison of the COSMOS 2□° field with other fields observed with the *Hubble Space Telescope*, such as GEMS (Galaxy Evolution from Morphologies and SEDs; Rix et al. 2004), GOODS (Great Observatories Origins Deep Survey, Giavalisco et al. 2004) and HUDF (Hubble Ultra Deep Field, Beckwith et al. 2006). For reference, the full Moon (0.5 deg in diameter) is also shown. The large area of the COSMOS panchromatic project has several major advantages, compared to other surveys. First, the full range of large scale structure at $z \sim 1$ is sampled, opening a new dimension for galaxy evolution studies. Secondly, for the first time in-depth studies of objects in rare phases (e.g. star forming ULIRGs) out to high redshifts, and over the full electromagnetic spectrum, are possible due to the large comoving volumes observed.

The radio observations of the COSMOS field, performed with the Very Large Array at 20 cm (see Chap. 2) are the current state-of-the-art in the radio regime, as they combine high sensitivity and high spatial resolution over such a large area. The VLA-COSMOS field contains $\sim 3,600$ sources brighter than $\sim 50~\mu\text{Jy beam}^{-1}$ (4.5σ) at a resolution of $1.5''$, and probes an unique and key area of parameter space, bridging the gap between shallow, wide

field surveys, such as FIRST (with about one million source entries), and ultra-sensitive ($\sim 5\mu$Jy), narrow field ($\sim 15'$) studies sampling only a few hundred sources with very un-uniform noise (e.g. Fomalont et al. 2006; see also Tab. 2.1). Possible comparative surveys are the Phoenix deep field, done with the ATCA (Hopkins et al.2003) or the VIRMOS 02hr field (Bondi et al. 2003). However, both surveys have a lower angular resolution which hampers the identification of the correct counterparts at other wavelengths.

One of the major advantages of the VLA-COSMOS survey is the large area observed with fairly uniform noise, yielding a statistically significant sample of faint radio sources reaching out to relevant depths. In particular, large comoving volumes observed at different cosmic times allow sampling high numbers of the rare highest luminosity galaxies (equivalent to ULIRGs) which represent an important galaxy evolutionary stage (as described in Sec. 1.1). Further, the most massive, radio selected, galaxies that locally strongly depend on environment (as shown in Sec. 1.2) are observed over the full range of LSS. The additional advantage is the full panchromatic coverage of the field, allowing in-depth studies of the radio population, with the potential of putting an end to the controversy about the composition of the submillijansky radio population using a newly developed panchromatic method that efficiently separates radio-luminous AGN from star forming galaxies (see Chap. 3). Further, the cosmic star formation history of the spatially rare objects (ULIRGs) at the high-luminosity end can for the first time be robustly derived using high-quality radio data (see Chap. 4).

The VLA-COSMOS 1.4 GHz survey of the 2$\square$° COSMOS field is presented in Chap. 2, where the observations, data reduction, imaging and extensive tests are discussed. In Chap. 3 the classification of the VLA-COSMOS radio population is presented, and the composition of the submillijansky radio sources is studied using the full COSMOS panchromatic data-set. The cosmic star formation history since $z = 1.3$ is is constrained in Chap. 4 using the well defined sample of VLA-COSMOS intensively star forming galaxies. An in-depth case study of a peculiar radio galaxy in a merging cluster environment is given in Chap. 5. The major scientific results presented in this thesis and future prospects are summarized in Chap. 6.

Chapter 2

The VLA-COSMOS Survey: Source catalog of the Large Project

In this Chapter the VLA-COSMOS Large Project is described, from initial observations to the final source catalog which is publically available. This work has been published in the COSMOS ApJS special issue as:

Schinnerer, E., Smolčić, V., Carilli, C. L., Bondi, M., Ciliegi, P., Jahnke, K., et al., 2007, ApJS, 172, 46, *The VLA-COSMOS Survey. II. Source Catalog of the Large Project*[1]

Abstract

The VLA-COSMOS large project is described and its scientific objective is discussed. We present a catalog of $\sim 3,600$ radio sources found in the $2\square°$ COSMOS field at $1.4\,\mathrm{GHz}$. The observations in the VLA A and C configuration resulted in a resolution of $1.5'' \times 1.4''$ and a mean rms noise of $\sim 10.5(15)\,\mu\mathrm{Jy/beam}$ in the central $1(2)\,\square°$. 80 radio sources are clearly extended consisting of multiple components, and most of them appear to be double-lobed radio galaxies. The astrometry of the catalog has been thoroughly tested and the uncertainty in the relative and absolute astrometry are $130\,\mathrm{mas}$ and $<55\,\mathrm{mas}$, respectively.

2.1 Introduction

The radio source counts above the milli-Jansky level are dominated by radio galaxies and quasars powered by active galactic nuclei (AGN) in elliptical host galaxies. How-

---

[1] Although second author in the published version, the work presented in this Chapter done by the author of this thesis (VS) accounts for $\sim 80\%$ full time work during more than the first half of the PhD (> 1.5 years), and specifically includes $\sim 70\%$ of the VLA-COSMOS data reduction; performing extensive tests on the optimal imaging set-up (including self-calibration); imaging about 80% of the data; performing and writing up the tests presented in the paper on the flux calibration and (relative and absolute) astrometry, as well as correlating the FIRST, NVSS and VLA-COSMOS catalogs for comparison of integrated flux densities of common sources; and producing 8/18 figures presented in the paper. The source catalog was produced by MB and PC (INAF, Bologna, Italy). The VLA observational set-up was done by ES (PI; MPIA, Germany) and CC (NRAO, Socorro), and the catalog verification by ES and KJ (MPIA, Germany).

ever, deep radio surveys at $1.4\,\text{GHz}$ show an upturn in the integrated source counts at sub-mJy levels revealing the presence of a population of faint radio sources far in excess of those expected from the high luminosity radio galaxies and quasars which dominate at higher fluxes (Windhorst et al. 1985b; Hopkins et al. 1998; Ciliegi et al. 1999; Richards 2000; Prandoni et al. 2001; Hopkins et al. 2003; Huynh et al. 2005). While radio sources with relatively bright optical counterparts are starburst galaxies (e.g. Benn et al. 1993; Afonso et al. 2005), the ones with fainter optical counterparts are often redder as expected for early type galaxies (Gruppioni et al. 1999). Recent detailed multi-wavelength follow-up of faint radio sources showed a mixture of active star forming galaxies and AGN hosts (Roche et al. 2002; Afonso et al. 2006). The exact mixture of these different populations (high-z AGN out to the highest redshifts, intermediate-z post starburst, and lower-z emission line galaxies) as a function of radio flux level is not very well established, especially in the μJy regime.

In order to fully investigate the nature and evolution of the μJy population it is necessary to couple deep radio observations with high quality imaging and spectroscopic data from other wavelengths covering as much of the electromagnetic spectrum as possible. The international COSMOS (Cosmic Evolution) survey (Scoville et al. 2007a)[2] provides such a unique opportunity. COSMOS is a pan-chromatic imaging and spectroscopic survey of a $1.4° \times 1.4°$ field designed to probe galaxy and SMBH (super-massive black hole) evolution as a function of cosmic environment. One major aspect of the COSMOS survey is the HST Treasury project (Scoville et al. 2007c), entailing the largest ever allocation of HST telescope time. The equatorial location of the COSMOS field offers the critical advantage of allowing major observatories from both hemispheres to join forces in this endeavor. State-of-the-art imaging data at all wavelengths (X-ray to centimeter, e.g. Hasinger et al. 2007; Schinnerer et al. 2007; Taniguchi et al. 2007; Capak et al. 2007; Bertoldi et al. 2007; Aguirre et al. 2007; Schinnerer et al. 2004) plus large optical spectroscopic campaigns using the VLT/VIMOS and the Magellan/IMACS instruments (Lilly et al. 2007; Impey et al. 2007; Trump et al. 2007) have been or are currently being obtained for the COSMOS field. These make the COSMOS field an excellent resource for observational cosmology and galaxy evolution in the important redshift range $z \sim 0.5 - 3$, a time span covering $\sim 75\%$ of the lifetime of the universe.

One major scientific rationale of the COSMOS survey is to study the relation between the large scale structure (LSS) and the evolution of galaxies and SMBHs. In a ΛCDM cosmology, galaxies in the early universe grow through two major processes: dissipational collapse and merging of lower mass protogalactic and galactic components. Their intrinsic evolution is then driven by the conversion of primordial and interstellar gas into stars, with galactic merging and interactions triggering star formation and starbursts. Mergers also can perturb the gravitational potential in the vicinity of the black hole, thus initiating or enhancing AGN activity. Several lines of evidence suggest that galaxy evolution and black hole growth are closely connected; COSMOS offers the chance to observe this connection directly. While there is general agreement over this qualitative picture, the

---

[2]http://www.astro.caltech.edu/~cosmos

timing/occurrence of these events and their dependence on the local environment remains to be observationally explored (e.g. Ferguson et al. 2000). To study LSS it is essential to obtain high spatial resolution data over the entire electromagnetic spectrum covering a significant area on the sky, like $2\square°$ as in the case of the COSMOS survey. Also, surveys of active galactic nuclei benefit from such a combination of areal coverage and depth.

For the radio observations at $1.4\,\mathrm{GHz}$, it was essential to match the typical resolution for optical-NIR ground-based data of $\sim 1''$ to fully exploit the COSMOS database. Therefore observations with the NRAO Very Large Array (VLA) had to be conducted in the A-array that provides a resolution of about $2''$ (FWHM) at $1.4\,\mathrm{GHz}$. Mosaicking is necessary to cover the large area of the COSMOS field. The VLA-COSMOS survey consists of the pilot project (Schinnerer et al. 2004), the large project (presented here) and the ongoing deep project (focusing on the central $1\square°$; Schinnerer et al., in prep.). The VLA-COSMOS pilot project tested the mosaicking capabilities in the VLA A-array at $1.4\,\mathrm{GHz}$ in the wide-field imaging mode and has provided the initial astrometric frame for the COSMOS field.

Here we present the source catalog derived from the $1.4\,\mathrm{GHz}$ image of the VLA-COSMOS large project. The paper is organized as follows: after a brief description of the survey objective (Sec. 2.2), the details of the observations and data reduction are presented in Sec. 2.3 and Sec. 2.4, respectively. In Sec. 2.5, we discuss our tests for flux and astrometric calibration. The VLA-COSMOS catalog is described in Sec. 2.6, while the context of the VLA-COSMOS survey within the COSMOS project is discussed in Sec. 2.7.

2.2 Survey objective

Unlike most existing deep survey fields, the COSMOS field is equatorial and hence has excellent accessibility from all ground-based facilities (current and future such as [E]VLA and ALMA). In addition, it has an extensive multi-wavelength coverage (Scoville et al. 2007a). This makes it an ideal field to analyze the (faint) radio source population as a function of redshift, environment, galaxy morphology and other properties. The VLA-COSMOS radio observations were matched to study a range of important issues related to the history of star formation, the growth of super-massive black holes, and the spatial clustering of galaxies. The ongoing spectroscopic surveys within the COSMOS project are also targeting well-defined samples of radio sources as part of the overall program. In addition, the VLA-COSMOS radio survey is providing the absolute astrometric frame for the COSMOS field (Aussel et al., in prep), which is important given the field's large size.

In this paper we describe in detail the observing procedure, and various tests on data quality and characteristics (astrometry, fitted source parameters, etc.; see also the pilot project paper by Schinnerer et al. 2004). The completeness tests and the number counts of this survey are under-way (Bondi et al., in prep.) as well as the identification of optical counterparts using the space- and ground-based COSMOS imaging data (Ciliegi et al., in prep.). The full source catalog is available from the COSMOS archive at IPAC/IRSA[3]. Subsequent papers will consider important scientific issues such as: (i) the evolution of

---

[3]http://www.irsa.ipac.caltech.edu/data/COSMOS/

radio-loud AGN as a function of environment, including comparison to X-ray AGN and clusters (see also Smolčić et al. 2007a, Chap. 5), and a search for type-II radio QSOs, and (ii) a dust-unbiased survey of star forming galaxies, as revealed in the sub-mJy radio source population, including consideration of the evolution of the radio-FIR correlation out to $z \sim 1$ through comparison with the Spitzer data, and of extreme, high z starbursts as seen in the MAMBO 250 GHz COSMOS survey (Bertoldi et al. 2007). In the following sections we describe the goals of these two key science programs in more detail.

2.2.1   Survey area

The sub-mJy radio source counts provide one of the best indicators of the effect of cosmic variance: number counts of sub-mJy radio sources in fields of order of $\sim 10'$ in diameter show a factor three variation (e.g. Hopkins et al. 2003), indicating that such field sizes are inadequate to map cosmic large scale structure. Thus to properly sample the faint radio source population and map out its cosmic structure to the largest relevant scales, it is necessary to survey a large area at the same resolution and sensitivity. Proper studies of source clustering require hundreds to thousands of sources. In order to enable detailed studies of environmental effects on faint, distant radio source distributions and properties, all as a function of redshift, several thousand sources are required as well.

Deep radio imaging of the $2\square°$ COSMOS field with $\sim 3,600$ sources allows one to probe a - unique and - key area of parameter space. The combination of high sensitivity and high spatial resolution over a large area (see Tab. 2.1) bridges the gap between shallow, wider field surveys, such as FIRST (Becker et al. 1995) and NVSS (Condon et al. 1998) with about one million source entries, and ultra-sensitive ($\leq 5-7\mu\text{Jy}$), narrow field (single VLA primary beam $\sim 30'$ FWHM) studies of a few hundred sources, such as those by Fomalont et al. (2006); Richards (2000). Surveys which are comparable in scope to the VLA-COSMOS large project are the Phoenix deep field survey (PDS), undertaken with the ATCA (Hopkins et al. 2003), and the VVDS 02hr field done with the VLA in B-array (Bondi et al. 2003). These surveys produce a lower angular resolution and a slightly higher rms (see Tab. 2.1).

2.2.2   Star forming galaxies

Tracing the evolution of the cosmic star formation history from optical surveys bears the large uncertainty of dust corrections (e.g Steidel et al. 1999b). Deep VLA observations of the COSMOS field can provide a unique, unobscured look at star forming galaxies and highly extincted galaxies in the full range of environment, especially in combination with the deep (sub)mm data (Bertoldi et al. 2007; Aguirre et al. 2007) and deep Spitzer infrared imaging (Sanders et al. 2007) to which the high resolution of the VLA images provides means to properly identify luminous infrared galaxies (see Fig. 2.1). The VLA radio data will particularly be helpful to (a) trace the cosmological star formation history and (b) test the FIR/radio correlation at high redshifts. The radio luminosity of local galaxies is well-correlated with their star formation (SF) rate (Condon 1992), and needs,

Table 2.1 Radio Surveys at 1.4 GHz

Field	Area [$\square°$]	rms [μJy/beam]	resolution [$''\times''$]	# of objects	Reference
COSMOS (large)	2	10.5	1.5×1.4	3643	this paper
COSMOS (pilot)	0.837	25	1.9×1.6	246	Schinnerer et al. 2004
HDFN	0.35	7.5	2.0×1.8	314	Richards 2000
SSA 13	0.32	4.8	1.8	810	Fomalont et al. 2006
FIRST	10,000	150	5	1,000,000	Becker et al. 1995
FLS	5	23	5	3565	Condon et al. 2003
VVDS	1	17	6	1054	Bondi et al. 2003
ATHDFS	0.35	11	7.1×6.2	466	Norris et al. 2005, Huynh et al. 2005
ATESP	26	79	14×8	2960	Prandoni et al. 2001
PDS	4.56	12	12×6	2090	Hopkins et al. 2003
ELAIS[a]	4.22	27	15	867	Ciliegi et al. 1999
Lockman	0.35	120	15	149	de Ruiter et al. 1997
NVSS	34,000	350	45	1,700,000	Condon et al. 1998

[a]consists of 3 fields of the ELAIS survey: N1, N2, and N3

unlike optical tracers, no correction for dust obscuration. Thus radio sources with correct spectral identification (as star forming galaxies) can be independently used to estimate the SF history (of the luminous sources).

Recent work by Haarsma et al. (2000) for three deep radio surveys confirms the trend of rising star formation rate between $z = 0$ and $z = 1$, however their calculated star formation rates are significantly larger than even dust-corrected optically selected star formation rates. A key uncertainty is the contribution of AGN to the faint (< 1mJy) radio population, with estimates ranging from 20% to 80% for surveys down to $40\,\mu$Jy. The (far)IR-radio correlation for star forming galaxies appears to hold out to high redshift (Garrett 2002; Appleton et al. 2004). However, the number of star forming sources detected at 1.4 GHz is small above $z = 0.5$. A thorough understanding of the IR-radio correlation out to higher redshifts is important, as it has been widely used as a distance measure for sub-mm sources without any optical counterparts (Carilli & Yun 2000; Aretxaga et al. 2005). Also, an important question for active star forming galaxies is the role of mergers, in particular at higher redshift. The FIR imaging alone will lack sufficient resolution to address this issue, while the optical imaging will suffer from the standard problem of obscuration in these very dusty systems. Only arcsecond resolution radio data will allow the determination of the spatial distribution of star formation in dusty starbursts on scales relevant for merging galaxies (~ 10 kpc).

2.2.3   Active galactic nuclei

Only a large field and deep radio survey can provide information about the evolution of the currently highly uncertain faint-end of the radio luminosity function. The fundamental problem in the study of the evolution of radio-loud AGN has been that samples are drawn from either very wide field, but very shallow surveys, or very deep, but very small field surveys. The former are limited at high redshifts to only extreme luminosity sources,
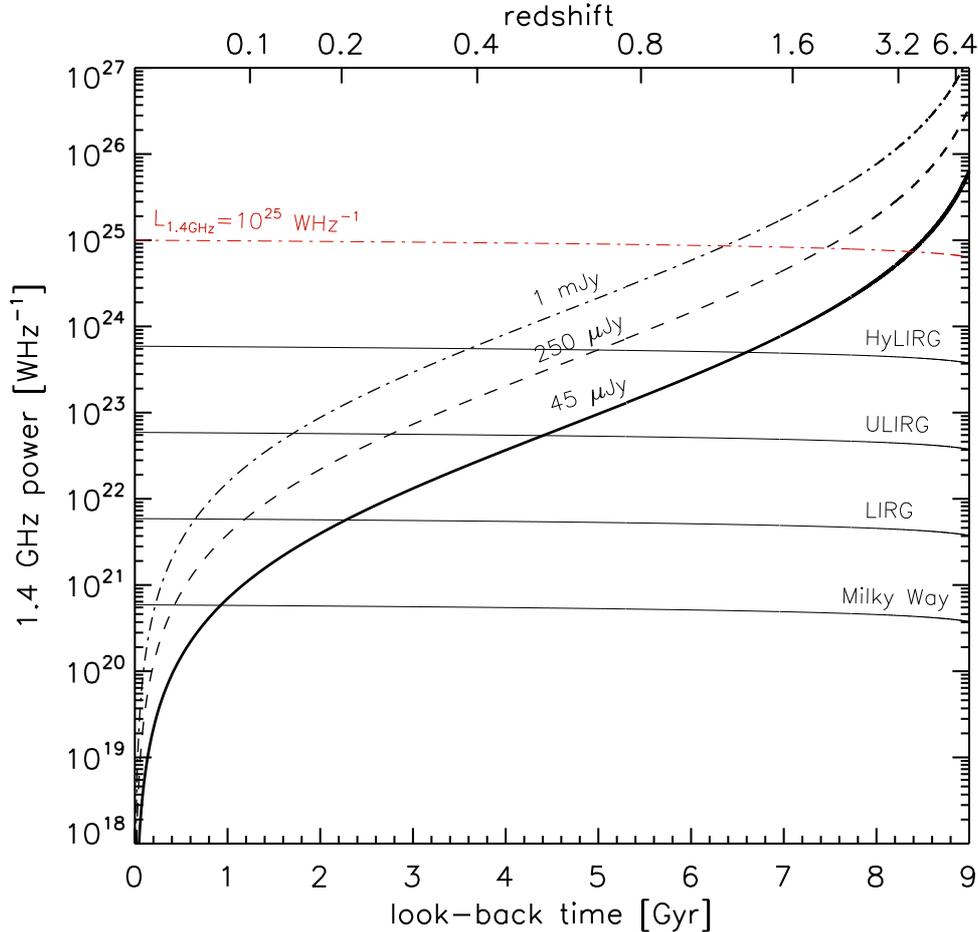
Figure 2.1 The sensitivity limit as a function of (intrinsic) 1.4 GHz luminosity (or power). The limit for the VLA-COSMOS large project corresponds to the bold solid line. The expected luminosities for various classes of galaxies are indicated by the solid horizontal lines. The expected radio power was calculated using the local IR-radio relation (Condon 1992) and assuming a spectral index of $\alpha = 0.8$. The horizontal dashed-dotted line corresponds to the assumed dividing line between radio-quiet and radio-loud AGN. (See text for details.)

while the latter are plagued by relatively small number statistics and number variance. The VLA-COSMOS survey was designed to enable the study of the demographics and evolution of AGN by encompassing a large cosmological volume and by providing good statistics on both radio-loud and radio-quiet AGN as a function of redshift.

Only sub-mJy sensitivities over a wide area are adequate to detect relatively weak (FRI) radio AGN to very high redshift (z $\sim$ 6) while providing a large number ($\sim$ 1000) of AGN sources. At lower redshift, z $\sim$ 1, a sensitivity of $1\sigma \approx 10\,\mu$Jy/beam is good enough to detect a significant fraction of radio-quiet, optically-selected QSOs. Moreover, questions regarding redshift evolution of FRI and FRII sources, their parent galaxy properties, and environmental dependencies can be addressed independently for QSOs and radio galaxies. Such observations are sensitive enough to reach the classic boundary between radio-loud and radio-quiet AGN (log $L_{1.4\,\mathrm{GHz}}$ [W Hz^{-1}] = 25) at z $\sim$ 4-5 (depending on the exact

Table 2.2 VLA-COSMOS Large Project Pointing Centers

Pointing #	R.A. (J2000)	DEC (J2000)	Remark
F01	10:02:28.67	+02:38:19.84	
F02	10:01:28.64	+02:38:19.84	
F03	10:00:28.60	+02:38:19.84	
F04	09:59:28.56	+02:38:19.84	
F05	09:58:28.52	+02:38:19.84	
F06	10:01:58.66	+02:25:20.42	
F07	10:00:58.62	+02:25:20.42	P1 in pilot project
F08	09:59:58.58	+02:25:20.42	P2 in pilot project
F09	09:58:58.54	+02:25:20.42	
F10	10:02:28.67	+02:12:21.00	
F11	10:01:28.64	+02:12:21.00	P3 in pilot project
F12[a]	10:00:28.60	+02:12:21.00	P4 in pilot project
F13	09:59:28.56	+02:12:21.00	P5 in pilot project
F14	09:58:28.62	+02:12:21.00	
F15	10:01:58.66	+01:59:21.58	
F16	10:00:58.62	+01:59:21.58	P6 in pilot project
F17	09:59:58.58	+01:59:21.58	P7 in pilot project
F18	09:58:58.54	+01:59:21.58	
F19	10:02:28.67	+01:46:22.24	
F20	10:01:28.64	+01:46:22.24	
F21	10:00:28.60	+01:46:22.24	
F22	09:59:28.56	+01:46:22.24	
F23	09:58:28.52	+01:46:22.24	

[a]COSMOS field center

spectral index; see Fig. 2.1). Highly luminous radio-loud objects such as Cygnus A with $\log L_{1.4\,GHz} [W\,Hz^{-1}] \sim 34$ (Carilli & Barthel 1996) should be observable out to their epoch of formation.

2.3 Observations

The goal of the large project of the VLA-COSMOS survey was to image the entire COSMOS field with an as large as possible uniform rms coverage while minimizing the observing time required. Since the observations had to be finished within one configuration cycle, special requirements arose for the pointing lay-out and the observing strategy.

2.3.1 Lay-out of the pointing centers

The pointing lay-out was designed to maximize the uniform noise coverage while minimizing the number of pointings required to limit overhead due to slewing ($\sim$30 s slewing time for each change of pointing). A hexagonal pattern of the pointing centers provides both a uniform sensitivity distribution and a high mapping efficiency for large areas (see Condon et al. 1998). To minimize the effect of bandwidth smearing, we used – as already tested in the pilot observations (Schinnerer et al. 2004) – a separation of 15′ between the individual field centers. A total of 23 separate pointings was required to fully cover the 2□° of the COSMOS field (see Tab. 2.2 and Fig. 2.2).
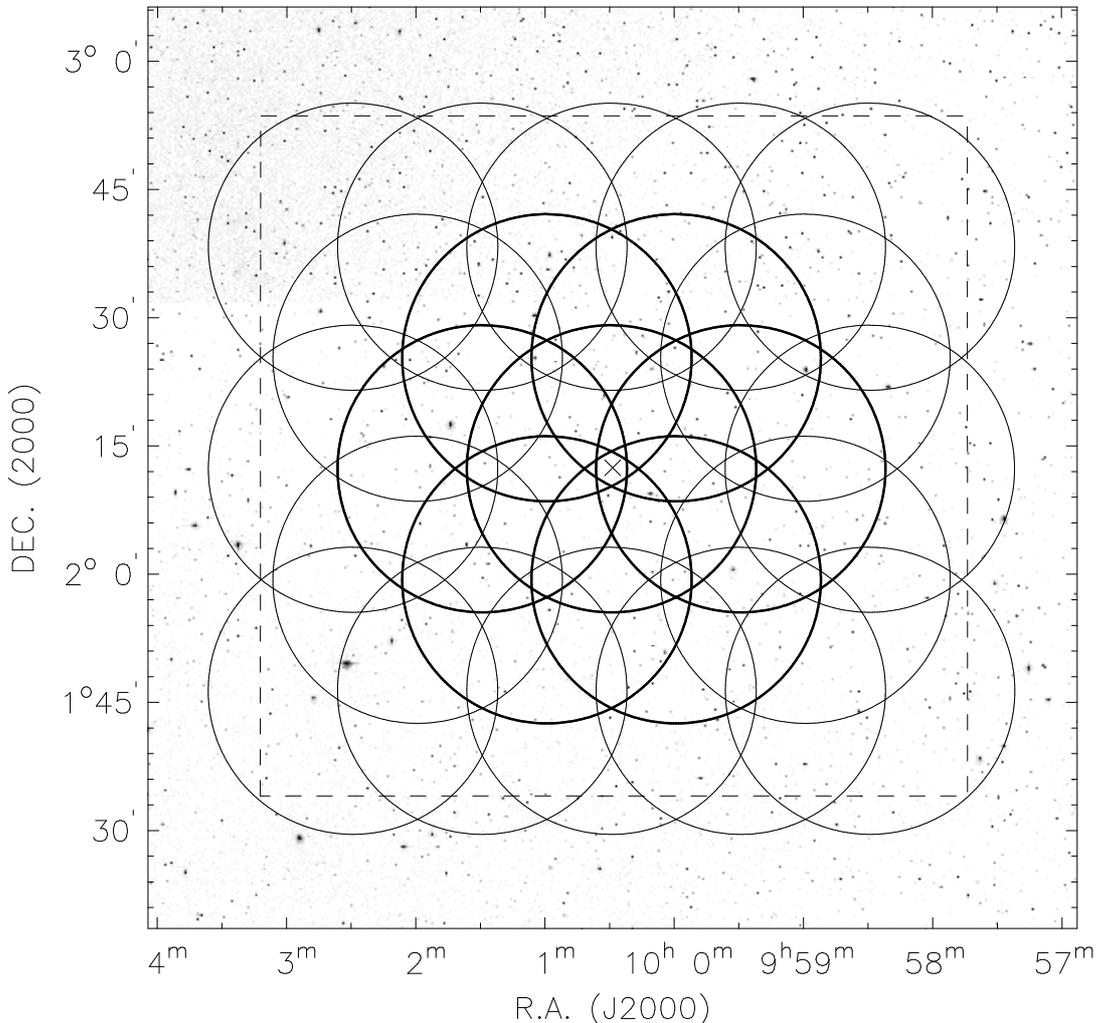
Figure 2.2 The pointing pattern of the VLA-COSMOS Large Project overlaid onto a DSS image of the area of the COSMOS field. The heavy-outlined circles indicate the pointings observed in the VLA-COSMOS pilot project (Schinnerer et al. 2004). Each pointing has a radius of 16.8′ corresponding to the cut-off radius used for making the mosaic. The dashed line marks the outline of the COSMOS field covered by ACS tiles from the HST-COSMOS survey (see Scoville et al. 2007c).

2.3.2   Correlator set-up and calibrators

We used the standard VLA L-band continuum frequencies of 1.3649 and 1.4351 GHz and the multi-channel continuum mode to minimize the effect of bandwidth smearing (in the A configuration). This results in two intermediate frequencies (IF) with two polarizations, providing 6 useable channels of 3.125 MHz each, or a total bandwidth of 37.5 MHz (observed with both polarizations). (Nominally, 7 channels are available, however, due to the largely reduced sensitivity in the last channel, we only used channels 1 to 6.)

The quasar 0521+166 (3C 138) served as flux and bandpass calibrator and was observed at the beginning of each observation. To allow for good correction of atmospheric amplitude

and phase variations, we selected the quasar 1024-008 which was already used in the pilot observations (Schinnerer et al. 2004). 1024-008 is about 6.1° away from the COSMOS field center and has a flux of about 1 Jy at 1.4 GHz. Its positional accuracy is better than 0.01″ (VLA Calibrator Manual 2003); the positional difference is less than 0.001″ between coordinates listed in the VLA Calibrator Manual and its ICRF (International Celestial Reference Frame; Fey et al. 2004) position.

The quasar 0925+003 at a distance of about 9° from the COSMOS field center was observed to test the absolute astrometric accuracy of the observations. Its positional accuracy is known to better than 0.002″, and its 1.4 GHz flux is similar to the one of 1024-008. It was also used to test the flux calibration (see Section 2.5).

2.3.3   Observing strategy

This project holds the status of a VLA Large Project, as it required 240 hrs of observing time in the A configuration alone. The observations were scheduled in blocks of 6 hrs centered at the Local Siderial Time (LST) of 10:00 hr. This ensured that the COSMOS field was always above 40° elevation during our observations to keep the system temperature of the L-band receivers low. These observing blocks were scheduled over 42 days between September 23th, 2004 and January 9th, 2005 for the A configuration, and between August 26th, 2005 and September, 25, 2005 for the C configuration. The observing time for the C configuration consisted of 4 observing blocks each 6 hrs long, except for the last observation that was 1.5 hrs longer.

In order to minimize the impact of varying observing conditions – especially during the A array observations – onto the mosaic we adopted the following scheme: (a) all 23 pointings were observed with about 6.5 minutes integration time twice each day, (b) the starting pointing was changed each time, (c) the flux calibrator 0521+166 was only observed at the beginning (since interpolation between days in case of a loss was acceptable[4] (d) the phase calibrator 1024-008 was observed every 28 to 35 minutes, and (e) the test calibrator 0925+003 was observed twice each day after about one-third and two-thirds of the available observing time. The rotation of the pointings with observing days also resulted in a more complete uv coverage, and therefore a rounder synthesized (i.e. DIRTY) beam.

2.4   Data reduction and imaging

2.4.1   Data reduction

The data reduction was done using the Astronomical Imaging Processing System (AIPS; Greisen 2003) following the standard routines as described in the VLA handbook on Data Reduction. For the flux calibration and the correction of the atmospheric distortions we used the pseudo-continuum channel. Before and after this calibration, uv points (of the

---

[4]During the observations this happened only once, and the flux of the phase calibrator 1024-008 was fairly stable through the curse of observations (see Sec. 2.5.1).

two calibrators 0521+166 and 1024-008) affected by radio frequency interference (RFI) were flagged by hand using the AIPS task 'TVFLAG'. As the data were obtained in the multi-channel continuum mode, a bandpass calibration was performed on the 'Line' data after the flux and phase calibration of the pseudo-continuum channel had been transfered to the 'Line' data. In order to exclude remaining RFI in the source data (i.e. the individual COSMOS fields), we checked all channels (per IF and polarization) for RFI using 'TVFLG' and flagged affected points accordingly. During all A-array observations, significant RFI (affecting $\sim 15\%$ of the data) was found to be present on IF2 in channel 4 to 6. In addition, all uv data points in the A-array data above an amplitude of 0.4 Jy were clipped, since no such strong source is present in any individual field. The C-array observations were affected by strong RFI and solar interference, so that only baselines larger than 2.5 kλ and 1 kλ were included from the data of the first three days and the last day of observations, respectively. The clipping level was set to 0.45 Jy for the C-array data.

2.4.2 Imaging

We performed substantial testing for best imaging quality including the application of self-calibration on the COSMOS fields themselves. It was found that no combination of parameters for the self-calibration in the task 'CALIB' would yield a significant improvement of the rms (of $> 3\%$). A robust weighting of 0 provided the best compromise for the combined A+C array data between a fairly Gaussian synthesized beam (Fig. 2.3), and still good sensitivity, i.e. the deviation from Gaussianity only starts below $\pm 10\%$ of the peak. This proved to be especially important for fields which contained bright sources (with peak fluxes up to 10 mJy/beam) where tests showed that sidelobe artifacts are lowest when using a robust weighting of 0. The nominal increase in the noise compared to natural weighting is 1.265. However, the gain in better cleaning results around bright sources is larger than this nominal increase. Thus in order to achieve an uniform as possible rms across the entire COSMOS field, a robust weighting of 0 is used.

In order to avoid geometric distortions due to the non-planarity of the wide-field on the sky, each field was divided into 43 facets of 2048×2048 pixels which were imaged using the option DO3DIMAG in the AIPS task 'IMAGR'. The pixel scale of $0.35''$/pixel has been well matched to the A+C-array beam size of FHWM $1.5'' \times 1.4''$ (PA $\sim -50^o$) for a robust weighting of 0 (Fig. 2.3 and 2.4). For each field, a contiguous area of about $1°$ diameter was covered by the facets. Additional smaller facets of 128×128 pixels were made using the task 'SETFC' for positions of NVSS sources with peak fluxes above 0.1 Jy and within a radial distance of $1.5°$ from the pointing center. This ensured that sidelobes from strong sources outside the central $1°$ were CLEANed as well.

Since most of the COSMOS fields are affected by the sidelobes of radio galaxies with peak fluxes between 1 to 15 mJy/beam, best CLEANing results were obtained if CLEAN boxes for individual sources were provided. This ensured that CLEANing of negative or positive residuals was minimized. In order to derive the CLEAN boxes for each field, we used the AIPS task 'IMAGR' to interactively select the CLEAN boxes in all facets where significant sources were present. This procedure was performed combining the data of
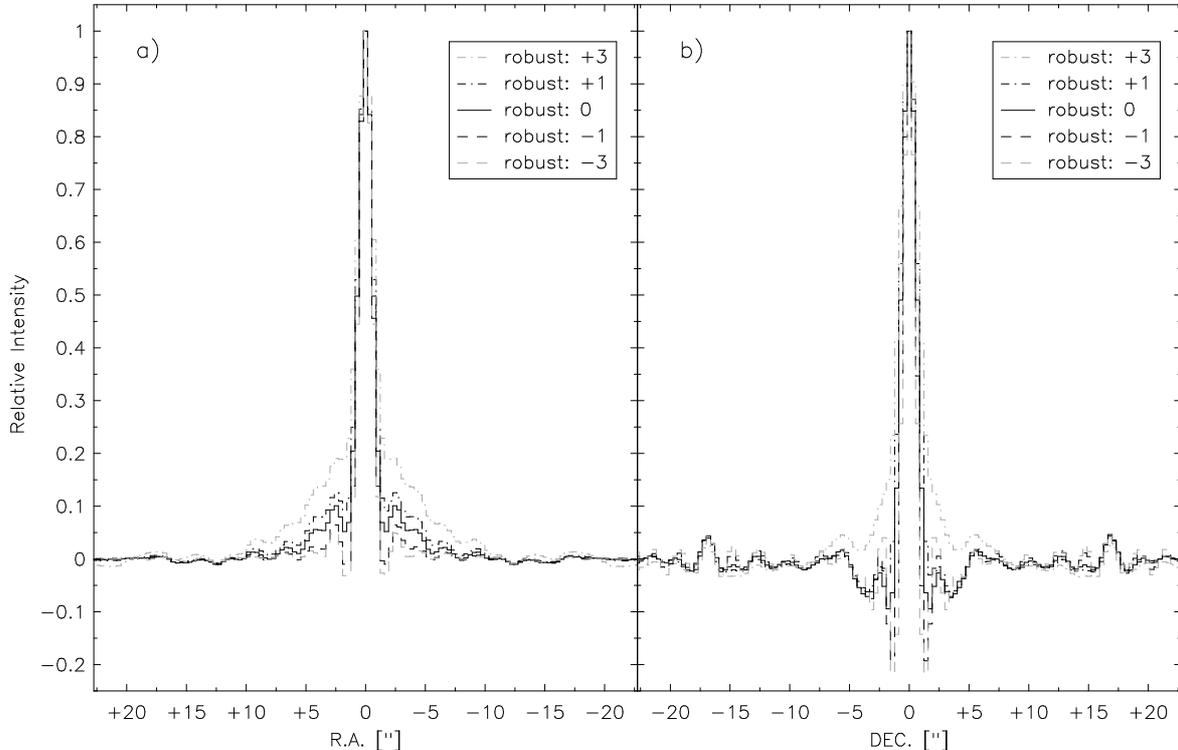
Figure 2.3 Cuts along the x- (*a*) and y-axis (*b*) of the synthesized (i.e. DIRTY) beam for different values of the robust weighting: +3 (*grey dashed dotted line*), +1 (*dashed dotted line*), 0 (*solid line*), -1 (*dashed line*), and -3 (*grey dashed line*). A value of 0 for the robust parameter gave the best compromise between synthesized beam shape and rms noise (see text for details).

all polarizations and IFs into one single image to obtain the highest possible S/N image. The resulting list of CLEAN boxes was saved. In addition, we required that CLEAN components were subtracted from the *uv* data after a facet had been cleaned. This way, CLEAN components in overlapping facets were not treated separately. In addition, this requirement also reduced the effect of sidelobe bumps from strong sources in neighboring facets.

We would like to note at this point that the reduction process of the VLA-COSMOS Pilot and Large dataset was not exactly identical. While self-calibration was applied to the Pilot data, this step was not done while reducing the Large survey data: after detailed empirical testing of the improvements due to self-calibration in the VLA-COSMOS Large project, we concluded that no significant improvement was achieved, likely due to the lack of sufficiently bright sources in all parts of the entire COSMOS field. Since self-calibration adjusts the observed visibility phases to model phases, it has the potential to alter the position of a given source. However, it is expected that these effects cancel out when using several sources within a given pointing.

For the final stage of CLEANing, it turned out that the well known 'beam squint' of the VLA (i.e. slightly different pointing centers for R and L polarization), and the slightly different frequency coverages required separate imaging of all polarizations and
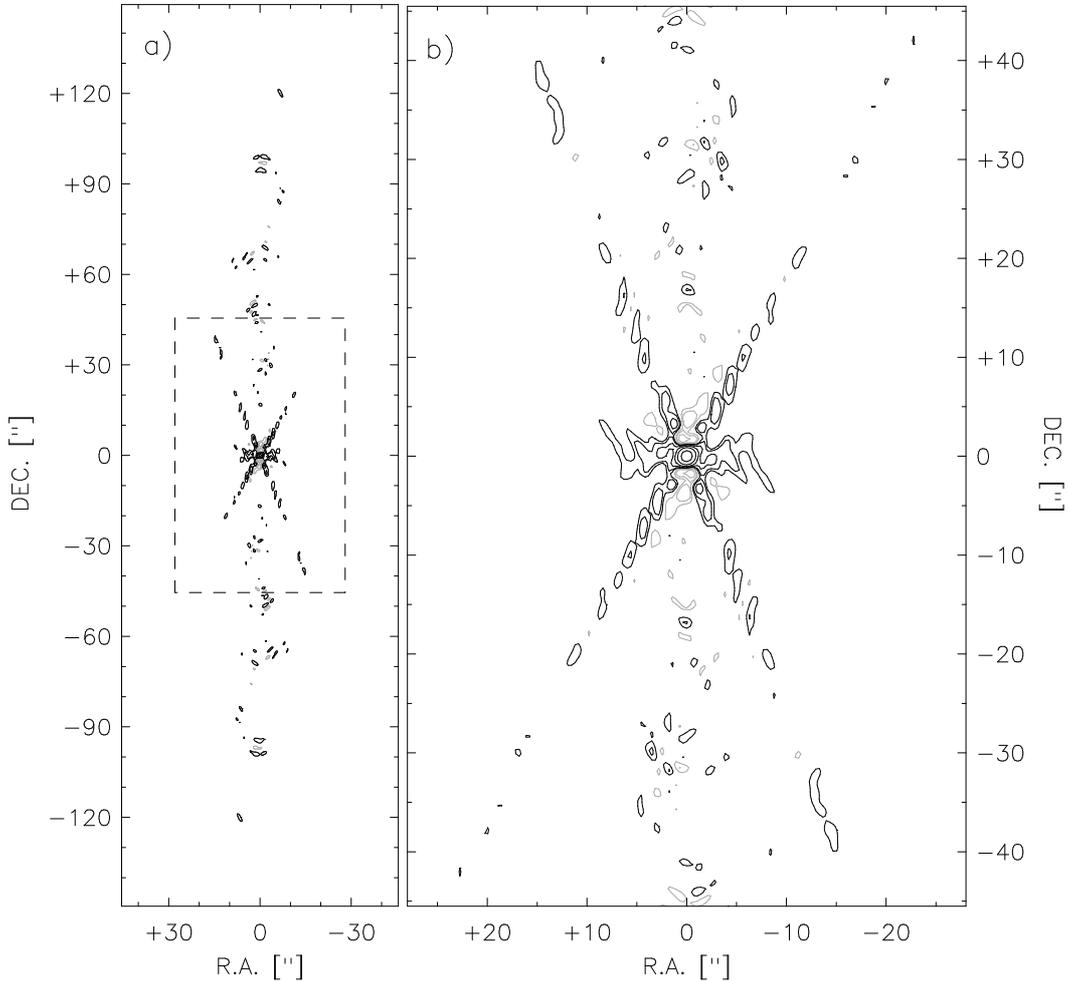
Figure 2.4 Representative synthesized beam belonging to pointing field 12 for a robust weighting of 0. *a)* Large field view with contours of 2.5, 5, 10, 20, 40 and 80% of the maximum. The dashed box outlines the area shown in *b)*. *b)* Zoom into the central part of the synthesized beam with contours of 2, 4, 8, 16, 32, and 64% of the maximum. (The corresponding negative contours are shown in light gray.) The first peaks of the sidelobes are below 10% of the maximum, overall the shape of the synthesized beam is fairly well-behaved given the declination of the COSMOS field.

IF combinations. The four separate 'IMAGR' runs were performed with the same list of CLEAN boxes in the automatic mode. The number of iterations was set to 100,000, with a flux limit of $45\,\mu$Jy/beam ($\sim 1.5\sigma$ in a single image of a field) and a gain of 0.1 to optimize the CLEANing of the facets. The 43 facets forming the contiguous area were combined using the AIPS task 'FLATN'. The four separate images were then combined using the AIPS task 'COMB' to obtain a single image for each field. Due to the combination of bandwidth smearing and a significant drop in sensitivity outside the radius of the Half Power Beam Width, we decided to use a cut-off radius of 0.4 (corresponding to a radius of $16.8'$) when combining the individual fields into the final mosaic using the task 'FLATN'. The resulting image is shown in Fig. 2.5.
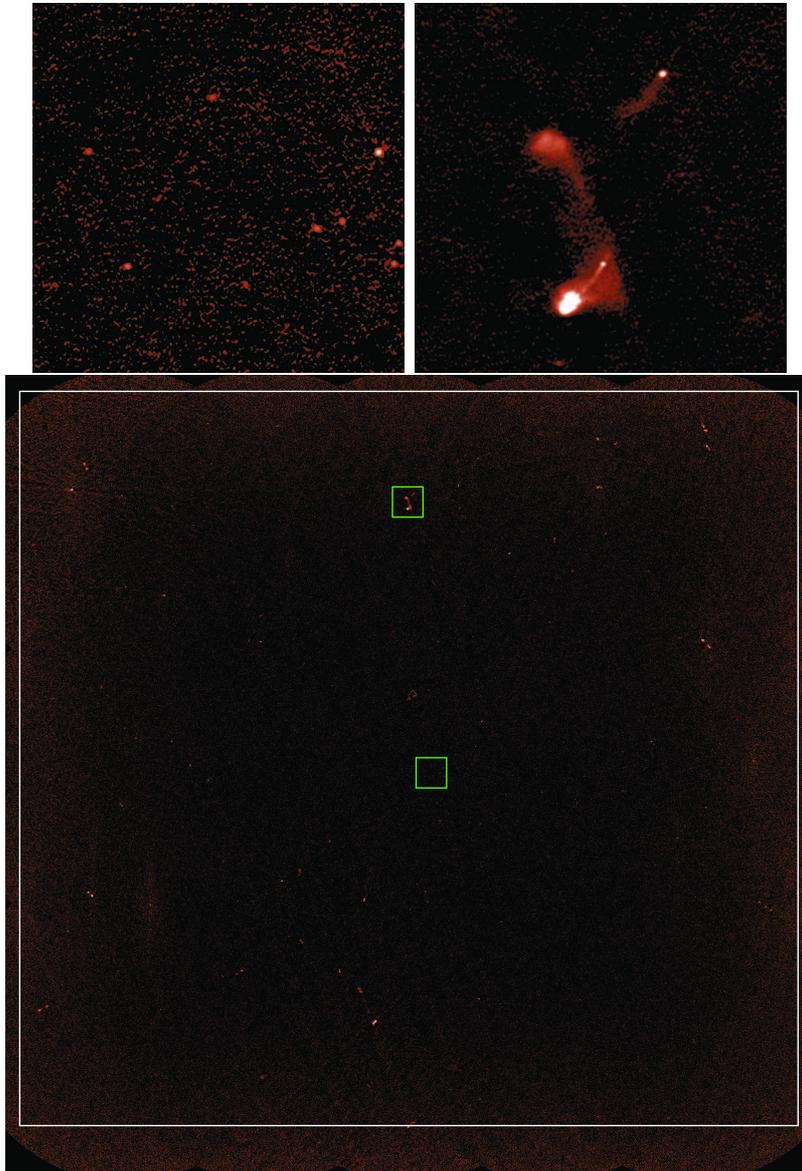
Figure 2.5 The COSMOS field as observed at 1.4 GHz. *Bottom:* The 2□° COSMOS field with the ACS coverage (from Scoville et al. 2007c) indicated by the gray box. The two green boxes outline the regions shown in the top panels. *Top:* Two regions enlarged demonstrate the quality of the data from the VLA-COSMOS large project. The left (right) panel represents the lower (upper) green box in the bottom panel. Each panel has a size of $2.8' \times 2.8'$ corresponding to about 0.1% of the total area.

2.5   Tests

We performed a number of tests to evaluate our flux (see Sec. 2.5.1) and astrometric calibration (see Sec. 2.5.2) as well as the impact of the CLEAN procedure. For the last point, we performed a Gaussianity test on the noise. The noise was extracted from a roughly $16' \times 11'$ box close to the COSMOS field center. The individual noise pixels

show a Gaussian distribution (Fig. 2.6). A Gaussian fit gives an rms of $10.09\,\mu$Jy/beam (σ) (corresponding to a FWHM of $23.76\,\mu$Jy/beam). All noise distributions extracted for various boxes across the part of the field that has an uniform background showed a Gaussian distribution demonstrating that no artifacts have been introduced during the CLEAN process.
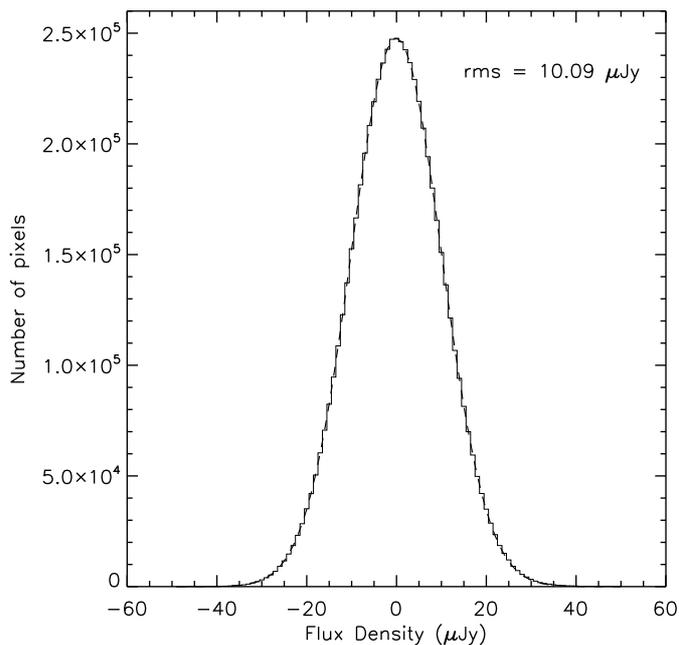
Figure 2.6 Distribution of the noise. Pixel values extracted from a $16' \times 11'$ box close to the COSMOS field center show a Gaussian distribution in agreement with our assumption of Gaussian noise. The fitted Gaussian (dashed line) has a rms of $10.09\,\mu$Jy/beam (σ) (i.e. a FWHM of $23.76\,\mu$Jy/beam). Noise distributions extracted from different boxes located through out the uniform part of the field look similar.

2.5.1 Flux calibration

The second phase calibrator 0925+003 was observed twice each day to allow for assessment of the absolute astrometry and the flux calibration. Most of the following tests were performed on the A-array only data, since it covered a wide range in time. We imaged the calibrator 0925+003 for each day, as well as the two observations per day separately. All IFs were combined at once, since the source of interest is at the phase center and any effects due to misalignment should be negligible. The images were cleaned with 1000 iterations. The resulting typical resolution and rms were $1.96'' \times 1.60''$ (FWHM) and $\sim 870\,\mu$Jy/beam, respectively. The position and flux of 0925+003 were derived by Gaussian fitting using the AIPS task 'JMFIT' on the individual images.

For most of the days 0521+166 served as the flux calibrator. The trends of the peak flux of 0925+003 and 1024-008 are not the same over the course of the observations in the A configuration (Fig. 2.7) indicating no systematic effects in the flux calibration. Note that the error in the flux estimation for calibrator 1024-008 is significantly higher on day MJD 60038 (November 11th, 2004). This is due to strong interferences that could not be entirely removed in the uv data points.

We compared the peak flux density values of 0925+003 of the two observations per day (Fig. 2.8). The median offset is $4.5\,$mJy/beam which corresponds to less than 1% of the
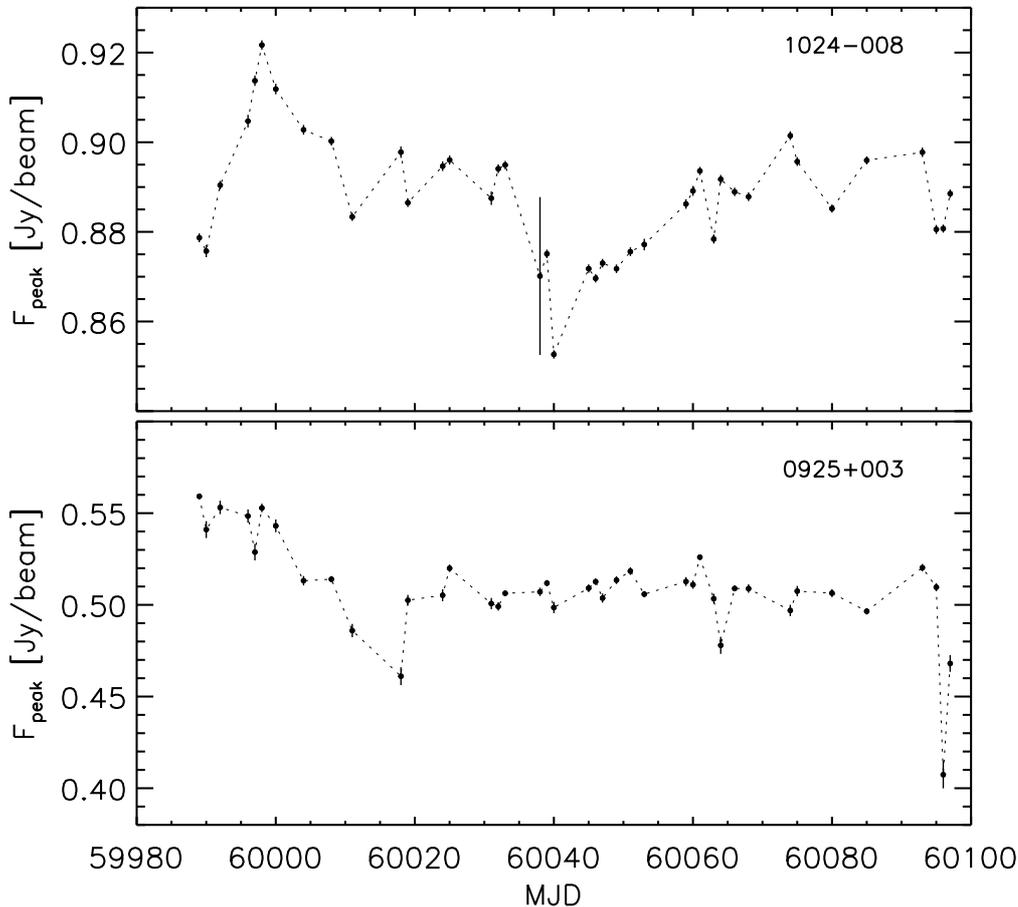
Figure 2.7 Comparison between the flux of the two calibrators 1024-008 and 0925+003 as a function of observing date. The dots show the peak flux density with indicated 3σ errors.

total flux density of 0925+003. The outliers correspond to days MJD 59990 (September 24th, 2004), 60011 (October 15th, 2004) and 60096 (January 8th, 2005). The rms in the maps for those days is about $1.3 - 2.6$ times the typical rms in the 0925+003 maps. The higher noise is likely to be caused by worse weather conditions (e.g. it was snowing on November 13th, 2004) and/or technical problems during observations (e.g. RFI, intermittent fluctuations of the system temperature T_{SYS}, data corruption on particular antennas). Thus we conclude that our flux calibration is within the errors expected.

2.5.2   Absolute and relative astrometry

Given the angular resolution of the combined A+C array data of $1.5'' \times 1.4''$ (FWHM), we expect to achieve a positional accuracy of $\sim 0.15''$ (corresponding to 1/10th of the beam size; see Fomalont 1999) for high S/N sources and $\sim \frac{\text{FHWM}}{\text{S/N}}$ for lower S/N cases when extracting the source position within the COSMOS field.

In order to assess the quality of the absolute astrometric calibration, all observations of
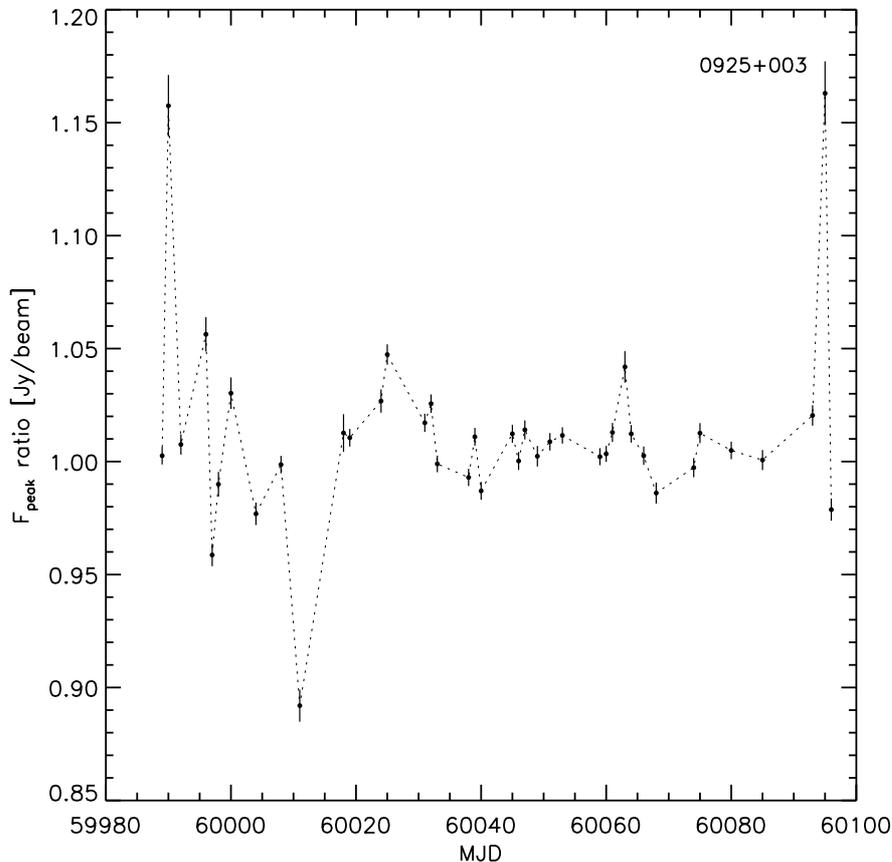
Figure 2.8 The peak flux density variations (dots) of the two observations per day for calibrator 0925+003 shown as a ratio of the measured peak flux densities. 3σ errors are indicated.

0925+003 were combined into a single image. A non-zero offset in RA and DEC of 53 mas and 45 mas, respectively, has been found relative to the nominal position of 0925+003. This offset is likely the result of the large angular separation of 14.5° between the two calibrators (i.e. 0925+003 and 1024-008), which could lead to residual phase transfer errors due to, for example, differential refraction corrections. We consider this offset as an upper limit to our absolute astrometry error, since the (center of the) COSMOS field is only 6° away from the phase calibrator 1024-008.

To test the quality of our relative astrometry, we extracted sources from each single field and compared their positions to the ones extracted from the combined mosaic. We searched for sources using the AIPS task 'SAD' (Search And Destroy). On single fields we ran 'SAD' searching for sources with fluxes higher than $100\,\mu$Jy/beam. 'SAD' looks for points above the specified flux limit and merges such points into contiguous "islands". Then it fits components within these "islands". For our astrometric tests, we run 'SAD' rejecting components within an island with both peak and integrated flux values lower than $100\,\mu$Jy/beam which corresponds to $\sim 7\sigma$ in a single field. On average ~ 150 sources were found per pointing. (In Sec. 2.6 we describe how 'SAD' was run on the mosaic.) After source extraction we only matched positions of objects which have a deconvolved major axis of $< 3''$ FWHM and are within a radius of $\sim 17'$ from the pointing center

(which corresponds to our primary beam cut of 0.4) in the specific field. We analyzed the offsets in right ascension (Δ RA) and declination (Δ DEC) in the central $0.87\square°$ where the rms noise is basically uniform. The results are shown in Fig. 2.9. The offsets in Δ RA and Δ DEC are (-10 ± 127) mas and (-12 ± 131) mas, respectively. To search for possible systematic effects, we analyzed the ΔRA and ΔDEC offsets in different parts of the central $0.87\square°$ area. As seen from Fig. 2.10, there are no significant systematic effects in our relative astrometry as a function of position within the COSMOS field.
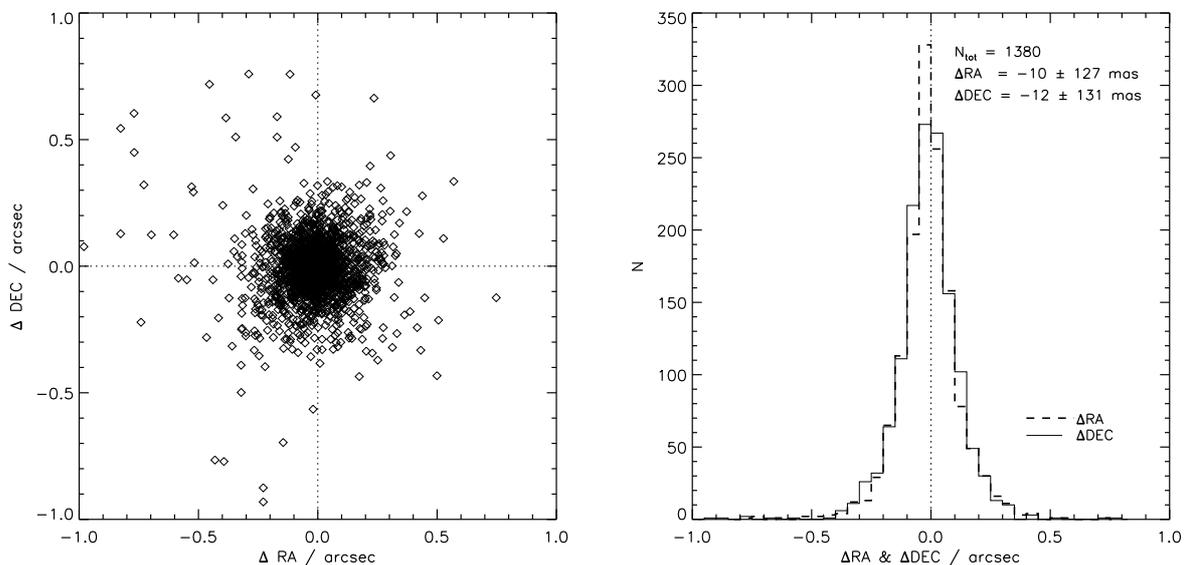
Figure 2.9 The left panel compares the offset in RA (ΔRA) with the offset in DEC (ΔDEC) when positions in single pointings are matched to positions in the combined mosaic (see text for details). The reference position is the one extracted from the mosaic. The right panel shows the distributions of ΔRA (thick dashed line) and ΔDEC (thin solid line). The total number of sources, mean and standard deviation of the offsets are indicated.

To get a deeper insight into our astrometry we cross-correlated the COSMOS mosaic source catalog with the VLA FIRST survey catalog (Becker et al. 1995). To minimize the number of spurious matches, we used a search box size of $2''$ on a side. Only sources with a major axis $< 3''$ and COSMOS to FIRST fluxes comparable within 20%, i.e. $0.8 < S_{COSMOS}^{int}/S_{FIRST}^{int} < 1.2$, were compared. Multiple component sources and FIRST sources with side lobe flags ($flag = 1$) were excluded. Our final sample of matched sources contains only 28 objects. The mean offsets and the 1σ errors for $\Delta RA = RA_{COSMOS} - RA_{FIRST}$ and $\Delta DEC = DEC_{COSMOS} - DEC_{FIRST}$ are (-110 ± 273) mas and (67 ± 232) mas, respectively. Given the low number of matched sources and the FIRST survey's astrometric accuracy of 500 mas (or more) for individual sources (White et al. 1997), we conclude that the inferred positional offsets are within the source extraction errors of both surveys.

In addition, we compared the positions of radio sources extracted from the VLA-COSMOS Pilot and the Large project. However, we consider this not a completely independent test, as the same phase calibrator was used for both projects. We find a median
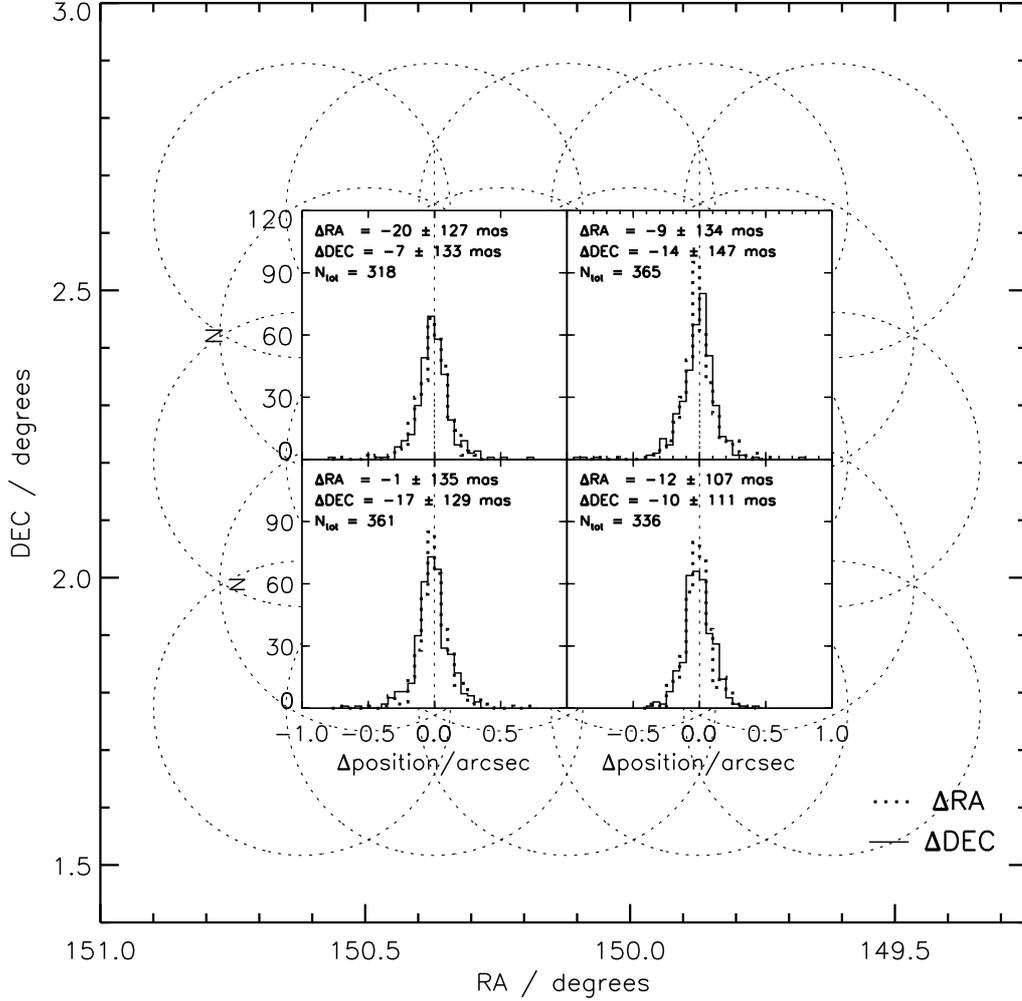
Figure 2.10 Distributions of ΔRA (thick dashed line) and ΔDEC (thin solid line) for different parts in the inner $0.87\square°$ area. The positions of the four panels in the diagram correspond exactly to the analyzed area. The mean and standard deviation of the offsets and the total number of sources are indicated in each panel. For clarity the pointing pattern of the VLA-COSMOS is shown in the background (dotted circles).

offset of -50 mas and 90 mas in ΔRA and ΔDEC, respectively, while the rms scatter is 161 mas and 189 mas for the first and latter. The rms scatter is slightly higher than the above derived accuracy of our relative astrometry ($\sim$130 mas) using only the Large project. However, this is expected as the rms and the beam size of the Pilot project is larger: $25\,\mu$Jy/beam vs. $10\,\mu$Jy/beam and $1.9'' \times 1.6''$ vs. $1.5'' \times 1.4''$. The derived astrometric differences between the Pilot and the Large projects are well within our errors (see Sec. 2.4.2 for data reduction difference between both projects). Hence, we conclude that our relative astrometric accuracy for the VLA-COSMOS Large project is $\sim$130 mas and discard this higher rms scatter found from the comparison to the Pilot data.

Based on arguments presented above, we conclude that the overall astrometric errors of our derived source positions are dominated by the uncertainty in the position extraction

(due to our beam size) of $\sim 130\,$mas. Our absolute astrometric accuracy is likely to be better than $55\,$mas.

2.6 The VLA-COSMOS catalog

2.6.1 Source extraction

In order to select a sample of radio components from the largest imaged area above a given threshold, defined in terms of the local signal to noise ratio, we adopted the following approach. First the software package SExtractor was used to estimate the local background in each mesh of a grid covering the whole surveyed area (see Bertin & Arnouts 1996, for a general description of SExtractor). Different noise maps with mesh sizes ranging from 25 to 100 pixels were produced and examined. The fractional difference between the rms measured in the SExtractor noise maps and the rms directly measured on the real map is very small ($\sim 2\%$) over the whole map (see Fig. 2.11). In the end, we adopted a mesh size of 50 pixels corresponding to $17.5''$ which was found to be the best compromise between closely sampling the variations in rms and avoiding contamination by larger radio sources. The rms values range from about $9\,\mu$Jy/beam in the inner regions to about $20\,\mu$Jy/beam at the edges of the mosaic with values as high as $30 - 40\,\mu$Jy/beam around the few relatively strong sources (see Fig. 2.12). The mean rms in the inner $1\square°$ is $10.5\,\mu$Jy/beam, the mean rms over the $2\square°$ area is $15.0\,\mu$Jy/beam. The cumulative area as a function of rms is shown in Fig. 2.13.
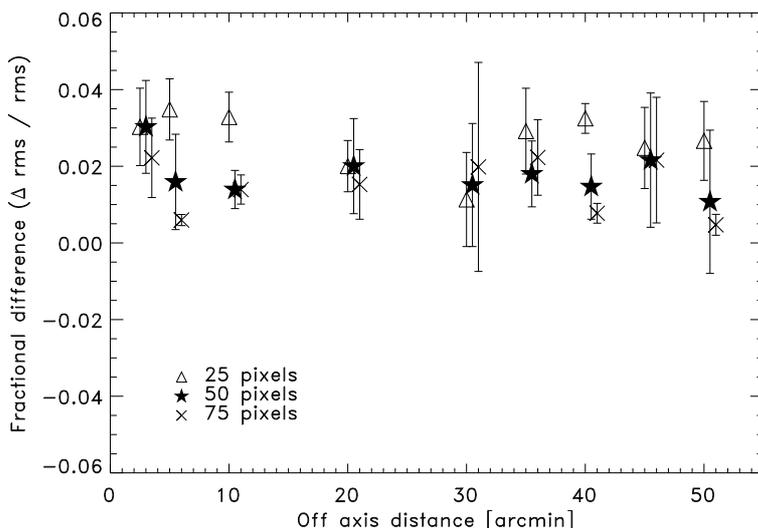
Figure 2.11 Fractional difference between the directly measured rms value in a 100×100 pixel box and the corresponding value of the SExtractor noise map as a function of the radial distance for three different noise maps with mesh sizes of 25, 50 and 75 pixels, respectively. The x-positions have been shifted by $0.5'$ for clarity.

As a next step, the AIPS task 'SAD' was used to obtain a catalog of candidate components. 'SAD' attempts to find all the components whose peaks are brighter than a given flux level. In order to detect radio components down to the $30\,\mu$Jy/beam level 'SAD' was run several times with different search levels (with a decreasing flux limit) using the resulting residual image each time. We recovered all the radio components with a peak flux $S_{\mathrm{peak}} > 30\,\mu$Jy/beam (corresponding to roughly 3σ in the higher sensitivity regions). For
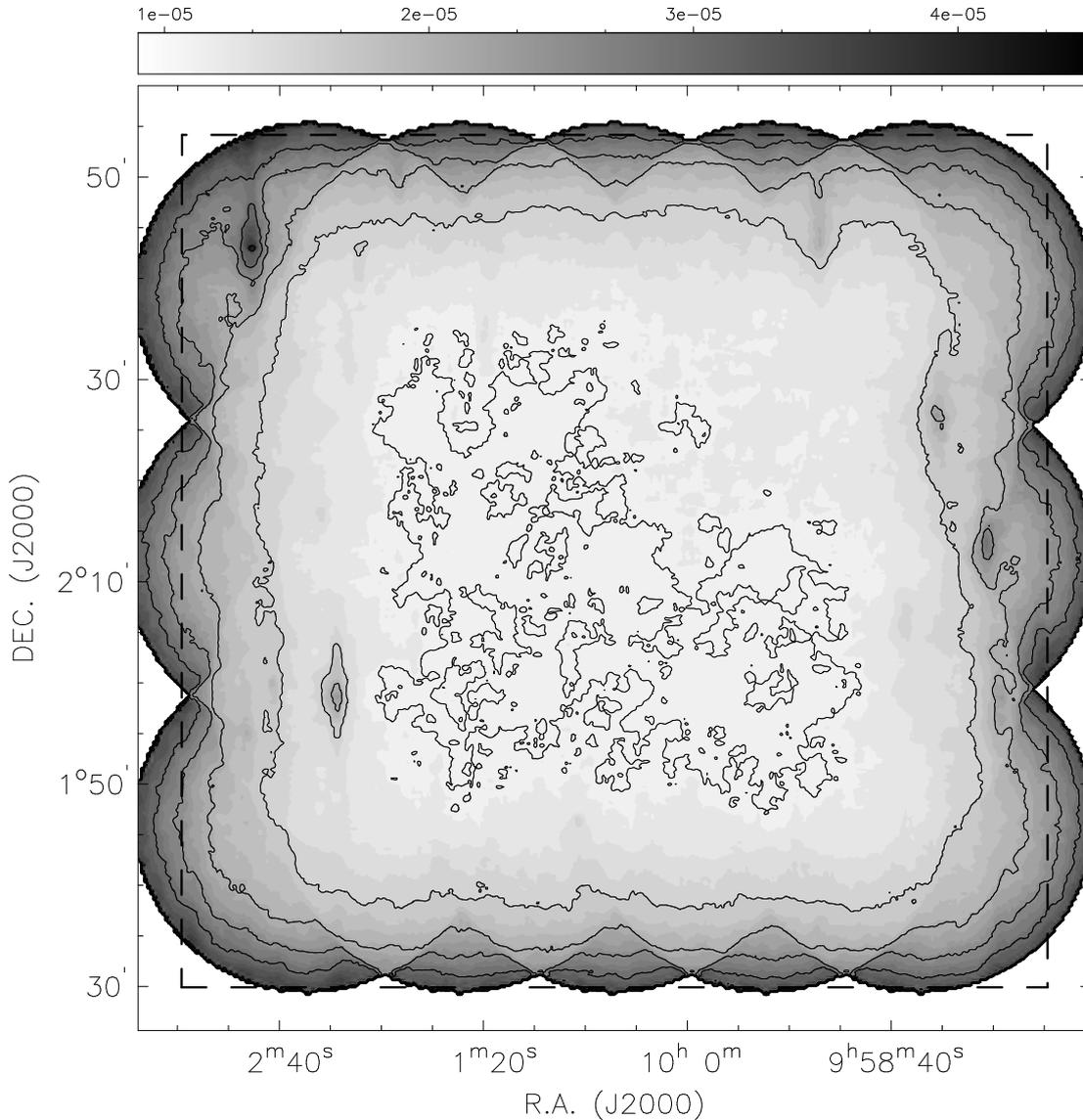
Figure 2.12 Sensitivity map of the area covered by the VLA Large Project derived using SExtractor with a mesh size of 50 pixel. The rms is fairly uniform except for areas around strong radio sources. Lighter shades indicate lower rms noise values. The contours correspond to rms levels of 10, 15, 20, 25, 30, and 40 μJy/beam. The dashed box outlines the area which was searched for radio components.

each component 'SAD' provides peak flux, total flux, position and size estimated using a Gaussian fit.

However, for faint components the Gaussian fit may be unreliable and a better estimate of the peak flux (crucial for the selection based on S/N) can be obtained with a non-parametric second-degree interpolation using the AIPS task 'MAXFIT'. We ran 'MAXFIT' on all the components found by 'SAD' and selected only those components for which the peak flux density found by 'MAXFIT' was greater or equal to 4.5 times the local rms as derived from the noise map. The (non-parametric) peak position and flux density as
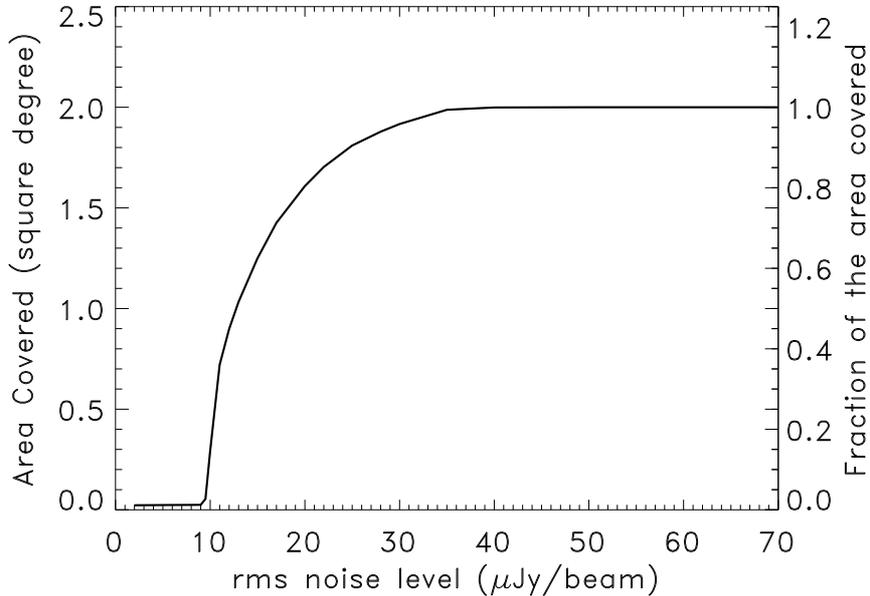
Figure 2.13 Plot of the rms noise level vs. cumulative as well as fractional area covered. The full area covered is $2\square°$ and is indicated in Fig. 2.12.

determined by 'MAXFIT' were kept, as the so derived values should be less affected by assumptions on the real brightness distribution.

Finally, we visually inspected the S/N mosaic image (Fig. 2.14) for components that could have been missed by 'SAD'. The most likely reason for missing sources is that 'SAD' only recovers components that can be fitted by a Gaussian fulfilling certain parameters. Thus, if the fit for a potential component fails, this component is rejected from the catalogue provided by 'SAD'. Therefore, the AIPS tasks 'JMFIT' and 'MAXFIT' were run on these potential components to derive their properties.

In order to exclude 1-pixel wide noise peaks above the detection threshold (4.5σ), more scrutiny was used for the 294 components fitted with both sizes smaller than the CLEAN beam. Only those components (171) for which JMFIT was able to estimate an upper limit to the source size greater than the CLEAN beam were kept while the remaining (123) were identified as noise spikes and excluded from the catalogue. As a result of the whole procedure a total of 3823 components have been selected (3204 from 'SAD'+'MAXFIT' and 619 from the S/N image). A more complete analysis on the completeness and possible biases affecting the catalogue will be described in a future paper along with the number counts (Bondi et al., in prep).

2.6.2 Description of the catalog

Some of the components clearly belong to a single radio source (e.g. jets and lobes of an extended radio galaxy), in other more complex cases we have also used the optical ground- and space-based images to discriminate between different components of the same radio source or separate radio sources. The final catalog (see Tab. 2.3; see below) lists 3643 radio
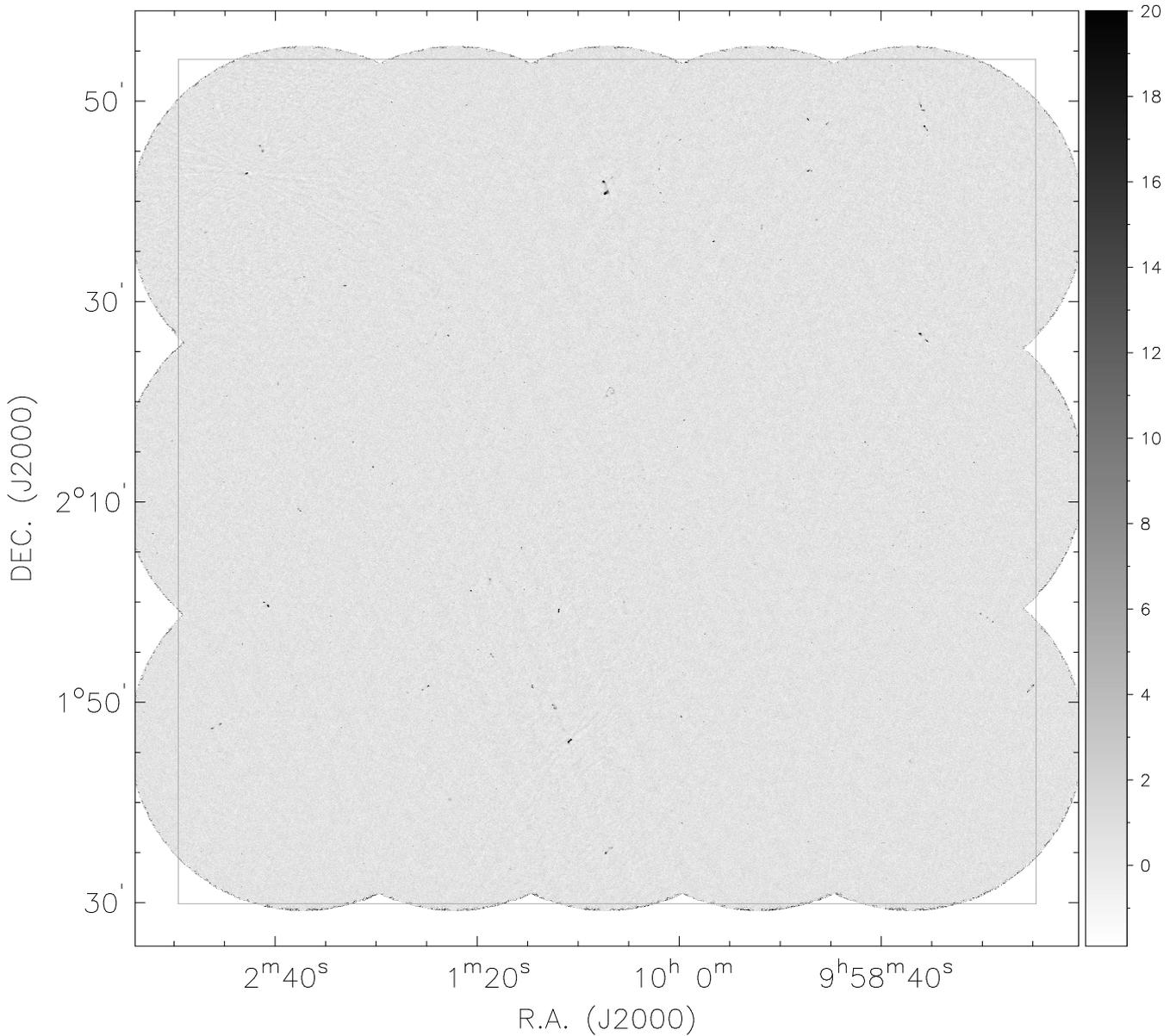
Figure 2.14 Map of the S/N of the VLA-COSMOS Large Project as constructed using the SExtractor sensitivity map (Fig. 2.12). Lighter shades indicate lower S/N values. The dashed box shows the area in which radio sources were identified (see also text).

sources of which 80 are multiple, i.e. better described by more than a single component. These sources are identified by the flag 'mult=1' (Tab. 2.3). For these sources, the listed center is either the one of the radio core or the optical counterpart when either of these could be reasonably identified or the luminosity weighted mean position. In addition, we visually inspected weak ($\leq 6\sigma$) sources close to bright sources with significant sidelobes. A total of 72 sources potentially lying on sidelobe spikes are flagged with 'slob=1'.

In Fig. 2.15 we plot the ratio of the total integrated flux density S_{total} and the peak flux density S_{peak} as functions of the signal to noise ratio S/N (S_{peak}/rms) for all the 3643 sources in the catalog. To select the resolved sources, we determined the lower envelope of the points in Fig. 2.15 which contains 99% of the sources with $S_{total} < S_{peak}$, and mirrored it above the $S_{total}/S_{peak} = 1$ line (upper envelope in Fig. 2.15). We have considered the 1601 (44%) sources laying above the upper envelope resolved. The envelope can be described by the equation

$$S_{total}/S_{peak} = 1 + [100/(S_{peak}/rms)^3]$$

The resolved sources are flagged in the catalog by 'res=1'. For the unresolved sources the total flux density is set equal to the peak brightness and the angular size is undetermined.
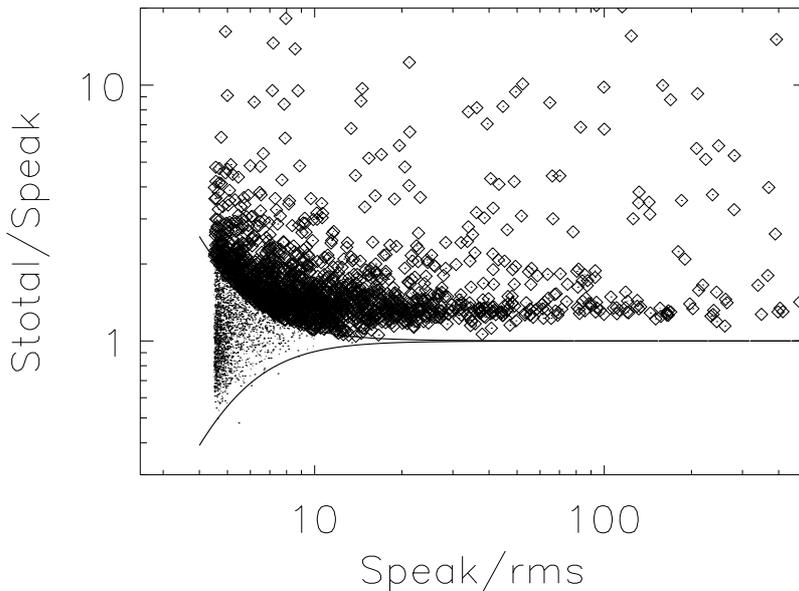
Figure 2.15 Ratio of the total flux S_T to the peak flux S_P as a function of the signal-to-noise ratio of the peak flux and the local rms. The solid line shows the upper and lower envelopes of the flux ratio distribution containing the sources considered unresolved (see text). Open symbols show sources considered resolved.

We calculated the uncertainties in the peak flux density S_{peak} and integrated flux S_{total} using the equations given by Condon (1997) as outlined in e.g. Hopkins et al. (2003); Schinnerer et al. (2004). For the positional uncertainties we used the equations reported in (Bondi et al. 2003, their equations 4 and 5), using 130 mas as the calibration error in right ascension and declination (see also Condon et al. 1998, their equation 27).

For each of the 80 sources fitted with multiple components (see Fig. 2.16) we list in the multiple source catalog (see Tab. 2.4) (i) an entry for each of the components identified with a trailing letter (A, B, C, ...) in the source name (from Tab. 2.3), and (ii) an entry for the whole source as it is listed in the source table (Tab. 2.3). In these cases the total flux was calculated using the task 'TVSTAT', which allows the integration of map values over irregular areas, and the sizes are the largest angular sizes. For these sources the peak flux (at the listed position) is undetermined and therefore set to a value of '-99.999'.

For each source we list the source name as well as its derived properties and their uncertainties. All 3643 radio sources are listed in right ascension order in Tab. 2.3 with the

following columns[5]:

Column(1): Source name
Column(2): Right ascension (J2000.0)
Column(3): Declination (J2000.0)
Column(4): rms uncertainty in right ascension
Column(5): rms uncertainty in declination
Column(3): Peak flux density and its rms uncertainty
Column(4): Integrated flux density and its rms uncertainty
Column(5): rms measured in the SExtractor noise map
Column(9): Deconvolved source size – major axis $\theta_{M,dec}$
Column(10): Deconvolved source size – minor axis $\theta_{m,dec}$
Column(11): Deconvolved source – position angle PA_{dec} (counterclockwise from North)
Column(12): Flag for resolved (1) and unresolved (0) sources
Column(13): Flag for source with multiple (1) or single (0) components
Column(14): Flag for potentially spurious source due to sidelobe (1), otherwise (0)

The individual components contributing to our multi-component sources are listed in Tab. 2.4. The columns are the same as for Tab. 2.3. The (cumulative) peak and integrated flux distribution of the sources in VLA-COSMOS large project are shown in Fig. 2.17.

---

[5]Due to bandwidth smearing effects the peak flux and, hence, the integrated flux for unresolved sources can be underestimated by up to (10-15)%. An analysis of this will be presented in Bondi et al. (in prep.).

Table 2.3 1.4 GHz Source Catalog of the VLA-COSMOS Large Project (abridged)

Name	R.A. (J2000.0)	Dec. (J2000.0)	$\sigma_{R.A.}$ ['']	$\sigma_{Dec.}$ ['']	S_{peak} [mJy/beam]	S_{total} [mJy]	rms [mJy/beam]	$\theta_{M,dec}$ ['']	$\theta_{m,dec}$ ['']	PA_{dec} [^{o}]	Flags res[a]	slob[b]	mult[c]
COSMOSVLA_J095738.80+024203.2	09 57 38.800	+02 42 03.19	0.19	0.19	0.112 ± 0.024	0.112 ± 0.024	0.024	0.00	0.00	0.0	0	0	0
COSMOSVLA_J095738.97+021630.3	09 57 38.972	+02 16 30.32	0.19	0.19	0.112 ± 0.025	0.112 ± 0.025	0.025	0.00	0.00	0.0	0	0	0
COSMOSVLA_J095739.10+021503.1	09 57 39.097	+02 15 03.05	0.19	0.19	0.119 ± 0.024	0.129 ± 0.024	0.024	0.00	0.00	0.0	0	0	0
COSMOSVLA_J095739.23+024539.0	09 57 39.229	+02 45 39.02	0.19	0.19	0.126 ± 0.028	0.126 ± 0.028	0.028	0.00	0.00	0.0	0	0	0
COSMOSVLA_J095739.39+023655.5	09 57 39.390	+02 36 55.47	0.19	0.19	0.111 ± 0.024	0.111 ± 0.024	0.024	0.00	0.00	0.0	0	0	0
COSMOSVLA_J095739.44+021850.9	09 57 39.441	+02 18 50.87	0.18	0.18	0.133 ± 0.027	0.133 ± 0.027	0.027	0.00	0.00	0.0	0	0	0
COSMOSVLA_J095739.71+023103.5	09 57 39.712	+02 31 03.53	0.13	0.13	0.124 ± 0.027	0.124 ± 0.027	0.027	0.00	0.00	0.0	0	0	0
COSMOSVLA_J095739.81+013653.4	09 57 39.814	+01 36 53.40	0.17	0.17	0.156 ± 0.030	0.156 ± 0.030	0.030	0.00	0.00	0.0	0	0	0
COSMOSVLA_J095740.60+020145.1	09 57 40.602	+02 01 45.13	0.20	0.19	0.225 ± 0.035	0.377 ± 0.105	0.035	2.52	0.00	55.8	1	0	0
COSMOSVLA_J095740.99+024921.1	09 57 40.986	+02 49 21.13	0.18	0.18	0.154 ± 0.034	0.154 ± 0.034	0.034	0.00	0.00	0.0	0	0	0
COSMOSVLA_J095741.11+015122.6	09 57 41.107	+01 51 22.58	0.13	0.14	-99.990 ±-99.990	45.620 ± -99.990	0.024	53.00	9.00	0.0	1	0	1
COSMOSVLA_J095741.25+024346.2	09 57 41.250	+02 43 46.20	0.19	0.19	0.123 ± 0.025	0.123 ± 0.025	0.025	0.00	0.00	0.0	0	0	0
COSMOSVLA_J095741.34+020346.1	09 57 41.338	+02 03 46.13	0.22	0.22	0.152 ± 0.031	0.152 ± 0.031	0.031	0.00	0.00	0.0	0	0	0
COSMOSVLA_J095741.52+023841.2	09 57 41.525	+02 38 41.21	0.18	0.17	0.116 ± 0.023	0.116 ± 0.023	0.023	0.00	0.00	0.0	0	0	0
COSMOSVLA_J095741.74+025004.0	09 57 41.737	+02 50 03.96	0.19	0.19	0.160 ± 0.034	0.160 ± 0.034	0.034	0.00	0.00	0.0	0	0	0
COSMOSVLA_J095741.89+020426.4	09 57 41.895	+02 04 26.42	0.17	0.17	0.181 ± 0.031	0.181 ± 0.031	0.031	0.00	0.00	0.0	0	0	0
COSMOSVLA_J095742.30+020426.1	09 57 42.305	+02 04 26.07	0.13	0.13	11.371 ± 0.031	20.492 ± 0.228	0.031	1.88	0.35	57.1	1	0	0
COSMOSVLA_J095742.61+022827.8	09 57 42.612	+02 28 27.81	0.20	0.19	0.133 ± 0.029	0.133 ± 0.029	0.029	0.00	0.00	0.0	0	0	0
COSMOSVLA_J095742.71+024540.4	09 57 42.711	+02 45 40.41	0.17	0.17	0.134 ± 0.026	0.134 ± 0.026	0.026	0.00	0.00	0.0	0	0	0
COSMOSVLA_J095743.04+015650.8	09 57 43.044	+01 56 50.82	0.15	0.15	0.425 ± 0.030	0.747 ± 0.098	0.030	2.11	0.20	129.1	1	0	0
COSMOSVLA_J095743.23+013851.0	09 57 43.228	+01 38 51.05	0.17	0.17	0.139 ± 0.025	0.139 ± 0.025	0.025	0.00	0.00	0.0	0	0	0
COSMOSVLA_J095743.40+015620.7	09 57 43.400	+01 56 20.72	0.34	0.19	0.183 ± 0.030	0.289 ± 0.102	0.030	2.64	0.30	73.2	1	0	0
COSMOSVLA_J095743.73+014132.5	09 57 43.729	+01 41 32.47	0.18	0.17	0.121 ± 0.022	0.121 ± 0.022	0.022	0.00	0.00	0.0	0	0	0
COSMOSVLA_J095743.87+023038.5	09 57 43.872	+02 30 38.52	0.15	0.14	0.412 ± 0.026	0.727 ± 0.084	0.026	1.98	0.33	57.7	1	0	0

[a] Flag if source is – according to Fig. 2.15 – resolved (1) or unresolved (0) [b] Flag if source is potentially spurious due to sidelobe bump (1) or not (0) [c] Flag if source consists of multiple components (1) or a single component (0) Catalog of radio sources at 1.4 GHz detected in the COSMOS field with a S/N≥4.5 in the VLA-COSMOS large project data (see Sec. 2.6). Radio sources with multiple Gaussian fits are flagged ('mult=1'), their multiple components are listed separately in Tab. 2.4. The table is available in its entirety via the link to a machine-readable version above and/or via the COSMOS archive at IPAC/IRSA[a]. A portion is shown here for guidance regarding its form and content.

[a]http://www.irsa.ipac.edu/data/COSMOS/tables/

Table 2.4 Multi-components of sources in the VLA-COSMOS catalog (abridged)

Name	R.A. (J2000.0)	Dec. (J2000.0)	$\sigma_{\text{R.A.}}$ ['']	$\sigma_{\text{Dec.}}$ ['']	S_{peak} [mJy/beam]	S_{total} [mJy]	rms [mJy/beam]	θ_{M} ['']	θ_{m} ['']	PA [^{o}]	res^a	Flags slob^b	mult^c
COSMOSVLA_J095741.11+015122.6A	09 57 39.708	+01 51 41.59	0.13	0.13	1.971 ± 0.026	8.612 ± 0.202	0.026	3.36	2.56	124.8	1	0	0
COSMOSVLA_J095741.11+015122.6B	09 57 39.858	+01 51 43.67	0.13	0.13	1.463 ± 0.026	4.289 ± 0.151	0.026	2.64	1.85	84.7	1	0	0
COSMOSVLA_J095741.11+015122.6C	09 57 40.100	+01 51 38.36	0.24	0.24	0.227 ± 0.026	10.694 ± 1.260	0.026	13.17	7.03	133.9	1	0	0
COSMOSVLA_J095741.11+015122.6D	09 57 41.107	+01 51 22.58	0.14	0.13	0.497 ± 0.025	0.754 ± 0.069	0.025	1.62	0.50	114.2	1	0	0
COSMOSVLA_J095741.11+015122.6E	09 57 41.686	+01 51 11.30	0.22	0.21	0.314 ± 0.024	8.037 ± 0.820	0.024	11.14	5.54	130.0	1	0	0
COSMOSVLA_J095741.11+015122.6F	09 57 42.166	+01 51 03.17	0.13	0.13	2.227 ± 0.024	12.488 ± 0.229	0.024	3.73	2.49	134.7	1	0	0
COSMOSVLA_J095741.11+015122.6	09 57 41.107	+01 51 22.58	0.13	0.14	-99.990 ±-99.990	45.620 ±-99.990	0.024	53.00	9.00	0.0	1	0	1
COSMOSVLA_J095755.84+015804.2A	09 57 55.792	+01 58 05.76	0.13	0.14	0.791 ± 0.022	3.370 ± 0.155	0.022	3.51	2.07	150.5	1	0	0
COSMOSVLA_J095755.84+015804.2B	09 57 55.847	+01 58 01.95	0.17	0.14	0.501 ± 0.022	1.657 ± 0.151	0.022	3.85	1.86	108.6	1	0	0
COSMOSVLA_J095755.84+015804.2C	09 57 55.898	+01 58 04.18	0.18	0.23	0.531 ± 0.022	1.714 ± 0.214	0.022	5.89	2.06	31.4	1	0	0
COSMOSVLA_J095755.84+015804.2	09 57 55.840	+01 58 04.24	0.13	0.16	-99.990 ±-99.990	6.450 ±-99.990	0.022	21.96	6.86	0.0	1	0	1
COSMOSVLA_J095756.45+025155.6A	09 57 56.418	+02 51 56.26	0.34	0.25	0.170 ± 0.031	0.302 ± 0.111	0.031	2.84	0.54	122.4	1	0	0
COSMOSVLA_J095756.45+025155.6B	09 57 56.484	+02 51 54.91	0.19	0.18	0.167 ± 0.031	0.167 ± 0.031	0.031	0.00	0.00	0.0	0	0	0
COSMOSVLA_J095756.45+025155.6	09 57 56.451	+02 51 55.59	0.20	0.43	-99.990 ±-99.990	0.300 ±-99.990	0.031	3.75	1.43	0.0	1	0	1
COSMOSVLA_J095800.80+015857.2A	09 58 00.619	+01 58 53.03	0.18	0.17	0.348 ± 0.019	3.684 ± 0.303	0.019	7.16	2.59	51.5	1	0	0
COSMOSVLA_J095800.80+015857.2B	09 58 00.798	+01 58 57.15	0.13	0.13	7.204 ± 0.019	16.624 ± 0.183	0.019	1.89	1.58	156.5	1	0	0
COSMOSVLA_J095800.80+015857.2	09 58 00.798	+01 58 57.15	0.13	0.13	-99.990 ±-99.990	18.875 ±-99.990	0.019	10.00	3.00	0.0	1	0	1
COSMOSVLA_J095815.51+014923.7A	09 58 15.502	+01 49 24.61	0.16	0.23	0.145 ± 0.014	0.496 ± 0.083	0.014	3.49	1.62	5.7	1	0	0
COSMOSVLA_J095815.51+014923.7B	09 58 15.520	+01 49 22.18	0.20	0.34	0.080 ± 0.014	0.080 ± 0.014	0.014	0.00	0.00	0.0	0	0	0
COSMOSVLA_J095815.51+014923.7	09 58 15.509	+01 49 23.75	0.15	0.24	-99.990 ±-99.990	0.500 ±-99.990	0.014	3.75	1.43	0.0	1	0	1

^{a} Flag if component is – according to Fig. 2.15 – resolved (1) or unresolved (0) ^{b} Flag if component is potentially spurious due to sidelobe bump (1) or not (0) ^{c} Flag if source consists of multiple components (1) or one of its single components (0) List of individual components that made up the 80 radio sources that were fitted by multiple Gaussian. These multi-component sources are flagged in Tab. 2.3 by a 'mult=1'. The table is available in its entirety via the link to a machine-readable version above and/or via the COSMOS archive at IPAC/IRSA. A portion is shown here for guidance regarding its form and content.

COSMOSVLA_J095847.48+023410.2

COSMOSVLA_J095848.38+025011.3

COSMOSVLA_J095901.52+024740.6

COSMOSVLA_J095901.71+025336.5

COSMOSVLA_J095908.32+024309.6

COSMOSVLA_J095908.96+024813.5

COSMOSVLA_J095909.70+024505.0

COSMOSVLA_J095919.03+014036.1

COSMOSVLA_J095919.72+023410.3

COSMOSVLA_J095927.25+023729.2

COSMOSVLA_J095929.23+022844.7

COSMOSVLA_J095929.41+020943.5

COSMOSVLA_J100018.51+023256.5   COSMOSVLA_J100026.50+024229.9   COSMOSVLA_J100027.32+022111.3

COSMOSVLA_J100028.29+024103.4   COSMOSVLA_J100028.31+013507.9   COSMOSVLA_J100043.17+014607.9

COSMOSVLA_J100045.41+014712.7   COSMOSVLA_J100045.70+013919.7   COSMOSVLA_J100047.59+020958.8

COSMOSVLA_J100047.60+015910.3   COSMOSVLA_J100049.59+014923.7   COSMOSVLA_J100057.46+024217.2

COSMOSVLA_J100058.05+015129.0

COSMOSVLA_J100101.32+022159.4

COSMOSVLA_J100102.39+020529.1

COSMOSVLA_J100106.76+013320.0

COSMOSVLA_J100109.29+021721.8

COSMOSVLA_J100114.13+015444.3

COSMOSVLA_J100114.86+020208.9

COSMOSVLA_J100119.58+015516.4

COSMOSVLA_J100124.10+024936.4

COSMOSVLA_J100129.15+015949.8

COSMOSVLA_J100129.36+014027.1

COSMOSVLA_J100129.49+023353.7

COSMOSVLA_J100131.37+022639.3

COSMOSVLA_J100136.46+022641.9

COSMOSVLA_J100140.13+015130.0

COSMOSVLA_J100147.48+015101.9

COSMOSVLA_J100151.44+022532.2

COSMOSVLA_J100201.18+021327.1

COSMOSVLA_J100209.38+022052.3

COSMOSVLA_J100212.07+023134.9

COSMOSVLA_J100229.89+023225.3

COSMOSVLA_J100230.12+020912.5

COSMOSVLA_J100231.41+015138.4

COSMOSVLA_J100238.68+022152.2

Figure 2.16 Radio sources fitted by multiple Gaussian components and identified as a radio group (see Tab. 2.4). The source name is given at the top of the individual panels. The grey-scale is from -4σ to 10σ of the local rms (Tab. 2.3). The contours start at 4σ in steps of $2^n \times \sigma$ with $n = 2, 3, 4, 5, \ldots$. (The local rms is listed in Tab. 2.3.) The beam is shown for reference in the bottom left corner.

2.6.3 Comparison to other surveys

We compared the catalog of the VLA-COSMOS large project with the catalogs of the NVSS, FIRST and VLA-COSMOS pilot project. All three surveys were also conducted
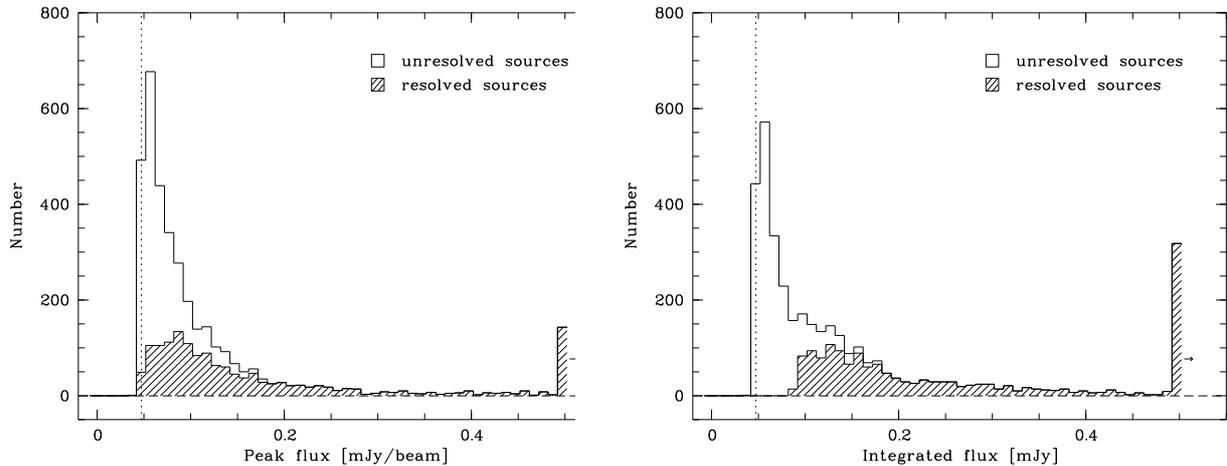
Figure 2.17 Cumulative number distribution of the VLA-COSMOS sources as a function of peak (*left*) and integrated (*right*) flux density. The shaded area corresponds to sources that are resolved (see text).

at 1.4 GHz, however the NVSS and FIRST surveys used the D- and B-array, respectively (Condon et al. 1998; White et al. 1997).

Within the area searched for the VLA-COSMOS large project, the NVSS and FIRST catalogs list 119 and 184 sources, respectively. About 10% of the sources in these catalogs have no counterpart in the VLA-COSMOS survey nor in the other survey, i.e. they are unique to the catalogs of the NVSS or FIRST survey. Given the sensitivity of the VLA-COSMOS survey this suggests that these sources are likely false detections[6] as it seems unlikely that all of them are highly variable sources. We cross-correlated the NVSS and FIRST catalogs with the catalog of the VLA-COSMOS large project using a search radius of 5″ and 1″, respectively. Figure 2.18 compares the integrated fluxes derived for the individual sources. The agreement between the values of the VLA-COSMOS and the NVSS/FIRST survey is fairly good, except for a number of NVSS sources where our observations have probably resolved out a large extended flux component. (Note that some of the VLA-COSMOS multi-component sources consist of more than one FIRST source, explaining most of the large discrepancies in Fig. 2.18.)

For 30 sources from the VLA-COSMOS pilot project no counterpart is present in our catalog of the large project. Given that the sensitivity of the large project is at least a factor of 2.5 better, these sources are likely false detections. Thus the fraction of false detections is about 10 % in the pilot catalog. The signal-to-noise ratio S/N of the sources is below 4.3σ of the fitted peak flux and its calculated error. (This roughly corresponds to a S/N of 5.5 and lower.) This is a factor of 2 more than expected from the algorithm used which was set to a false detection rate of 5 % (Schinnerer et al. 2004). As all of the false detection are lying in areas with a large gradient in the background (i.e. overlap areas of the individual pointings at the edge of the field), this strongly suggests that the local rms was underestimated in these areas and that the used mesh size of 47″ was too large

---

[6]The FIRST survey notes on their web-site (`http://sundog.stsci.edu/`) that sidelobe flagging near the equator is not as reliable as for the northern part of the survey.
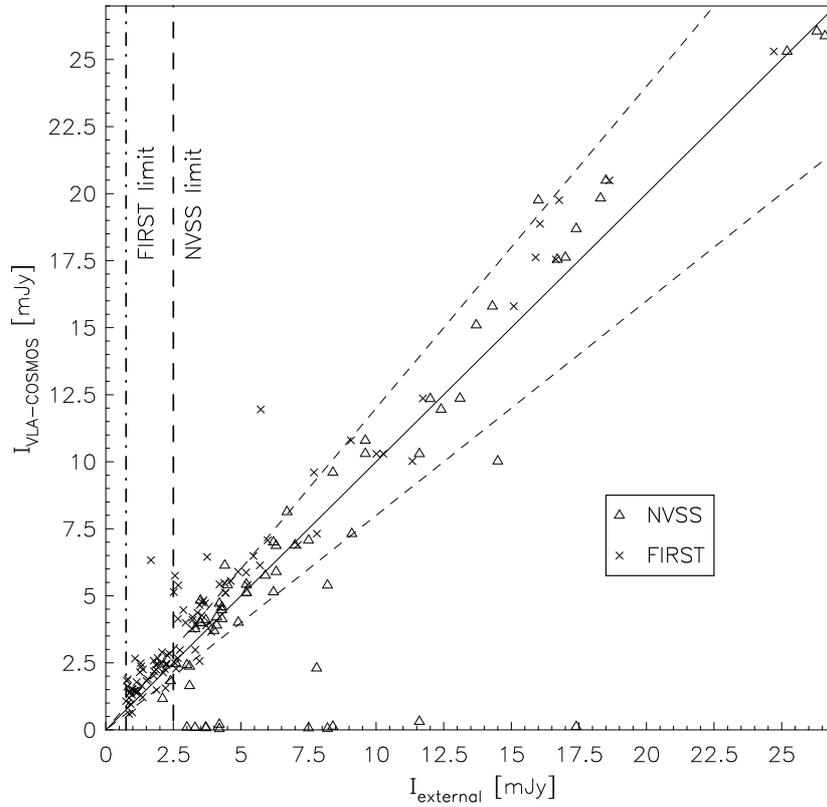
Figure 2.18 Comparison of the derived integrated flux in the VLA-COSMOS large project $I_{VLA-COSMOS}$ and the NVSS and FIRST surveys $I_{external}$. The solid diagonal line represents a flux ratio of unity, while the dashed lines show the $\pm 20\%$ lines. The vertical lines denote the (5σ) detection limit of the NVSS and FIRST surveys (Condon et al. 1998; White et al. 1997). The counterparts to VLA-COSMOS sources lie within radii of $5''$ and $1''$ for the NVSS and FIRST survey, respectively. The large discrepancies in the derived integrated flux for several NVSS sources is likely due to the large difference in resolution (NVSS: $45''$ FWHM vs. VLA-COSMOS:$\sim 1.5''$ FWHM), while the discrepancies in the integrated flux for the FIRST sources are mainly due to the fact that these are part of multi-component VLA-COSMOS sources.

in these areas. (For the large project a mesh size of $17.5''$ is used, see Sec. 2.6.1.) We also compared the measured peak and integrated fluxes of both VLA-COSMOS projects. For sources in the pilot project with significant detection ($S/\delta S > 4.5$) the measured peak (integrated) flux agrees within 20% for about 66% (50%) of the sources. However, the flux measurements agree within the quoted errors for most sources. The agreement in the integrated flux (also with the error) is lower for very bright sources (≥ 1mJy). This is very likely due to the fact that the large project data is more sensitive to low level extended structure due to its higher sensitivity as well as the shorter baselines from the C array observations.

2.7 The VLA-COSMOS survey in the COSMOS context

All data obtained by the COSMOS collaboration will be made available to the public via the COSMOS archive at IPAC/IRSA. The final reduced and calibrated data of the VLA-COSMOS pilot project can already be found there. For the large project of the VLA-COSMOS survey, the final reduced and calibrated A+C 1.4 GHz image covering the entire COSMOS field as well as the source catalogs described here are available as well.

One unique aspect of the overall COSMOS survey is the large ongoing spectroscopic effort (Lilly et al. 2007; Impey et al. 2007). Given the fortunate timing of observations, source lists from the VLA-COSMOS survey do provide target lists for these spectroscopic surveys. The Magellan-COSMOS survey (Impey et al. 2007) is targeting potential AGN candidates (from the X-ray and radio surveys) down to an $i_{AB} = 23.0$ mag. Most VLA-COSMOS sources with optical counterparts fulfilling this criteria are being observed by this survey. At the time of writing, for over 200 radio sources a spectral classification has already been obtained, with an expected total of 500 sources (Trump et al. 2007). In addition, the zCOSMOS survey (Lilly et al. 2007) is including VLA-COSMOS sources with optical counterparts down to $B_{AB} = 25.0$ mag in their target lists as compulsory targets.

Therefore, we expect that over 1,500 VLA-COSMOS sources will have optical spectra, once the spectroscopic surveys are completed. These spectra do not only provide very accurate redshifts, but also allow a better classification of the nature of the host galaxy (AGN vs. star formation). Thus the VLA-COSMOS survey will provide the largest sample of radio sources with spectral information in the redshift range $z > 0.3$. For comparison, in the local universe, the largest samples of radio sources with optical spectra are the combined 2dFGRS+NVSS with 757 sources (Sadler et al. 2002a) and the combined SDSS+FIRST with 5454 entries (Ivezić et al. 2002). Together with the information available from the other wavelengths covering the X-ray to mm regime, COSMOS will provide a unique dataset for the study of the faint radio source population.

Chapter 3

A new method to separate star forming from AGN galaxies at intermediate redshift: The submillijansky radio population in the VLA-COSMOS survey

In the previous Chapter the VLA-COSMOS Large Project which yielded to date the largest sample of faint radio sources was presented. In this Chapter a new method is developed that efficiently discriminates between the two main extragalactic radio populations – AGN and star forming galaxies, and it is applied to the VLA-COSMOS radio sources. Further, this new method, combined with the full COSMOS panchromatic (X-ray to radio) data, is utilized to study the composition of the submillijansky radio sources. At the time of writing this work has been submitted to ApJ as:

V. Smolčić, E. Schinnerer, M. Scodeggio, P. Franzetti et al., *A new method to separate star forming from AGN galaxies at intermediate redshift: The submillijansky radio population in the VLA-COSMOS survey*

Abstract

We explore the properties of the submillijansky radio population at 20 cm by applying a newly developed color-based method, in conjunction with complementary multi-wavelength data, to separate star forming (SF) from AGN galaxies at intermediate redshifts ($z \lesssim 1.3$). The main feature of our method is an efficient discrimination of SF galaxies and AGN (i.e. LINERs, Seyferts, type 2 QSOs, absorption-line AGN) using only photometric – optical rest-frame – data which are available for large numbers of galaxies even at high and intermediate redshifts. The method is based on the locally found tight correlation between rest-frame colors of emission-line galaxies and their position in the emission-line based Baldwin, Phillips & Terlevich (BPT) diagram, which is commonly used for spec-

troscopically separating low-luminosity AGN from SF galaxies. We extensively test our classification method at intermediate redshifts, and show that it agrees remarkably well with other independent classification schemes which rely on mid-infrared colors and optical spectroscopy. Based on a large sample of local galaxies, drawn from the SDSS and NVSS sky surveys, we infer the completeness and contamination of the samples of SF and AGN galaxies, selected using only their rest-frame color properties. We show that in a radio selected optical sample our method selects $\sim 85\%$ and $\sim 95\%$ complete samples of SF and AGN galaxies, respectively. Further, although optical rest-frame colors are used for the SF/AGN separation, our separation method is shown not to be biased against dusty starburst galaxies. This classification method is calibrated and tested here on a radio selected optical sample, however it carries the potential to be generally applied to any given sub-set of galaxies where SF and AGN galaxies are the two dominant sub-populations.

In order to quantify the properties of the submillijansky radio population, we analyze $\sim 2,400$ radio sources, detected at 20 cm in the VLA-COSMOS survey with a signal to noise ≥ 5. About 90% of these have submillijansky fluxes. We make use of the multi-wavelength (X-ray to radio) observations of the COSMOS field, and apply our classification method to $\sim 1,560$ of the radio sources that have optical counterparts brighter than $i_{AB} = 26$. We separate them into five classes of objects: 1) star candidates, 2) quasi stellar objects (QSOs), 3) active galactic nuclei (AGN), 4) star forming (SF), and 5) high redshift ($z > 1.3$; high-z) galaxies. Further, for the high-z galaxies, as well as the VLA-COSMOS radio sources with no optical counterparts brighter than $i_{AB} = 26$ we utilize optical, near- and mid-infrared observed color properties to study their nature.

Our results show that in the VLA-COSMOS radio-optical sample only 2 objects ($\sim 0.1\%$) are consistent with having stellar properties, and less than 10% are identified as type 1 QSOs. Out of 941 galaxies at $z \leq 1.3$ 340 are classified as star forming, and 601 as AGN. We show that the 476 galaxies in the radio-optical sample above $z = 1.3$ consist of a mixture of SF and AGN galaxies, and that this is also the case for the 830 radio sources without identified optical counterparts (brighter than $i = 26$). Further, our results yield that *SF galaxies are not the dominant population at submillijansky flux levels, as often previously assumed, but that they make up an approximately constant fraction of $30 - 40\%$ in the flux range of $\sim 50\ \mu Jy$ to $0.7\ mJy$.* In summary, based on the entire VLA-COSMOS radio population at 20 cm, we find that the radio population at these fluxes is a mixture of roughly $30 - 40\%$ of SF and $50 - 60\%$ of AGN galaxies, with a minor contribution ($\sim 10\%$) of QSOs.

3.1 Introduction

The most straight-forward information that can be derived from extra-galactic radio sky surveys are the radio source counts, which have been extensively studied in the last three decades (Condon 1984a; Windhorst et al. 1985a; Gruppioni et al. 1999; Seymour et al. 2004; Simpson et al. 2006). If space was Euclidian, and there was no cosmic evolution of radio sources, then the differential source counts would follow a power law with exponent of 2.5 (see e.g. Peterson 1997). Hence, the observed slope (and the change of the

slope) of the radio source counts in different flux ranges provides an insight, although quite indirect, into the global properties of extra-galactic radio sources, and their cosmic evolution. Past studies have shown that at 1.4 GHz fluxes above ~ 100 mJy the source counts are dominated by 'radio-loud' AGN with luminosities above the Fanaroff & Riley (1974; FR) break ($\sim 2 \times 10^{25}$ W Hz^{-1}; Willott et al. 2002). Decreasing from about 100 mJy to 1 mJy, the source counts follow a power law (e.g. Windhorst et al. 1985a), and are mostly made up of 'radio-loud' objects with luminosities below the FR break (FR Class I sources). However, the differential source counts change their slope again, i.e. they flatten below 1 mJy, and these sub-mJy radio sources have often been interpreted as a rising new population of objects, which does not contribute significantly at higher fluxes (e.g. Condon 1984a).

To date the exact composition of this faint radio population (hereafter 'population mix') is not well determined, and it is rather controversial. Windhorst et al. (1985a) suggested that the majority of sub-mJy radio sources are faint blue galaxies, presumably undergoing significant star formation. Optical spectroscopy, obtained by Benn et al. (1993), supported this idea, and the source counts at faint levels were successfully modeled with a population of intermediate-redshift star forming galaxies (Seymour et al. 2004). However, spectroscopic results by Gruppioni et al. (1999) suggested that early-type galaxies were the dominant population at sub-mJy levels. Further, it was recently suggested and modeled that the flattening of the source counts may be caused by 'radio-quiet' AGN (radio-quiet quasars and type 2 AGN), rather than star forming galaxies (Jarvis & Rawlings 2004); observations support this interpretation (Simpson et al. 2006). Based from the combination of optical and radio morphology as an identifier for AGN and SF galaxies, Fomalont et al. (2006) suggested that at most 40% of the sub-mJy radio sources are comprised of AGN, while Padovani et al. (2007) indicated that this fraction may be $60-80\%$ (the latter based their SF/AGN classification on a combination of optical morphologies, X-ray luminosities, and radio–to–optical flux ratios of their radio sources).

Two main reasons exist for such discrepant results. First, the identification fraction of radio sources with optical counterparts, which is generally taken to be representative of the full radio population, spans a wide range in literature (20% to 90%) depending on the depth of the available optical data. Second, the methods that were used to separate AGN from SF galaxies have been very heterogeneous in the past, ranging from pure radio luminosity or morphology cuts, through observed color properties to optical spectroscopy.

The two main populations of radio sources in deep radio surveys at 1.4 GHz (20 cm) are active galactic nuclei (AGN) and star forming (SF) galaxies (Condon 1984a; Windhorst et al. 1985a). At this frequency the radio emission predominantly arises from synchrotron emission powered either by accretion onto the central super-massive black hole (SMBH) or by supernovae remnants (e.g. Condon 1992). It was shown that radio properties such as the distributions of mono-chromatic luminosities of SF and AGN galaxies (Seyferts, LINERs) are comparable and overlapping (at least locally; e.g. Sadler et al. 1999). Hence, in order to disentangle SF and AGN galaxies in the radio regime, observations at other wavelengths are required.

Studies of extra-galactic radio sources in the *local universe* ($z < 0.3$) have been in-

vigorated due to the recent advent of panchromatic photometric and spectroscopic all-sky surveys, such as e.g. NVSS (Condon et al. 1998), FIRST (Becker et al. 1995), SDSS (York et al. 2000), IRAS (Neugebauer et al. 1984), 2dF (Colless et al. 2001) which provide additional panchromatic photometric (e.g. Simpson et al. 2006) and/or optical-IR spectro-scopic (e.g. Sadler et al. 1999; Best et al. 2005) observations. For example, the panchro-matic properties of radio sources were studied to full detail (Ivezić et al. 2002; Obrić et al. 2006), as well as the environmental dependence of radio luminous AGN and SF galaxies (Best 2004), and their luminosity function (Sadler et al. 1999; Jackson & Londish 2000; Chan et al. 2004; Best et al. 2005). Further, radio emission as a star formation rate in-dicator was well calibrated using a local sample (Bell 2003) and compared to other star formation tracers (Hopkins et al. 2003).

However, it still remains to uncover the global properties of the *intermediate-redshift* ($z \lesssim 1.3$) radio sources. For example, the cosmic star formation history of the universe (i.e. the global star formation rate per unit comoving volume as a function of redshift) was not determined with a high accuracy using radio data (see e.g. Haarsma et al. 2000; Hopkins 2004), the radio luminosity function for SF and AGN galaxies at $z > 0.3$ is not known, and the exact composition of the sub-millijansky radio population is still unknown and a matter of debate (Condon 1984a; Windhorst et al. 1985a; Gruppioni et al. 1999; Seymour et al. 2004; Jarvis & Rawlings 2004; Simpson et al. 2006).

In this work and in a number of accompanying papers, we will focus on these properties of radio sources using the 1.4 GHz VLA-COSMOS survey (Schinnerer et al. 2007, Chap. 2). The main aim of the current paper is twofold. First, we develop a method based only on multi-wavelength photometric data to efficiently separate SF from AGN galaxies in the VLA-COSMOS 20 cm survey. Secondly, we use this classification to derive the composition of the sub-mJy radio population. In Sec. 5.2 we describe the COSMOS multi-wavelength data, and in Sec. 3.3 we present the cross-correlation of the sources detected at 1.4 GHz with catalogs at other wavelengths. In Sec. 3.4 we describe our source classification methodology and introduce our 'rest-frame color based classification method' (see below), which we calibrate and extensively test using a large well-characterized sample of local galaxies. We present the classification of the VLA-COSMOS 1.4 GHz radio sources with identified optical counterparts in Sec. 3.5, and in Sec. 3.6 we compare our classification method with other classification schemes proposed in the literature. In Sec. 3.7 we study the 'population mix' in the VLA-COSMOS radio survey, based on the entire sample of VLA-COSMOS radio sources. We summarize our results in Sec. 5.6.

Throughout the paper we report magnitudes in the AB system, and assume the follow-ing cosmology: $H_0 = 70, \Omega_M = 0.3, \Omega_\Lambda = 0.7$. We define the radio synchrotron spectrum as $F_\nu \propto \nu^{-\alpha}$, and assume $\alpha = 0.8$ if not stated otherwise. Hereafter, we refer to our method to classify the VLA-COSMOS radio sources into five sub-types of objects (star candidate, QSO, AGN, SF, high-z galaxy) as *"classification method"*, and to our method to disentangle only the SF from AGN galaxies, based on rest-frame color properties, as *"rest-frame color based selection method"*.

3.2   The multi-wavelength data set

In this section we describe the COSMOS multi-wavelength data used for the work presented here.

3.2.1   Radio data

The COSMOS field was observed at 1.4 GHz (20 cm) with the NRAO Very Large Array (VLA) in A- and C- configuration (VLA-COSMOS Large Project; for details see Schinnerer et al. 2007, Chap. 2). The final map, encompassing $2\square°$, has a resolution of $1.5'' \times 1.4''$, and a mean rms of $\sim 10.5\,[15]\,\mu$Jy/beam in the central $1\,[2]\square°$.

The VLA-COSMOS source catalog reports the peak and total (i.e integrated) flux density for each object. For extended sources the total flux is derived by integrating over the object's size (see Schinnerer et al. 2007, Chap. 2 for details), while for unresolved sources it is set to be equal to the peak flux. Bondi et al. (2007) have shown that bandwidth smearing effects (i.e. chromatic aberration), combined with the pointing layout of the VLA-COSMOS observations, systematically decrease the measured source's peak flux to $\sim 80\%$ of its true value, while the total flux remains unaffected. Therefore, to correct for this, all peak fluxes in the catalog need to be increased by 25%. However, such an effect further entails a necessary re-definition of the sources in the field considered to be unresolved (cf. Fig. 14 in Schinnerer et al. 2007, Chap. 2 and Fig. 2 in Bondi et al. 2007). Therefore, to properly correct for bandwidth smearing effects, we have re-selected the unresolved sources following Bondi et al. (2007), and set their total fluxes to be 1.25 times their peak (respective integrated) fluxes. Throughout the paper we will use the integrated flux, corrected for bandwidth smearing where needed, as the representative flux for each source.

In order to minimize the number of possible spurious radio sources ($\sim 50\%$ below 5σ), we select only objects from the catalog that were detected at a signal to noise of $\geqslant 5$, and are located outside regions contaminated by side-lobes from nearby bright sources. This yields 2388 (out of 3643; i.e. $\sim 65\%$) sources, 78 of which consist of multiple components.

3.2.2   Near-ultraviolet, optical and infrared imaging data

The NUV to MIR imaging data and photometry for the COSMOS survey used here include data taken during 2003–2006 with ground – (Subaru, KPNO, CTIO, CFHT) and space (HST, Spitzer) – based telescopes, covering a wavelength range from 3500 Å to 8 μm, described them in more detail below.

Ground based data

The data reduction of the COSMOS ground-based observations in 15 photometric bands ranging from NUV to NIR, and the generation of the photometric catalog, is presented in Capak et al. (2007) and Taniguchi et al. (2007). Here we make extensive use of the COS-MOS photometric catalog. The photometric catalog was selected using the 0.6'' resolution

i^+ image. However, the photometry was obtained from the PSF (point-spread function) matched images, which degrades the resolution to $\sim 1.8''$. The median 5σ depths in AB magnitudes in the catalog for the u^*, B_J, g^+, V_J, r^+, i^+, i^*, z^+ and K_s bands[1] are 26.4, 27.3, 27.0, 26.6, 26.8, 26.2, 24, 25.2 and 21.6, respectively (see also tab. 2 in Capak et al. 2007). It is noteworthy that the detection completeness of the catalog is above 87% for objects brighter than $i = 26$.

Space based data

The HST/ACS observations, which covered $1.8\square°$ of the $2\square°$ COSMOS field, are described in Scoville et al. (2007c) and Koekemoer et al. (2007). The F814W band imaging has a resolution of $0.09''$ and a 5σ point-source sensitivity of $I_{AB} = 28.6$ (see also Capak et al. 2007). The ACS source catalog, which we utilize here, was constructed by Leauthaud et al. (2007), with special care given to the separation of point-sources from extended objects.

The Spitzer observations of the COSMOS field in all seven bands (3.6, 4.5, 5.8, 8.0, 24, 70, 160 μm) are described in Sanders et al. (2007). The $3.6-8\,\mu$m band catalog is available to full depth for the entire field. The resolution in the 3.6, 4.5, 5.8, 8.0 μm bands is $1.7''$, $1.7''$, $1.9''$, and $2''$, respectively. The catalog was generated using SExtractor on the four IRAC channels in dual mode, with the 3.6 μm image as the detection image. The 5σ depth for point-sources at 3.6 μm is 1 μJy, corresponding to an AB magnitude of 23.9. In this work we also make use of the MIPS 24 μm catalog obtained from the shallow observations of the entire COSMOS field during Cycle 2 of the S-COSMOS program (see Sanders et al. 2007 for details). The resolution and 5σ depth of the catalog are $6''$ and 0.3 mJy, respectively. The latter corresponds to an AB magnitude of 17.7. For the purpose of this paper, we will use only sources that were detected at 24 μm at or above the 3σ level corresponding to their local rms.

3.2.3 X-ray data

The full $2\square°$ COSMOS field was observed with the XMM-Newton satellite EPIC camera for a total net integration time of 1.4 Ms (for a description of the XMM-COSMOS survey see Hasinger et al. 2007). The limiting flux of the XMM-COSMOS survey is 10^{-15} erg cm^{-2} s^{-1} and 5×10^{-15} erg cm^{-2} s^{-1} in the soft ($0.5-2$ keV) and hard ($2-10$ keV) bands, respectively. The X-ray point-source detection is described in Cappelluti et al. (2007), and the optical identifications of the X-ray sources for the first 12 observed XMM fields (over a total of $1.3\square°$) are presented by Brusa et al. (2007). For the analysis presented here we utilize the catalog with 1865 optical counterparts of the XMM-COSMOS point sources, drawn from the full $2\square°$ XMM-Newton mosaic (Brusa et al. in prep).

---

[1]The '+' super-script and 'J' sub-script designate the Subaru filters, while the '*' sign stands for CFHT filters.

3.2.4 Photometric redshifts

The COSMOS photometric redshifts (Ilbert et al. in prep) utilized here are based on an a large amount of deep multi-color data (Taniguchi et al. 2007): 6 broad optical bands obtained at the Subaru telescope (u^+, g^+, r^+, i^+, z^+) and 2 at CFHT (u^* and i^*), 8 intermediate and narrow band filters from the Subaru telescope ($IA427$, $IA464$, $IA505$, $IA574$, $IA709$, $IA827$, $NB711$, $NB816$), deep Ks-band data from the WIRCAM/CFHT camera (McCracken et al., in prep), and $3.6\mu m$ and $4.5\mu m$ data from the SPITZER IRAC camera (Sanders et al. 2007). The photometric redshifts are estimated via a standard χ^2 fitting procedure (Arnouts et al. 2002) using the code *Le Phare*[2] written by S. Arnouts & O. Ilbert. A major feature of this method is the calibration of the photometric redshifts using a spectroscopic sample of ~ 1000 bright galaxies ($I_{AB} < 22.5$) obtained as part of the zCOSMOS survey (Lilly et al. 2007). We follow exactly the same calibration method as described in Ilbert et al. (2006): a) a calibration of the photometric zero-points, and b) an optimization of the template SEDs (spectral energy distributions). This calibration method allows us to remove systematic offsets in the estimates of the photometric redshifts. A direct comparison between the photometric redshifts and the zCOSMOS spectroscopic redshifts shows that the photometric redshifts reach an accuracy of $\sigma\left(\frac{\Delta z}{1+z}\right) \sim 0.014$ at $i < 22.5$. The fraction of catastrophic failures is less than 1% at $i < 22.5$. Such an accuracy and robustness can be achieved thanks to both the intermediate bands and deep NIR photometric data. The photometric redshifts for the entire COSMOS population will be described in full detail in Ilbet et al. (in prep). The galaxies in the sample used here are radio selected, i.e. they are not randomly drawn from the global COSMOS population. Therefore, in Fig. 3.1 we show the comparison of the photometric and spectroscopic redshifts for a sub-sample of our VLA-COSMOS sources with available spectroscopy (see next section). The accuracy is $\sigma\left(\frac{\Delta z}{1+z}\right) = 0.027$, which is somewhat lower than the accuracy for the full sample of COSMOS sources, however it is still satisfactory.

As photometric redshift codes generally take into account only galaxy SED models, the photometric redshifts for broad line AGN are usually poorly estimated, and alternative ways for their redshift computations have to be applied. At the time of writing, no accurately estimated photometric redshifts for broad line AGN exist for the COSMOS project. The photometric redshifts for broad line AGN will be presented in a future publication (Salvato et al. in prep).

3.2.5 Optical spectroscopic data

The ongoing COSMOS optical spectroscopic surveys (Trump et al. 2007; Impey et al. 2007; Lilly et al. 2007) provide to date 657 spectra, with good redshift estimates, for objects in the VLA-COSMOS 1.4 GHz radio sample described in Sec. 3.2.1. We augment this spectroscopic data set with available spectroscopic information for 65 galaxies from the SDSS DR4 "main" spectroscopic sample, 13 objects from the SDSS DR5 quasar catalog (Schneider et al. 2005), 2 sources from the 2dF survey, as well as for 27 objects taken

---

[2]www.lam.oamp.fr/arnouts/LE_PHARE.html
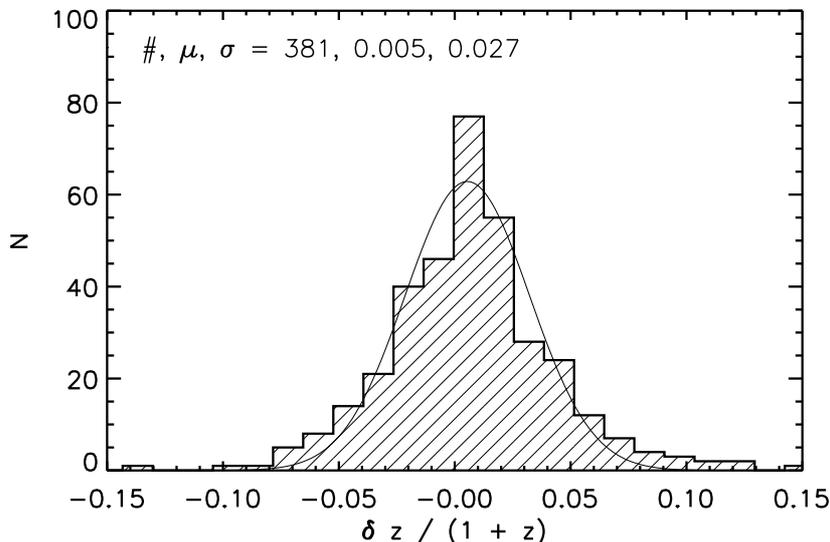
Figure 3.1   Comparison of the photometric and spectroscopic redshifts for the VLA-COSMOS radio sources with optical counterparts (see Sec. 3.3.1) for which spectroscopy is available. The shown distribution was limited to spectroscopic redshifts ≤ 1.3, consistent with the redshift range used in this work. Note the excellent accuracy of the photometric redshifts.

with the MMT 6.5 m telescope, and presented by Prescott et al. (2006). Thus, a total of 764 spectra is available. However, as a number of sources were spectroscopically observed multiple times, we have spectroscopic information for 520 unique sources in our radio sample. Throughout the paper, we use the spectroscopic redshifts, where available. We also use this sub-set of radio sources with observed optical spectra as a control sample to verify the presented classification method.

3.3 VLA-COSMOS 1.4 GHz radio sources at other wavelengths

In this section we define the *'matched' radio source sample*, a sample of radio sources with optical counterparts cross-correlated with the panchromatic COSMOS observations, as well as the *'remaining' radio source sample*, both of which will be used throughout the paper. First, we restrict the full VLA-COSMOS radio source sample to objects which have optical counterparts (Sec. 3.3.1). Then we positionally match these objects with sources detected in the MIR (Sec. 3.3.2) and X-ray (Sec. 3.3.3) spectral ranges. In Sec. 3.3.4 we describe the remaining radio sources that are either without identified or with identified but flagged optical counterparts.

3.3.1 Positional matching of the COSMOS radio and NUV/optical/NIR catalogs

The VLA-COSMOS Large Project source catalog contains 2388 radio sources detected at a signal to noise ≥ 5 and outside side-lobe-contaminated regions (see Sec. 3.2.1). 78 of these consist of multiple components. For the purpose of this paper we match these radio sources with sources that have also been detected in the optical regime, and are reported in the COSMOS photometric catalog (Capak et al. 2007). In order to obtain a sample with reliable radio-optical counterparts, we positionally match the radio sources only with

optical sources brighter than $i = 26$. The reason for this is illustrated in Fig. 3.2, where we show the distance between the radio sources and their nearest optical counterparts as a function of the i band magnitude. As the median distance rapidly increases for $i > 26$ (most probably introducing a significant number of false match associations) we apply a cut of $i = 26$ to the NUV-NIR photometric catalog before matching the radio and optical catalogs.
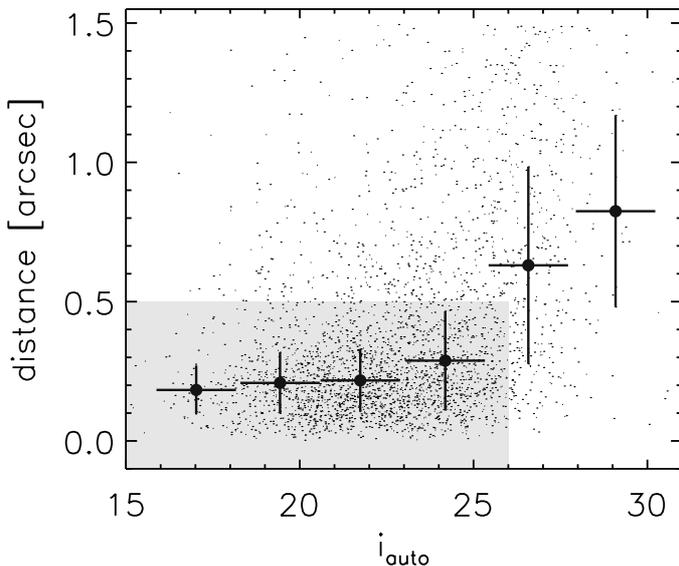
Figure 3.2 Distance as a function of i band magnitude for radio sources in the VLA-COSMOS survey (with S/N ≥ 5) positionally matched to the closest optical counterpart (small dots). The large dots show the median distance for each magnitude bin (the width of the bin is indicated by horizontal lines) and the corresponding interquartile range (vertical lines). Note that the median distance is significantly larger beyond $i = 26$, presumably introducing a significant number of false match associations. The shaded area indicates the allowed matching region, which is set by the matching radius ($0.5''$) and the magnitude cut-off ($i = 26$) used to find secure optical counterparts for the radio sources in the sample (see text for details).

Hence, to find the corresponding optical counterpart for each radio source (excluding multi-component sources, which are separately addressed below), we search for the nearest optical neighbor within a radial distance of $0.5''$. The search radius was chosen in such a way that it balances a high completeness of true matches and a low false-match contamination rate: A cut-off of $0.5''$ essentially includes all true matches in the sample, with a false association rate (computed from the source density in the matched catalogs) of only $\sim 4\%$. The high completeness and low contamination are due to the excellent astrometric accuracy of both the COSMOS radio and optical data. Our matching yielded 1749 radio sources with securely identified optical counterparts. However, 252 ($\sim 15\%$) of these are located in masked-out regions (i.e. around bright saturated stars) in the photometric catalog. Thus, their NUV-NIR photometry, as well as the photometric redshift computation has a significantly reduced accuracy. We exclude these objects from our main sample.

The multi-component radio sources in the VLA-COSMOS survey consist of radio sources which could not be fitted using a single Gaussian function (see Schinnerer et al. 2007, Chap. 2). The radio morphologies of such sources can be fairly complex (e.g. single or double lobed radio galaxies), and this makes it substantially more difficult to associate such radio sources with the appropriate optical counterparts (see e.g. Ivezić et al. 2002; Best et al. 2005). In order to avoid any biases which may be caused using an automatic association procedure, the optical counterparts of the VLA-COSMOS multi-component radio sources were determined visually. The 1.4 GHz catalog contains 78 multi-component sources detected at or above 5σ, and 65 were securely associated with an optical counter-

part with $i < 26$, however 4 are located inside masked-out areas (around bright saturated stars) in the photometric catalog, and we therefore exclude them from the main sample.

In summary, the applied matching criteria yield 1814 ($\sim 76\%$ of the 2388 radio sources with S/N ≥ 5) radio sources with secure optical counterparts down to $i = 26$, 65 of which are multiple component sources. The most accurate NUV-NIR photometry (i.e. excluding flagged regions around saturated objects) was obtained for 1558 ($\sim 86\%$ of 1814), 61 of which are multiple-component radio sources. Hereafter, we refer to this latter sample of 1558 radio sources, which make up $\sim 65\%$ of the radio sources with S/N ≥ 5, and that were matched to the NUV-NIR catalog, as the *'matched' radio source sample.* For reference, the 1.4 GHz total flux distributions for the complete radio sample, the matched radio sample, and the sub-sample with available spectroscopy is shown in the top panel in Fig. 3.3. The distribution of the i band magnitude for the matched radio sample, as well as the spectroscopic sub-sample, is shown in the bottom panel in Fig. 3.3. It is also worth noting that our cross-correlation is consistent with the results of the maximum likelihood ratio technique applied to VLA-COSMOS sources (Ciliegi et al. in prep), however our restrictions for the masked-out regions in the photometric catalog, as well as the optical magnitude limit, are more conservative, as the analysis presented here strongly relies on accurate NUV to NIR photometry.

A further data set that we use in the analysis presented here is the HST/ACS point-source information. We extract this information for each radio source in our matched sample by positionally matching the optical counterparts of the radio sources with point-sources identified in the HST/ACS F814W source catalog (Leauthaud et al. 2007). Using a matching radius of $0.5''$ yields 47 objects in our matched radio sample classified as point sources based on the HST/ACS F814W images. The mean distance between the matched objects is only $(0.12 \pm 0.07)''$.

3.3.2   Radio – optical sources with IRAC and MIPS detections

We cross-correlate the matched radio source sample with the S-COSMOS – IRAC catalog using a maximum allowed distance to the optical counterparts of our radio sources of $0.5''$. [Note that such a cross-correlation allows for a maximum distance between the radio and MIR sources to be $1''$.] Such an adopted search radius essentially selects a complete radio – optical – MIR sample with a false match association for the MIR sources of $\lesssim 1\%$ with the optical counterparts, and $\lesssim 4\%$ with the radio counterparts. In summary, out of 1558 radio sources in the matched radio sample, 1448 (93%) have secure MIR counterparts.

The 24 μm fluxes for all our radio sources were obtained from the COSMOS field observations using the S-COSMOS – MIPS shallow survey with a resolution of $6''$. Although a relaxed search radius of $5''$ was used to find the radio – 24 μm counterparts, the median distance is only $0.19''$ with an interquartile range of $0.16''$. About 50% (799 out of 1558) sources in the matched radio sample have a MIPS counterpart at 24 μm with a signal to noise at or above 3.
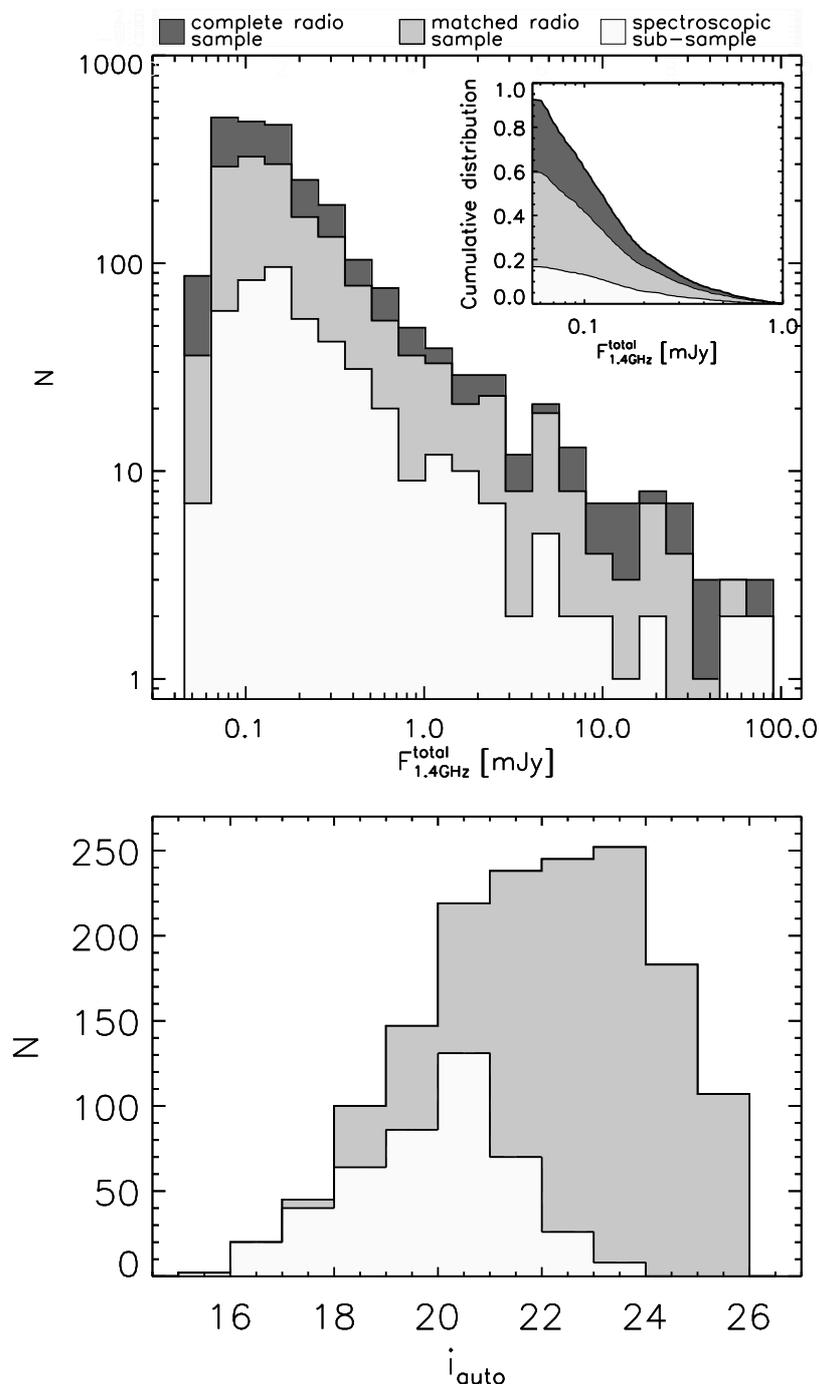
Figure 3.3 *Top panel*: The distribution of the total 1.4 GHz (20 cm) flux density for i) the complete radio source sample (S/N ≥ 5; dark-grey shaded histogram), ii) the matched radio sample (grey-shaded histogram) and iii) the spectroscopic sub-sample (light-grey shaded histogram). The inset shows the cumulative distribution for the three samples computed as a function of *decreasing* total flux. Note that the spectroscopic sub-sample fairly represents the faint radio population as a function of the total flux. *Bottom panel*: Distribution of the *i* band magnitude (Subaru where available, otherwise CFHT) for sources in the VLA-COSMOS matched radio source sample, and the spectroscopic sub-sample in the same notation as in the top panel.

3.3.3 Radio – optical sources with point-like X-ray emission

Using the maximum likelihood ratio technique Brusa et al. (2007) presented the optical identifications of the X-ray point-sources (Cappelluti et al. 2007) detected in the XMM-COSMOS survey (Hasinger et al. 2007). Here we utilize their identifications to match the sources in our matched radio sample with detected X-ray point sources. Out of 1558 radio sources with optical counterparts, 179 (12% of 1558) are identified as point-sources in the X-ray bands. 17 of these have multiple counterpart candidates as defined by Brusa et al. (2007). In these cases, if we assume that the radio sources are physically associated with the X-ray sources, then the radio data, which have a significantly better astrometric accuracy, can be used to constrain more precisely the optical counterpart of this given object. A visual inspection of the 17 sources, classified as having ambiguous identifications by Brusa et al. (in prep), strongly suggests that their most probable optical counterparts, reported in the X-ray – optical catalog, are real associations. Hence, we proceed in our analysis taking all 179 X-ray detected point sources to be true counterparts of the objects in the matched radio sample.

3.3.4 Radio sources with photometrically flagged or without optical counterparts at other wavelengths

In Sec. 3.3.1 we have defined the matched radio sample which consists of 1558 1.4 GHz sources that have optical counterparts out to an i band magnitude of 26, and within a radial distance of less than $0.5''$. These sources were also required to have the most accurate NUV-NIR photometry, i.e. counterparts within flagged regions due to saturation and belending effects in the NUV-NIR images were excluded. Thus, 830 radio sources remain with no identified optical counterparts within these limits, 256 (i.e. $\sim 30\%$) of which have counterparts with $i \leq 26$ that lie in masked-out regions. Hereafter, we will refer to this sample of sources as the *'remaining radio source sample'*. We positionally match these sources to the IRAC catalog using a maximum allowed distance of $1''$, and find 610 ($\sim 75\%$) matches. Based on Poisson statistics and the source density of the MIR sources, such a search radius essentially includes all true matches with a false contamination rate of $\lesssim 4\%$. It is worth noting that more than one half of the remaining 25% of the radio objects were independently identified as possible spurious sources, based on visual inspection, while the other half are either located in blended regions in the IRAC images or slightly further away than the allowed $1''$ from the position reported in the IRAC catalog (the morphology of the IRAC sources being often extended). Thus, we consider these $\sim 75\%$ of radio – MIR matches representative of the entire remaining radio population. Out of the 830 sources 318 (i.e. $\sim 40\%$) have MIPS 24 μm detections (S/N ≥ 3), and 31 ($\sim 4\%$) have XMM point source counterparts (these 31 objects are a sub-sample of the 256 objects in the flagged regions). In Sec. 3.7 we analyze the properties of these remaining sources, and their contribution to the 'population mix' in the VLA-COSMOS survey. The summary of the multi-wavelength cross-correlation of the VLA-COSMOS radio sources is given in Tab. 3.1.

Table 3.1 Multi-wavelength cross-correlation of VLA-COSMOS 1.4 GHz radio sources

	total	z_{spec}	IRAC[1]	MIPS[2]	XMM[3]
total radio sample	2388	520	2058	1117	210
matched radio sample*	1558	447	1448	799	179
stars	2	0	2	2	0
QSOs	139	31	122	78	43
SF galaxies[i]	340	150	322	280	16
AGN galaxies[i]	601	262	579	267	98
high-z galaxies[ii]	476	4	423	172	22
remaining radio sample**	830	73	610	318	31

[1] Detected in the Spitzer/IRAC 3.6 μm band.
[2] Detected in the Spitzer/MIPS 24 μm band within the shallow
MIPS COSMOS survey at or above a signal to noise of 3.
[3] X-ray point-sources associated with optical counterparts as described in Brusa et al. (2007)
* Radio source sample positionally matched to optical sources with AB
$i \leq 26$ and outside masked-out regions in the NUV-NIR photometric catalog.
[i] Galaxies at redshift ≤ 1.3.
[ii] Galaxies at redshift > 1.3.
** Radio sources a) without optical counterparts with $i \leq 26$ ($\sim 70\%$), or b) with optical counterparts
($i \leq 26$) that lie in masked-out areas in the photometric catalog ($\sim 30\%$).

3.4 Classification Methodology

Extra-galactic radio sources consist of two main populations: star forming and AGN galaxies. We further divide the AGN class into two main sub-classes: QSOs (often unresolved in optical images, with broad emission lines in their spectra and high optical luminosity) and objects where the AGN does not dominate the entire SED, such as Type 2 QSOs, low-luminosity AGN (Seyfert and LINER galaxies) and absorption-line AGN (resolved in optical images, with both broad, narrow or no emission lines in their optical spectra). Throughout the paper, we will mostly refer to the latter sub-class only as 'AGN'.

The well-calibrated tools for disentangling SF galaxies from low-luminosity AGN (Seyfert and LINERs) are spectroscopic diagnostic diagrams in the optical, which have been originally proposed for local galaxies by Baldwin et al. (1981). Baldwin et al. have shown that two emission line flux ratios ([OIII 5007]/Hβ vs. [NII 6584]/Hα; hereafter *BPT diagram*) are sufficient to efficiently separate galaxies dominated by star formation from those dominated by the emission caused by a central super-massive black-hole. Their method has been later revised (Veilleux & Osterbrock 1987; Kewley et al. 2001), and expanded to other emission line flux ratios, easily attainable for higher redshift ($z \lesssim 0.7$) galaxies (Rola et al. 1997). These diagnostics have been extensively used in the past for a successful separation of SF and AGN galaxies in the local universe (Sadler et al. 1999; Kauffmann et al. 2003a; Brinchmann et al. 2004; Obrić et al. 2006; Smolčić et al. 2006). However, the main drawback of spectroscopic observations is that they are very expensive in terms of telescope time, especially when large numbers of faint objects need to be observed. Therefore, al-

ternative methods, which are based only on photometric data, have to be invoked for the separation of SF from AGN galaxies without the need for time-consuming spectroscopy. Here we develop such a method (hereafter 'rest-frame color based classification method'), which we apply in the next sections to the VLA-COSMOS galaxies in the matched radio sample in order to identify SF and AGN galaxies. The basic idea of our rest-frame color based classification method is outlined as follows.

Recently, based on 99,000 galaxy spectra from the Sloan Digital Sky Survey (SDSS) "main" spectroscopic sample from the First Data Release (a flux limited sample, $r_{\mathrm{Pet}} <$ 17.77, over $1360\square°$; hereafter "SDSS main galaxy sample") it was shown that the overall NUV to NIR SED of galaxies is a one-parameter family, and further that spectral diagnostic parameters, such as line strengths, appear to be well correlated with the overall galaxy's SED (see Obrić et al. 2006; Smolčić et al. 2006). In particular, Smolčić et al. (2006) have found *a tight correlation between rest-frame colors of emission-line galaxies and their position in the emission-line based BPT diagram*. This correlation thus provides a powerful tool for disentangling SF from AGN galaxies using only photometric data, i.e. rest-frame colors, and we utilize it as the key of our rest-frame color based classification method.

3.4.1   Calibration of the rest-frame color based classification method in the local universe

The rest-frame colors P1 and P2

Smolčić et al. (2006) used the SDSS main galaxy sample to synthesize rest-frame magnitudes in the modified Strömgren photometric system (uz,vz,bz,yz encompassing the wavelength range of $3200 – 5800$Å; Odell et al. 2002)[3], and study the rest-frame color properties of these galaxies. In order to optimally quantify the distribution of galaxies in the rest-frame color-color space, they defined a set of principal component axes ($P1$,$P2$), where $P1$ measures the position along the galaxy locus, and $P2$ the position perpendicular to it (see Fig. 4 in Smolčić et al. 2006). As the galaxy locus is slightly curved, the functional form of the rest-frame colors is given separately for the blue and red ends, with a boundary at $vz - yz = 0.646$. Hence, for galaxies with $vz - yz \leq 0.646$ ($P1$,$P2$) are given as:

$$P1 = \quad 0.911 \, (c_1 - 0.646) + 0.412 \, (c_2 - 0.261) \tag{3.1}$$

$$P2 = -0.412 \, (c_1 - 0.646) + 0.911 \, (c_2 - 0.261), \tag{3.2}$$

and for galaxies with $vz - yz > 0.646$ as:

$$P1 = \quad 0.952 \, (c_1 - 0.646) + 0.307 \, (c_2 - 0.261) \tag{3.3}$$

$$P2 = -0.307 \, (c_1 - 0.646) + 0.952 \, (c_2 - 0.261), \tag{3.4}$$

---

[3]The filter response curves of the modified Strömgren system are available at http://www.mpia-hd.mpg.de/COSMOS/

where $c_1 = vz - yz$ and $c_2 = bz - yz$. We use these equations to derive the rest-frame colors $P1$ and $P2$ for the galaxies in the matched radio sample. However, for the rest-frame color based classification method we utilize only the $P1$ color, which strongly correlates with emission line properties of AGN and SF galaxies (see Sec. 3.4.1).

The local sample

In order to obtain insight into the efficiency of the rest-frame color based classification method, we construct a large sample of well-known low-redshift galaxies ($0.01 < z < 0.3$), whose properties are assumed to present well the properties of the galaxies in the VLA-COSMOS matched radio sample. The local sample was generated from the SDSS main galaxy sample, positionally matched to sources detected in the 1.4 GHz NVSS survey. Additionally, a sub-sample of galaxies detected with IRAS was constructed (see Obrić et al. 2006 for details about the cross-correlation of the SDSS, NVSS, IRAS catalogs). The SDSS/NVSS sample contains 6966 galaxies and the SDSS/NVSS/IRAS sample 875 galaxies with available SDSS optical spectroscopy. The computation of rest-frame colors ($P1$,$P2$) for these galaxies is presented in Smolčić et al. (2006). It is noteworthy to mention that given a) the detection limits, and b) the areal coverage of the NVSS and VLA-COSMOS surveys, both surveys observe approximately the same populations of objects, although over different redshift intervals (see Fig. 1 in Schinnerer et al. 2007, Chap. 2). Assuming that evolutionary effects with redshift do not significantly alter the reliability of the identification method presented below, at least out to $z = 1.3$, this makes the local sample of galaxies representative of the galaxies in the VLA-COSMOS matched radio sample.

Based on *spectral line* properties we separate the local sample into three classes of objects: *AGN, star-forming galaxies and composite objects*, where the latter are considered to have a comparable contribution of both star formation and AGN activity. This is done as follows. First, galaxies *with emission lines in their spectra* are separated into these three classes using their position in the BPT diagram, shown in the bottom panel in Fig. 3.4, where we also indicate the chosen boundaries between these classes[4] (see Kewley et al. 2001; Kauffmann et al. 2003c). Second, as the galaxies that have *no emission lines* in their spectra cannot be star forming (see also Sec. 3.4.1 for a discussion of this point), and as all of the objects in the SDSS/NVSS sample are observed to have 1.4 GHz emission which arises either from AGN or star formation activity in a galaxy, we define galaxies without emission lines in their spectra as AGN (see also Best et al. 2005 who classified these types of objects as absorption line AGN).

The completeness and contamination of the photometrically selected samples of star forming galaxies and AGN

In the top panel in Fig. 3.4 we show the distribution of $\sim 3,400$ SDSS/NVSS emission line galaxies in the ($P1$,$P2$) rest-frame color-color diagram. The color code is determined

---

[4]Note that the classification of AGN, SF, and composite galaxies based on the BPT diagram changed compared to the one used in Smolčić et al. (2006).

by the position of a galaxy in this plane. The bottom panel shows the BPT diagram for the same galaxies with the colors adopted from the upper panel. For these radio luminous galaxies, a strong correlation exists between their rest-frame optical colors and emission line properties, in particular between $P1$ and $\log([NII\ 6584]/H\alpha)$. Such a correlation was already shown in Smolčić et al. (2006) for the full "main" spectroscopic galaxy sample, however here we show that it also holds for a radio-selected optical sample. We want to stress that the SDSS/NVSS galaxies with no emission lines in their spectra have typically red $P1$ colors, with a median $P1$ value of 0.46 and an interquartile range of 0.13 (see also e.g. Fig. 12 in Smolčić et al. 2006).

Smolčić et al. (2006) argued that the $P2$ color is a proxy for the galaxies' dust content, with higher values of $P2$ corresponding to higher dust attenuation. However, they also showed that the dynamic range of $P2$ (although very narrow) could not be reproduced entirely using stellar population synthesis models (Bruzual & Charlot 2003), which we strongly rely on throughout this work (see Sec. 3.4.2). Hence, we will not use $P2$ as a component for our rest-frame color based classification method; we will rather base our selection on the $P1$ color allone.

In order to assess the completeness and contamination of the photometrically selected samples of star forming galaxies and AGN only by imposing a rest-frame color cut, we show in Fig. 3.5 the differential and cumulative distributions of $P1$ for the SDSS/NVSS star forming, composite and AGN galaxies. Here the classification is based on the BPT diagram for the galaxies with emission line in their spectra, while all galaxies without emission lines are included in the AGN class. These 'absorption line AGN' constitute the major fraction of all the AGN ($\sim 80\%$). The top panel shows the $P1$ histograms for these three types of objects, normalized by the total number of objects. In the middle panels in Fig. 3.5 we show the fractions for the SF, AGN and composite galaxies for the selection of SF (left panel) and AGN (right panel) galaxies. The fractions were computed in such a way that for each $P1$ value ($P1_i$) the distributions were normalized to the total number of galaxies in the sample with $P1 \leq P1_i$ (for SF galaxies; left panel), or $P1 > P1_i$ (for AGN galaxies; right panel). In this way, we obtain the fraction of SF, AGN and composite galaxies within the full sample that was selected only by applying a $P1$ color-cut. Further, in the bottom panels in Fig. 3.5 we show the cumulative distributions of the SF (left panel) and AGN (right panel) galaxies, scaled to the total number of SF and AGN galaxies, respectively, thus showing their completeness as a function of $P1$. As a compromise between completeness and contamination of the photometrically selected samples of galaxies, we choose a color-cut of $P1=0.15$ as the dividing photometric value between star forming galaxies and AGN. Thus, selecting galaxies with $P1 \leq 0.15$, and defining them as the 'photometrically selected sample of star forming galaxies', leads to a sample that contains $\sim 20\%$ AGN, $\sim 10\%$ composite objects, and $\sim 70\%$ 'real' (i.e. spectroscopically identified) SF galaxies (see middle left panel in Fig. 3.5). The latter make-up $\sim 85\%$ of *all* 'real' SF galaxies (see bottom left panel in Fig. 3.5). On the other hand, using the color cut as defined above to generate the 'photometrically selected AGN galaxy sample' ($P1>0.15$) leads to a sample that contains $\sim 5\%$ SF galaxies, $\sim 15\%$ composite objects, and $\sim 80\%$ 'real' AGN galaxies (see middle right panel in Fig. 3.5), where the latter make-up $\sim 90\%$ of *all* 'real' AGN
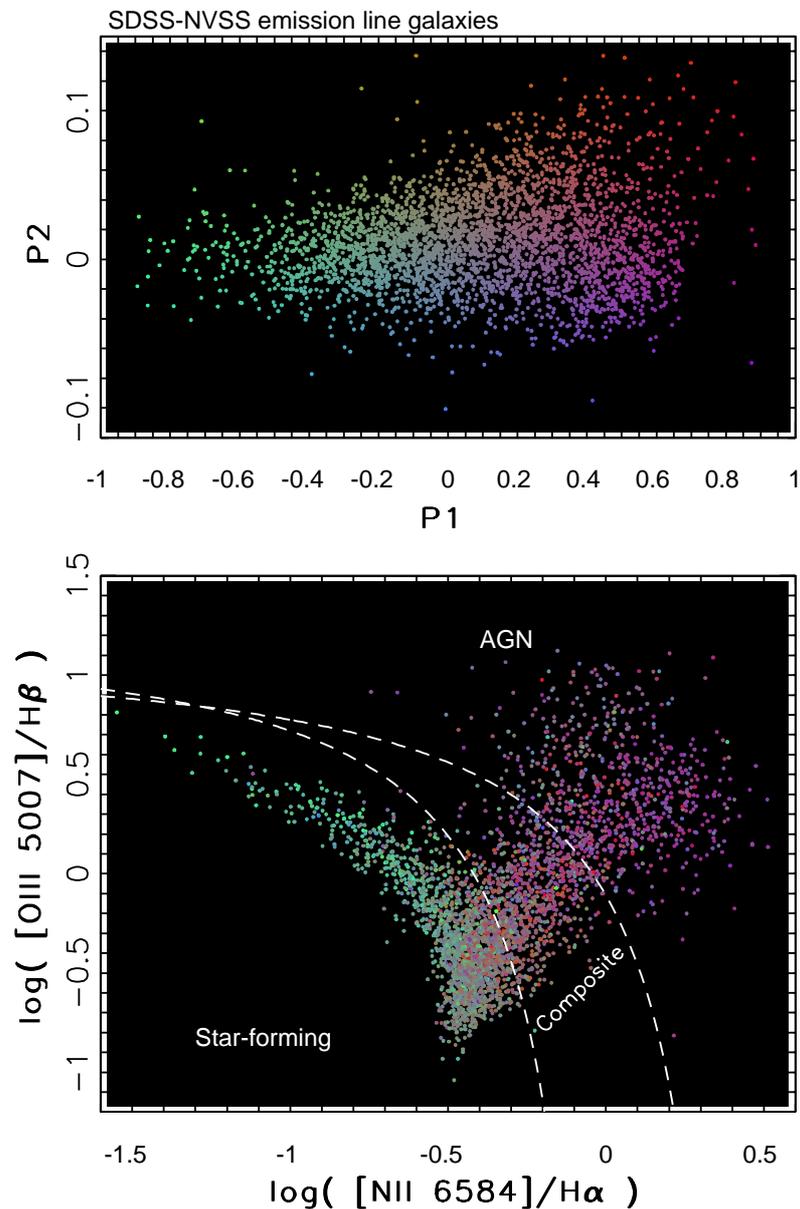
Figure 3.4 *Top panel:* The distribution of $\sim 3,400$ SDSS emission line galaxies, in the redshift range of 0.01 to 0.3, drawn from the DR1 "main" spectroscopic sample, which were also detected by the 1.4 GHz NVSS survey, in a diagram constructed with the principal rest-frame colors ($P1,P2$). Each dot corresponds to one galaxy, and the color code is determined by the position in this plane. The *bottom panel* shows the distribution of these galaxies in the (BPT) diagram (Baldwin et al. 1981). The lower dashed line separates the regions populated by star-forming and composite galaxies (Kauffmann et al. 2003c). The upper dashed line separates the regions populated by composite and AGN galaxies (Kewley et al. 2001). The dots are colored according to their $P1$ and $P2$ values given in the top panel. Note the strong correlation between the rest-frame colors and the emission line flux ratios (see text for details).

galaxies (see bottom right panel in Fig. 3.5). We will use these estimates in the following analysis to statistically correct the photometrically selected SF and AGN samples in the VLA-COSMOS survey.

Is the rest-frame color based selection method biased against dusty starburst galaxies?

One of the main advantages of radio observations is that the intrinsic physical properties that drive the radio emission can be derived without any need for dust-extinction corrections (as radio emission passes freely through dust). In particular, radio observations provide a dust-unbiased view of star-formation (see Condon 1992 for a review; see also Haarsma et al. 2000). Hence, it is important to address whether our rest-frame color selection technique misses out dusty starburst galaxies. In order to do this we study a sub-sample of SDSS/NVSS galaxies that were also detected with the IRAS satellite at IR wavelengths.

As shown in Sec. 3.4.1, our rest-frame color cut of $P1 \leq 0.15$ selects $\sim 85\%$ of all the spectroscopically identified SF galaxies. In the following we address the composition of the 'missed' $\sim 15\%$ of the SF galaxies, that are missed by the imposed rest-frame color criterion, in order to show that our selection does not introduce any biases, for example against the most luminous IR galaxies which would imply that the galaxies with the highest star-formation rates would not be selected in the SF sample. About 30% of the SF galaxies with $P1 > 0.15$ have IRAS detections, which is consistent with the fraction of IRAS detections in the SF sample with $P1 \leq 0.15$. This already suggests that the composition of the *missed* SF galaxies is not significantly different from the composition of the *selected* SF galaxies. Further, the fractions of luminous and ultra-luminous IR galaxies (see below) in the spectroscopically classified SF samples with $P1 \leq 0.15$ and $P1 > 0.15$ appear to be consistent with each other. Thus, the rest-frame color based classification method does not introduce a bias against dusty starburst galaxies.

However, we further investigate this using the 875 galaxies detected by the SDSS, NVSS, and IRAS sky surveys. The BPT diagram for ~ 830 SDSS/NVSS/IRAS emission line galaxies is shown in Fig. 3.6, color-coded using the $(P1, P2)$ plane. It is noteworthy that in the entire SDSS/NVSS/IRAS sample only 48 objects (i.e. $\sim 5\%$) were identified as absorption line AGN, i.e. having no emission lines in their optical spectra. It is possible that very high dust obscuration may suppress the detection of emission lines in the optical spectrum. In order to investigate this, we performed a visual inspection of the 48 color-composite images of these objects obtained by SDSS and searched for signatures of HII regions. This analysis suggests that at the most 30% of these galaxies may possibly be undergoing star formation (e.g. possible galaxy merger, or extended morphology). Therefore, only a negligible fraction of less than 1.5% of the SDSS/NVSS/IRAS galaxies may be so heavily dust-obscured that no emission lines would be detected in their optical spectra.

In the top panel of Fig. 3.7 we show the differential distribution of $P1$ for the complete sample of 875 SDSS/NVSS/IRAS galaxies separated into AGN, star-forming and composite
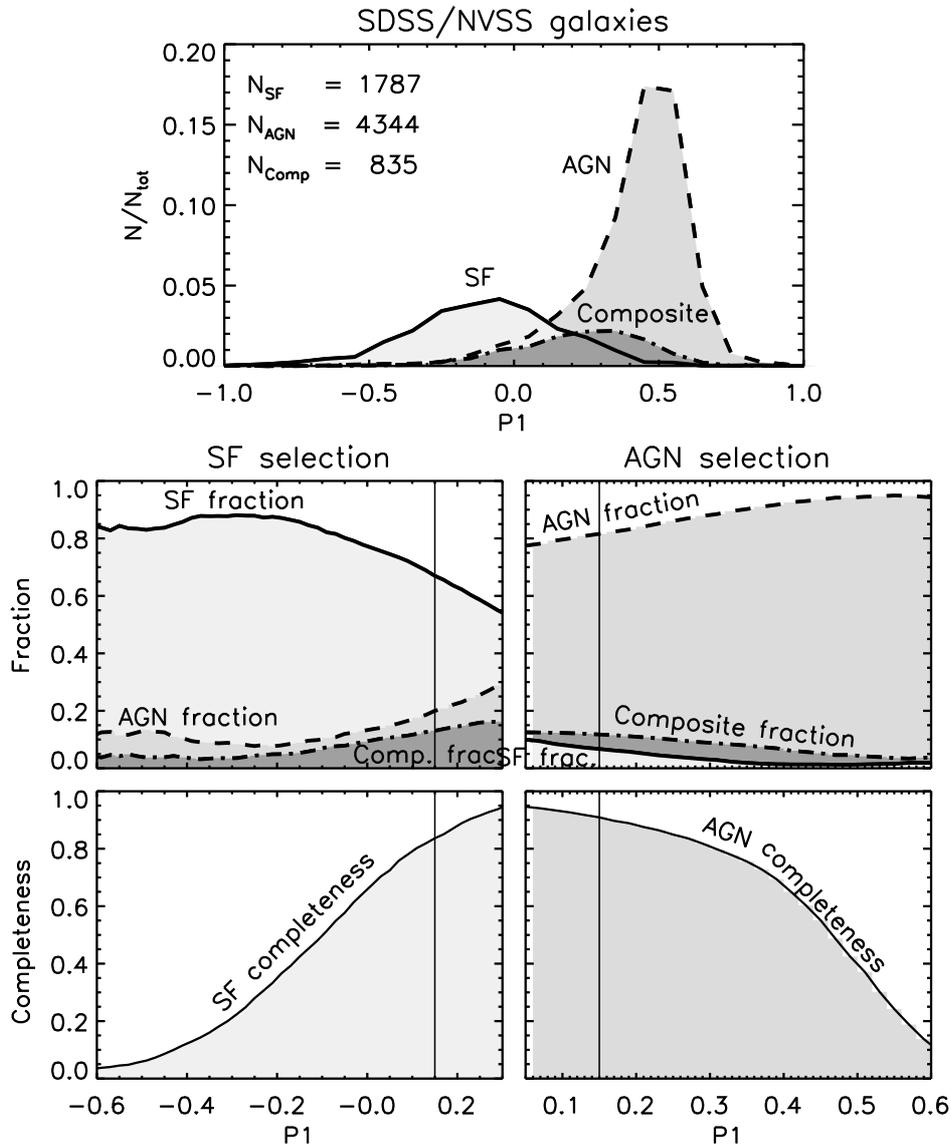
Figure 3.5 Differential and cumulative distributions of the rest-frame color $P1$ for $\sim 7,000$ SDSS galaxies, in the redshift range of 0.01 to 0.3, drawn from the DR1 "main" spectroscopic sample, that have 1.4 GHz NVSS detections. The galaxies were spectroscopically classified as star forming (SF; thick line), AGN (dashed line) or composite (dot-dashed line; see text for details). The *top panel* shows the $P1$ histograms for these three types of objects. The *middle left panel* shows the fraction of these three types of galaxies as a function of $P1$. These distributions are normalized in such a way that for each $P1$ value the fraction of the three types of galaxies within the total selected sample can be read off. The *bottom left panel* shows the cumulative distribution of $P1$ for SF galaxies, thus showing to which completeness the 'real' (i.e. spectroscopically classified) SF galaxies are selected for any given $P1$ color-cut. The *bottom and middle right panels* are analogous to the bottom and middle left panels, but for AGN galaxies. Note also that the cumulative distributions for AGN were computed as a function of decreasing $P1$. The vertical (thin solid) lines in the middle and bottom panels designate the value of $P1$, chosen to separate SF galaxies from AGN.
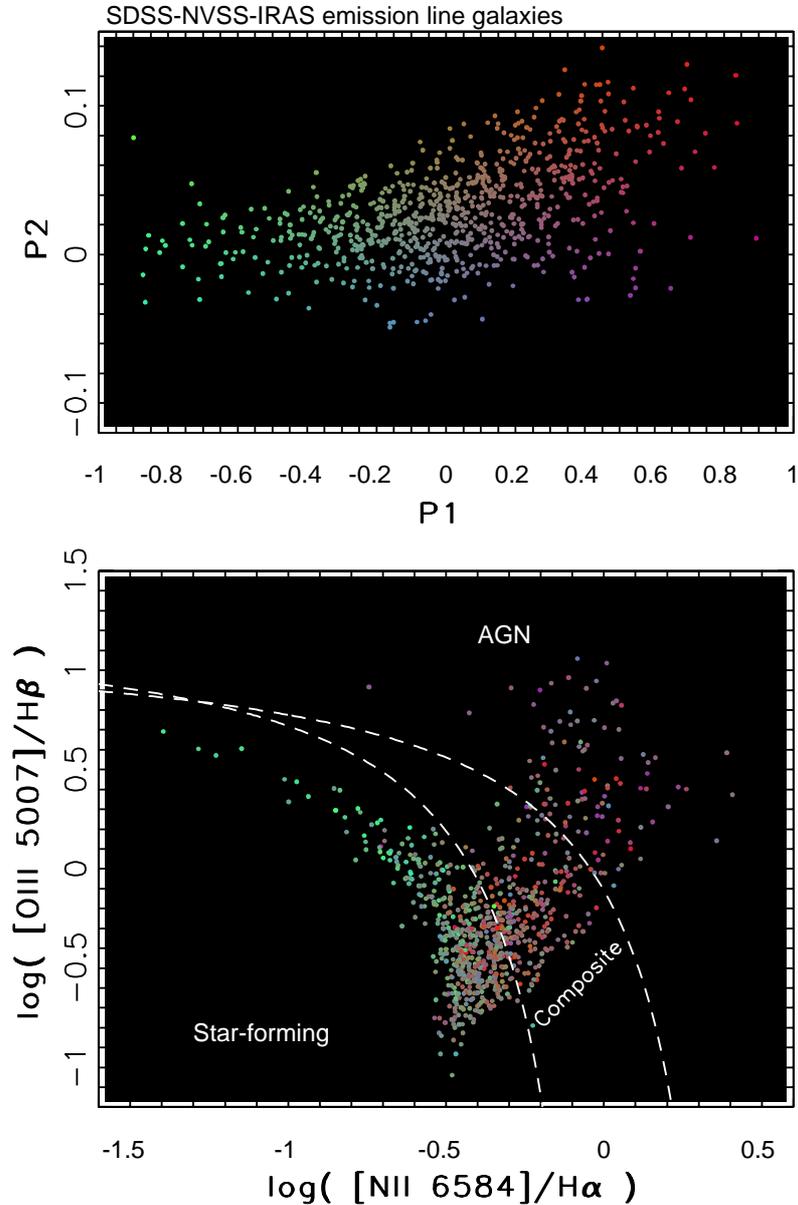
Figure 3.6   Analogous to Fig. 3.4 but for ~ 830 SDSS/NVSS/IRAS emission line galaxies.

galaxies as described in Sec. 3.4.1, and in the middle panel we show the corresponding fraction (analogous to the middle left panel in Fig. 3.5). Using a rest-frame cut-off of 0.15 the selected sample of star forming galaxies, detected in the IR regime, contains $\sim 70\%$ 'real' (i.e. spectroscopically identified) SF galaxies (that make up $\sim 85\%$ of *all* 'real' SF galaxies; see bottom panel), 10% AGN, and 20% composite objects. This is fairly consistent with the properties of the entire SDSS/NVSS sample, and that the selection criteria for SF and AGN galaxies adopted on the basis of the analysis of the full SDSS/NVSS sample works almost equally efficiently also for the IRAS detected sub-sample.

In order to assess the fraction of dusty starburst galaxies that we omit using the rest-frame color selection, in the bottom panel of Fig. 3.7 we show the cumulative distributions of the spectroscopically identified star forming galaxies as a function of $P1$ for i) all star forming galaxies, ii) luminous IR galaxies (LIRGs; $L_{IR} = 10^{11-12}$ $L_\odot$) and iii) ultra-luminous IR galaxies (ULIRGs, $L_{IR} > 10^{12}$ $L_\odot$). [The total IR luminosities were computed following Sanders & Mirabel (1996).] A $P1$ cut of 0.15 misses only $\sim 10\%$ and $\sim 5\%$ of luminous and ultra-luminous starburst galaxies, respectively. In order to test this issue further, we have synthesized the $P1$ color for the 'standard' dusty starburst galaxies M 82 (a typical LIRG), and Arp 220 (the prototypical ULIRG) using spectral templates given in Polletta et al. (2006; see also Silva et al. 1998). The $P1$ colors for M 82 and Arp 220 are 0.078 and 0.149, respectively, implying that M 82 would not have been missed by the rest-frame color based classification method, while Arp 220, although close to the adopted limit in $P1$, still lies within our selection criterion. Based on the tests presented above we conclude that our rest-frame color based classification method is not significantly biased against dusty starburst galaxies.

3.4.2 Application of the rest-frame color based classification method to the multi-wavelength photometry of the VLA-COSMOS radio − optical galaxies

In Sec. 3.4.1 we have presented our rest-frame color based classification method, which we have calibrated using a local galaxy sample, drawn from the SDSS and NVSS sky surveys. Using galaxies from this sample, that were also detected by the IRAS satellite in the IR, we have shown that the method is not significantly biased against selecting dusty starburst galaxies (star forming LIRGs and ULIRGs). This is an important point for a radio sample as radio emission is an efficient tracer of star formation, and of particular importance especially in the most dusty systems. Therefore, having studied the rest-frame color based classification method to a broad extent, and assuming that evolutionary effects with redshift do not significantly affect the reliability of the classification, we can safely apply it to the galaxies in the VLA-COSMOS 1.4 GHz matched radio sample (Sec. 3.5.3) in order to separate SF from AGN galaxies at intermediate redshifts. However, first we need to derive the rest-frame $P1$ color from the observed SED of the VLA-COSMOS galaxies. We do this via high-resolution SED fitting, described in Sec. 3.4.2, and we test the accuracy of the rest-frame color synthesis in Sec. 3.4.2, and its effect on the selection of SF and AGN galaxies in Sec. 3.4.2.

Derivation of rest-frame colors

In order to estimate the rest-frame colors $P1$ and $P2$ for each galaxy in the matched radio sample that we do not classify as a star or QSO (see Sec. 3.5), we use the GOSSIP (Galaxy Observed Simulated SED Interactive Program) software package (Franzetti 2005; PhD Thesis), designed for fitting a galaxy's SED to a set of chosen spectral models. The SED of the galaxies in our sample, that we use for fitting, extends from 3500 Å to 2.5 μm and we fit
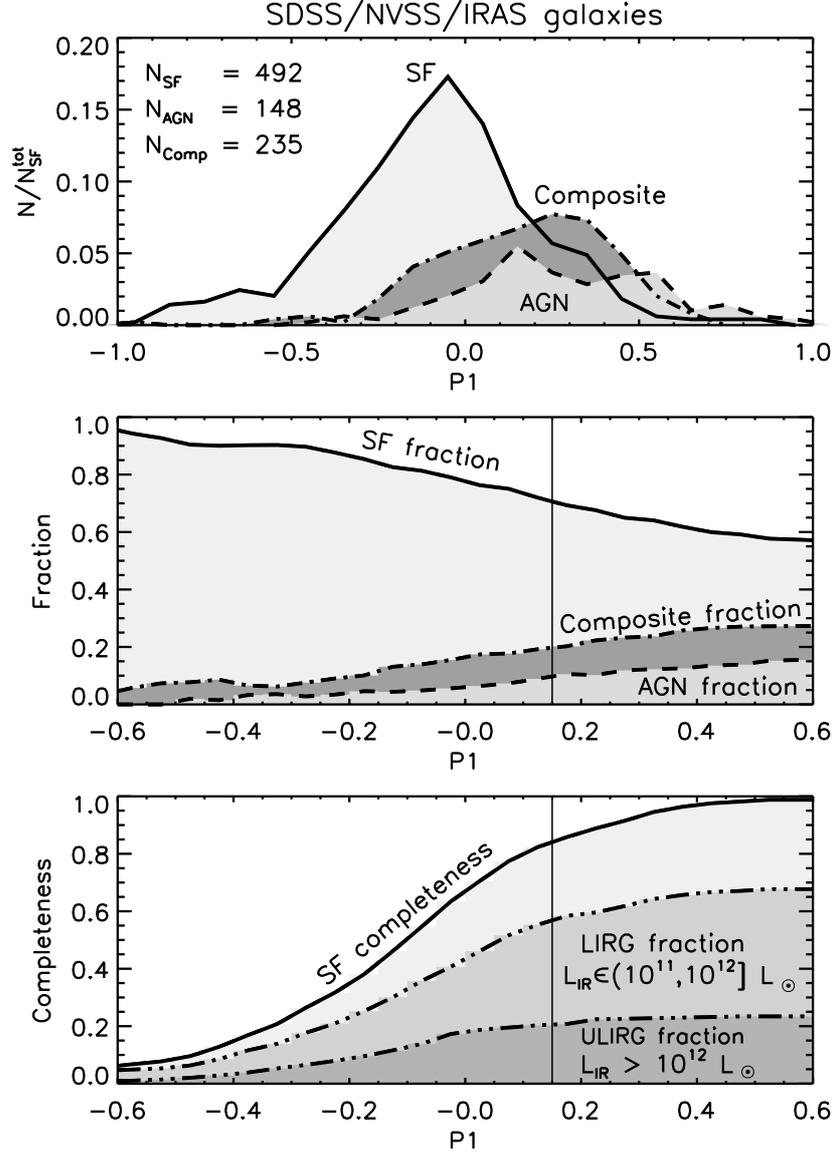
Figure 3.7 Differential and cumulative distributions of the rest-frame color $P1$ for 875 SDSS galaxies from the DR1 "main" spectroscopic sample, that have NVSS and IRAS detections. The galaxies were spectroscopically classified as star forming (SF; thick line), AGN (dashed line) or composite (dot-dashed line; see text for details), and their $P1$ histograms are shown in the *top panel*. The *middle panel* shows the fraction of $P1$ for SF, AGN and composite galaxies, analogous to the middle left panel in Fig. 3.5. The vertical thin solid line shows the chosen $P1$ color cut-off. The *bottom panel* shows the cumulative distribution of $P1$, normalized to SF galaxy counts (thick line). Also shown are the $P1$ distributions of SF galaxies with IR luminosities greater than 10^{11} $L_\odot$ and 10^{12} $L_\odot$ consistent with LRIGs and ULIRGs, respectively. Note that our rest-frame color based classification method is not strongly biased against dusty starburst galaxies.

to each observed SED a realization of $\sim 100,000$ spectra built using the Bruzual & Charlot (2003) stellar synthesis evolutionary models. The library of model spectra was parameterized similarly to Salim et al. (2007). Previous versions of this library have been used in Kauffmann et al. (2003a) and Kong et al. (2004). Star formation histories have been parameterized by an underlying continuous star formation history (decaying exponentially), and randomly superimposed bursts. We thus cover ages between 10^8 and 1.35×10^{10} years, specific star formation rates between 10^{-15} yr^{-1} and 3.93×10^{-8} yr^{-1} and metallicities from a tenth to twice solar. The approach of fitting the multi-wavelength broad-band SED to obtain physical parameters has been validated at low redshifts in Salim et al. (2007).

For each object in our sample the model spectra in our library are redshifted to the galaxy's measured redshift (spectroscopic where available, otherwise photometric), then each spectrum is convolved with the observed filter response function[5], and then fitted to the available observed photometric data, using a direct χ^2 minimization procedure. Output parameters, such as e.g. rest-frame colors, stellar mass or the 4000 Å break, are taken from the best fit model spectrum. In order to derive physically meaningful output parameters, we restrict the fitting procedure to models that have an age smaller than that of the Universe at the galaxy's redshift.

Tests on the derived rest-frame colors

In this section we test the accuracy of the synthetic magnitudes and colors derived via SED fitting (see previous section) in order to assess the expected uncertainties of the $P1$ color synthesis for the galaxies in the VLA-COSMOS matched radio sample.

The accuracy of the synthesized (relative to observed) magnitudes and colors is summarized in Fig. 3.8 for *all* galaxies in the matched radio sample (objects that were not classified as stars or QSOs; see Sec. 3.5). The colors and magnitudes are reproduced with a satisfying accuracy (~ 0.07 and ~ 0.04, respectively). The synthesized V_J shows a slight systematic offset (~ 0.05), which may arise from the incomplete knowledge of the filter response curve and/or the presence of strong spectral emission lines which are not taken into account in the model spectra. Nonetheless, we can conservatively conclude that the overall accuracy of the synthetic magnitudes and colors is ~ 0.1. It is also noteworthy that $P1$ is derived from a rest-frame spectral range of $3800 - 5800\text{Å}$, which corresponds to observed V, r, i and z band ranges for redshifts of roughly 0.1 to 0.9. Thus the obtained color and magnitude accuracies in these observed spectral ranges mimic adequately the rest-frame spectral range of interest.

In order to test the accuracy of the derived rest-frame colors further, we synthesize P1 for a sample of ~ 1700 local SDSS/NVSS galaxies. For these galaxies the P1 colors, computed from their spectrum (with an accuracy of better than 0.03 magnitudes; see Smolčić et al. 2006), are also available. Thus, comparing the rest-frame color synthesized via SED fitting with the reference rest-frame color derived from the spectrum gives us a direct measure of the accuracy of our synthetic $P1$ color. In Fig. 3.9 we show the

---

[5]The COSMOS filter response curves can be found here: http://www.astro.caltech.edu/~capak/cosmos/filters
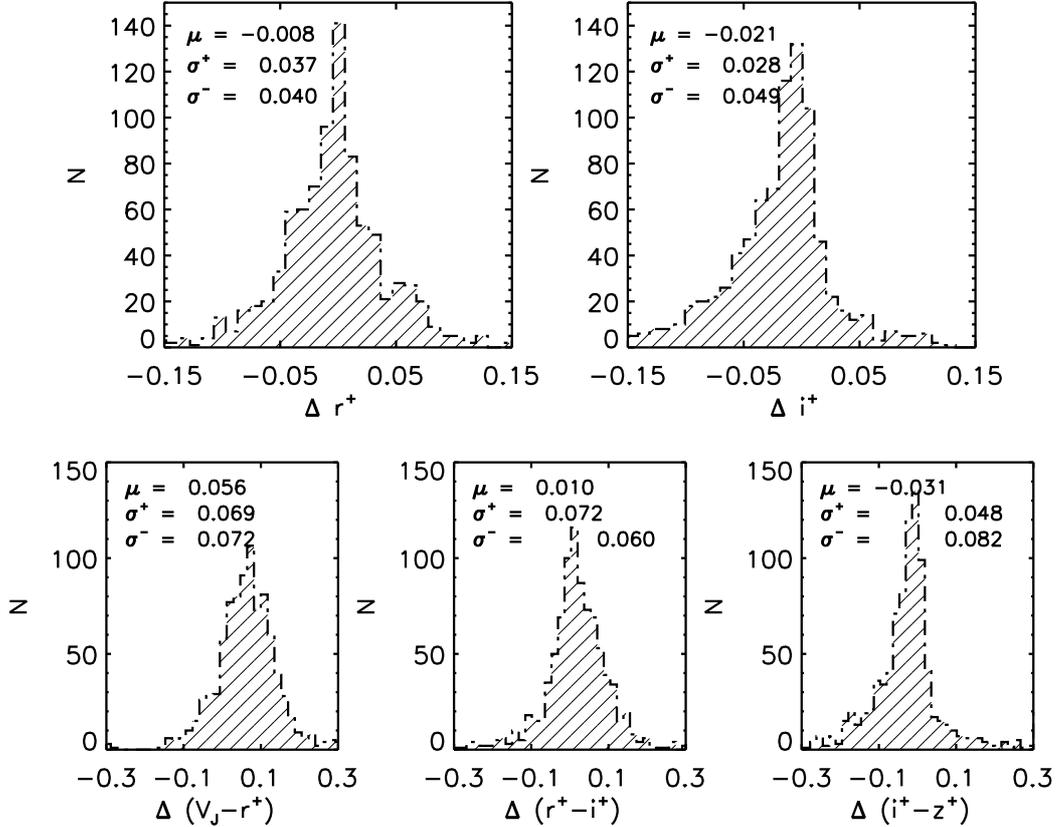
Figure 3.8   Comparison of synthesized and observed magnitudes (top panel) and colors (bottom panel) for *all* VLA-COSMOS objects from the matched radio sample that were not classified as stars or QSOs. In each panel the median, and the upper and lower limit of the 68% confidence interval are indicated. The reproduced color accuracy is ~ 0.1.

derived accuracy for all ~ 1700 galaxies (top panel). The mean color difference is 0, with the expected root-mean-square-scatter of ~ 0.1. It is also worth noting that the SED fitting procedure is not exactly the same in the case of SDSS and VLA-COSMOS galaxies (different filter response curves, wavelength, magnitude and redshift range), and that the spectroscopically derived $P1$ color carries its own uncertainties. Therefore, the derived accuracy in Fig. 3.9 may be considered as an upper limit at the bright magnitude end ($r_{\mathrm{Pet}} < 17.7$). Combining the results from Fig. 3.8 and Fig. 3.9 (top panel) we conclude that the synthesized rest-frame color $P1$ is accurate to ~ 0.1 mag.

In the bottom panel in Fig. 3.9 we show the difference of the $P1$ color as a function of the synthesized (GOSSIP) $P1$ color for the SDSS/NVSS galaxies. A slight systematic trend is present as a function of the derived $P1$ color. In order to obtain an insight into the origin of these systematics, we have visually investigated the SDSS spectra for a sub-set of these galaxies with large (> 0.2), and insignificant (< 0.01) offsets in $P1$. We found that galaxies with large offsets are galaxies with strong emission-lines in the rest-frame wavelength range of $3800 - 5800$ Å (e.g. Hβ, OII, OIII), which is used to derive the $P1$ color, while this is not the case for the galaxies with insignificant offsets. The latter tend to be either absorption line systems, or galaxies with weak emission-lines. Therefore,

we conclude that the observed systematic trend presumably arises from the presence of strong emission lines in the galaxies' SEDs, which are not taken into account in the BC03 model spectra. In our further analysis of the galaxies in the VLA-COSMOS matched radio sample, we use the median offset, shown in the bottom panel in Fig. 3.9, to correct the $P1$ color derived for the galaxies in the matched radio sample, and we consider the synthetic $P1$ color to be accurate to ~ 0.1 mag.
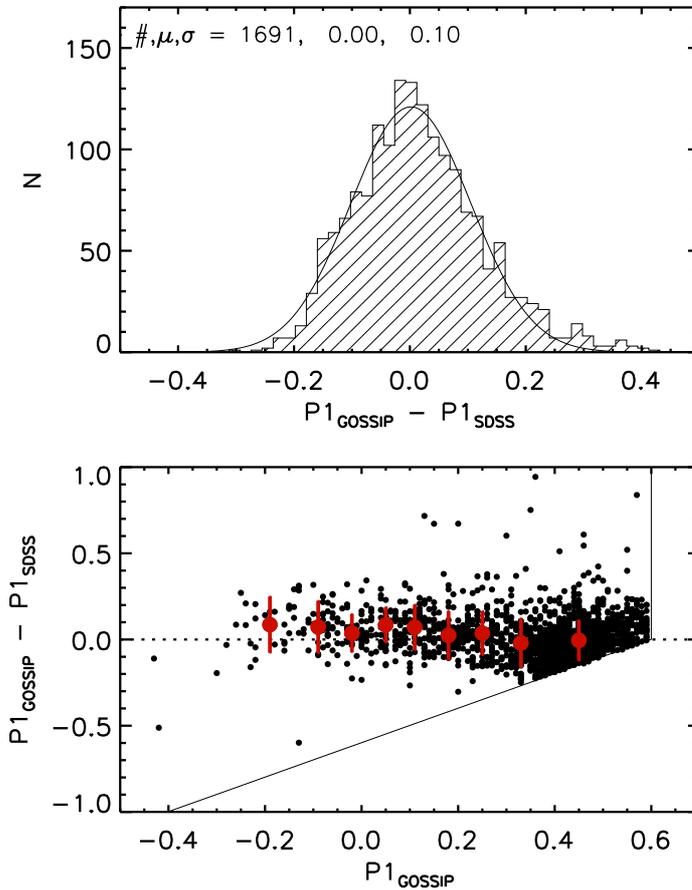
Figure 3.9   The comparison of the $P1$ color synthesized from the SDSS spectrum ($P1_{\mathrm{SDSS}}$ that has a typical error of 0.03) and via SED fitting ($P1_{\mathrm{GOSSIP}}$) for ~ 1700 SDSS/NVSS galaxies from the DR1 "main" spectroscopic sample (top panel). The $P1$ color is reproduced with a spread of ~ 0.1. The bottom panel shows the difference in the $P1$ color as a function of $P1_{\mathrm{GOSSIP}}$. The thin solid lines show the upper $P1$ limits of 0.6, imposed for this analysis. Note the slight systematic trend in the derived $P1$ color as a function of $P1_{\mathrm{GOSSIP}}$ (the large dots are the median offsets, with indicated 1σ error bars). The trend presumably arises due to the presence of strong emission-lines in the rest-frame wavelength range of $3800 - 5800$ Å, that are not taken into account in the BC03 models. We use these offsets to correct for these systematics in the derivation of $P1$ for the clean radio sample (see text for details).

Uncertainty of the rest-frame color based classification method due to the uncertainties of the synthetic $P1$ color

Our rest-frame color based classification method is a purely photometric technique designed for disentangling SF from AGN galaxies based only on the distribution of their rest-frame color $P1$. In the previous section we have shown that the synthesized $P1$ color is accurate to ~ 0.1 mag. However, an error of 0.1 mag for 68% of the galaxies, and 0.2 for 95%, may substantially alter the SF/AGN selection, introducing the largest uncertainty for the galaxies that have $P1$ colors close to the chosen boundary of $P1$=0.15. Nonetheless, we can account for these uncertainties in a statistical manner, by Monte Carlo simulations, as follows.

We simulate the $P1$ error distribution using a randomly drawn Gaussian distribution with a standard deviation of 0.1 centered at zero (see Fig. 3.9). These errors are then added to the galaxies' $P1$ colors derived from the best fit template in the SED fitting, and the SF/AGN selection (see Sec. 3.5.3) is applied. By repeating this procedure 10,000 times we obtain a robust statistical distribution of the number of selected SF and AGN galaxies. The mean numbers of galaxies classified in this way as SF or AGN are 356 and 585, respectively, with a root-mean-square scatter of only 7. We reach the same result if we model the error distribution using two separate Gaussian distributions for blue and red galaxies.

Applying our SF/AGN selection using the P1 distribution obtained from the best fit template in the SED fitting yields 340 SF and 601 AGN galaxies (see Sec. 3.5.3). Thus, $\sim 5\%$ less SF galaxies are selected. This is easily understood as the blue tail of the $P1$ distribution contains a smaller number of galaxies than there are in the prominent red peak (see e.g. Fig. 3.5). Therefore, a normal error distribution will systematically scatter more galaxies to the blue $P1$ region, than to the red one. We conclude that the photometric errors of the synthesized $P1$ color introduce a number uncertainty of $\sim 5\%$ in favor of SF galaxies. Although $\sim 5\%$ is not significant, it is necessary to keep this bias in mind in the analysis of the 'population mix' of submillijansky radio sources (Sec. 3.7.2).

3.4.3 Towards the classification of the VLA-COSMOS matched radio sample: Outline and nomenclature

In Sec. 3.4.1 we have presented the calibration and effectiveness of the rest-frame color based classification method for separating *galaxies* dominated by star formation from those dominated by AGN activity. For this we have used the SDSS "main" spectroscopic sample – a pure *galaxy* sample that by definition does not contain any star-like objects (Strauss et al. 2002). This, obviously, implies that the same effectiveness of the method can only be reached if the rest-frame color based classification method is applied to a comparable sample, i.e. *galaxies only*. However, our VLA-COSMOS matched radio sample consists not only of galaxies, but also of stellar like sources, where the latter are either stars or quasi stellar objects (QSOs). Therefore, we classify the sources in the matched radio sample into five sub-types – a) star candidates, b) quasi stellar objects (QSOs), c) active galactic

nuclei (AGN), d) star forming (SF), and e) high redshift ($z > 1.3$; high-z) galaxies. The latter three sub-types compose our *"VLA-COSMOS galaxy sample"*. The properties of each sub-type are summarized as follows.

Stars: Point-sources in the optical, with their SEDs best fit using a stellar template.

OSQs: Point-sources in the optical (stellar-like SEDs are excluded; see above). This criterion essentially requires that the emission of the nucleus in the optical strongly dominates over the emission of the host galaxy. Thus, this sample predominantly contains broad line AGN (i.e. type-1 AGN), with power law spectra in the optical.

AGN: Galaxies (not point-sources) whose rest-frame color properties are consistent with properties of AGN ($P1 > 0.15$, X-ray luminosity above 10^{42} erg s^{-1} if X-ray detected). This selection requires that the *optical* emission either shows signs of both, the emission from the central AGN as well as the emission from the underlying host galaxy, or only the latter. Thus, this sample essentially includes Seyfert and LINER types of galaxies, as well as absorption line AGN, and we limit it to redshifts of $z \leq 1.3$.

SF galaxies: Galaxies whose rest-frame color properties are consistent with properties of star forming galaxies ($P1 \leq 0.15$). Thus, the emission of these galaxies is dominated by the emission originating from regions of substantial star formation. This sample is also limited to redshifts ≤ 1.3.

high-z galaxies: Galaxies (not point-sources) with redshifts beyond $z = 1.3$.

3.5   Classification of VLA-COSMOS sources in the matched radio sample

In this section we present the classification of the entire VLA-COSMOS matched radio sample into star candidates (Sec. 3.5.1), QSOs (Sec. 3.5.2), SF, AGN and high-z galaxies (Sec. 3.5.3).

3.5.1   Star candidates

In order to identify star candidates in the VLA-COSMOS matched radio source sample, we make use of the COSMOS stellar catalog (Tasca et al. in prep), that was constructed from the HST/ACS catalog (Leauthaud et al. 2007) using stellar templates to fit the entire SED of each source. In Fig. 3.10 we show the color-color distribution for $\sim 2,000$ objects in the COSMOS field securely classified as stars (with photometric errors better than 0.05), which form well defined loci in the broad-band color-color diagrams. Cross-correlating our matched radio sample with the COSMOS stellar catalog yields only 2 objects detected in the radio regime that are consistent with having stellar properties. The color properties

of these objects are shown in Fig. 3.10. Within the error-bars they are consistent with the main stellar loci. Note, however, the r^+-i^+ color excess of one of the star candidates in the r^+-i^+ vs. g^+-r^+ color-color diagram (middle panel in Fig. 3.10), which suggests consistency with properties of e.g. cataclysmic variables (e.g. Szkody et al. 2002, 2003), or unresolved binary star systems containing a white dwarf and a late type star (e.g. Smolčić et al. 2004). The best fit stellar templates for these objects were taken from the PHOENIX library (Hauschildt et al. 1997) and represent dwarfs with effective temperatures in the range of 4100 to 5000 K and $\log{(g)}$ in the range of 3 to 3.5. The 1.4 GHz total fluxes for these two objects are 126 and 152 μJy, and the corresponding i band AB magnitudes are 25.34 and 23.28, respectively. It is noteworthy that both objects have IRAC counterparts, but no associated X-ray emission. We consider these two sources to be star candidates, however a more detailed analysis (using for example spectroscopy), which is beyond the scope of this paper, would be needed to verify this. Such a low fraction of identified stars is consistent with star detection rates in other deep radio surveys (e.g. Fomalont et al. 2006).

The two star candidates in our radio sample form only $\sim 0.1\%$ of the VLA-COSMOS radio sources, and we exclude them from our sample for further analysis.
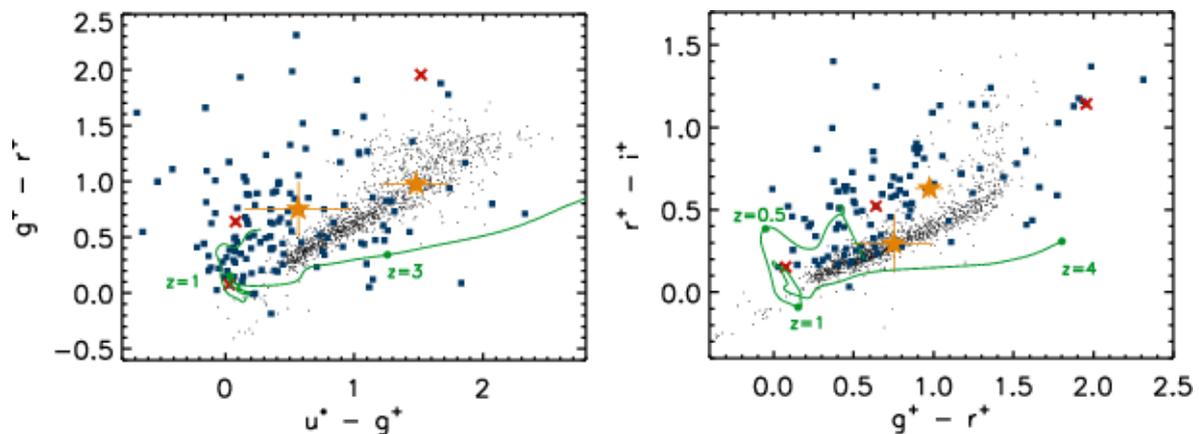
Figure 3.10   Color-color diagrams for COSMOS stars and VLA-COSMOS QSOs (see text for details). The stars (black dots) form a narrow, well defined, locus in each diagram. The star symbols (yellow) show 2 objects detected in the VLA-COSMOS radio survey, identified as star candidates (see text for details). VLA-COSMOS objects classified as QSOs by our selection criteria (blue squares) are also shown, and they occupy the 'standard' QSO regions in these diagrams (see text for details). The crosses (red) show objects classified as a QSO by our technique, yet their spectra were identified as red galaxies. QSO evolutionary tracks are shown to guide the eye (green curved lines).

3.5.2   Quasi stellar objects

Identification based on morphology

In order to identify QSOs in our matched radio sample we rely on an optical classification, rather than using X-ray emission, due to the much higher sensitivity of the observations in

the optical (5σ sensitivity limit in the Subaru i band is 26.2; see Capak et al. 2007). For example, if one would select AGN relying purely on e.g. X-ray – to – optical flux ratios, which are generally greater than 0.1 for both broad and narrow line AGN (e.g. Maccacaro et al. 1988; Alexander et al. 2001), with our optical limit of $i = 26$ (corresponding to r^+ of ~ 27) the depth of the X-ray point-source detection would have to be about 2 orders of magnitude deeper than it currently is in order to select a complete sample of AGN. Further, a clear distinction between broad and narrow line AGN would not be possible. Hence, here we identify a QSO by requiring that a given source in the matched radio sample is optically compact. In Fig. 3.11 we show the fitted i band FWHM of the sources in the COSMOS photometric catalog (Capak et al. 2007) as a function of their i band magnitude. Point-sources (black squares), selected from the HST/ACS catalog (Leauthaud et al. 2007), form a locus in this plane, separated from the area occupied by extended sources. However, the point-source locus is fairly scattered, especially at faint magnitudes, and thus makes a single automatic cut at a certain FWHM value inefficient. For this reason, we classify sources within the FWHM range of $1.85'' - 2.05''$ as QSOs only if their optical HST morphology was visually confirmed to be 'point-source dominated'. However, we consider *all* sources below FWHM of $1.85''$ to be QSOs. We further supplement this sample with 12 objects that were classified as point-sources in the HST/ACS catalog, but do not satisfy the above criteria.

In summary, out of 1558 objects we identify 139 (i.e. 11.5%) as QSOs. In Fig. 3.10 we show their broad-band (u^*,g^+,r^+,i^+) color-color properties. As expected, the non-stellar emission of the selected objects confines them to regions typical for QSOs, which are separated from the main stellar loci in these diagrams (e.g. Brusa et al. 2007; Richards et al. 2002). A minor fraction of these objects lie on the stellar loci. However, in the BzK diagnostic diagram, which is an efficient tracer for stars (Daddi et al. 2004) these sources are offset from the stellar locus, verifying their non-stellar nature.
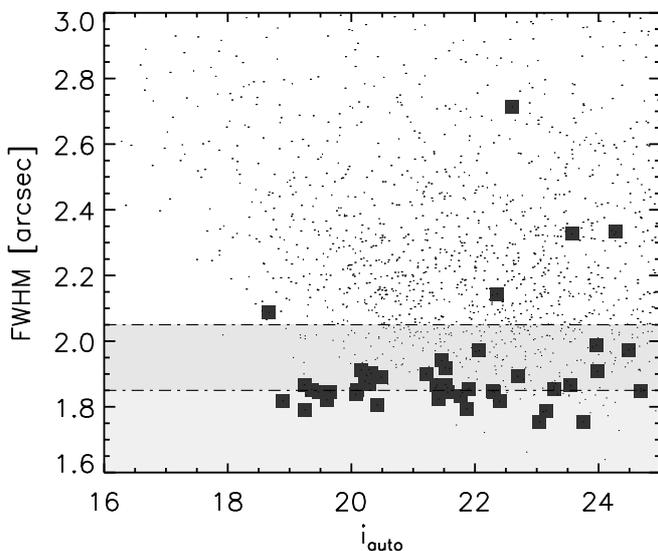
Figure 3.11 FWHM of the optical counterparts of the matched radio sources (small dots) as a function of i band magnitude, taken from the COSMOS photometric catalog (Capak et al. 2007). Grey squares represent the HST/ACS point sources in the sample. Unresolved sources form a separated locus in this diagram. We identify QSOs by requiring that a source is optically compact by choosing an absolute separation value of FWHM $\lesssim$ $1.85''$ (below lower dash-dotted line; light-grey shaded area). In the range of FWHM $\in$ $(1.85, 2.05]''$ (between upper and lower dash-dotted lines; dark-grey shaded area) we identify objects as QSOs only if they were visually confirmed to be point-source dominated (see text for details).

As AGN dominated systems usually have soft X-ray to optical flux ratios in the range

of about 0.1 to 10 (e.g. Maccacaro et al. 1988; Alexander et al. 2001), we can use the X-ray to optical flux properties of the identified QSOs to further test our selection criteria. 43 objects in our QSO sample were detected as X-ray point-sources, and their X-ray to optical flux ratios are consistent with the expected values. The median r^+ magnitude for these sources is 21.3. For the remaining QSO candidates, that were not detected in the X-rays, the median r^+ is 24.4. Therefore, these sources are also consistent with the expected X-ray to optical flux ratios, however beyond our X-ray point-source detection limit (10^{-15} erg cm^{-2} s^{-1} in the soft band). We conclude that the independent analysis of the X-ray properties of our selected QSOs verifies the validity of our selection.

Spectroscopic verification

A sub-sample of 31 objects of the 139 previously identified QSOs have available optical spectroscopy with secure classifications (Trump et al. 2007; Prescott et al. 2006; Colless et al. 2001; Schneider et al. 2005), and only 3 of these objects were classified as red galaxies (Trump et al. 2007), while all the others have AGN classifications. The 3 galaxies classified as ellipticals were identified as QSO candidates by our method based on visual/morphologic classification, which suggests the presence of dominating nuclear emission. The color properties of two of theses objects (see red crosses in the top panel in Fig. 3.10) are also consistent with the color properties of quasars.[6] Thus, we conclude that the selected QSO sample is not significantly ($\lesssim 10\%$) affected by contamination of non-QSO objects.

In order to assess the completeness of the selected QSO sample, we search for objects that are spectroscopically classified as QSOs and 'missed' by our classification method. Our criteria yielded 139 objects classified as QSOs in the matched radio sample, and in the remainder of the sample (i.e. the 1417 sources that were not classified as star candidates or QSOs) spectroscopic classifications are available for 397 objects. Out of these, 9 were spectroscopically classified as QSOs. Two SDSS examples, for which COSMOS HST/ACS imaging is available, are shown in Fig. 3.12. They obviously show extended optical emission, and a substantial light component arises from the host galaxy itself. The median redshift of these 9 objects is only 0.4. It is noteworthy that all of these objects have X-ray point source detections, and all except one have X-ray luminosities higher than 10^{42} erg s^{-1}. Therefore these galaxies will be selected into our AGN class, hence not contaminating the SF galaxy sample (see Sec. 3.5.3). As the spectroscopic sub-sample fairly represents the full matched radio sample (see Fig. 3.3), we conclude, based on the above analysis, that the sample of identified QSOs is about 80% complete. As expected, the incompleteness is mostly due to relatively low redshift, low-luminosity AGN.

3.5.3   Star forming and AGN galaxies

In the previous sections we have identified 2 star candidates and 139 QSOs in the matched radio sample. We will refer to the 1417 remaining sources in the matched radio source

---

[6]For example, in the u^*-g^+ vs. g^+-r^+ color-color diagram (top panel in Fig. 3.10) red galaxies would occupy the upper right quadrant (see e.g. Strateva et al. 2001).
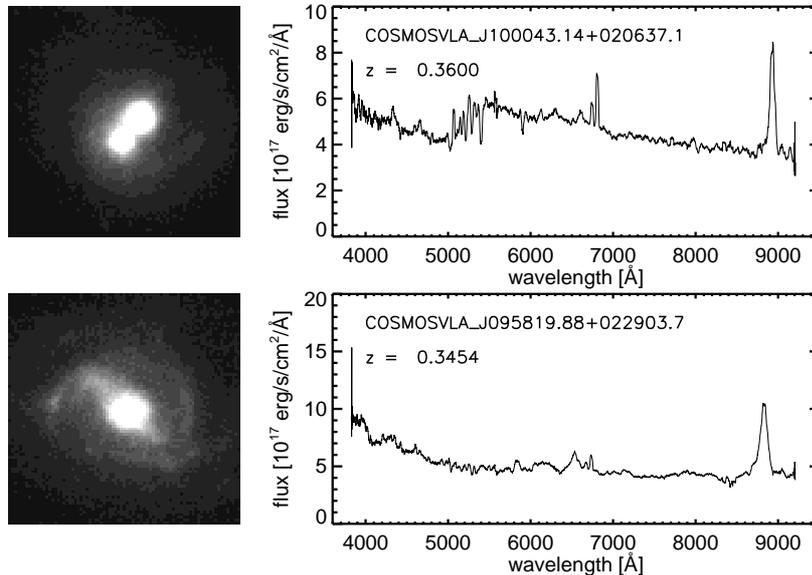
Figure 3.12   HST/ACS stamps (4″ on the side; left column) and the corresponding SDSS spectra (smoothed using 20 Å wide bins; right column) for two sources that were spectroscopically classified as QSOs, but missed by our QSO selection method. The morphology of these sources is clearly extended (in particular the source in the top panel is possibly a merging system with double nuclei visible, and extending beyond the shown 4″).

sample as the 'galaxy sample'. Before applying the rest-frame color based classification method to our VLA-COSMOS galaxies in order to separate SF from AGN galaxies, we restrict the galaxy sample to 941 galaxies with redshifts $\leq$ 1.3, as a) the photometric redshifts are less reliable beyond this redshift, and b) the library of BC03 model spectra that we use for the SED fitting may not be appropriate for fits beyond this redshift as the distribution of priors was set to optimally match this intermediate redshift range. Hereafter, we will call the sample of 476 galaxies with redshifts greater than 1.3 high redshift (high-z) galaxies.

We perform an SED fit using GOSSIP (as described in Sec. 3.4.2) for each of the 941 objects in the matched radio 'galaxy' sample out to $z = 1.3$. The distribution of the rest-frame color $P1$ for these galaxies is shown in Fig. 3.13. The distribution is very similar to that of the local sample (see top panel in Fig. 3.5) with a peak at $P1 \sim$ 0.4 (AGN) and a prominent tail towards bluer values (SF galaxies). We inspected the behavior of the median value of the synthesized $P1$ color for the entire $z \leq 1.3$ galaxy sample as a function of redshift, and we found no significant evolution in the median color. We reached the same conclusion analyzing the median $P1$ colors of the SF and AGN sub-populations. This implies that a fixed cut in the color can safely be applied to the entire galaxy population out to $z = 1.3$.

The SED fitting was performed via a χ^2 minimization procedure. The median value of the reduced χ^2 of the SED fits, computed using the best fit model spectrum, is 0.6 with an interquartile range of 2. Only 10% of the fitted objects have reduced χ^2 values above 5, and only 5% above 10. A visual inspection suggests that these galaxies are

either nearby galaxies, which are resolved and often saturated in the Subaru i band, or QSO contaminants. While the latter predominantly have blue $P1$ colors, the synthesized $P1$ color for the first class of galaxies still appears to be a valid tracer for the SF/AGN separation, and therefore we do not reject them from the sample.
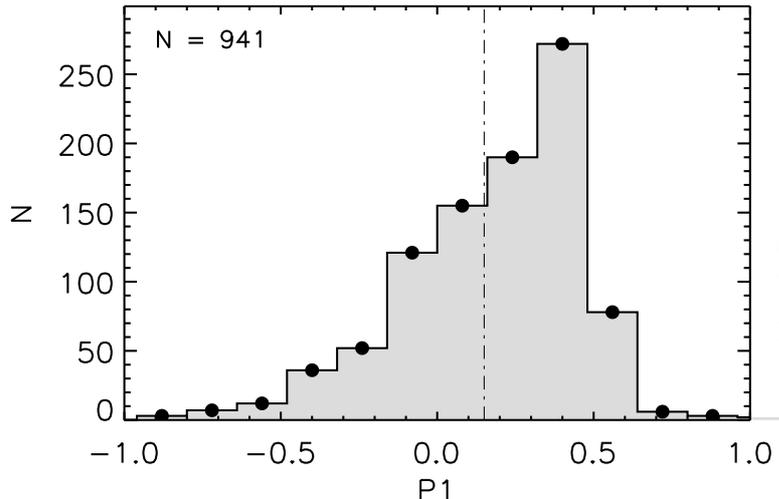
Figure 3.13 The distribution of the synthesized rest-frame $P1$ color, corrected for the systematics (see bottom panel in Fig. 3.9), for the objects in the matched radio *galaxy* sample with $z \leq 1.3$. Note, that the expected distribution from our local sample, showing a prominent tail towards bluer values of $P1$, is reproduced. The dash-dotted line shows our chosen boundary for separating star forming from AGN galaxies.

In order to select SF and AGN galaxies we require that the synthesized $P1$ color is ≤ 0.15 and > 0.15, respectively. However, to improve our selection at this point we make use of the X-ray properties in the soft band of the 114 galaxies that were detected as X-ray point sources. Namely, if the soft X-ray luminosity of an object is greater than 10^{42} erg s^{-1} we consider it to be an AGN, regardless of its $P1$ color. Note that this criterion is expected to reduce the contamination of the SF sample by objects with blue rest-frame colors, such as QSOs missed by our selection. In summary, our selection yields 340 SF and 601 AGN galaxies in our matched radio galaxy sample with $z \leq 1.3$. We analyze these galaxies further in Sec. 3.7.

3.6   Comparison with other selection methods

In this Section we compare our classification method, that we have applied to an intermediate redshift population, with other classification methods used for both local and intermediate redshift populations in the literature (Lacy et al. 2004; Stern et al. 2005; Best et al. 2005). We also study the 24μm properties of our radio sources, and their correlation to the 1.4 GHz emission.

3.6.1   3.6-8 μm color – color diagnostics

QSOs, whose UV to NIR continuum is dominated by a power law, tend to be redder than other types of galaxies in the MIR. Hence, they occupy a distinct region in MIR color space, and several color-color criteria were suggested for their selection (Lacy et al. 2004; Stern et al. 2005). In Fig. 3.14 we compare our classification method with those proposed

in the MIR using a sub-sample of the matched radio sources that were also detected with IRAC ($\sim 90\%$ have IRAC counterparts; see Sec. 3.3.2). We indicate the QSO (dots), AGN (thin contours) and star forming (thick contours) galaxies selected using our method. The dashed lines in the top and bottom panel in Fig. 3.14 show the color-color criteria proposed by Lacy et al. (2004) and Stern et al. (2005), respectively, for the selection of broad-line AGN. As expected, the majority of objects selected as QSOs by our method falls within this region, reassuring the efficiency of the classification method presented here. There are several QSO candidates outside these regions, which is not surprising as the suggested 'quasar regions' do not select a 100% complete sample of QSOs, and a certain amount of outliers is expected (see Stern et al. 2005 for a discussion of this point). In Sec. 3.5.2 we have inferred that our selected sample of QSOs is not significantly contaminated by different types of objects, which is affirmed by this independent analysis.

Stern et al. (2005) showed that at redshifts of $\lesssim 1$ galaxies span a large range in the $m_{5.8} - m_{8.0}$ color, which is consistent with the horizontal extent of our selected star forming and AGN galaxies (see bottom panel in Fig. 3.14). However, typical low luminosity AGN and starburst galaxies cannot be clearly divided using these diagnostic diagrams (see also color evolutionary tracks in Fig. 3.23). Nonetheless, elliptical galaxies (which correspond to our class of absorption line AGN) tend to occupy the bottom left regions in both diagrams, and close to these regions the distributions of our identified AGNs peak. On the other hand, the peak of the distribution of our selected star forming galaxies in these diagrams is clearly displaced from the one for AGN. This independently confirms that indeed two different populations of galaxies are selected using our rest-frame color based classification method.

Further, Stern et al. (2005) showed that narrow line AGN appear spread out in both the QSO and galaxy regions, which is also a result of our selection method [note that the selected AGN are present in both regions]. The last point we want to stress is that the star forming galaxy locus in these diagrams is also consistent with the expected colors, as a 'contamination' by star forming galaxies of the QSO locus is expected, especially close to the boundary. In summary, the classification method presented here agrees remarkably well with the expected properties of QSOs, AGN and star forming galaxies at intermediate redshifts in the MIR range encompassing 3.6-8 μm.

3.6.2 24 μm properties: The 24 μm – radio correlation

A tight mid-IR (as well as far- and total- IR) – radio correlation is expected for star forming galaxies, while 'radio-loud' AGN are expected to strongly deviate from it (e.g. Condon 1992; Bell 2003; Appleton et al. 2004). The 60 μm – radio correlation for low-luminosity AGN was studied by Obrić et al. (2006) in the local universe. Based on a selection utilizing the BPT diagram they have shown that also low -luminosity AGN follow a tight FIR – radio correlation, however with a slightly different slope and a larger scatter than SF galaxies. In this section we investigate the 24 μm – radio correlation for our selected SF and AGN galaxies. In particular, if our SF/AGN separation method is successful, then a difference in the 24 μm compared to 20 cm properties is expected to be seen for the two populations.

Our rest-frame color based classification method has identified 340 SF galaxies. Out of
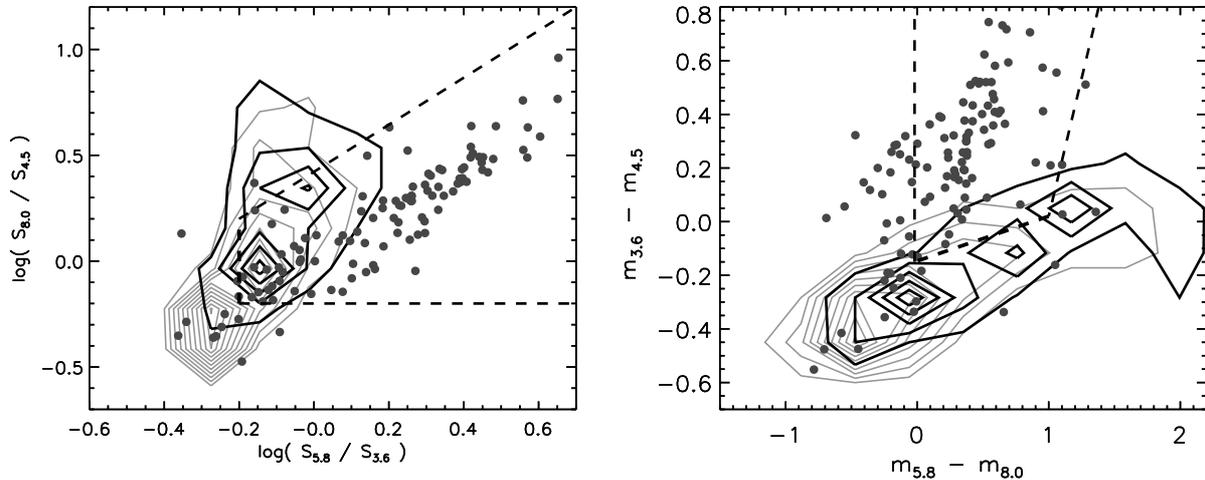
Figure 3.14   IRAC color-color diagrams in two representations (left and right panel) used as diagnostic tools for the separation of QSOs (broad line AGN) from 'normal' galaxies (Lacy et al. 2004; Stern et al. 2005). Filled circles display the 122 QSOs selected by our morphologic method that have IRAC detections; thin and thick contours show the 579 AGN and 322 star forming galaxies separated by our rest-frame color based classification method, respectively, that have IRAC counterparts. The contour levels in both panels are in steps of 7 starting at 7. The dashed lines in the left and right panels show the empirically selected regions for identifying broad-line AGN proposed by Lacy et al. (2004) and Stern et al. (2005), respectively.

these 82% (280) were detected at 24 μm with a signal to noise $\geq$ 3. On the other hand, out of 601 selected AGN only 44% (267) have a MIPS 24 μm detection with S/N $\geq$ 3. In Fig. 3.15 we show the 24 μm vs. 1.4 GHz luminosity[7] (top panel) for our SF and AGN galaxies, where the 24 μm data was not k-corrected. A correlation between the two luminosities exists for both types of objects detected at 24 μm, although on average for a given $L_{1.4GHz}$ the 24 μm luminosity is slightly lower for AGN than for SF galaxies (see also below). For the SF and AGN galaxies that were not detected at 24 μm we have computed upper limits of the 24 μm luminosity using the detection limit of the S-COSMOS MIPS shallow survey which is 0.3 mJy. These limiting luminosities are also shown in Fig. 3.15. Note that for AGN galaxies, as 56% of them are not detected at 24 μm, the scatter in the correlation is significantly increased by these objects.

To quantify the correlation, we derive the classical q parameter (e.g. Condon 1992) as the logarithm of the 24 μm to 1.4 GHz observed flux ratios. This parameter essentially measures the slope of the correlation, and in the bottom panel in Fig. 3.15 we show it as a function of $L_{1.4GHz}$ for our SF and AGN galaxies, with indicated upper limits (derived as described above). The q parameter seems to show a decreasing trend with increasing radio luminosity. However, this trend is dominated by the objects that have only estimated upper limits, and therefore may be mimicked by the flux limits of the samples. A more detailed analysis of this issue is beyond the scope of this paper.

The distribution of the q parameter for SF and AGN galaxies is shown in Fig. 3.16, for galaxies detected at 24 μm and those which only have upper limits. The median q value for SF galaxies is 0.82 ± 0.05 with a scatter of ~ 0.3 when all objects (also the upper limits)

---

[7]The computation of 1.4 GHz radio luminosity is given in Appendix B.1.
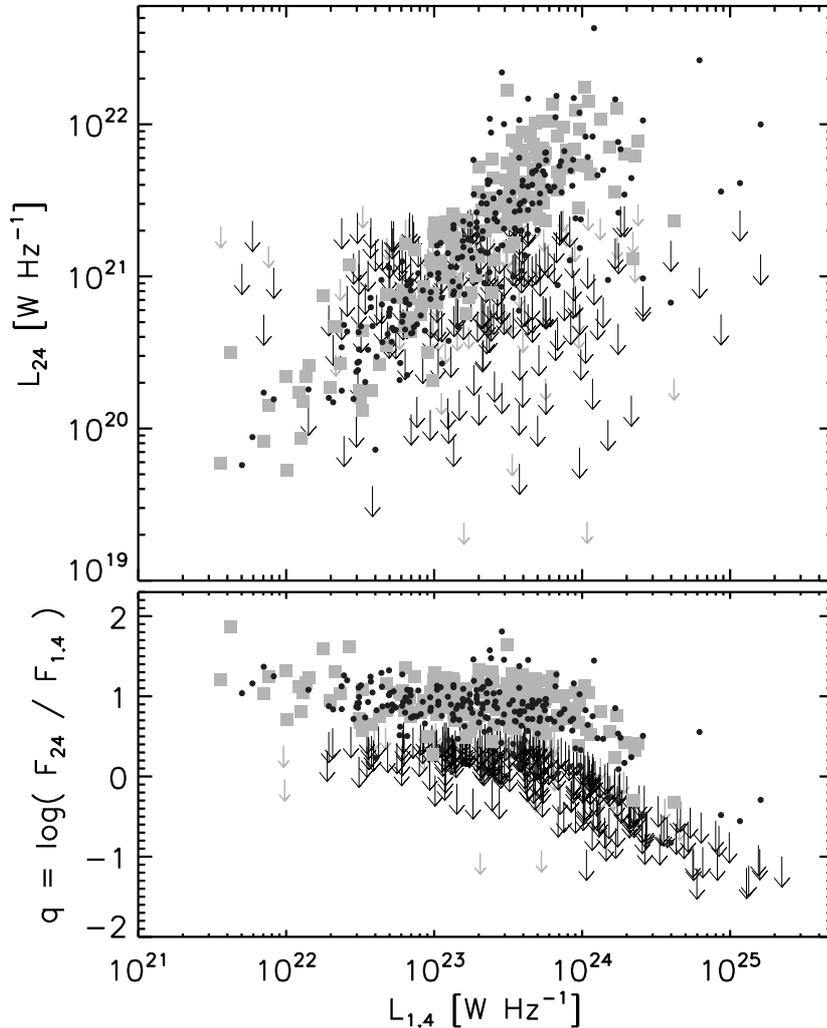
Figure 3.15   *Top panel*: 24 μm luminosity vs. 1.4 GHz luminosity for our selected SF (grey squares) and AGN (black dots) galaxies. Upper 24 μm luminosity limits for the radio SF (18%) and AGN (56%) galaxies that were not detected at 24μm are indicated by grey and black arrows, respectively. *Bottom panel*: The q parameter, defined as the logarithm of the 24 μm to 20 cm flux ratio, as a function of 20 cm luminosity for SF (grey squares) and AGN (black dots) galaxies. Upper limits are indicated by arrows, as in the top panel. Note the much larger scatter in q for AGN than for SF galaxies.

are taken into account. On the other hand, the median q value for the AGN galaxies is 0.51 ± 0.02, significantly lower than for SF galaxies. We also find a larger spread in q (~ 0.4) for the AGN population. Note, however, that the spread quoted here should be considered somehow tentative, especially for AGN, as the *exact q* values for the fraction of objects not detected at 24 μm are not known. Nonetheless, this does not affect the estimates of the median values. Our q parameter derived for SF galaxies is remarkably consistent with the one inferred by Appleton et al. (2004) at 24 μm. Combining Spitzer – MIPS and VLA observations in the First Look Survey with optical spectroscopy, they have found a q value of 0.84 with a spread of 0.28 (with no k-corrections applied). They have also shown that the FIR luminosities of AGN tend to be lower for a given radio luminosity,

Figure 3.16   The distribution of the q parameter (see also Fig. 3.15) for SF (top panel) and AGN (bottom panel) galaxies. In both panels the solid histograms show the distribution of the 1.4 GHz sources detected at 24 μm while the dash-dotted histograms show the distribution of the upper limits of q obtained for the radio sources that were not detected at 24 μm (see text for details). The solid vertical line in each panel designates the median value of the entire distribution, also indicated in the top left in each panel.
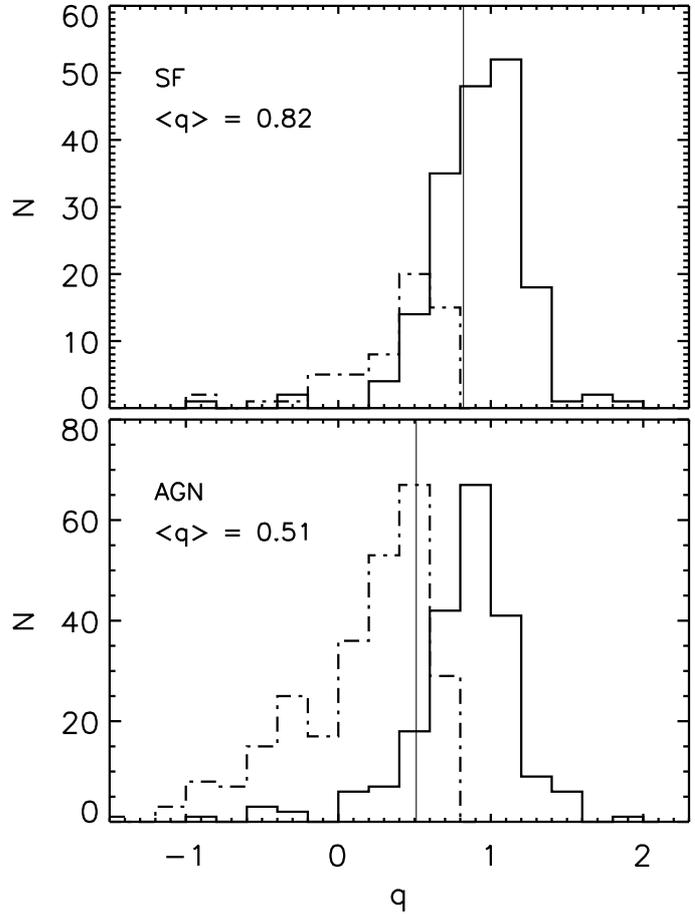
consistent with our findings here.

Finally, in Fig. 3.17 we show the q parameter as a function of redshift for our SF and AGN galaxies. q does not depend on redshift, both for SF and AGN galaxies, implying that the MIR – radio correlation with the same slope is valid out to high redshifts ($z \sim 1.3$). This result is again consistent with those presented in Appleton et al. (2004).
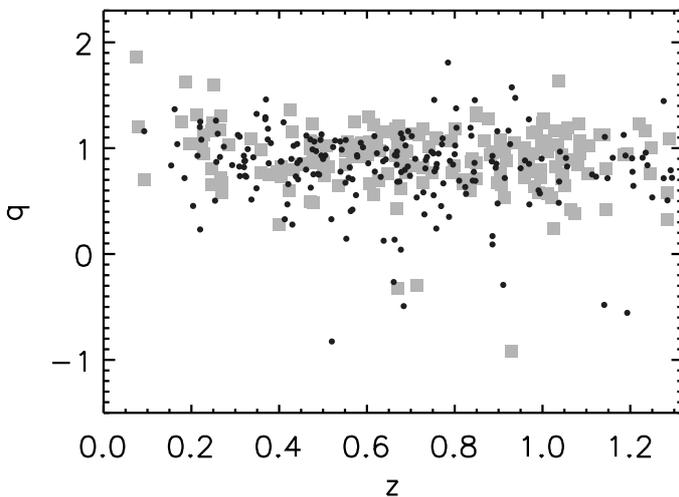
Figure 3.17 q as a function of redshift for SF (grey squares) and AGN (black dots) galaxies. Note that q does not depend on redshift, implying that the 24 μm–radio correlation holds out to high redshift (see text for details).

In summary, the above results have shown that the 24 μm – radio correlation has different properties for our selected SF and AGN galaxies, which verifies the efficency of our rest-frame color based classification method.

3.6.3 Selection based on optical spectroscopic properties, radio luminosity and stellar mass

Best et al. (2005) defined a sample of ~ 3000 local ($0.01 < z < 0.3$) galaxies from the SDSS DR2 "main" spectroscopic sample matched with sources above 5 mJy detected in the NVSS survey. They further divided the radio – optical source sample into AGN and SF galaxies making use of the galaxies' location in the plane spanned by the 4000 Å break [$D_n(4000)$] and radio luminosity [$L_{1.4GHz}$] normalized by stellar mass [M_*]. In Fig. 3.18 we compare our rest-frame color based classification method with the one utilized by Best et al. (2005) in the local universe. The $D_n(4000)$ vs. $\log(L_{1.4GHz}/M_*)$ distribution for all galaxies in the matched radio source sample is shown in Fig. 3.18. The 1.4 GHz luminosity for these galaxies was derived as described in Appendix B.1, and $D_n(4000)$ and M_* from the best fit template from the SED fitting (see Sec. 3.4.2). The average errors are indicated. The dashed line corresponds to the separation between SF and AGN proposed by Best et al. (2005), and the two types of symbols designate the SF (squares) and AGN (dots) galaxies identified by our rest-frame color based classification method. We want to note that Best et al. calibrated their separation method using a slightly different selection of objects in the BPT diagram (see their Fig. 9) with respect to the one we use here. Therefore, a perfect correspondence between our and the Best et al. method is not to be expected, even if our derived quantities were absolutely accurate. The area in the $D_n(4000)$ vs. $\log(L_{1.4GHz}/M_*)$ plane where the major disagreement is expected, due to the different selections in the BPT diagram, is in the range of 1.4 $< D_n(4000) < 1.6$, and $11 < \log(L_{1.4GHz}/M_*) < 12$. This is the region where a larger fraction of Seyfert and LINER galaxies is located (see Fig. 9 in Best et al. 2005), and, different from Best et al., we define these galaxies exclusively as AGN. In this region in Fig. 3.18 we indeed see the largest disagreement between the two classifications. Further, the existence of objects with $D_n(4000) < 1.3$ that we classify as AGN is not surprising, but it rather reflects the dual properties of composite objects, which in this case were classified as AGN by our rest-frame color based classification method. We also want to note that the average error in the synthesized $D_n(4000)$ [derived from comparison with the spectroscopic and synthetic $D_n(4000)$ in the local sample] is fairly large, and thus prevents a more detailed comparison between the two selection methods. Overall, given the error bars and the difference in the basic selections of the two methods, as well as the fact that our $D_n(4000)$ values are *not* spectral measurements on the data, but values taken from the best fit template, we conclude that our rest-frame color based classification method agrees well with the one proposed by Best et al. (2005) in the local universe.

In summary, our rest-frame color based classification method for separating SF from AGN galaxies agrees well with other selection schemes, proposed in the literature, which

are based both on MIR colors and optical spectroscopic diagnostics.
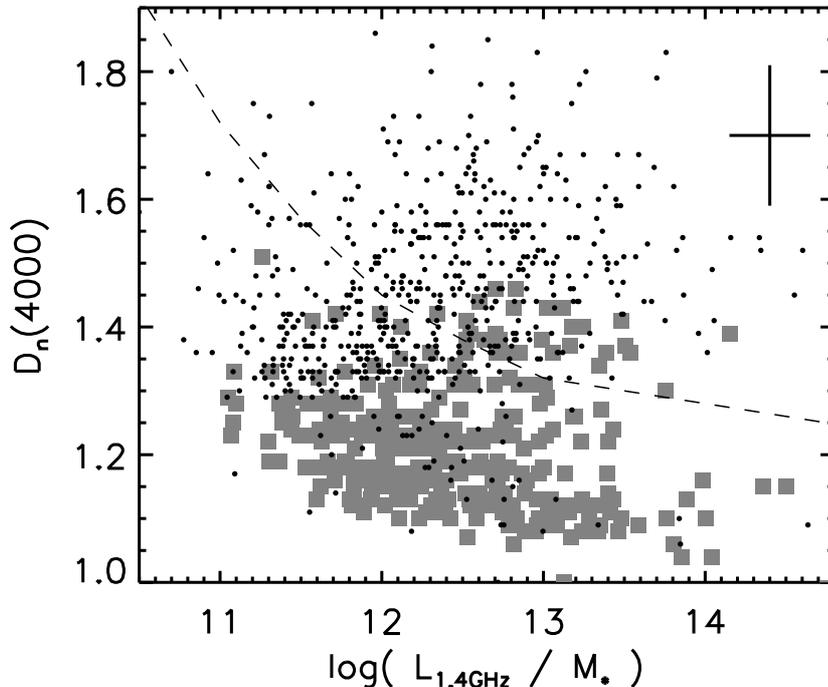
Figure 3.18   The 4000 Å break, $D_n(4000)$, vs. 1.4 GHz radio luminosity normalized by stellar mass, $L_{1.4GHz}/M_*$ for galaxies in the matched radio sample. M^* and $D_n(4000)$ were synthesized via SED fitting by GOSSIP. The black and grey symbols show objects classified by our rest-frame color based classification method as AGN and star forming galaxies, respectively. The dashed line corresponds to the separation proposed by Best et al. (2005). The average errors of the synthesized quantities are shown in the top right. A good consistency between the two selection methods exists, given the large error bars, as well as a slightly different selection rational used here and in Best et al. (2005a; see text for details).

3.7   Discussion: The composition of the faint radio population

In previous Sections we have presented, tested, and discussed in detail the photometric classification method which we used to separate the matched radio source sample into stars, QSOs, star forming, AGN and high-z galaxies. In this Section we discuss the properties of the 'population mix' in the VLA-COSMOS survey: In Sec. 3.7.1 we describe the redshift and luminosity distributions of the selected SF and AGN galaxies, and in Sec. 3.7.2 we study the contribution of different source types to the sub-mJy radio population. We show, based on the matched radio sample, as well as on the remaining radio sources with no optical counterparts (brighter than $i = 26$), that star forming galaxies do not dominate the sub-mJy sources, but that the majority of these sources is rather comprised of AGN and QSOs.

3.7.1 The redshifts and luminosity distributions of SF and AGN galaxies out to $z = 1.3$

The rest-frame color based classification method yielded 340 star forming and 601 AGN galaxies out to redshifts of 1.3. In the top panel in Fig. 3.19 we show the redshift distribution for these galaxies using redshift bins of 0.217 in width. We use such wide redshift bins to assess the *average* properties of the radio population, reducing the effects of fluctuations due to the strong and narrow overdensities which are known to exist in the COSMOS field (Scoville et al. 2007b; Finoguenov et al. 2007; Smolčić et al. 2007a, see Chap. 5). Poisson errors are indicated for each bin. The deficit of galaxies at the low-redshift end reflects the relatively small comoving volume sampled by the $2\square°$ area of the COSMOS field at these redshifts. The decline in the number of sources at the high-redshift end, on the other hand, reflects the detection limit of the VLA-COSMOS survey. The redshift distribution of the number of star forming galaxies seems to be more uniform than the one for AGN, in particular the relative number of star forming galaxies compared to AGN rises at higher redshifts ($z \gtrsim 1$). This may be explained by the relatively high number density of ULIRGs expected at these redshifts (Le Floc'h et al. 2005; Caputi et al. 2007) in conjunction with the VLA-COSMOS detection limit which at these redshifts allows to sample only radio luminosities larger than 3×10^{23} WHz^{-1} (see Fig. 3.20 below). Further, as the comoving volume surveyed at $z \sim 1$ is larger than the one surveyed locally, the probability of detecting a ULIRG is also increasing at these redshifts. Effects of cosmic variance as a function of redshift cannot be excluded, however they should be smaller than for other deep radio surveys that typically probe significantly smaller areas.

In the bottom panel in Fig. 3.19 we show the fractional contribution of the SF and AGN galaxies to the $z \leq 1.3$ matched radio population, as a function of redshift. On average, we find that the mean fractional contribution of SF and AGN galaxies to the $z \leq 1.3$ matched radio population is $(34 \pm 14)\%$ and $(66 \pm 14)\%$, respectively. This is strikingly similar to the relative numbers of SF and AGN galaxies in the local Universe. Namely, if we apply the adopted $P1$ color cut to the SDSS/NVSS galaxy sample (see Sec. 3.4.1), we find that $\sim 32\%$ of the galaxies are star forming, and $\sim 68\%$ are AGN. If, as shown by the tests described in Sec. 3.4.1, our rest-frame color based classification method can reliably be applied also to high redshift galaxies, then the similarity of the SF and AGN fractions suggests that the two populations have similar evolutionary properties out to $z \sim 1.3$.

In Fig. 3.20, we show the 1.4 GHz luminosity as a function of redshift for the selected SF and AGN galaxies out to $z = 1.3$. We also indicate the expected luminosity ranges for Milky Way type galaxies, LIRGs, ULIRGs and HyLIRGs, which were derived using the total IR – radio correlation (Bell 2003). It is noteworthy that the majority of galaxies with luminosities typical for HyLIRGs ($L_{IR} > 10^{13}$ L$_\odot$) was classified by the rest-frame color based classification method as AGN, consistent with the expected properties of these galaxies (e.g. Veilleux et al. 1999; Tran et al. 2001). This point is seen more clearly in Fig. 3.21, where we show the distribution of the 1.4 GHz luminosity for the selected star forming and AGN galaxies. The median luminosities are $\sim 1.6 \times 10^{23}$ W Hz^{-1} and $\sim 3.2 \times 10^{23}$ W Hz^{-1} for SF and AGN galaxies, respectively. Although the median luminosities of the two popu-
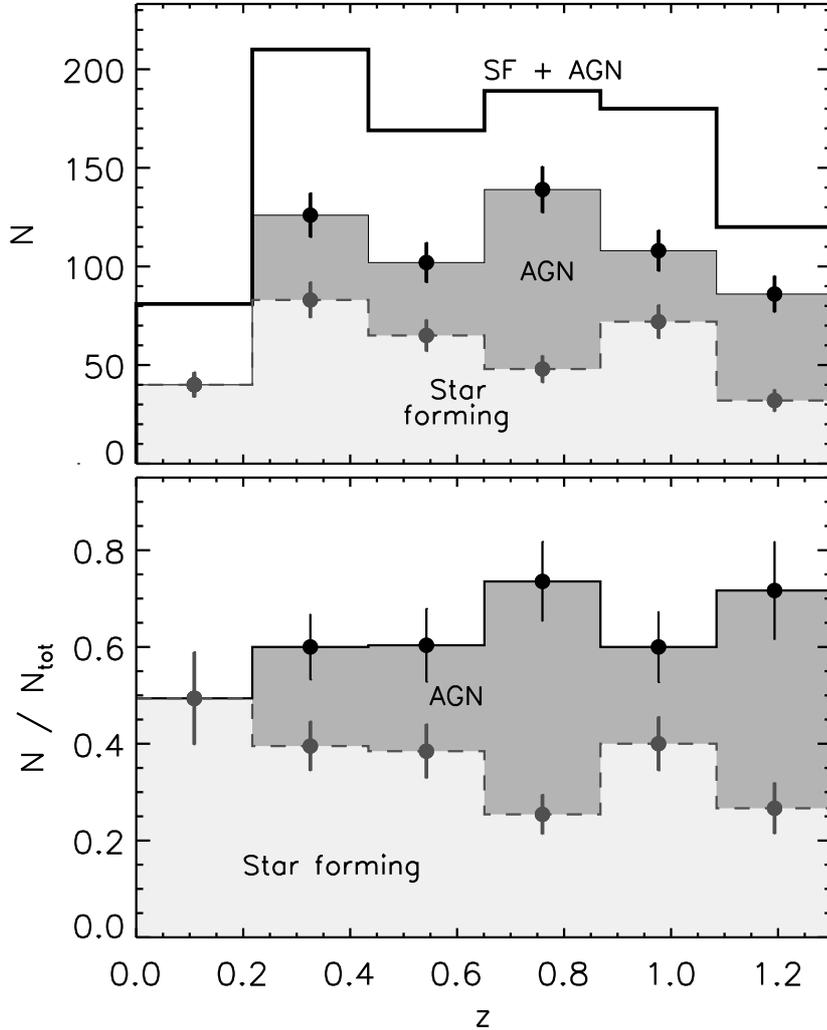
Figure 3.19   *Top:* Redshift distribution of i) the galaxies in the matched radio sample out to $z = 1.3$ (thick line), ii) the 340 selected star forming galaxies (light-grey shaded histogram) and iii) 601 identified AGN (dark-grey shaded histogram). *Bottom:* The fractional distribution of the SF and AGN galaxies compared to the total number of galaxies in the matched radio sample out to $z = 1.3$ as a function of redshift. In both panels Poisson errors are indicated.

lations are different only by a factor of 2, there are some significant differences at both high and low radio luminosity. At high luminosities there is the strong decline of the number of SF galaxies with luminosities above $\sim 10^{24}$ W Hz^{-1}, while AGN show an extended tail towards the brightest 1.4 GHz luminosities. Such a behavior is consistent with results from local studies, which suggested that 'normal'[8] galaxies tend to have $L_{1.4GHz} \lesssim 10^{24}$ W Hz^{-1} (e.g. Condon 1992). It is noteworthy, that our SF and AGN galaxies were identified completely independently from their radio luminosity, yet their 1.4 GHz luminosities match

---

[8] 'Normal' galaxies, in terms of radio properties, are broadly defined as galaxies whose radio emission is not powered by a super-massive black hole. These galaxies are a mix of spiral, dwarf irregular galaxies, peculiar and interacting systems, as well as E/S0 galaxies with ongoing star formation (see Condon 1992 for a review).

Figure 3.20 1.4 GHz luminosity as a function of redshift for the 340 selected star forming galaxies (grey squares) and 601 AGN (black dots). The horizontal (dot-dashed) lines correspond to 1.4 GHz luminosities typical for various classes of galaxies, obtained using the total IR – radio correlation (Bell 2003). The solid curved line corresponds to the VLA-COSMOS 5σ limit of ~ 50 μJy. Note also that the VLA-COSMOS survey is sampling the entire LIRG and ULIRG populations out to redshifts of ~ 0.4 and ~ 1, respectively.
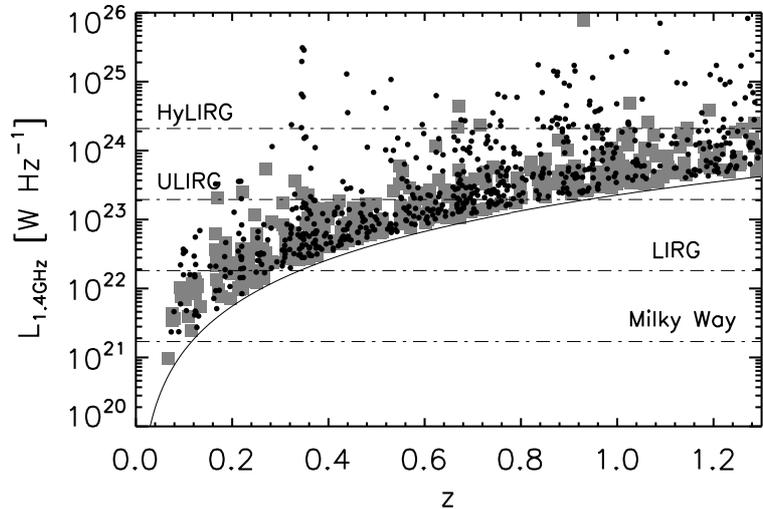
the expectations based on local studies. At low luminosity ($\lesssim 2 \times 10^{22}$ W Hz^{-1}; below the typical LIRG radio luminosity) the fraction of SF galaxies increases and the numbers of SF and AGN galaxies are similar to each other.
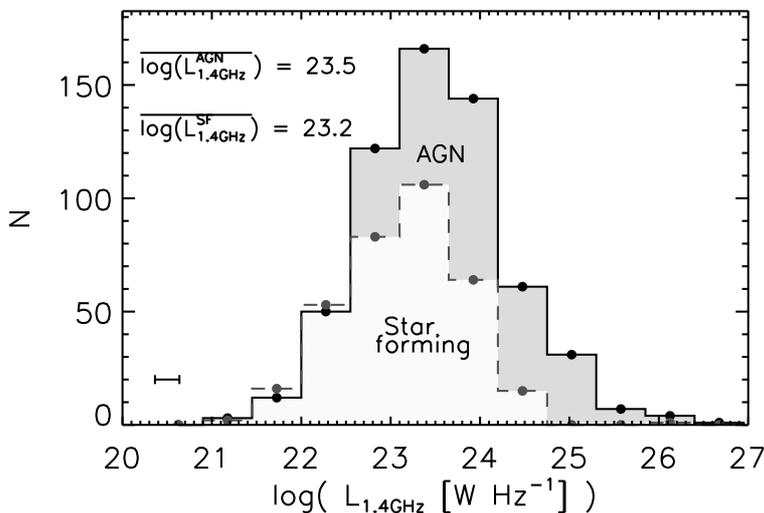
Figure 3.21 Distribution of the logarithm of the 1.4 GHz luminosity for the selected star forming (light-grey shaded histogram) and AGN (dark-grey shaded histogram) galaxies. The median $\log(L_{1.4GHz})$ values for the star forming and AGN samples are given in the top left corner, and the average error in $\log(L_{1.4GHz})$ is shown in the bottom left of the panel.

Further, the luminosity distribution shown in Fig. 3.21 agrees well with local results, which have shown that $L_{1.4GHz}$ for star forming and (absorption and emission line) AGN shows overlapping distributions, and consequently no clear separation (e.g. Sadler et al. 1999; Jackson & Londish 2000; Chan et al. 2004). In the local universe Sadler et al. (1999) inferred a median $L_{1.4GHz}$ for SF and AGN galaxies to be $\sim 3 \times 10^{22}$ W Hz^{-1} and $\sim 3 \times 10^{23}$ W Hz^{-1}, respectively. Hence, our median value for the luminosity of VLA-COSMOS AGN (3.2×10^{23} W Hz^{-1}) out to $z = 1.3$ matches the one inferred locally, however for SF galaxies (1.6×10^{23} W Hz^{-1}) it is higher than that derived by Sadler et al. (1999). The

latter is easily understood as the combined effect of the higher median redshift (~ 0.7) of the galaxies in our *flux limited* sample (thus not probing low $L_{1.4GHz}$) and of the higher level of star formation activity, which is observed going from redshift 0 to 1 (Madau et al. 1996; Hopkins 2004) also implying higher $L_{1.4GHz}$ (Condon 1992; Bell 2003).

3.7.2   The 'population mix' in the VLA-COSMOS survey

In this Section we study the contribution of different sub-populations to the the total sub-mJy radio population. The key question we want to answer is: Is the sub-mJy population dominated by any particular sub-population, which may be the main cause for the observed flattening of the differential radio source counts below 1 mJy (for VLA-COSMOS source counts; see Bondi et al. 2007)?

Is the matched radio sample at sub-mJy levels dominated by star forming galaxies?

In order to obtain an insight into the 'population mix' of the faint radio sources in the matched radio source sample, in Fig. 3.22 we show the distribution of the 1.4 GHz total flux, F_{tot}, for the SF and AGN galaxies in the matched radio sample out to $z = 1.3$, as well as for the identified QSOs.[9] Note, that the remaining $z > 1.3$ galaxies in the matched radio sample are defined as high redshift (high-z) galaxies. The flux bins in Fig. 3.22 are 0.15 mJy wide. Such wide bins allow us to study the average behavior of the galaxies in the sub-mJy population with decreasing fluxes. Our main aim is to answer one of the more controversial questions in radio astronomy: *Is the sub-mJy radio population dominated by star forming galaxies or any other distinct sub-population?*

From the top panel in Fig. 3.22 it is obvious that at fluxes above ~ 0.7 mJy we are hampered by low number statistics (the total number of sources in each bin is below 20). Therefore, for the purpose of this paper we will focus only on sources with fluxes below 0.7 mJy down to the VLA-COSMOS 5σ limit of ~ 50 μJy.

The middle panel in Fig. 3.22 shows the fractional distribution of the identified populations in the matched radio sample, with indicated Poisson errors. Our findings are as follows. QSOs contribute to the matched radio sample at a constant level of about 10%. AGN galaxies below $z = 1.3$ show a decreasing trend with decreasing fluxes, with their contribution to the matched radio sample dropping from $\sim 60\%$ to less than 40%. The SF galaxies at $z \leq 1.3$ in the flux range of 50 μJy to 0.7 mJy contribute fairly constantly at the given fluxes, with an average contribution of about 20%. Note that the possible increment from 0.7 mJy to 50 μJy of only $\sim 10\%$ is not significant. In Sec. 3.4.2 we have inferred that the photometric errors in the synthesized $P1$ color introduce a positive bias of $\sim 5\%$ for SF galaxies. As this bin contains the lowest number of SF galaxies, it is the most affected by this bias. In Sec. 3.4.1, based on the local SDSS/NVSS sample of galaxies, we have shown that our rest-frame color based classification method selects $\sim 70\%$ of 'real' SF

---

[9]Photometric redshift information for QSOs in the COSMOS survey is not available at this point.

galaxies, which make-up $\sim 85\%$ of the complete sample of SF galaxies, while the photometrically selected AGN sample is contaminated by SF galaxies at the 5% level. Assuming that the percentages of completeness and contamination, derived from the analysis of the SDSS/NVSS sample of galaxies, can be safely applied also to our VLA-COSMOS sample, we can use them to correct the observed fractions. Even with the correction the fractional contribution of SF galaxies at $z < 1.3$ in the matched radio population essentially stays the same, i.e. about $\sim 20\%$ at fluxes in the range from 50 μJy to 0.7 mJy. Contrary to previous studies (e.g. Seymour et al. 2004; Benn et al. 1993), our results show that SF galaxies at intermediate redshifts are not the dominant population at sub-mJy flux levels. However, it may be possible that a significant number of SF galaxies at $z > 1.3$ exists, which may contribute strongly to the sub-mJy population. We investigate this possibility in the bottom panel in Fig. 3.22 and in Fig. 3.23, and show below that this is not the case.

About 30% of the matched radio sample consists of galaxies at redshifts beyond $z = 1.3$ (high-z; see bottom panel in Fig. 3.22). The contribution of these galaxies marginally increases from 20% at 0.7 mJy to 35% at 50 μJy. Although we were not able to apply our rest-frame color based classification method to these galaxies in order to classify them, we can nevertheless draw some conclusion about their nature by studying their multi-wavelength properties. Therefore, in Fig. 3.23 we plot the MIR diagnostic diagram, for the high-z galaxies and compare their properties to the classified sources in the matched radio sample. We overlay non-evolving color tracks for the typical starburst galaxy M82, an elliptical 13 Gyr old galaxy, and a Seyfert-2 type SED, obtained from a composite spectrum of 28 randomly chosen Seyfert galaxies (Polletta et al. 2006). As expected, the properties of high-z galaxies are consistent with properties of higher redshift ($z > 1.5$) galaxies. However, the region they occupy in this MIR color-color diagram is occupied in a similar way by different sub-populations, such as star forming, Seyfert-type, and passively evolving galaxies, in the redshift range from about 1.5 to 3 (see color tracks in Fig. 3.23). Further, it is possible that a fraction of these sources are broad line AGN as they are located within the area outlined by dashed lines, which was proposed by Stern et al. (2005) for the selection of AGN Type-1 (see also Caputi et al. 2007). This is further strengthened by the 22 high-z sources which were also identified as X-ray point sources, and lie within the Type-1 AGN selection region. Further, given the high redshift of these sources, combined with the XMM detection limit, it is highly unlikely that any of these sources may be star forming (see e.g. Fig. 14 in Trump et al. 2007). This analysis alone already indicates that the matched radio sources beyond $z = 1.3$ are most probably a mixture of different sub-populations.

The population mix in the high-z sample is further affirmed by the distribution of the high-z galaxies in the BzK diagram (shown in Fig. 3.24), which is commonly utilized for the selection of $z > 1.4$ galaxies, and separates well passively-evolving galaxies from those originally defined as 'star forming' at $z > 1.4$ (Daddi et al. 2004). Form Fig. 3.24 it becomes obvious that the BzK criterion does not select a pure 'star forming' sample at $z > 1.4$, as initially postulated, but a sample that is comprised of both SF galaxies and low-luminosity AGN. In addition, the X-ray detected high-z sources, which may be classified
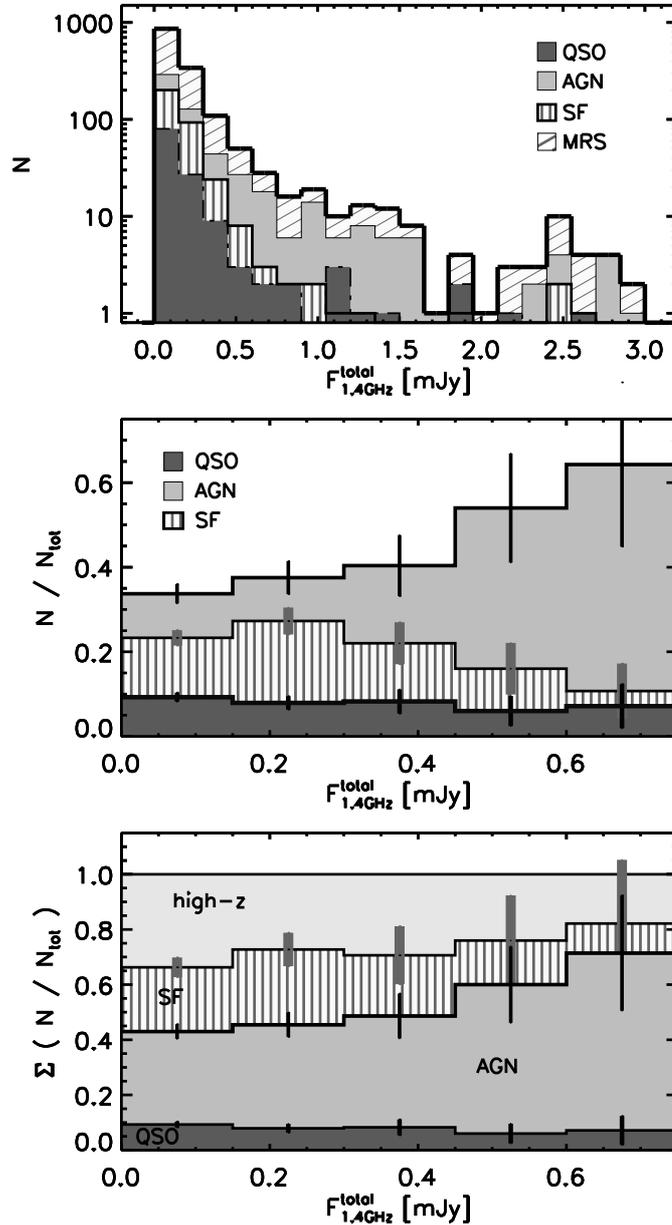
Figure 3.22 *Top:* The distribution of the 1.4 GHz total flux for the star forming (vertically hatched histogram) and AGN galaxies (light-grey shaded histogram) in the matched radio sample out to $z = 1.3$ (see also Fig. 3.21). Shown is also the distribution for the selected QSOs (dark-grey shaded histogram), for which good redshift information is not available at this point. 'MRS' stands for the 'matched radio sample'. *Middle:* The relative contribution of SF, AGN galaxies out to $z = 1.3$, and QSOs to the matched radio sample. Note that the missing fraction of sources consists of the high redshift (high-z) objects, which we define as galaxies in our matched radio sample with $z > 1.3$. *Bottom:* The cumulative distribution of SF, AGN galaxies out to $z = 1.3$, QSOs and high-z galaxies in the matched radio sample. The indicated error bars in the middle and bottom panels are derived from Poisson statistics. Note also the different flux scales in the top and the middle/bottom panels.
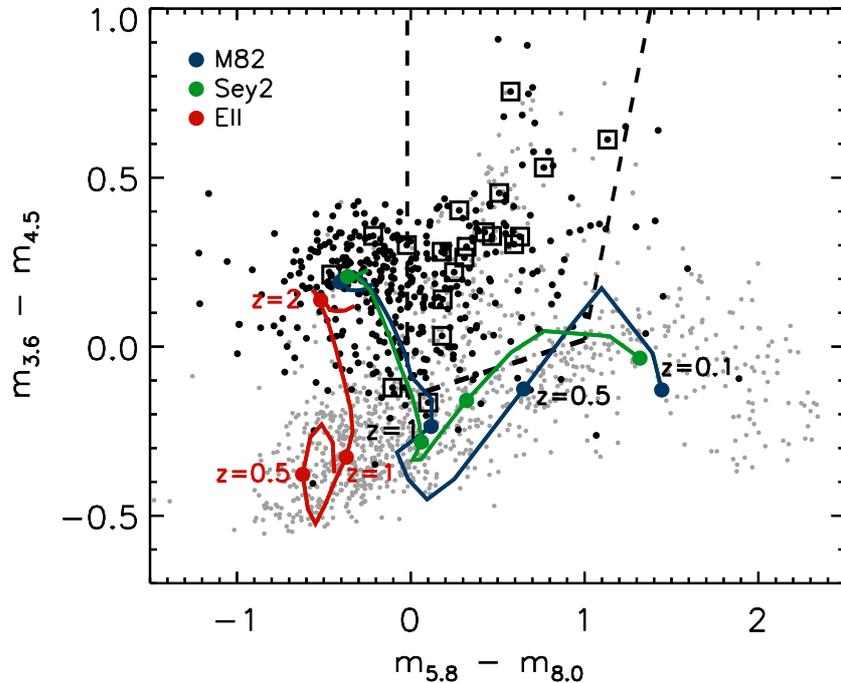
Figure 3.23 MIR color – color digram (analogous to Fig. 3.14 , bottom panel) for the full matched radio sample. Gray dots represent sources classified using our classification method (i.e. SF and AGN galaxies out to $z = 1.3$, and QSOs), while the black dots show the high-z sources (galaxies in the matched radio sample beyond $z = 1.3$). Open black sqares represent the high-z sources that have an XMM point source counterpart. The dashed lines are indicated to guide the eye, and correspond to the AGN type-1 selection region, proposed by Stern et al. (2005). The curved green, blue, and red lines correspond to the color-color tracks, obtained from SEDs of the starburst galaxy M 82, a composite of 28 Seyfert 2 galaxies, and a 13 Gyr old elliptical galaxy, respectively, in the redshift range $0.1 – 2.5$.

as AGN with high confidence as discussed above, also lie within this region. Therefore, the SED color tracks combined with the distribution of the high-z galaxies (black dots in Fig. 3.24), and the X-ray detected subsample suggest that our $z > 1.3$ matched sources are a fair mixture of SF and AGN galaxies, yielding that the high-z galaxies continue to consist of *different* galaxy populations at higher redshifts.

For reference, the i band magnitude distribution for the identified sub-samples in the matched radio sample is shown in Fig. 3.25. Note that the high-z galaxies are the faintest optical sources, consistent with the expectations for high redshift sources drawn from a flux limited sample. However, we want to mention that even in the most extreme case that all of the high-z galaxies were star forming, still the fractional contribution of star forming galaxies to the matched radio source population would not dominate over the contribution of AGN and QSOs, but the two contributions would rather be comparable.

As shown in Fig. 3.24 it is likely that both classes of objects contribute similarly to the high-z galaxies, although their exact relative fractions cannot be determined from this analysis. However, if we assume that roughly 50% of the high-z galaxies are SF galaxies, then the fraction of SF galaxies in the matched radio sample would increase to less than 40%. Therefore, we conclude that the population of star forming galaxies is not the dominant population at sub-mJy levels, at least in our sample of radio sources with

optical counterparts out to $i = 26$.

Our results are strikingly similar to the recent results by Padovani et al. (2007), who studied the sub-mJy radio source population in the Chandra Deep Field South down to a 5σ limit of 42 μJy. They found that SF galaxies make up only about 20% to 45% (i.e. roughly 1/3) of the sub-mJy radio sources.
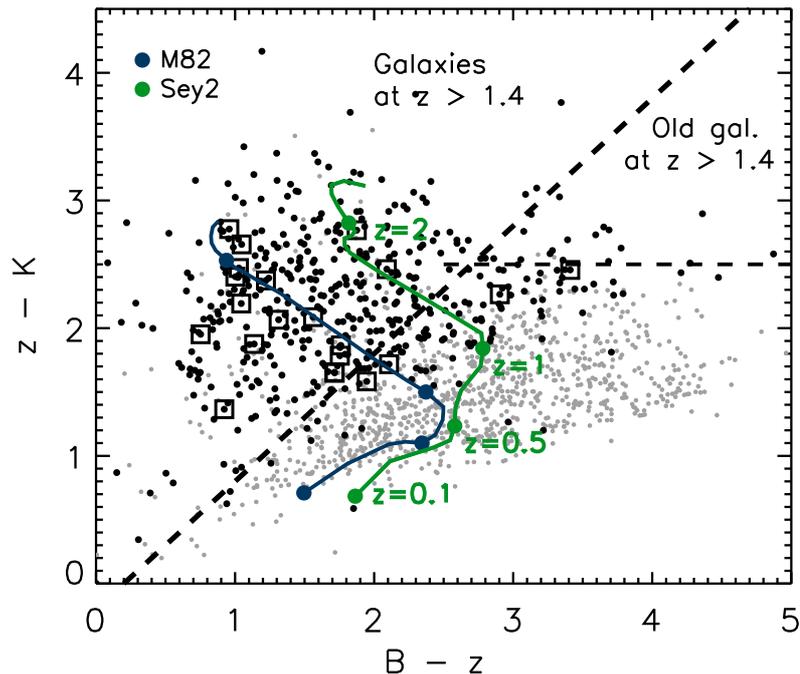
Figure 3.24 $B - z$ vs. $z - K$ color-color diagram for the entire matched radio sample. The symbols are analogous to Fig. 3.23: Gray dots represent sources identified using our classification method (i.e. SF and AGN galaxies out to $z = 1.3$, and QSOs), the black dots show the high-z sources, and open squares show XMM detected point sources in the high-z sample. The dashed lines separate regions of passively evolving (top right; outlined by the diagonal and horizontal dashed lines) and star-forming galaxies (left of the diagonal dashed line) at $z > 1.4$, adopted from Daddi et al. (2004). The curved green and blue lines correspond to the color-color tracks, obtained from SEDs of the starburst galaxy M 82, and a Seyfert 2 composite, respectively, in the redshift range from 0.1 to 2.5. Note, that Seyfert type of galaxies at $z > 1.4$ are also present in the region of 'star-forming galaxies', as initially postulated by Daddi et al. (2004).

The contribution to the sub-mJy radio population from radio sources with no, or with flagged, optical counterparts

Most of the previous studies (as well as our study up to this point) of the faint radio population have relied on sub-samples of the observed radio sources, that have been identified with optical counterparts out to $i = 26$, as representative of the entire sub-mJy radio population. For example, Benn et al. (1993) used a sample of only 87 out of 523 (i.e. less than 20%) 1.4 GHz radio sources above 0.1 mJy, for which they obtained optical spectroscopy ($B < 22$), to conclude that above 1 mJy about 50% of the galaxies were SF or Seyfert galaxies, while below 1 mJy the fraction increases to $\sim 90\%$. Further, Gruppioni et al. (1999) studied optical spectroscopic properties of 34 radio sources above 0.2 mJy in the
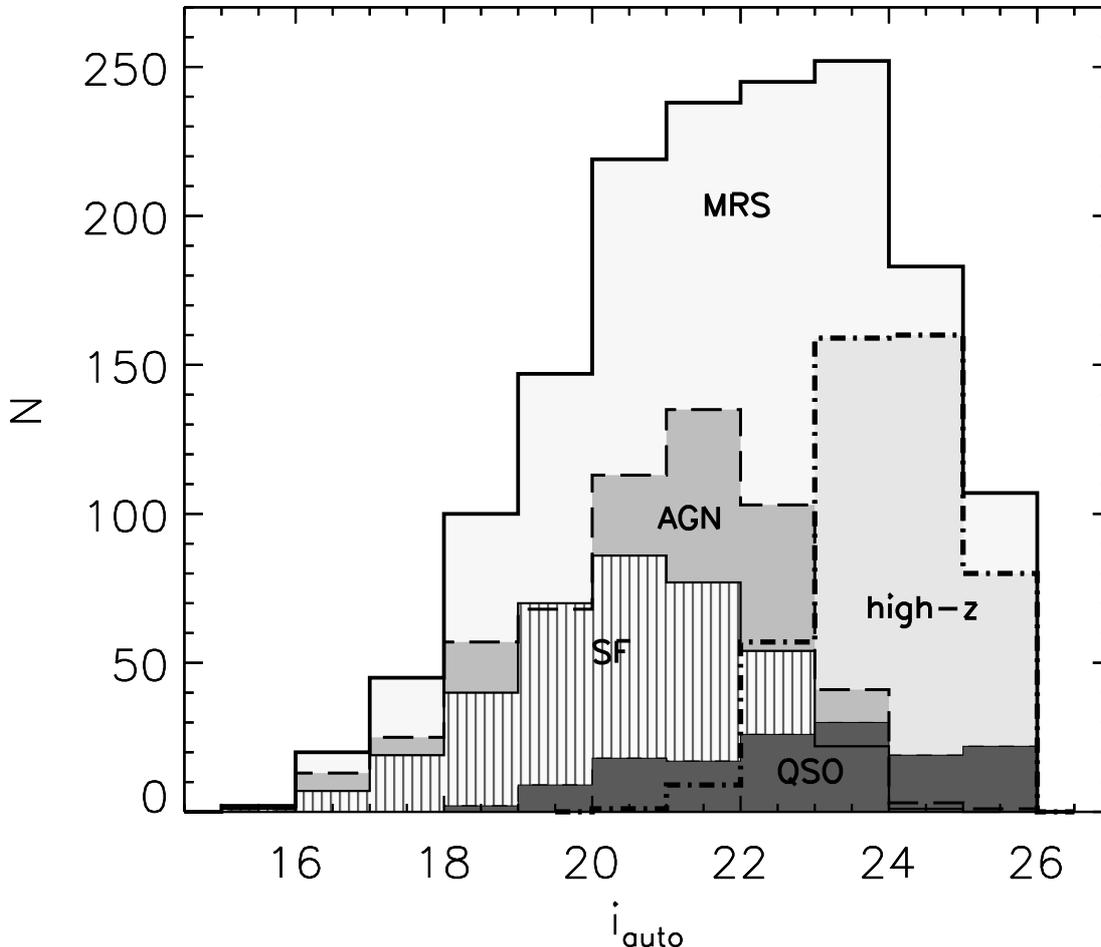
Figure 3.25 Distribution of the *i* band magnitude (Subaru where available, otherwise CFHT) for sources in the VLA-COSMOS matched radio sample (MRS). Also shown are the distributions for the identified sub-samples of sources: OSOs, star-forming (SF), AGN, and high-z galaxies

Marano Field down to $B = 24$. This sample comprised $\sim 60\%$ of the entire sample of faint radio sources, and they concluded that the SF galaxies do not constitute the main galaxy population of their radio sources, and even at sub-mJy levels the majority of their radio sources were identified with early type galaxies, consistent with AGN. Gruppioni et al. attributed the difference in their results compared to the results from Benn et al. (1993) to the fainter optical magnitude limit reached for their radio sample. In this work we have an order of magnitude larger sample size (1558 sources with optical counterparts), and a significantly deeper optical limit ($i = 26$) than previous studies. However, still our matched radio source sample consists of only $\sim 65\%$ of the VLA-COSMOS 1.4 GHz sources. Therefore, it is important to investigate the contribution of the remaining $\sim 35\%$ of the radio sources, with no identified or flagged optical counterparts, to the sub-mJy population. It may indeed be possible that a 'missing' population of objects, that significantly contributes to the sub-mJy population, is 'hidden' in this sample. We show below that this is not the case.

If the above hypothesis is true, then the properties (such as e.g. MIR colors) of these

remaining objects are expected to be distinct from the properties of objects in the matched radio sample. In order to shed light on this, in Fig. 3.26 (top panel) we show the distribution of the total flux for the 1558 sources in the matched radio sample, and for the remaining 830 sources that were a) not identified with optical counterparts with $i \leq 26$ or b) have optical counterparts with $i \leq 26$ but in photometrically masked-out region (see Sec. 3.3.1). The bottom panel shows the fractional contribution of these two samples compared to the entire VLA-COSMOS 1.4 GHz population. The fraction of matched radio sources is statistically consistent to be constant at $\sim 65\%$ at all faint flux levels, although formally it decreased from $\sim 75\%$ at ~ 0.7 mJy to $\sim 60\%$ at the limit of the VLA-COSMOS survey. On the basis of these high percentages, it is unlikely that any further population, that is not present in our matched radio sample, could account for a significant fraction of the sub-mJy population. This is further strengthened by the distribution of the remaining
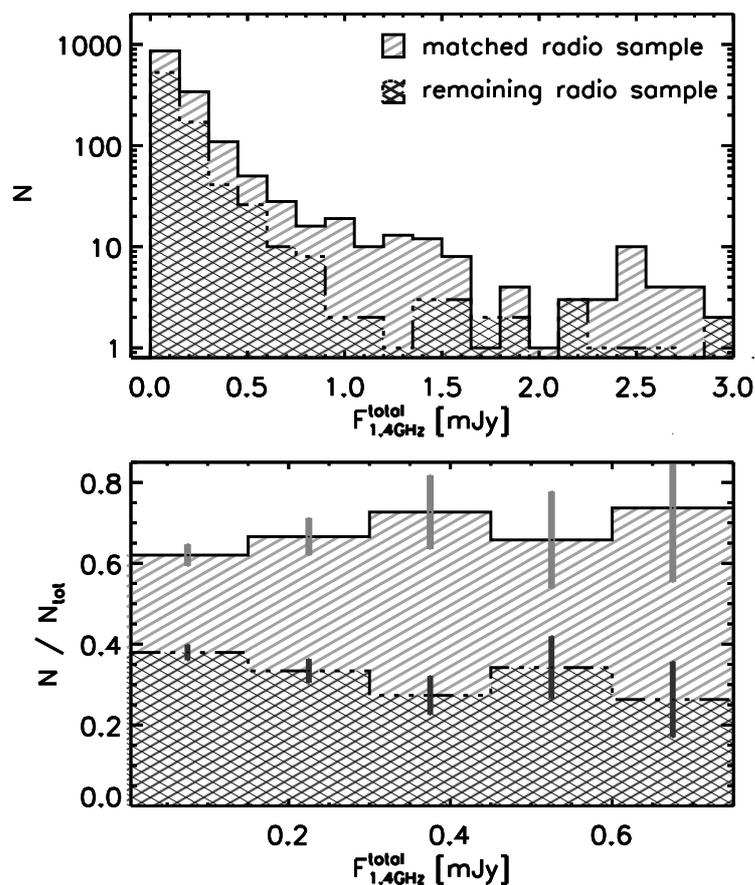
Figure 3.26   *Top:* The distribution of the 1.4 GHz total flux for sources in the matched radio sample (single hatched histogram), and for other VLA-COSMOS sources that have either no identified, or a photometrically flagged, optical counterpart brighter than $i = 26$ (cross-hatched histogram). *Bottom:* The fractional distribution of the two samples compared to the entire sample of 1.4 GHz radio sources. Indicated error bars are derived from Poisson statistics.

sources in the MIR color-dolor diagram, shown in Fig. 3.27, which is consistent with the expected distribution for a mixed sample of star forming, AGN galaxies, and QSOs at all

redshifts in the range from the local to the highest observable redshifts. An additional affirmation of the mix of population arises from the 31 sources that have been detected as X-ray point sources (see Fig. 3.27). It is worth noting however, that $\sim 60\%$ of these sources are consistent with higher redshift objects ($z \gtrsim 1.3$), while this is true only for $\sim 50\%$ of the galaxies in the matched radio sample (see Fig. 3.23). We therefore conclude that the radio sources without identified, or with flagged, optical counterparts brighter than $i = 26$ are most likely comprised of a mixture of different source populations (SF, AGN, QSO), similar to, although on average at higher redshift then the radio sources in our matched radio sample. Further, the relatively small total percentage of these sources cannot significantly alter the results about the 'population mix' in the 1.4 GHz VLA-COSMOS radio sample, inferred in the previous section.
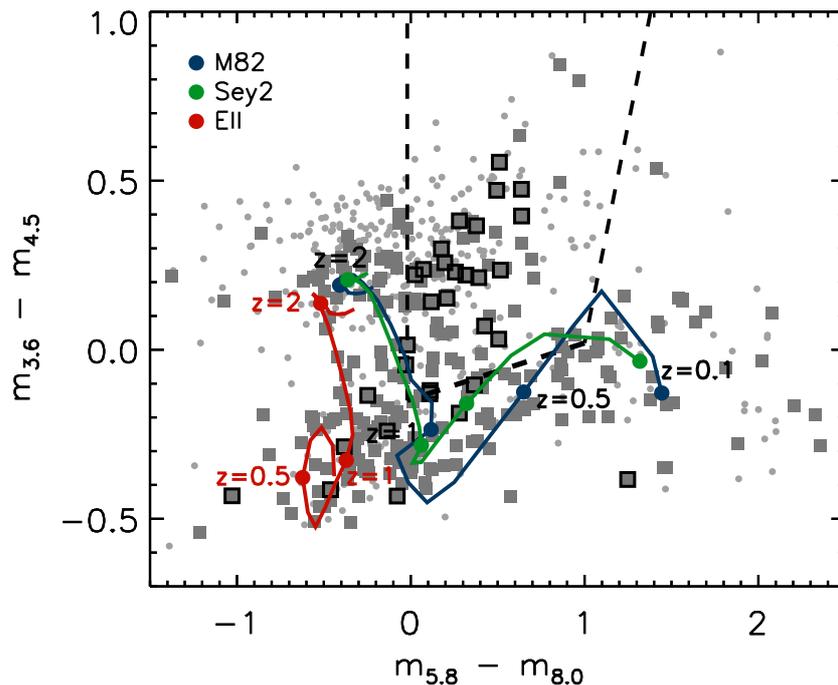
Figure 3.27   Analogous to Fig. 3.23, but for 813 VLA-COSMOS 1.4 GHz sources (grey dots) that have either no identified, or a photometrically flagged, optical counterpart brighter than $i = 26$, but that have IRAC detections (i.e. $\sim 75\%$; see Sec. 3.3.4). Grey squares indicate the sources that have an optical counterpart with $i \leq 26$, but that is within a masked-out area. Black open sqares represent the sources that have XMM point source detections. The clumping of objects in the upper left quadrant is consistent with both star forming, Seyfert and passive galaxies, in the redshift range from about 1.5 to 3, suggesting that over $\sim 60\%$ of the VLA-COSMOS 'remaining' sources are high redshift galaxies or QSOs.

3.7.3 Concluding remarks on the composition of the faint radio population

The faint – submillijansky – radio population comprises the radio population responsible for the upturn of the differential radio source counts below 1 mJy (see e.g. Bondi et al. 2007), and it has been the subject of many studies, and a matter of great debate in the past three decades (Condon 1984a; Windhorst et al. 1985a; Gruppioni et al. 1999; Seymour et al. 2004; Simpson et al. 2006). This radio population has been interpreted as a 'new' rising population of objects, that do not significantly contribute at higher radio flux levels. However, results from studies that tried to reveal the exact composition of the sub-mJy population have been highly discrepant. It was suggested that the majority of this faint radio population consists of faint blue galaxies, and it was assumed that these galaxies are undergoing significant star formation (Windhorst et al. 1985a). The spectroscopic study by Benn et al. (1993), although analyzing only less than 20% of their radio sample, supported this result indicating that the fraction of SF and Seyfert galaxies rises from about 50% to 90% in the range from super- to sub-mJy fluxes. However, Gruppioni et al. (1999), who performed a deeper optical spectroscopic analysis of a larger fraction ($\sim 60\%$) of their radio sources, disagreed with this result identifying the majority of their sub-mJy radio sources with early type galaxies, in which the radio emission is produced by AGN. Recently, using a combination of optical and radio morphology as an identifier for AGN and SF galaxies on $\sim 90\%$ of their radio sources in the SSA13 field, Fomalont et al. (2006) suggested that less than $\sim 40\%$ of the radio sources below 1 mJy are AGN. On the other hand, Padovani et al. (2007) based their SF/AGN classification on a combination of optical morphologies, X-ray luminosities and radio–to–optical flux ratios of their radio sources in the CDFS (Chandra Deep Field South), and indicated that only about $20 - 40\%$ of the faint radio sources are made-up of star forming galaxies.

As already mentioned in the Sec. 3.1 there are two main reasons for such controversial results in the past literature: a) The identification fraction of radio sources with optical counterparts spans a wide range (20% to 90%) in samples from radio deep fields, and b) the methods for the separation of SF from AGN galaxies have been highly heterogeneous. Further, the first and second point seem to exclude each other. Namely, the most efficient separation methods (e.g. intermediate- to high- resolution optical spectroscopy) generally led to a small identification fraction, whereas large radio samples with high optical identification fractions usually lacked robust SF/AGN indicators. In this paper we have tried to make a strong conjunction of these two points. We introduced a new method to separate SF from AGN galaxies, which relies strongly on rest-frame color properties, and thus allowed us to perform a robust classification of $\sim 65\%$ ($= 1558$) of the 1.4 GHz VLA-COSMOS radio sources down to ~ 50 μJy with identified optical counterparts out to $i = 26$ without the need for e.g. optical spectroscopy. Thus, we managed to reach both a high identification fraction and a robust source classification. However, in order to avoid any possible biases, we also utilized the full panchromatic COSMOS data set to put constraints on the properties of the remaining $\sim 35\%$ of the radio sources that were not identified with optical counterparts with $i \leq 26$, or that have optical counterparts with $i \leq 26$ but with

uncertain photometry due to blending and saturation in the optical images. In short, we have obtained a complete view of the 'population mix' of the sub-mJy radio sources, using to date the largest sample of 2388 faint ($5\sigma \approx 50 \ \mu$Jy) radio sources at 1.4 GHz. Our combined methods allow us to reveal the true nature of the sub-mJy radio sources in the VLA-COSMOS survey on a sound statistical basis.

Jarvis & Rawlings (2004) first suggested that the observed flattening of the differential radio source counts below 1 mJy may be caused by 'radio-quiet' AGN, i.e. radio-quiet QSOs and type-2 AGN (consistent with our 'AGN' class), rather than star forming galaxies. Making use of the observed correlation between X-ray and radio luminosity and the empirically derived X-ray luminosity function, they computed the 1.4 GHz luminosity function for radio-quiet AGN out to high redshifts, and used it as the key ingredient to model the radio source counts at faint flux levels (see Jarvis & Rawlings 2004 and references therein). However, they did not take into account SF galaxies as an important population to explain the shape of the counts. Such an interpretation managed to represent the differential radio source counts well down to $\sim 250 \ \mu$Jy, but failed at fainter fluxes. Our results, derived in the previous sections, show that indeed star forming galaxies are not the dominant population at sub-mJy levels in the range of 50 μJy to 0.7 Jy, however they still contribute about 30% to 40% at these fluxes. Based on our large sample of 2388 VLA-COSMOS radio sources we find that our classified AGN, which comprise mostly of low-luminosity and type-2 AGN, make up $50 - 60\%$ of the faint radio population with a decreasing trend towards fainter fluxes, while the identified QSOs, which are mostly type-1 AGN, form a minor contribution of $\sim 10\%$ of the sub-mJy radio population in the range of 50 μJy to 0.7 Jy. Thus, our observational results show that the 'population mix' in the faint radio population contains a fair contribution of both SF galaxies and (low-luminosity and obscured) AGN, at least down to 50 μJy. Thus, separate luminosity functions for both populations have to be taken into account in order to fully explain the flattening of the radio source counts below 1 mJy. The 1.4 GHz luminosity function for star forming and AGN galaxies at intermediate redshift, as well as the modeling of the 1.4 GHz radio source counts using these new observational constrains and further analyses of the 'population mix' in the VLA-COSMOS survey, is going to be fully addressed and presented in a number of up-coming publications.

3.8   Summary

We have explored the properties of the sub-mJy radio population, detected at 20 cm (1.4 GHz) in the VLA-COSMOS survey, by introducing a new method to separate star forming from AGN galaxies. The main feature of our classification method is an effective identification of star forming galaxies and low-luminosity AGN (i.e. LINERs and Seyferts), based only on optical rest-frame color properties. Based on a large number of local ($z < 0.3$) galaxies with available high resolution spectroscopy we have shown that, at least in a radio selected sample, such a purely photometric separation is possible due to the tight correlation between rest-frame colors of emission-line galaxies and their position in the

emission-line based BPT diagram, which is commonly used for spectroscopically separating these two types of galaxies. Making use of the full COSMOS photometric data set, in conjunction with the rest-frame color based classification method, we have performed an in-depth analysis of 2388 VLA-COSMOS sources detected at 1.4 GHz with a signal to noise ≥ 5. We classified the radio sources with optical counterparts brighter than $i = 26$ into five classes of objects: a) star candidates, b) quasi stellar objects, c) AGN, d) star forming galaxies, and e) galaxies at redshifts greater than 1.3. For the latter class, as well as for the radio sources without, or with photometrically flagged, optical counterparts with $i \leq 26$, we have used observed optical to MIR color properties to study their nature. Our classification method, tests, and results are summarized as follows.

We have positionally matched the 2388 VLA-COSMOS detected at 1.4 GHz with S/N ≥ 5 with sources detected at other frequencies (optical/NIR, MIR, X-ray). About 65% of the radio sources have optical counterparts with $i \leq 26$ which are not located in blended or saturated regions. This sample, which we defined as the *matched radio source sample*, essentially contains all true matches with a false association rate (obtained from Poisson statistics) of only $\sim 4\%$. Further, $\sim 90\%$ of the sources in the matched radio source sample have IRAC counterparts, and $\sim 10\%$ have X-ray point source counterparts. Out of the remaining $\sim 35\%$ of the radio sources without identified, or with identified but photometrically uncertain, optical counterparts brighter than $i = 26$, $\sim 75\%$ were associated with sources detected in the MIR wavelength regime with Spitzer – IRAC. The lower fraction of IRAC counterparts in this sample is mostly due to blending effects, and possibly to a small number of spurious radio sources.

The heart of our classification method, which allows us to disentangle SF from low-luminosity (i.e. LINERs, Seyferts) and absorption-line AGN is the use of only photometric – optical rest-frame color – properties. This method was thoroughly tested using a large number of local galaxies drawn from the SDSS "main" spectroscopic sample, positionally matched to the NVSS and IRAS sky surveys. For the SF/AGN separation we use the $P1$ rest-frame color, which is a linear superposition of Strömgren colors in the wavelength range of $3500 - 5800$ Å. We have adopted a $P1$ color cut of 0.15 as the boundary between SF and AGN galaxies. Based on the local sample, which is a fair representation of the VLA-COSMOS sources at higher redshift, we have shown that such a color selection yields a 'photometrically selected sample of SF galaxies' that is contaminated by AGN and composite objects at the 20% and 10% levels, respectively, and it contains about 70% of 'real' (i.e. spectroscopically identified) SF galaxies, and those make-up $\sim 85\%$ of the complete sample of all 'real' SF galaxies. In addition, we have analyzed the properties of the missed 'real' SF galaxies due to the single rest-frame color criterion applied, and we have shown that, although the rest-frame classification method is based on optical properties, it is not biased against dusty starburst galaxies (i.e. LIRGs and ULIRGs). Further, the 'photometrically selected sample of AGN galaxies' is made-up of about 5% SF and 15% composite galaxies, and contains $\sim 80\%$ of 'real' AGN galaxies, which compose $\sim 90\%$ of *all* 'real' AGN galaxies.

For the galaxies in the VLA-COSMOS matched radio source sample, we have synthesized the rest-frame color $P1$ using the SED fitting code GOSSIP with a realization of $100,000$ model spectra built using the Bruzual & Charlot (2003) stellar synthesis evolutionary models. We have extensively tested the achieved accuracy of the synthetic magnitudes and colors, and showed that the $P1$ color, derived via SED fitting, is accurate to ~ 0.1 mag.

Using the full COSMOS multi-wavelength data set we have identified the radio sources in the matched radio sample as a) star candidates, b) QSOs, c) AGN, d) SF, and e) high redshift (high-z) galaxies. Comparing our classification with separation methods used in the literature which are based on both MIR color and optical spectroscopic properties of galaxies, we have shown that our selection technique agrees remarkably well with other, completely independent, methods, thus confirming the robustness and effectiveness of our classification method, also at intermediate redshifts. Further, we have used optical to MIR color properties to get an insight into the nature of the high-z galaxies, as well as the radio sources without (or with flagged) optical counterparts brighter than $i = 26$. The main characteristics of these sub-types are outlined as follows.

Star candidates: We have identified 2 star candidates ($\sim 0.1\%$ of the 1558 radio – optical sources). The 1.4 GHz total fluxes for these 2 objects are 126 and 152 μJy, and no X-ray emission was detected. Nonetheless, the final verification of the true stellar nature has to await for the completion of the COSMOS spectroscopic programs.

QSOs: We have identified 139 ($\sim 9\%$) QSOs in the matched radio source sample based on their compact optical morphology. We have verified our selection using a sub-sample of the selected QSOs with available spectroscopy, and we have shown that the selected sample is $\sim 80\%$ complete, and essentially not contaminated by other kinds of sources. The optical and MIR color properties, as well as X-ray to optical flux ratios, of the selected objects are consistent with properties of QSOs, further affirming the efficiency of our selection.

SF/AGN galaxies: We have identified 601 ($\sim 60\%$) AGN and 340 ($\sim 40\%$) SF galaxies out to $z = 1.3$ using our rest-frame color based classification method, i.e. applying a color cut of $P1 > 0.15$ for AGN, and $P1 \leq 0.15$ for SF galaxies.

high-z galaxies: The galaxies in the matched radio sample above a redshift of 1.3 were not classified using the rest-frame color based classification method due to higher uncertainties at these redshifts. Nonetheless, their optical to MIR colors, and X-ray properties strongly suggest that they are a mixture of both SF and AGN galaxies predominantly at $z > 1.3$ and Fig. 3.24).

Remaining radio sources: The MIR color properties of the radio sources *without or with flagged* optical counterparts brighter than $i = 26$ suggest that their composition is similar to the composition of the sources in the matched radio sample, i.e. they also consist of a mixture of SF and AGN galaxies. However, the fraction of these sources that is located at redshifts beyond ~ 1.3 is higher than the one in the matched radio sample, indicating that these sources have a higher median redshift than the sources with identified optical counterparts brighter than $i = 26$ and outside blended and saturated regions in the optical images.

We studied the properties of the SF and AGN galaxies out to $z = 1.3$ in the matched radio sample, and found that the median redshift of both types of galaxies is $z \sim 0.7$. Further, their median 1.4 GHz luminosities, drawn from our flux limited sample, are very similar, i.e. they differ only by a factor of 2 (AGN: 3.2×10^{23} W Hz^{-1}; SF: 1.6×10^{23} W Hz^{-1}). However, only a minor fraction of the identified SF galaxies have luminosities above 2×10^{24} W Hz^{-1}, while AGN show a strong tail towards higher 1.4 GHz luminosities. Such a behavior is consistent with the expectations based on results from previous – local universe – studies, combined with the rising level of star formation activity in the universe in the redshift range from 0 to 1.

$\sim 80\%$ of our selected star forming galaxies have MIPS 24 μm detections at or above a signal to noise of 3, while this is true for only $\sim 40\%$ of our selected AGN. We have derived the classical q parameter [$\log(F_{24\ \mu m}/F_{1.4\ GHz})$], which measures the slope of the 24 μm– radio correlation. The q parameter is significantly different for SF (0.82 ± 0.05) and AGN (0.51 ± 0.02) galaxies, when all radio detected sources are taken into account (given the upper limits from the 24 μm detection sensitivity). When only the 24 μm detected sources are taken into account the q parameter for SF and AGN galaxies is different by only $\sim 10\%$, consistent with findings in the local universe. Our results imply that the 24 μm– radio correlation holds out to at least $z = 1.3$.

We have explored to full detail the composition of the sub-mJy radio population making use of the entire sample of 2388 VLA-COSMOS radio sources detected above 5σ ($\approx 50\mu$Jy), in conjunction with the panchromatic (X-ray to radio) COSMOS data set. We find that SF galaxies are not the dominant population at submillijansky flux levels, as believed previously, but that they rather make up an approximately constant fraction of $30 - 40\%$ in the flux range of ~ 50 μJy to 0.7 mJy. The radio population at these fluxes is a mixture of roughly $30 - 40\%$ of SF and $50 - 60\%$ of AGN galaxies, with a minor contribution ($\sim 10\%$) of QSOs.

In summary, our newly developed method, in conjunction with the VLA-COSMOS 1.4 GHz observations, enabled us to make, for the first time, a thorough distinction between sources where the 1.4 GHz radio emission is predominantly driven by star formation processes from those where it is driven by SMBH processes, *regardless of the luminosity of the latter*, and apply it to currently the largest sample of 1558 1.4 GHz sources, with optical counterparts brighter than $i \leq 26$, and complete down to ~ 50 μJy. Further, utilizing the panchromatic COSMOS data we were able to put robust constraints onto the properties of the entire 1.4 GHz VLA-COSMOS radio sample containing 2388 sources, yielding the first clear insight into the characteristics of the submillijansky radio sources, showing that the faint radio sources are, contrary to common previous belief, a fair mixture of both SF and AGN galaxies.

Chapter 4

The dust un-biased cosmic star formation history derived using 1.4 GHz data from the VLA-COSMOS survey

In the previous Chapter the newly developed (rest-frame color based) classification method has been used to efficiently identify AGN and star forming galaxies in the VLA-COSMOS radio source sample. In this Chapter the cosmic star formation history since ~ 5 Gyr after the Big Bang is derived based on radio data utilizing this well defined sample of VLA-COSMOS star forming galaxies. The work presented in the following is about to be submitted to ApJ.

Abstract

We derive the cosmic star formation history (CSFH) based on 1.4 GHz radio data using an almost one order of magnitude larger sample of star forming galaxies, than available previously. We constrain the 1.4 GHz luminosity function for ~ 350 well selected VLA-COSMOS *star forming* galaxies out to $z = 1.3$, and find that a pure luminosity evolution is best described with $L_* \propto (1 + z)^{2.0 \pm 0.1}$. Based on the large $2\square°$ COSMOS field for the first time the high-luminosity end of the star forming galaxy luminosity function has been constrained with high precision allowing the derivation of the evolution of the cosmic star formation rate in the most intensely star forming galaxies (SFR $\gtrsim 100\ M_\odot$; ULIRGs). We find that the CSFH for *star forming* ULIRGs has declined slower since $z = 1.3$ than previously predicted based on MIR data, implying that the fraction of star forming galaxies in MIR-selected samples is likely lower than commonly assumed. Our overall derived CSFH confirms the high dust-obscuration corrections applied to star formation rate tracers at other wavelengths.

4.1   Introduction

Studies based on different galaxy star formation indicators (UV, optical, FIR, radio) agree that the cosmic star formation history (i.e. the total star formation rate per unit co-moving volume; CSFH hereafter) has declined by an order of magnitude since $z \sim 1$ (for a compilation see e.g. Hopkins 2004). One of the major difficulties of UV/optical based tracers is the significant model-dependent dust-obscuration correction that needs to be imposed on the data. This 'dust-obscuration problem' may be overcome by reaching to longer wavelengths, such as the IR and radio regimes. However, in these cases a multi-wavelength approach is essential as redshift information and a good star forming (SF) galaxy identification is required (Caputi et al. 2007, Smolčić et al. 2007 (Chap. 3); S07 hereafter). In this context the *radio* star formation tracer provides an important complementary view of the CSFH. First, radio emission is a dust-insensitive tracer of recent star formation (i.e. not affected by old stellar populations; see Condon 1992 for a review), and secondly, interferometric radio observations with $1 - 2''$ resolution allow more reliable identifications (compared to FIR/(sub-)mm) with objects detected at other wavelengths.

The dust-unbiased total CSFH has been constrained to a large amount using MIR ($24/8\mu$m) selected samples obtained by deep pencil-beam surveys (CDFS, GEMS, GOODS; Le Floc'h et al. 2005; Zheng et al. 2006; Caputi et al. 2007). Small area surveys, however, are generally affected by cosmic variance. At the high end of the star-forming luminosity function they do not observe a large enough comoving volume in order to fairly sample rare high-luminosity galaxies. In this Letter we focus on the derivation of the CSFH, with emphasis on the evolution of galaxies with high star formation rates ($\gtrsim 100\ M_\odot\ \mathrm{yr}^{-1}$; i.e. ULIRGs), using 1.4 GHz radio observations of the large (2□°) COSMOS field (Schinnerer et al. 2007; Scoville et al. 2007a).

Throughout the paper we report magnitudes in the AB system, use the standard cosmology ($H_0 = 70, \Omega_M = 0.3, \Omega_\Lambda = 0.7$), and define the radio synchrotron spectrum as $F_\nu \propto \nu^{-\alpha}$, assuming $\alpha = 0.7$.

4.2   The 1.4 GHz luminosity function for star forming galaxies in VLA-COSMOS

4.2.1   Star forming galaxy sample

The sample of SF galaxies used here is presented in S07, and briefly summarized below.

The VLA-COSMOS survey of the 2□° COSMOS field contains 2,388 sources detected at 20 cm with S/N $\geq$ 5. Positionally matching these sources to the COSMOS NUV-NIR catalog (Capak et al. 2007) S07 defined a sample of 1,558 radio-optical sources ($i \leq 26$) with the most accurate photometry. The remaining 830 sources consist of radio sources with photometrically flagged ($\sim 30\%$), or without ($\sim 70\%$), optical counterparts with $i \leq 26$.

Using the full COSMOS panchromatic data S07 classified the 1,558 radio – optical

sources into star candidates, QSOs, AGN, SF and high-z galaxies. Special care was given to the separation of SF galaxies from low-luminosity AGN (e.g. Seyfert, LINER and absorption-line AGN) out to $z = 1.3$ by developing a scheme, based on a rest-frame color which separates these two populations with high efficiency (see also Smolčić et al. 2006).

The final sample of selected SF galaxies in the VLA-COSMOS survey out to $z = 1.3$ contains 340 objects, 150 of which have available spectroscopic redshifts, while the remaining sources have reliable photometric redshifts ($\sigma\,(\Delta z/(1+z)) = 0.027$; see S07 and reference therein). Based on Monte Carlo simulations, S07 have shown that the photometric errors in the rest-frame color, used for the selection, introduce a number uncertainty of $\sim 5\%$ in favor of SF galaxies. In this work we use their sample of star forming galaxies, statistically corrected for this effect.

4.2.2 Derivation of the luminosity function (LF)

We derive the LF (Φ) for our SF galaxies in four redshift bins, chosen to sample approximately equal numbers of sources, using the standard $1/V_{\max}$ method (Schmidt 1968). We limit the accessible volumes a) on the bright end by the minimum redshift out to which an object could be observed due to the optical saturation limit of $i^* = 16$ (AB mag; see also Capak et al. 2007), and b) on the faint end by the maximum redshift out to which a galaxy could be observed given the flux limits on both the radio and optical data. In practice, the latter is dominated by the radio detection limits, rather than the optical, as the major fraction of the sources used here has i band magnitudes brighter than ~ 24 (see Fig. 25 in S07). In the computation of $V_{\max}$ we take into account the non-uniform rms noise level in the VLA-COSMOS mosaic. We use the differential visibility area of the VLA-COSMOS mosaic (i.e. fraction of areal coverage, A_i, vs. rms; for the cumulative representation see Fig. 13 in Schinnerer et al. 2007), and for a source with 1.4 GHz luminosity L_j we compute its maximum volume as $V_{\max}(L_j) = \sum_{k=1}^{n} A_k \cdot V_{\max}(z_{\max}^{A_k}, L_j)$.

Several corrections need to be taken into account in order to robustly derive the LF: i) the VLA-COSMOS detection completeness, ii) the fraction of sources not included in the radio-optical sample, and iii) the SF galaxy selection bias due to the rest-frame color uncertainties.

The detection completeness of the VLA-COSMOS survey has been derived by Bondi et al. (2007) via Monte Carlo – artificial source – simulations for the inner 1□°. Comparisons between real and simulated data showed that a power law angular size distribution with an exponent of 0.5 reproduces the data most accurately (see their Tab. 1). Assuming that the corrections hold for the full 2□° we utilize them to correct our LFs for the detection incompleteness of the VLA-COSMOS survey.

To correct for objects that are not contained within our conservatively defined radio-optical sample due to photometrically flagged regions in the optical images, we construct a correction curve as a function of total 1.4 GHz flux density using the inverse of the ratio of sources in the radio-optical sample and *all* sources that have optical counterparts with $i \leq 26$ (see Fig. 27 in S07). Hence, in the ith luminosity bin the comoving space density (Φ_i),

and its corresponding error (σ_i), are computed by weighting the contribution of each galaxy by the two correction factors, f_{det} and f_{flag}, which were obtained by linearly interpolating the two correction curves described above, respectively, at the total flux density of the given, j^{th}, source:

$$\Phi_i = \sum_{j=1}^{N} \frac{f_{det}^j \times f_{flag}^j}{V_{max}^j} \; ; \quad \sigma_i = \sqrt{\sum_{j=1}^{N} \left(\frac{f_{det}^j \times f_{flag}^j}{V_{max}^j} \right)^2} \qquad (4.1)$$

We take into account the selection bias caused by the rest-frame color uncertainties via Monte Carlo simulations. As described in S07 (Sec. 4.2.3.), we iteratively simulate the error distribution of the synthesized rest-frame color, and in each iteration we perform the selection of SF galaxies using the rest-frame color based classification method. This procedure is repeated 300 times, and in each step we derive the LF as described above. In this way we obtain 300 realizations of (Φ_i,σ_i) for each luminosity bin. We take the median values as representative.

4.2.3 The luminosity function

The LFs for our SF galaxies for the 4 chosen redshift bins are shown in Fig. 4.1. In each panel we show the two locally derived 20 cm LFs for SF galaxies given by Sadler et al. (2002b, see also Sec. 4.2.4), and Best et al. (2005). There is a good agreement between the local LFs, and the one derived from the VLA-COSMOS data in the lowest redshift bin (top left panel in Fig. 4.1). Although the 2$\square$° COSMOS field samples a small comoving volume at these redshifts, and a photometric identification of SF galaxies has been used, our LF in the lowest redshift range agrees remarkably well with the local LFs that were derived using all-sky surveys (NVSS) combined with good quality spectroscopic data (SDSS, 2dF) to identify SF galaxies.

At higher redshift we compare our LFs with the total IR LFs derived by Le Floc'h et al. (2005, hereafter LF05) based on a 24 μm selected sample in the CDFS (Chandra Deep Field South; top right and both bottom panels in Fig. 4.1). The total IR luminosity was converted to 1.4 GHz luminosity using the total IR-radio correlation (Bell 2003), which has an intrinsic scatter of ~ 0.26 dex (horizontal error bars in Fig. 4.1). The IR LFs were re-scaled to our redshift ranges either by combining two narrower redshift bins given in LF05 or by scaling a given comoving density using the evolution parameters, and their corresponding errors, given in LF05. The final errors of the IR LFs were obtained via error propagation. There is an excellent agreement between the 1.4 GHz and IR LFs. Note also that the VLA-COSMOS LFs constrain well the high-luminosity end, i.e. the galaxies with high SF rates.

4.2.4 The evolution of star forming galaxies

Sadler et al. (2002b) fitted the local 1.4 GHz radio LF by a double-exponential analytic
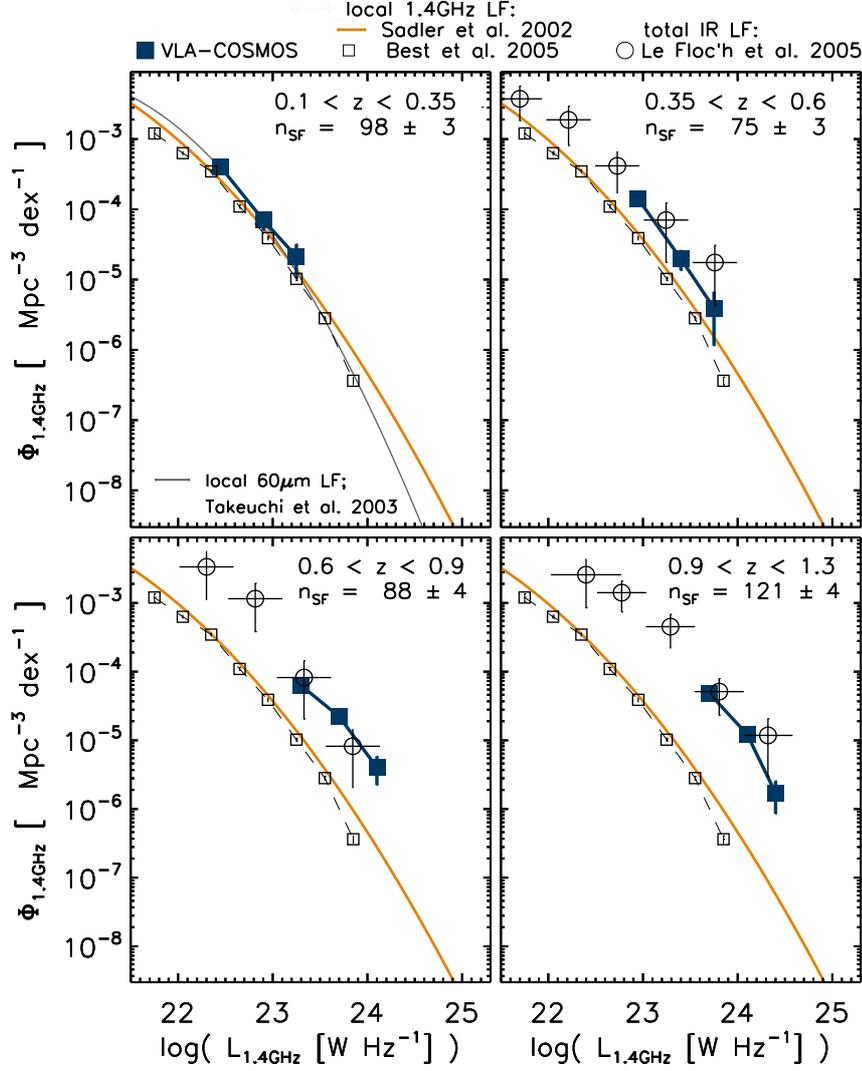
Figure 4.1 1.4 GHz luminosity functions (LFs) for star forming galaxies in the VLA-COSMOS survey, shown for four redshift ranges (filled blue squares), indicated in each panel. The number of galaxies in each redshift bin, statistically corrected for selection uncertainties (see text for details), is also indicated in each panel. The solid (orange) curve and open squares in each panel correspond to the local 20 cm LFs for star forming galaxies derived by Sadler et al. (2002b) and Best et al. (2005), respectively. In the top left panel, the local 60 μm LF is also shown (Takeuchi et al. 2003). In the top right, and bottom panels, we show the IR LFs (LF05) for the corresponding redshift ranges (open circles; see text for details). The total IR luminosity was converted to 1.4 GHz luminosity using the correlation given in Bell (2003). Note the good correspondence between the VLA-COSMOS LFs and the independently derived local and IR LFs.

function:

$$\Phi(L) = C \left[\frac{L}{L_*}\right]^{1-\alpha} \exp\left\{-\frac{1}{2\sigma^2}\left[\log\left(1 + \frac{L}{L_*}\right)\right]^2\right\} \qquad (4.2)$$

with $\alpha = 0.84$, $\sigma = 0.94$, $\Phi^* = 22.9 \times 10^{-3}$ Mpc^{-3}, and $L^* = 1.95 \times 10^{19}$ W Hz^{-1} (scaled to the cosmology used here; see Hopkins 2004). Comparing our derived LFs (see Fig. 4.1)

with the local LF implies strong evolution with look-back time, which is most commonly parameterized with a monotonic evolution of the local LF in both luminosity and density as a function of redshift:

$$\Phi'(L, z) = (1+z)^{\alpha_D} \times \Phi \left[\frac{L}{(1+z)^{\alpha_L}} \right] \tag{4.3}$$

where α_D and α_L are the characteristic density and luminosity evolution parameters, respectively. As the VLA-COSMOS data do not allow the derivation of the LF out to, and fainter than, L_*, at this point we cannot break the well known degeneracy between luminosity and density evolution (e.g. Hopkins 2004; LF05). Therefore, in the further analysis we take only pure luminosity evolution into account ($\alpha_D = 0$).

In Fig. 4.2 we show the luminosity density for our 4 redshift bins. We constrain possible evolution scenarios in two ways. First, in each redshift bin we separately fit pure luminosity evolution to our data (dashed curves in Fig. 4.2). Second, we obtain the *average* pure radio luminosity evolution of the local 1.4 GHz LF by summing the χ^2 distributions obtained for a large range of fixed α_L ($\alpha_D = 0$) in each particular redshift bin. The uncertainty in α_L is then taken to be the 1σ error obtained from the χ^2 statistics. The derived pure radio luminosity evolution of the local 20 cm LF yielded $\alpha_L = 2.0 \pm 0.1$ (see solid curve in Fig. 4.2). Haarsma et al. (2000) have found that a pure luminosity evolution with $\alpha_L \approx 2.74$ is a good representation of the evolution of their SF galaxies. However, no uncertainties were associated with this estimate. Given that their SF galaxy sample contained 37 galaxies out to $z \sim 2.5$ (which corresponds to only $\sim 10\%$ of our sample which reaches to $z = 1.3$), we consider that these two results are in rough agreement.

4.3   The cosmic star formation history (CSFH)

4.3.1   The total cosmic star formation history

We convert the 1.4 GHz radio luminosity to star formation rates (ψ) using the calibration given in Haarsma et al. (2000), based on the Condon (1992) model. After the conversion, we compute the star formation rate density (SFRD) for a given redshift bin as $\int \psi(L) \, \Phi(L, z)' \, dL$, where Φ' is the evolved LF (eq. 4.3), and we integrate over the entire SFRD curve. In Fig. 4.3 we show the CSFH derived using our VLA-COSMOS data fitted for pure luminosity evolution in each redshift bin separately (thick blue symbols). The SFRD uncertainties were derived from the 1σ errors of the best fit luminosity evolution parameter (α_L). It is worth noting that our CSFH uncertainties are significantly smaller compared to previous radio-based results at high redshifts (Haarsma et al. 2000, grey symbols in Fig. 4.3 at $z > 0.2$). The main reason for this is that the radio sample of star forming galaxies used here is almost one order of magnitude larger than the one used previously. In Fig. 4.3 we also show the local 1.4 GHz LF function evolved only in luminosity using the obtained average evolution (red curve; see Sec. 4.2.4). Superimposed are also the CSFH results from previous studies based on a range of SF estimators – UV, optical, FIR, and radio.
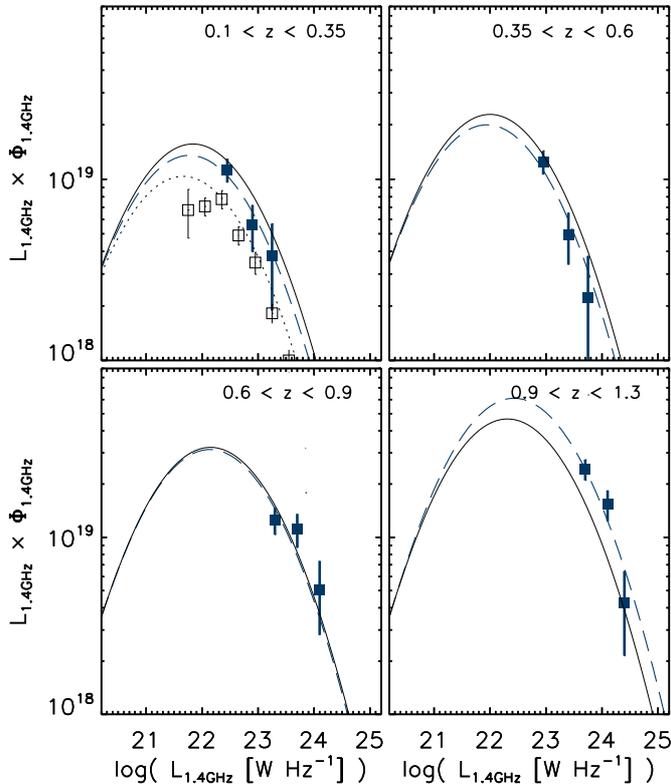
Figure 4.2 Luminosity density for VLA-COSMOS star forming galaxies (filled squares) in 4 redshift bins. The dotted curve and open squares in the top left panel correspond to the local 1.4 GHz data from Sadler et al. (2002b) and Best et al. (2005), respectively. The dashed curve in each panel represents the best fit pure luminosity evolution to the VLA-COSMOS data in each redshift bin separately using the local LF given by Sadler et al. (2002b). The solid curve in each panel shows the most probable pure luminosity evolution obtained by summing the χ^2 distributions obtained in all four redshift bins (see text for details).

A luminosity-dependent obscuration correction was imposed where necessary (see Hopkins 2004, and references therein). Overall, our derived CSFH agrees with the general trend of a rapid decline of almost an order of magnitude in the cosmic star formation rate density since $z \sim 1$. Note that if a different radio luminosity to SFR calibration is used, e.g. Bell (2003), the SFRD would decrease by a factor of ~ 2, however it would still be consistent with results from other studies (corrected for dust-obscuration). Our derived CSFH using the evolved local luminosity function suggests a possibly slower decline of the CSFH than obtained by the least-squares fit to other wavelength-based data at $z < 1$, when these are corrected for luminosity dependent dust-obscuration ($\log \text{SFRD} = 3.29 \log (1 + z) - 1.80$, adopted from Hopkins 2004; see dotted line in Fig. 4.3). However, the CSFH derived by the best fit evolution in our individual redshift bins (thick blue symbols in Fig. 4.3) is consistent with the best least-squares fit.

4.3.2 The CSFH of massively star forming galaxies

The VLA-COSMOS SF sample constrains well the high end of the LF for SF galaxies. Given the $2\square°$ VLA-COSMOS field the comoving volume sampled at $z = 1$ is $\sim 7 \times 10^6$ Mpc^3, corresponding roughly to half the volume observed locally by SDSS (DR1). Thus, for the first time this allows a robust derivation of the CSFH for galaxies forming stars at rates of $\gtrsim 100$ M$_\odot$ yr^{-1} out to $z = 1.3$. Such radio selected galaxies are equivalents to ultra-luminous IR galaxies (ULIRGs, L$_{\text{IR}} > 10^{12}$ L$_\odot$), and it is noteworthy that the VLA-COSMOS survey is sensitive to a *complete* sample of these galaxies out to $z \sim 1$ (see

Fig. 20 in S07).

In order to derive the evolution of the SFRD at the high-luminosity end, we integrate the SFRD curve, obtained from the best fit pure radio luminosity evolution in each particular redshift range (see dashed curves in Fig. 4.2), only for our SF galaxies that have $L_{1.4} \gtrsim 2 \times 10^{23}$ W Hz^{-1}, which corresponds to $L_{IR} > 10^{12}$ L$_\odot$ given the total IR-radio correlation (Bell 2003). For easy comparison between our radio and IR (LF05) results the total IR – radio correlation (Bell 2003) is used which differs by a factor of ~ 2 from Haarsma et al. (2000) used in Sec. 4.3.1. Hence, in this way both the radio and IR derived SFRDs, shown in Fig. 4.4, have been put on the same relative scale. The evolution of our *star forming* ULIRGs is consistent with the lower envelope predicted by LF05, although on average slightly flatter. The larger sample of ULIRGs in the VLA-COSMOS survey (due to the almost a factor of 3 larger field than the CDFS) yields a better constrained high end of the LF using the VLA-COSMOS data. Further, particular care was taken to separate the VLA-COSMOS population into SF and AGN galaxies, while no attempt has been made to minimize the AGN contamination in the IR sample. Within the assumptions made here our results are underpinning the findings of Caputi et al. (2007) and Daddi et al. (2007) on the AGN contamination of MIR samples. Caputi et al. (2007) have found $> 10\%$ of 24 μm-AGN at $z \sim 1$, and a factor of 2 more at $z \sim 2$, implying that the AGN fraction in MIR samples rises with redshift, while Daddi et al. (2007) have demonstrated that, at least at $z \sim 2$, the MIR AGN fraction is a function of stellar mass, and reaches $\sim 50 - 60\%$ for masses $> 4 \times 10^{10}$ $M_\odot$. Our findings are consistent with a lower fraction of massively star forming galaxies in MIR selected samples than often assumed.

4.4   Summary

We have derived the cosmic star formation history out to $z = 1.3$ using to date the largest sample of *radio-selected* star forming galaxies observed at 1.4 GHz (20 cm) in the VLA-COSMOS survey. The almost one order of magnitude increase in the number of radio selected SF galaxies out to high redshift, compared to previous studies (Haarsma et al. 2000), allowed to precisely constrain the evolution of the 1.4 GHz luminosity function for radio-selected *star forming* galaxies, as well as to significantly reduce the uncertainties of the radio-derived CSFH. We find that a pure radio luminosity evolution of VLA-COSMOS star forming galaxies is well described with $L_* \propto (1 + z)^{2.0 \pm 0.1}$. Our overall CSFH agrees well with past findings, when these are corrected for dust-obscuration where needed. This verifies the assumptions about large dust-obscuration corrections required, especially for short-wavelength (e.g. UV) star formation tracers. Making use of our large statistical sample of radio-selected *star forming* ULIRGs complete out to $z \sim 1$ we have robustly constrained the high-end of the SF galaxy LF at different cosmic times. Using these we have derived the CSFH of the most intensely star forming galaxies ($\gtrsim 100$ $M_\odot$ yr^{-1}; i.e. *star forming* ULIRGs) out to $z = 1.3$. We find an, on average, slower evolution of the cosmic star formation rate in star forming ULIRGs than predicted by MIR results (LF05) suggesting that the fraction of star forming galaxies in MIR samples is, likely, becoming
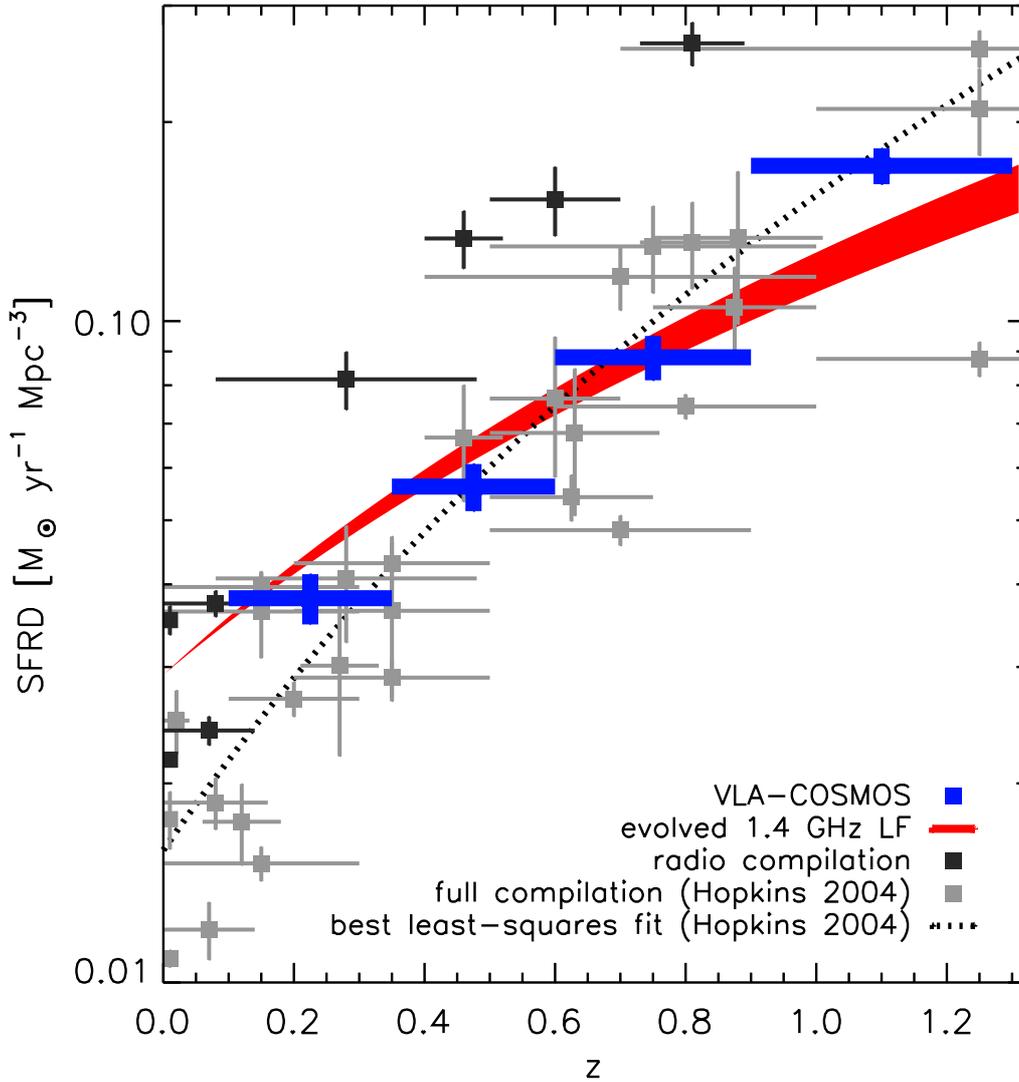
Figure 4.3   Star formation rate density as a function of redshift derived from 1.4 GHz VLA-COSMOS data (thick blue symbols). We also show the cosmic star formation history (CSFH) obtained by evolving the local star forming LF (Sadler et al. 2002b) using our derived average pure luminosity evolution ($\alpha_L = 2.0 \pm 0.1$; red curve). For comparison, the compilation of CSFHs, based on UV, Hα, FIR, and X-ray measurements, presented in Hopkins (2004), is also shown (light-grey squares). All have been corrected for dust-obscuration using luminosity-dependent corrections (see Hopkins 2004 for details). The dotted line is the best least-squares fit to the CSFH points at $z < 1$ obtained by Hopkins (2004); $\log \mathrm{SFRD} = 3.29 \log (1 + z) - 1.80$. Dark-grey symbols denote other radio estimates (Machalski & Godlowski 2000; Condon et al. 2002; Sadler et al. 2002b; Serjeant et al. 2002 for $z < 0.2$; Haarsma et al. 2000 for $z > 0.2$). For all radio data the 1.4 GHz luminosity to star formation rate calibration given in Haarsma et al. (2000) is used, based on the model developed in Condon (1992). Note that such radio-derived CSFHs may be a factor of ~ 2 lower given the calibration uncertainties (see text for details; see also Appendix B.2).

lower with redshift.
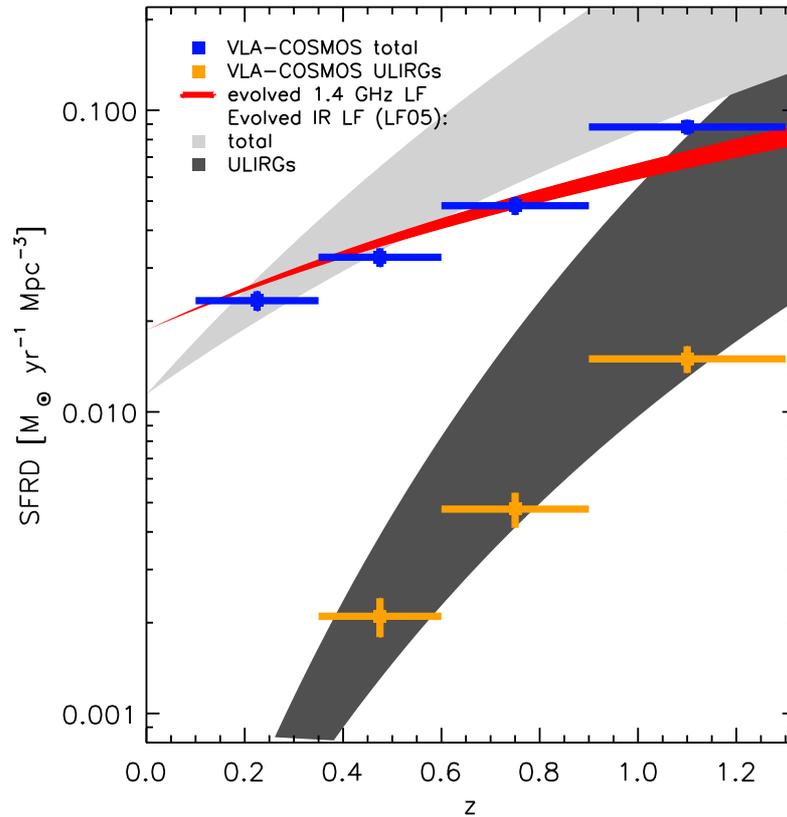
Figure 4.4   Cosmic star formation history derived from VLA-COSMOS data for the overall population (dark-blue symbols, red curve as in Fig. 4.3), and only for the star forming ULIRGs (light-blue symbols). We also indicate the evolved star formation rate density for the entire (light-grey shaded curve), and the ULIRG population (dark-grey shaded curve), derived from the evolved total IR luminosity function (LF05). Note that the IR- and radio-based star formation rates (SFRs) are put here to the same relative scale using the IR luminosity to SFR, and the 1.4 GHz luminosity to SFR, calibrations given in Bell (2003); see text for details.

Chapter 5

A wide angle tail radio galaxy in the COSMOS field: evidence for cluster formation

In this Chapter an in-depth panchromatic study of a peculiar radio galaxy – the wide angle tail radio galaxy CWAT-01, and its complex, merging cluster environment is presented. This work has been published in the COSMOS ApJS special issue as:

V. Smolčić, E. Schinnerer, A. Finoguenov, I. Sakelliou, C. L. Carilli, et al., 2007, ApJS, 172, 295, *A Wide-Angle Tail Radio Galaxy in the COSMOS Field: Evidence for Cluster Formation*
and has been awarded with the Ernst Patzer Award 2006 for best refereed publications by young MPIA scientists.

Abstract

We have identified a complex galaxy cluster system in the COSMOS field via a wide angle tail (WAT) radio galaxy consistent with the idea that WAT galaxies can be used as tracers of clusters. The WAT galaxy, CWAT-01, is coincident with an elliptical galaxy resolved in the HST-ACS image. Using the COSMOS multiwavelength data set, we derive the radio properties of CWAT-01 and use the optical and X-ray data to investigate its host environment. The cluster hosting CWAT-01 is part of a larger assembly consisting of a minimum of four X-ray luminous clusters within ~ 2 Mpc distance. We apply hydrodynamical models that combine ram pressure and buoyancy forces on CWAT-01. These models explain the shape of the radio jets only if the galaxy's velocity relative to the intra-cluster medium (ICM) is in the range of about $300 - 550$ km s^{-1} which is higher than expected for brightest cluster galaxies (BCGs) in relaxed systems. This indicates that the CWAT-01 host cluster is not relaxed, but is possibly dynamically young. We argue that such a velocity could have been induced through subcluster merger within the CWAT-01 parent cluster and/or cluster-cluster interactions. Our results strongly indicate that we are witnessing the formation of a large cluster from an assembly of multiple clusters, consistent with the

hierarchical scenario of structure formation. We estimate the total mass of the final cluster to be approximately 20% of the mass of the Coma cluster.

5.1   Introduction

Wide-angle tail (WAT) galaxies form a class of radio galaxies, usually found in clusters, whose radio jets have been bent into a wide **C** shape. The general morphology of WATs suggests that the sources interact significantly with their external environment. The most natural interpretation of the jet bending is that the jets are being swept back by ram pressure resulting from the high velocity motion of the associated active elliptical galaxy through its surrounding intra-cluster medium (ICM), first developed by Begelman, Rees, & Blandford (1979) and applied by a number of investigators (e.g. Burns 1981; Pinkney et al. 1994). In addition to ram-pressure, buoyancy forces were introduced to explain the bending of the jets (e.g. Gull & Northover 1973; Sakelliou et al. 1996). If the jet density is lower than the density of the surrounding medium, buoyancy forces will drag the jets towards regions of the ICM where the densities are equal.

A point first noticed by Burns (1981) was that WATs are usually associated with brightest cluster galaxies (BCG; D or cD galaxies), which are expected to reside at rest at the bottom of the clusters' gravitational potential well (Quintana & Lawrie 1982; Merritt 1984; Bird 1994). Thus the large velocities of the WAT host galaxies relative to the ICM needed for the ram pressure models to shape the jets seemed to be inconsistent with velocities typical for BCGs.[1] Therefore, it was necessary to evoke alternative scenarios to explain the bent shape of WAT galaxies (e.g. Eilek 1979). However, the most prominent explanation is that the jets are bent by ram pressure. It has been suggested in numerous studies that the necessary ram pressure may be provided during cluster mergers (e.g. Pinkney et al. 1994; Loken et al. 1995; Gomez et al. 1997; Sakelliou et al. 1996; Sakelliou & Merrifield 2000). This merger scenario is consistent with cosmological models, such as the cold dark matter model (CDM), which propose that the structure in the Universe is formed hierarchically with large features forming from mergers of smaller groups. The cluster potential well deepens then through accretion of poor clusters, dark matter and gas into more massive systems. The material is accreted from supercluster filaments which connect clusters into the large-scale structure of the Universe (Evrard 1990; Jing et al. 1995; Frenk et al. 1996; Burns et al. 2002).

Based on ROSAT PSPC X-ray observations of a sample of 9 Abell clusters containing WAT galaxies, Gomez et al. (1997) find evidence for statistically significant X-ray substructure in 90% (8 out of 9) of the clusters hosting WATs, as well as a strong correlation of the orientation of the jets and the direction of X-ray elongation within the core of the cluster. Combined with numerical hydro/N-body simulations their results are consistent with WAT

---

[1]Malumuth et al. (1992) have shown that the velocity dispersion of the cD population is 0.3 of the dispersion of the cluster population; Beers et al. (1995) have found a velocity difference between the peculiar velocity of the central galaxy and the mean of the rest of the cluster galaxies $\lesssim 150$ km s^{-1}; recently Oegerle & Hill (2001) , analyzing 25 Abell clusters, showed that peculiar velocities of cD galaxies differ only by ~ 160 km s^{-1} from the mean cluster velocities.

clusters undergoing mergers with groups or subclusters of galaxies. Sakelliou & Merrifield (2000) show that WATs are not generally located at the centers of their host clusters as defined by their X-ray emission. They also find that the orientation of the bent jets is found to be preferentially pointed directly towards or away from the cluster center. Thus, if the morphology is due to ram pressure, WATs are then primarily on radial orbits through the cluster. These results are explained as a natural consequence of cluster mergers creating WAT galaxies (for details see Sakelliou & Merrifield 2000 and references therein). Blanton et al. (2001) present optical imaging and spectroscopic observations of environments surrounding 10 bent radio sources. They find that the clusters display a range of line-of-sight velocity dispersions, $\sigma_{||}$, from about $300 - 1100$ km s^{-1}. The upper limit of $\sigma_{||}$ suggests that the host clusters are either massive clusters and/or merging systems with significant substructure.

Since WATs are usually found in cluster environments, they can be used as an efficient tool for cluster search, especially for high-redshift clusters where we are biased by the dimming of galaxies in the optical and the ICM in X-ray emission. This approach has been successfully tested by Blanton et al. (2000, 2001, 2003) using the VLA FIRST survey (Faint Images of the Radio Sky at Twenty centimeters survey; Becker, White, & Helfand 1995) to search for galaxy clusters via WAT galaxies. The highest redshift cluster they have identified to date is at $z = 0.96$ Blanton et al. (2003).

In this paper we discuss the properties of a WAT radio galaxy (hereafter CWAT-01) found in the VLA-COSMOS 2□° survey, previously detected, but not resolved by the NVSS (NRAO VLA Sky Survey; Condon et al. 1998) survey and not detected in the VLA FIRST survey (Becker, White, & Helfand 1995). The multiwavelength data set of the COSMOS survey (Scoville et al. 2007a) enables us to use the radio data to derive the properties of this radio galaxy and the optical/X-ray data to investigate its host environment. In Sec. 5.2 we present the data utilized here. Sec. 5.3 describes the radio and optical properties of CWAT-01. In Sec. 5.4 we introduce the cluster and independently analyze its properties in the X-ray and the optical. We discuss the results in Sec. 5.5 and summarize them in Sec. 5.6.

For calculations in this paper, we assume $H_0 = 70, \Omega_M = 0.3, \Omega_\Lambda = 0.7$. We define the synchrotron spectrum as $F_\nu \propto \nu^{-\alpha}$, with a positive spectral index, $\alpha > 0$, throughout the paper.

5.2 Observations and data reduction

5.2.1 Radio data

The 2□° COSMOS field was observed at 1.4 GHz with the NRAO Very Large Array (VLA) in A- and C- configuration for a total time of 275 hours (VLA-COSMOS survey; Schinnerer et al. 2007, Chap. 2). The final 2□° map has a typical rms of 10.5 (15) μJy/beam in the inner 1 (2) □° with a resolution of $1.5'' \times 1.4''$, thus making it the largest contiguous area covered in the radio-wavelengths regime with such a high sensitivity. The VLA-

COSMOS large project catalog (presented in Schinnerer et al. 2007, Chap. 2) contains ~ 3600 radio sources, ~ 90 of which are clearly extended (most of them are double-lobed radio galaxies). The sensitivity of the survey combined with the high resolution and the large area coverage makes the VLA-COSMOS project extremely valuable for e.g. studies of the sub-mJy radio population (i.e. the faint end of the radio luminosity function), dust-obscured star-formation history of the universe, evolution of radio-loud active-galactic nuclei (AGN). The survey utilized the standard VLA L-band continuum frequencies and the multi-channel continuum mode. The complete data reduction was performed using the standard VLA software AIPS. The A- and C-array data were combined in the uv plane and then imaged using the task IMAGR. Cleaning boxes around bright sources were defined manually, the two intermediate frequencies (IFs) and the left and right polarization were imaged separately and then combined into the final map. For more information about the survey and its scientific objectives see Schinnerer et al. (2007, Chap. 2). The local rms noise in the mosaic around CWAT-01 is ~ 10.5 μJy/beam.

Subsequent observations of CWAT-01 were obtained in June 2005 with the VLA in CnB configuration at 4.8 GHz. The standard C-band continuum frequencies were used and the observations were performed in the standard continuum mode. The CWAT-01 field was observed for 40 minutes on-source. After flux and phase calibration the data set was imaged using the AIPS task IMAGR. The IFs and the left and right polarization were imaged together. Clean boxes were defined manually, the number of CLEAN iterations in IMAGR was set to 3000 and the flux cut-off to 60 μJy. The uv data points were weighted using the natural weighting function ($UVWTFN$ was set to 'N'). Due to the asymmetric uv coverage the resolution of the 4.8 GHz map was tapered down to obtain a rounder beam (the UVTAPER option in IMAGR was set to 35 kλ). The resolution and rms noise in the tapered map are $7.27'' \times 5.53''$ and ~ 40 μJy/beam, respectively.

5.2.2   X-ray data

The COSMOS 2$\square^\circ$ field is being observed by the *XMM-Newton* satellite (Jansen et al. 2001) for an awarded time of 1.4 Msec (Hasinger et al. 2007). The data collected to date amount to 0.8 Msec over the 2$\square^\circ$ area with an effective depth of ~ 40 ksec, taking vignetting into account. In this study we utilize some of the results of Finoguenov et al. (2007) who identify clusters in the COSMOS field via diffuse X-ray emission. The flux limit for the cluster identification in the $0.5 - 2$ keV energy band is 2×10^{-15} erg cm^{-2} s^{-1}. Finoguenov et al. (2007) report four diffuse structures within $4'$ of CWAT-01, one of them containing CWAT-01.We perform the spectral analysis of the extended emission associated with the four identified clusters in the following way. The EPIC pn observations of the COSMOS field have been merged together and a uniform cleaning criterion for background flares has been subsequently applied. Observations that do not satisfy this criterion are removed. In this way we achieve a uniform background level for the clean dataset. The resulting file consists of a total of 365 ksec homogeneously cleaned data (for the whole 2$\square^\circ$ field). However, the region around CWAT-01 is still covered at an effective depth of 43 ksec as the removed observations are all located at the edge of the COSMOS field.

Since the instrumental background is not uniform over the detector, in order to estimate the background, we produce a background file from the same merged event file by excluding the area containing a detected X-ray source. This removes $\sim 20\%$ of the area, which we account for in correcting for the background. The background is further assumed to be the same in detector coordinates. In calculating the background spectrum, the sky position of the cluster is mapped to the detector, taking into account multiple pointings, which map the same region of the sky on different detector areas. The background spectrum is collected weighting accordingly the contribution in each detector pixel. For the clusters in this study the ratio of the background to signal accumulation times is 5, which is sufficient to reduce the statistical uncertainty associated with the background subtraction. The calculation of auxiliary response files is performed by the SAS-based task *clarf* of Finoguenov et al. (2004), which takes the mosaicing into account. The pn calibrations involved in the data reduction correspond to SAS (Science Analysis Software; Watson et al. 2001) version 6.5.

5.2.3 Optical data

The optical imaging data of the 2□° COSMOS field, we use in this paper, was obtained in Spring 2004 and 2005. Within the COSMOS HST Treasury project the 2□° field was imaged in 590 orbits during Cycles 12 and 13 using the Advanced Camera for Surveys (ACS; Scoville et al. 2007c). The F814W band imaging has a $0.07''$ resolution and a 10σ sensitivity of $I_{AB} = 27.2$. Each of the 590 fields consists of 4 exposures, which are calibrated and combined into a single image for each field using the *MultiDrizzle* software (for details see Koekemoer et al. 2007) The whole COSMOS field was imaged with the Suprime-Cam camera (SUBARU telescope) in 6 broad band filters, B_J, V_J, g^+, r^+, i^+, z^+ with 5σ sensitivity in AB magnitudes of 27.3, 26.6, 27.0, 26.8, 26.2, 25.2, respectively (Taniguchi et al. 2007; Capak et al. 2007). u^* and i^* band images of the whole 2□² COSMOS field were obtained with the CFHT (Canada France Hawaii Telescope). The 5σ sensitivity in AB magnitudes is 26.4 and 24.0 for u^* and i^*, respectively.

The COSMOS photometric catalog was constructed using the SUBARU i^+ band image. The details on constructing the photometric redshift catalog are described in Mobasher et al. (2007). The catalog produces photometric redshifts accurate to $dz/(1 + z) = 0.034$. We utilize these redshifts to study the optical (sub)structure of the clusters in latter sections.

5.2.4 Redshift

Trump et al. (2007) present spectroscopic redshifts of the first $\sim$500 X-ray and radio selected targets in the 2□° COSMOS field. The spectra were obtained using the Magellan IMACS instrument. They also perform a robust classification of the observed objects (for details see Trump et al. 2007 and references therein). In the cluster area around CWAT-01 (see Sec. 5.4.2) there are two galaxies that have IMACS spectra. Their properties, classification and redshifts are reported in Tab. 5.1.

Searching for high resolution ($R = 1800$) Sloan Digital Sky Survey (SDSS, York et al. 2000; Abazajian et al. 2003, 2004, 2005; Adelman-McCarthy et al. 2006) spectra, we find

Table 5.1 IMACS spectra in cluster assembly region.

name	RA	DEC	type	$z_{spec} \pm \Delta z_{spec}$
COSMOS J100021.81+022328.5*	10 00 21.816	+02 23 28.523	elliptical	0.22067 ± 0.00007
COSMOS J100025.30+022522.5	10 00 25.298	+02 25 22.476	elliptical	0.22090 ± 0.00013

*Corresponds to SDSS J100021.81+022328.46 (see Tab. 5.2)
Specifications of galaxies within the cluster area that have IMACS spectra (for details see Trump et al. 2007). The last column specifies the spectroscopic redshift and error.

Table 5.2 SDSS spectra in cluster assembly region.

name	plate	fiber	RA	DEC	$z_{spec} \pm \Delta z_{spec}$
SDSS J10004.35+022550.71	501	348	10 00 4.354	+02 25 50.711	0.2201 ± 0.0001
SDSS J10006.65+022225.98	501	353	10 00 6.654	+02 22 25.982	0.2221 ± 0.0002
SDSS J100021.81+022328.46*	501	388	10 00 21.815	+02 23 28.463	0.2206 ± 0.0001

*Corresponds to COSMOS J100021.81+022328.5 (see Tab. 5.1)
SDSS specifications of galaxies within the cluster area that have SDSS spectra. The last column specifies the spectroscopic redshift and error.

that 3 galaxies in our cluster area around CWAT-01 have SDSS spectra. One of them was observed with IMACS. The specifications of these galaxies are listed in Table 5.2. It is worth noting that the galaxies with spectroscopic redshifts are the most prominent galaxies within each cluster (see Sec. 5.4).

The mean spectroscopic redshift of the galaxies presented above is 0.2209 with an accuracy of 2.8×10^{-4}. Given the dispersion of the *photometric* redshift values they are compatible with a redshift of $z = 0.22$. Therefore, for the scope of this paper we adopt a mean cluster redshift of $z = 0.22$, based on four measured *spectroscopic* redshifts.

5.3   The wide angle tail galaxy: CWAT-01

The radio galaxy first resolved in the VLA-COSMOS survey, CWAT-01, has a morphology typical for wide angle tail (WAT) galaxies. Its radio jets are bent into a wide **C** shape (see Fig. 5.1 for example). In Sec. 5.3.1 we describe the structure of CWAT-01 and derive its radio properties in order to investigate the correlation to its host environment in latter sections. In Sec. 5.3.2 we describe the optical properties of the CWAT-01 host galaxy.

5.3.1   Radio properties of CWAT-01

The structure of CWAT-01

The radio galaxy discussed here was first detected in the NVSS survey (NVSS J100027+022104; Condon et al. 1998), but not resolved due to the low resolution of the NVSS (45"). It was first resolved in the 1.4 GHz mosaic of the central 1□° field from the VLA-COSMOS pilot project (Schinnerer et al. 2004). CWAT-01 was not detected in the FIRST survey as this survey over-resolves radio sources larger than $\sim 10''$ (and thus underestimates their fluxes; see Becker et al. 1995 for details). Hence, a galaxy like CWAT-01, which extends over more

than $1'$ on the plane of the sky and has a total flux density of ~ 13 mJy (see below), would be strongly resolved out in the FIRST survey, i.e. the galaxy would consist of multiple components and the flux from the extended regions ($\gtrsim 10''$) of each component would be missed. The individual parts of CWAT-01 that could have been detected by FIRST have flux densities below the detection limit of the FIRST survey (1 mJy). Thus, CWAT-01 or any fraction of the galaxy stays undetected in the FIRST survey.
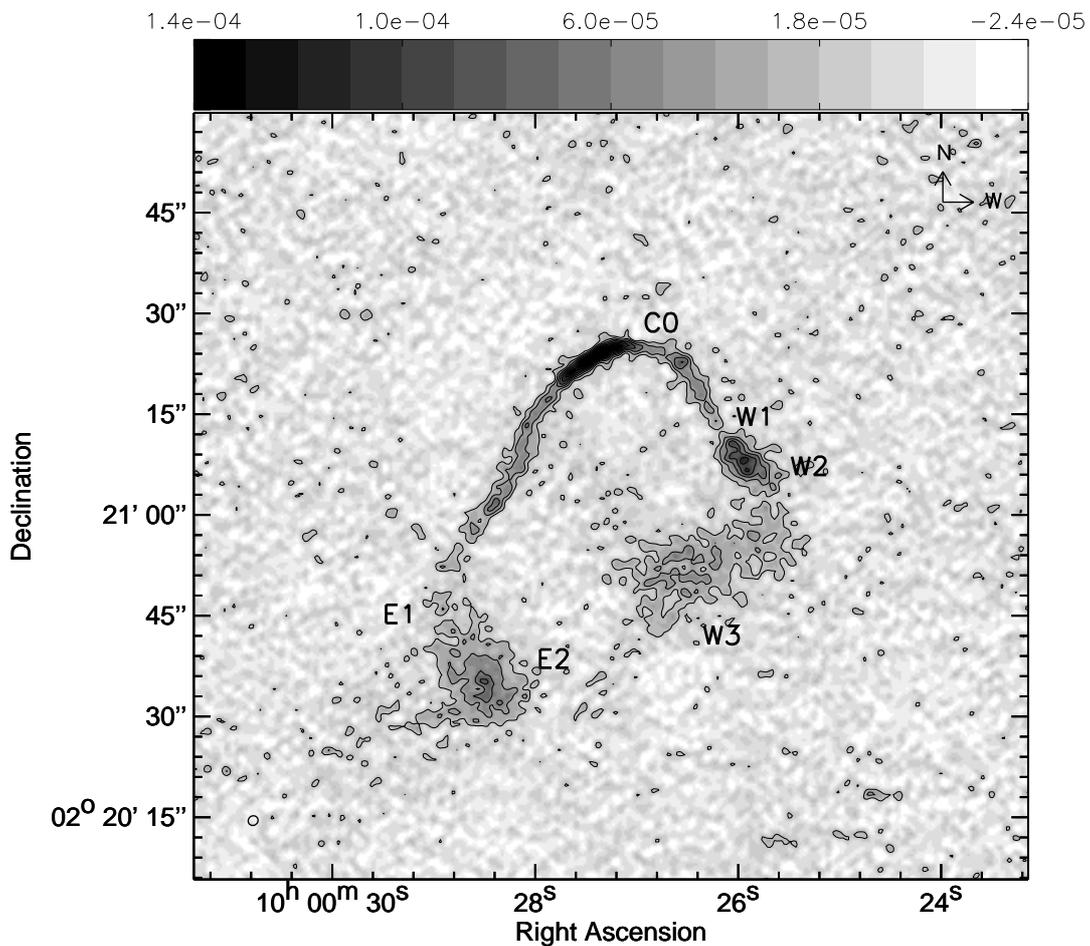
Figure 5.1 1.4 GHz radio map of the wide angle tail galaxy CWAT-01 in the COSMOS field in grey scale with contours overlaid. The contour levels are in steps of 2σ starting at the 2σ level ($1\sigma = 10.5\,\mu$Jy/beam). The clean beam is shown in the lower left corner (the resolution is $1.5'' \times 1.4''$). $C0$, $E1-2$ and $W1-3$ label features of the jets discussed in the text. The colorbar units are in Jy/beam.

Our new VLA-COSMOS observations, as part of the VLA-COSMOS large project (Schinnerer et al. 2007, Chap. 2), at 1.4 GHz provided significantly better data of this extended radio galaxy. The new 1.4 GHz VLA-COSMOS map of CWAT-01 is shown in Fig. 5.1 (the resolution is $1.5'' \times 1.4''$). The radio jets of the galaxy are curved in a **C** shape typical for WAT galaxies. The central radio peak of CWAT-01 is at $\alpha = 10\ 00\ 27.35$ and $\delta = +02\ 21\ 24.15$ (J2000) and its host galaxy is an elliptical galaxy with a photometric redshift of $z = 0.2 \pm 0.03$. The photometric redshift was taken from the COSMOS photometric

redshift catalog described in detail in Mobasher et al. (2007). The quoted error is the 1σ error obtained from the 95% confidence interval. The optical counterpart is discussed in more detail in Sec. 5.3.2. The jets are barely resolved in width (i.e. perpendicular to the jet axis) out to points E1 and W1 (see Fig. 5.1). The Eastern radio jet can be traced out to a projected distance of $\sim 1'$ (~ 210 kpc) from the central galaxy. At point E1 it bends to the west (in the projected plane), and broadens. The end of the jet is marked with E2 (see Fig. 5.1). The structure of the Western jet is more complex: It extends to a distance of $\sim 45''$ (~ 160 kpc) in the plane of the sky. From the core till W1 it is narrow, but indicates curvature in the northern part. After W1 the jet broadens and bends slightly to the west in the projected plane (W2). The faint feature labeled as W3 in Fig. 5.1 seems also to be part of CWAT-01. The integrated flux density of CWAT-01 at 1.4 GHz is 12.69 mJy. This is within the errors of the reported NVSS flux density of 13.5 ± 1.9 mJy. For consistency we will use the flux density derived from the VLA-COSMOS for calculations throughout the paper.

The bending angle of the jets, which we define as the angle between lines parallel to the part of the jet closest to the core (see Fig. 5.11, bottom panel), is $\sim 100°$. The asymmetry of the jets may be due to projection effects which would indicate that the whole structure is not moving only in the plane of the sky. However, with the data in hand we cannot reach any firm conclusions about projection effects nor rule them out. More radio bands and higher resolution radio data where relativistic core beaming effects could be explored might resolve this issue; i.e. on ~ 10 kpc scales from the radio core of the galaxy (where the bulk motion of the particles is relativistic) relativistic effects yield that the ratio of the radio brightness of the two jets can be correlated with the orientation angle.

Spectral index

The 4.8 GHz map at $7.27'' \times 5.53''$ resolution is shown in Fig. 5.2. The main features seen in the 1.4 GHz map (with a resolution of $1.5'' \times 1.4''$; Fig. 5.1) are still apparent although the much lower resolution reduces the amount of details. The total integrated flux at 4.8 GHz is 4.1 mJy. To obtain the spectral index map (shown in Fig. 5.3), the 1.4 GHz image was convolved to the resolution of the 4.8 GHz map and the two images were regridded to the same pixel scale. Pixels with values below 3σ in each map were blanked. The middle of the central feature is a flat spectrum region ($0.1 \lesssim \alpha \lesssim 0.3$), with the spectral index steepening to $\alpha \sim 1$ to the north-west edge in this feature. The outer region (corresponding to E1) with a flat spectrum ($0.2 \lesssim \alpha \lesssim 0.6$) suggests possible re-acceleration regions. The spectral index steepens to $\alpha \sim 1$ at E2. In W2 the spectrum emission is on average steeper than in the E1 feature, with an average spectral index corresponding to $\alpha \sim 0.7$. The mean spectral index in the total source is $\alpha = 0.6$ which we will use for calculations throughout this paper, unless mentioned otherwise.
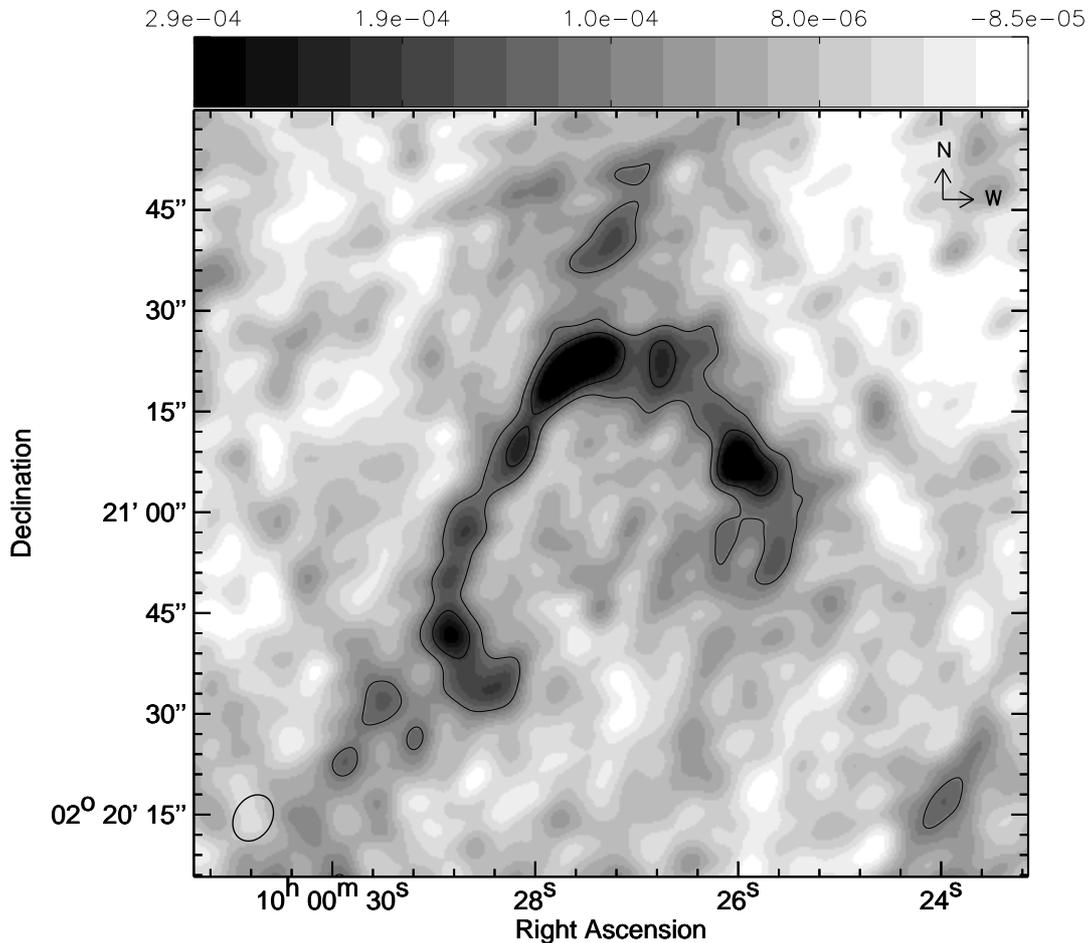
Figure 5.2   4.8 GHz radio map of CWAT-01 with contours overlaid. The contour levels are in steps of 2σ starting at the 3σ level ($1\sigma = 40\,\mu$Jy/beam). The clean beam is shown in the lower left corner (the resolution is $7.27'' \times 5.53''$). The colorbar units are in Jy/beam.

Radio power and luminosity

We compute the radio power of CWAT-01 at 1.4 GHz using a spectral index of $\alpha = 0.6$ (see Sec. 5.3.1) and the luminosity distance (1.1 Gpc) at $z = 0.22$. The radio power of CWAT-01 is then $P_{1.4} = 2.0 \times 10^{24}$ W Hz^{-1} which places the radio galaxy between FRIs and FRIIs where WATs are normally found (Hardcastle & Sakelliou 2004).

We also calculate the *total* radio luminosity, given by (e.g. O'Dea & Owen 1987):

$$L_{\text{tot}} = 1.2 \times 10^{27} D_{L,[\text{Mpc}]}^2 F_0 \nu_0^\alpha (1+z)^{-(1-\alpha)} \times$$
$$(1-\alpha)^{-1}(\nu_2^{1-\alpha} - \nu_1^{1-\alpha}) \; [\text{erg s}^{-1}] \tag{5.1}$$

where $D_{L,[\text{Mpc}]}$ is the luminosity distance expressed in Mpc and F_0 the flux density, at a fiducial frequency ν_0, expressed in Jy. We take the lower and upper frequencies to be $\nu_1 = 10$ MHz and $\nu_2 = 100$ GHz, respectively. The observed frequency is $\nu_0 = 1.4$ GHz.
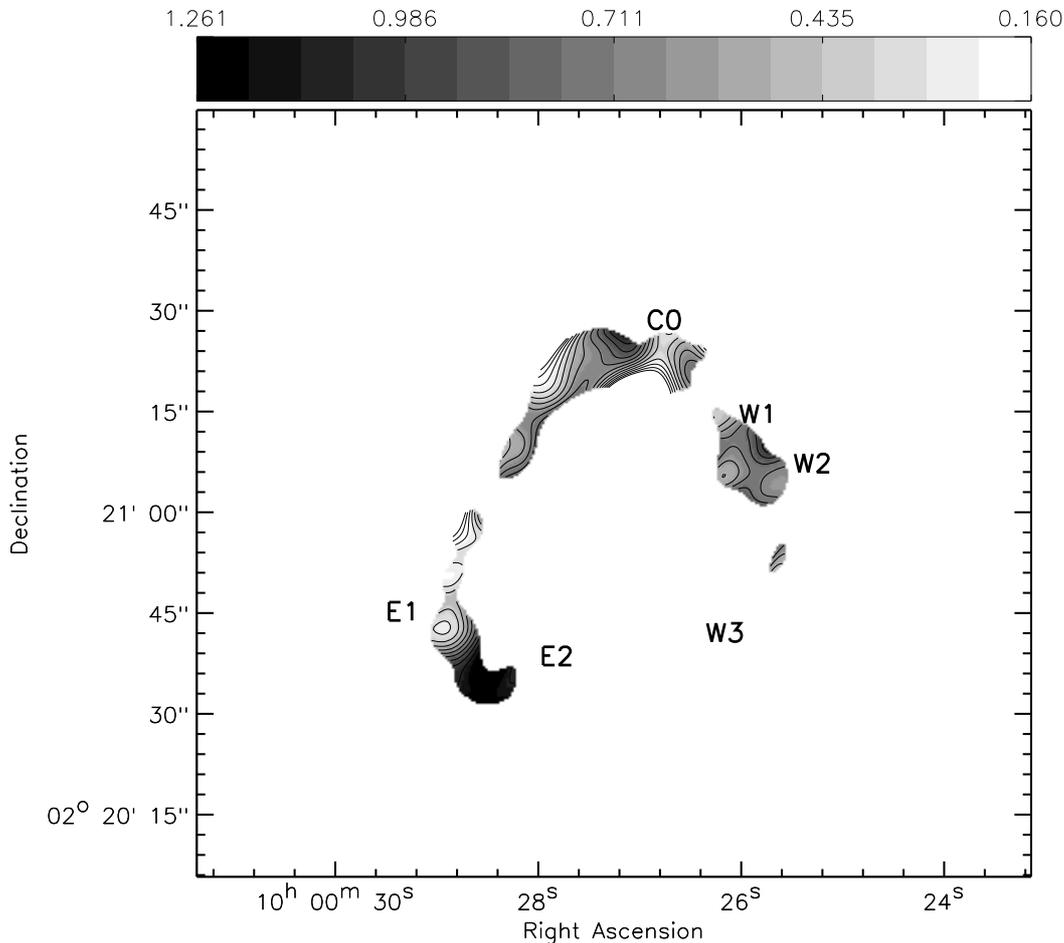
Figure 5.3 Spectral index map of CWAT-01 for pixels with values $> 3\sigma$ in both maps (1.4 GHz and 4.8 GHz). C0, E1-2, W1-3 are labeled as in Fig. 5.1 and are presented here for clarity. We define the spectral index as $F_\nu \propto \nu^{-\alpha}$ throughout the paper. The contour levels are 0.1, 0.2, 0.3 etc.

The total luminosity of CWAT-01 is then $L_{tot} = 3.2 \times 10^{41}$ erg s^{-1}, typical for peculiar radio galaxies (Pacholczyk 1970).

Magnetic field and minimum pressure

Assuming that the total energy in a radio galaxy is the sum of the energy of electrons, E_e, heavy particles, E_p, and the magnetic field, E_B, $E_{tot} = E_e + E_p + E_B$, we can estimate the minimum energy density, u_{me}, and the corresponding magnetic field, B_{me}, using the minimum energy condition which corresponds almost to equipartition between the relativistic particles and the magnetic field.[2] We adopt the expression from Miley (1980, for details

---

[2]Equipartition requires that the magnetic energy is equal to the total particle energy, i.e. $E_B = E_e + E_p$, while the minimum energy condition holds for $E_B = \frac{3}{4}(E_e + E_p)$. Hence, the computed total energy, $E_{tot} = E_e + E_p + E_B$, agrees within $\sim 10\%$ for the first and latter.

see Pacholczyk 1970):

$$u_{me} = \frac{7}{3} \frac{B_{me}^2}{8\pi} \ [\text{dyn cm}^{-2}] \tag{5.2}$$

$$B_{me} = 5.69 \times 10^{-5} \left[\frac{1+k}{\eta} (1+z)^{3+\alpha} \times \right.$$

$$\left. \frac{1}{\Theta_x \Theta_y l \sin^{3/2} \Phi} \cdot \frac{F_0}{\nu_0^\alpha} \frac{\nu_2^{1/2-\alpha} - \nu_1^{1/2-\alpha}}{\frac{1}{2} - \alpha} \right]^{2/7} \ [\text{G}] \tag{5.3}$$

where k is the ratio of relativistic proton to relativistic electron energies, η is the filling factor of the emitting region, z is the redshift, Θ_x and Θ_y correspond to the clean beam widths, l is the pathlength through the source along the line of sight, Φ is the angle between the uniform magnetic field and the line of sight, F_0 is the flux density at a fiducial frequency ν_0, ν_1 and ν_2 are the lower and upper frequency cutoffs and α is the spectral index. The minimum energy density and the corresponding magnetic field were measured in the middle of the diffuse portion of the Eastern radio jet in the 1.4 GHz map with the following assumptions: a) the radio plasma fills the volume completely ($\eta = 1$), b) the magnetic field is transverse to the line of sight ($\sin \Phi = 1$), c) the relativistic proton energy equals the relativistic electron energy ($k = 1$), d) there is cylindrical symmetry, and e) the radio spectrum spans from 10 MHz to 100 GHz. The mean spectral index derived from the spectral index map in this part of the jet corresponds to $\alpha = 0.65$. The resulting magnetic field is $B_{me} = 3.7 \ \mu$G and the minimum energy density is $u_{me} = 1.3 \times 10^{-12}$ dyn cm^{-2}. The minimum internal pressure within the jets is then $P_{min} = u_{me}/3 = 4.3 \times 10^{-13}$ dyn cm^{-2}.

The particle lifetime

The synchrotron age of the electrons at frequency ν is given by van der Laan & Perola (1969) assuming the following model: The electrons age as a result of synchrotron and inverse Compton losses due to the interaction with the cosmic microwave background (CMB). There is a brief "generation phase", during which the relativistic gas is presumably created by the active galaxy, and a long-term "remnant phase" during which the particle supply is switched off. The model computes the lifetime of the "remnant phase" as it assumes that the lifetime of the "generation phase" is much shorter:

$$t \sim 2.6 \times 10^4 \frac{B^{1/2}}{(B^2 + B_R^2)[(1+z)\nu]^{1/2}} \ [yr] \tag{5.4}$$

where B is the magnetic field in the jet and B_R is the equivalent magnetic field of the CMB radiation, $B_R = 4[1 + z]^4 \ \mu$G. In order to constrain the electron lifetime, we substitute into eq. [5.4] the magnetic field corresponding to the minimum energy condition, $B = B_{me}$, calculated for the region at the end of the radio jets at 1.4 GHz (E2 and W2 in Fig. 5.1). The magnetic field B_{me} is again derived making the same assumptions as in Sec. 5.3.1. The mean spectral index at the end of the Eastern and Western jet corresponds

to 0.9 and 0.7, respectively, and the minimum-energy magnetic fields are then $3.5\,\mu$G and $3.1\,\mu$G, respectively. Both values give the lifetime of an electron radiating at 1.4 GHz of ~ 13 Myr. Therefore, if we assume that there is no particle re-acceleration within the jets, the relativistic electrons created in or near the core could travel the whole jet length within their lifetime with bulk velocities in the range of about $(0.04 - 0.05)c$.
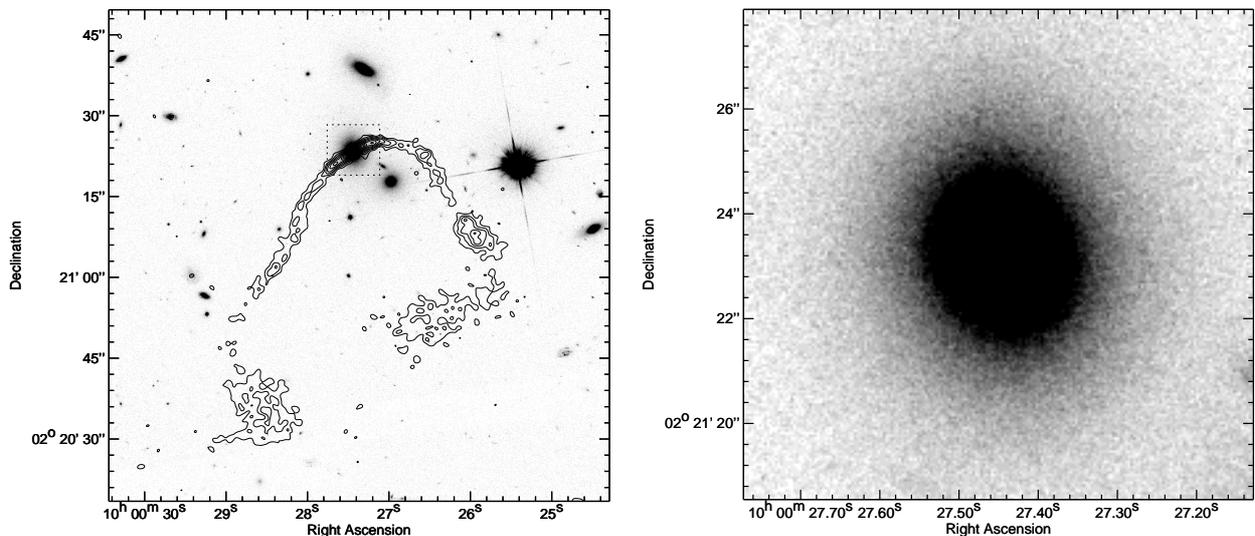
Figure 5.4 Top panel: HST-ACS FW814 band (grey scale) image of the CWAT-01 host galaxy with 1.4 GHz radio contours overlaid. The contour levels are in steps of 2σ starting at the 3σ level ($1\sigma = 10.5\,\mu$Jy/beam). The dashed box indicates the region shown in the bottom panel. Bottom panel: HST-ACS FW814 band image of the CWAT-01 host galaxy. The galaxy has a morphology of an elliptical galaxy.

5.3.2   The host galaxy

CWAT-01 is coincident with an elliptical galaxy, shown in Fig. 5.4, located at $\alpha = 10\,00\,27.43$ and $\delta = +02\,21\,23.62$ (J2000). The spectral energy distribution (SED) type, reported in the COSMOS photometric redshift catalog (Mobasher et al. 2007; Capak et al. 2007) is 1.33 (ellipticals and Sa/Sb correspond to 1 and 2, respectively; see Coleman et al. 1980; Kinney et al. 1996). The photometric redshift of the galaxy is $z = 0.2 \pm 0.03$ (the quoted error is the $1\,\sigma$ error obtained from the 95% confidence interval). We construct the surface brightness profile of the host galaxy (shown in Fig. 5.5) using the GIPSY ellipse fitting task ELLFIT on the background-subtracted HST-ACS F814W band image (Koekemoer et al. 2007). The surface brightness follows the $r^{1/4}$ law fairly well, but it deviates from it in the outer parts, indicating an excess in surface brightness, possibly an extended halo (see dashed line in Fig. 5.5). The early type morphology, the extensive envelope and the shallower surface brightness profile compared to the $r^{1/4}$ law suggest that the CWAT-01

host galaxy might be classified as a D type galaxy (e.g. Beers & Geller 1983). To obtain a better fit to the surface brightness, we fit the Sersic model $I(r) = I_{\mathrm{eff}} e^{b_n[1-(r/r_{\mathrm{eff}})^{1/n}]}$, $b_n \sim 2n - 0.324$, (Sersic 1968) to the data with effective radius, r_{eff}, effective intensity, I_{eff}, and Sersic index, n, as free parameters (solid line in Fig. 5.5). The data is very well fit by the Sersic law with $n = 5.0$, $r_{\mathrm{eff}} = 8.2$ kpc and an effective surface brightness of $\mu_{\mathrm{eff}} = -2.5 \log I_{\mathrm{eff}} - 48.6 = 22.1$ mag arcsec^{-2}. It has already been noted by Schombert (1987) that intrinsically bright ellipticals are flatter (i.e. have higher values of n) and that intrinsically faint ellipticals have more curvature (i.e. lower values of n) than predicted by the $r^{1/4}$ law. Typical values of n for brightest cluster galaxies (BCGs) are $n > 4$ (Graham et al. 1996). The effective radius and the Sersic index of the CWAT-01 host galaxy make it consistent with being a BCG at the low end of the n vs. r_{eff} correlation for BCGs (for details see Graham et al. 1996). In Sec. 5.4.2 we show that the CWAT-01 host galaxy is indeed the brightest galaxy in its parent cluster.
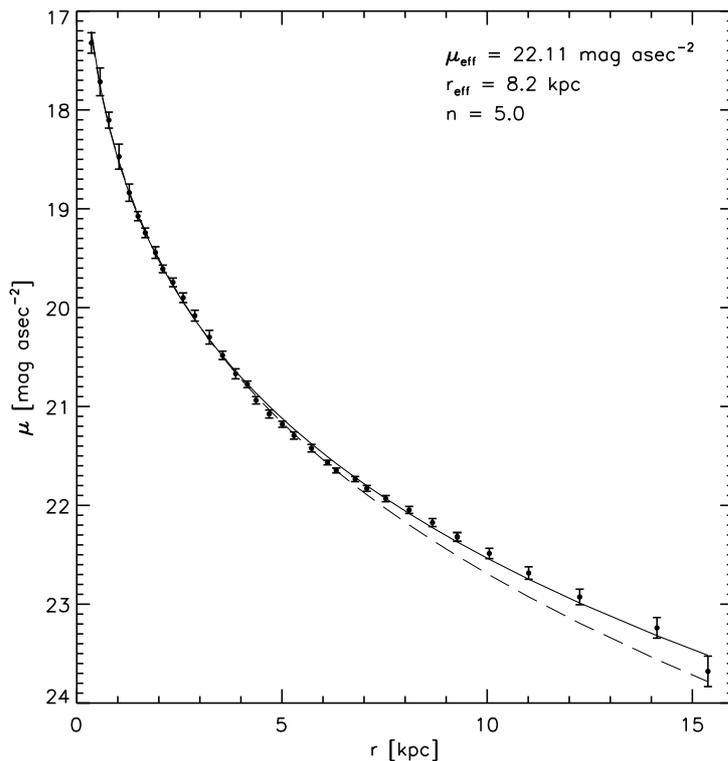
Figure 5.5 Surface brightness profile of the optical counterpart of CWAT-01. The surface brightness is expressed in AB95 magnitudes and was derived from the HST-ACS F814W band image (see text for details). The dots are the data points with 1σ error-bars. The de Vaucouleurs fit (dashed line) reveals an excess in surface brightness in the outer parts of the galaxy while the Sersic law fits the profile very well (solid line). The effective surface brightness, effective radius and Sersic index for the redshift of $z = 0.22$ are listed in the panel.

5.4 The clusters

WATs are normally found in cluster environments and are in general associated with the brightest cluster galaxy (BCG). The X-ray image of the field around CWAT-01 (described in Sec. 5.2.2) showed the presence of multiple extended X-ray sources around the WAT. Additionally, in the previous section we have shown that the CWAT-01 host galaxy has

the characteristics of BCGs. Taking advantage of the availability of the COSMOS multi-wavelength data set we investigate the nature and properties of CWAT-01's environment in this section.

The whole cluster structure detected via diffuse X-ray emission is part of the large-scale structure component, LSS #17, reported by Scoville et al. (2007b). The diffuse X-ray emission shows substructure itself. Throughout the paper we will use the following nomenclature. We refer to the whole area identified via diffuse X-ray emission as *cluster assembly*. The *cluster assembly* encompasses four subclumps (i.e. four individual diffuse X-ray emitting regions), which we call *clusters* or *poor clusters*, and is embedded in LSS #17; see for example Fig. 5.6 (top panel).

5.4.1   X-ray properties

The search for extended X-ray sources in the COSMOS $2\,\square°$ field (for details see Finoguenov et al. 2007) reveals 4 diffuse sources within $4'$ radius of CWAT-01. Fig. 5.6 (top panel) shows a part of the X-ray image in the $0.5 - 2$ keV band encompassing the cluster assembly. In the middle panel of Fig. 5.6 we display the same area in the sky, but from the wavelet reconstruction of the $0.5 - 2$ keV band image which was presented in Finoguenov et al. (2007) and utilized for their cluster search. CWAT-01 is located in the south-eastern cluster (hereafter *CWAT-01 parent cluster*).

Finoguenov et al. (2007) assign redshifts to the identified diffuse X-ray sources by analyzing redshift bins of width $\Delta z = 0.2$ using the COSMOS photometric redshift catalog (Mobasher et al. 2007). Three of the four diffuse X-ray sources described here are associated with a large galaxy concentration in the same redshift bin with the median photometric redshifts of the clusters of 0.22 (Finoguenov et al. 2007). A description of the cluster X-ray catalog names, their positions and fluxes is given in Table. 5.3. In the next sections we show that also the fourth diffuse X-ray source can be associated with an overdensity at a redshift of about $z = 0.22$.

For the purpose of this paper we assume that the clusters are all located at the same redshift and calculate their properties at $z = 0.22$.

The cluster assembly

For the spectral analysis we used the energy band of $0.5 - 3$ keV, since the counts at energies above 3 kev are dominated by background photons. Nonetheless, energies above 3 keV can be used to check the quality of the background subtraction and this was found to be satisfactory. Based on the surface brightness level, 5 main zones were constructed for the spectral analysis in such a way to avoid bright point-sources. The zones are shown in Fig. 5.6 (bottom panel). Zones *1* (which corresponds to the CWAT-01 parent cluster), *3*, and *4* are sampled with 3 subzones, labeled *a, b, c*. Table 5.4 summarizes the results of the spectral analysis based on the APEC thermal emission model (Smith et al. 2001). We report the temperature, normalization and their corresponding errors, the reduced χ^2 value and the number of degrees of freedom, $N_{d.o.f.}$. Zones *3b, 3c, 4b*, and *4c* turned out
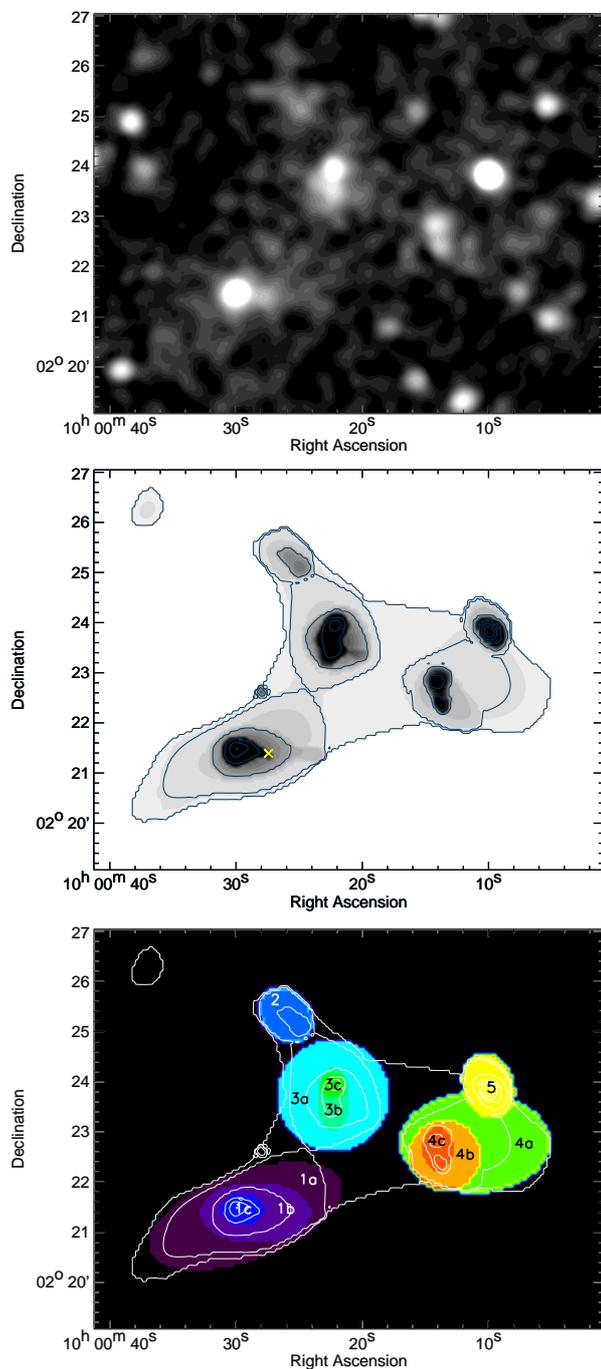
Figure 5.6   Top panel: X-ray image of the cluster area in the $0.5 - 2$ keV energy band, convolved with a Gaussian of $8''$ width. The color-scale is linear with lighter color displaying higher signal to noise. Middle panel: Wavelet reconstruction of the X-ray $0.5 - 2$ keV band image showing the cluster area (taken from Finoguenov et al. 2007). The contour levels are: 3×10^{-4}, 10^{-5}, 3×10^{-5}, 10^{-6}, 3×10^{-6}, 5×10^{-7} cnt/s/px. The position of the CWAT-01 host galaxy is indicated (cross). Bottom panel: 5 main zones with the corresponding subzones constructed for the X-ray spectral analysis are shown in color (see also Tab. 5.4). Each zone is labeled with its corresponding ID. X-ray contours (same as in top panel) are indicated to guide the eye.

Table 5.3 X-ray properties of 4 clusters adopted from Finoguenov et al. (2007).

main zone	catalog ID	RA	DEC	Flux ± err $[10^{-14} \text{ erg cm}^{-2} \text{ s}^{-1}]$	z_{photo}
1	78	10 00 28.337	+02 21 21.6	2.63 ± 0.15	0.22
2	82	10 00 25.454	+02 25 19.2	0.76 ± 0.07	0.22
3	85	10 00 21.852	+02 23 42.0	2.44 ± 0.15	0.22
4	87*	10 00 13.925	+02 22 48.0	1.24 ± 0.10	0.40

Description of the four X-ray luminous clusters adopted from Finoguenov et al. (2007): We list the main zone (column 1; see Sec. 5.4.1 and Fig. 5.6 for details) associated with the X-ray cluster catalog ID (column 2), the cluster's position (columns 3 and 4), the corresponding flux and error (column 5) and the photometric redshift (last column).
* Finoguenov et al. (2007) associate this extended X-ray emission with an optical overdensity at higher redshift. There seem to be, however, two X-ray features in their cluster catalog, one associated with this background cluster and the other with the overdensity we find at $z \sim 0.22$. [Note, that the position of this cluster is not exactly coincident with the location of zone *4a* (see Fig. 5.6), where we find the optical overdensity at $z \sim 0.22$.] The revised cluster catalog (Finoguenov et al. in prep), produced utilizing the complete set of *XMM-Newton* observations, will have a separate entry for the $z \sim 0.22$ structure .

to be non-thermal in origin, likely AGN, while zone *5* corresponds to a bright foreground star. A power-law fit with a photon index of $\Gamma = 2.3 \pm 0.1$ to zone *1c* gives a better χ^2 value ($\chi^2 = 1.2$ compared to $\chi^2 = 2.07$ for the thermal model), which indicates that a more plausible interpretation of this zone may be a background AGN, as suggested by Brusa et al. (2007). They associate the optical counterpart of this X-ray peak with a background ($z_{photo} = 0.89$) galaxy. The galaxy has a morphology of a spiral galaxy, clearly resolved in the HST-ACS image. Nevertheless, we expect the X-ray centroid of the CWAT-01 parent cluster to be located in the same area (i.e. associated with zone *1c*). The overall structure of the diffuse X-ray emission suggests that the center is approximately in zone *1c*. Furthermore, the center of mass calculated using stellar masses of the "high-density" galaxies (see Sec. 5.4.2 for details) is offset from the X-ray peak by $\sim 22''$ and is still within zone *1c*. Thus, for simplicity we take the X-ray peak as the center of the CWAT-01 parent cluster for calculations in this paper arguing that it is not far from where we would expect the cluster center to be. In Tab. 5.4 we also present the estimated properties of zone *1c*, assuming its thermal origin. The properties of this zone do not deviate strongly from the expectations of cluster X-ray emission. In addition, we emphasize that the mean values of the three-dimensional properties based on the spectral analysis results change only within $\sim 10\%$ when taking CWAT-01 as the cluster center and are consistent within the errors with the properties calculated taking the X-ray peak as the center.

The temperature of each of the four clusters (see Tab. 5.4) is consistent with the temperature range typical for poor clusters ($1-3$ keV; Finoguenov et al. 2001a). Following Henry et al. (2004) and Mahdavi et al. (2005), we estimate the cluster volume corresponding to the spectral extraction zones. The derived values for gas mass, gas density, entropy and pressure are listed in Tab. 5.5.

Using the luminosity-weighted temperatures of each of the four clusters (excluding zone *1c*), we estimate the total mass within the corresponding radius of the enclosed matter overdensity of 500 times the critical density (M_{500}^{tot}, r_{500} in the Table 5.5), using the *M-T*

Table 5.4 X-ray spectral analysis for the clusters

zone	kT [keV]	normalization [$\times 10^{-5}$]	χ_r^2	$N_{d.o.f.}$
1a	1.08 ± 0.26	5.4 ± 2.9	1.06	33
1b	2.26 ± 0.74	3.5 ± 1.4	1.12	19
1c	2.37 ± 0.45	4.1 ± 1.1	2.07	16
2	1.40 ± 0.45	2.0 ± 1.2	1.38	16
3a	1.46 ± 0.31	4.5 ± 2.2	1.18	31
3b*	-	-	-	-
3c*	-	-	-	-
4a	1.47 ± 0.61	2.2 ± 0.8	0.98	19
4b*	-	-	-	-
4c*	-	-	-	-
5+	-	-	-	-

* Nonthermal in origin
+ Foreground star
Results from the X-ray spectral analysis for the clusters using the APEC thermal model. Column 1 displays the spectral extraction zone (see Fig. 5.6 for reference). The temperature is given in column 2, the normalization in column 3, the χ^2 value in column 4, and the number of degrees of freedom, $N_{d.o.f.}$, in the last column.

Table 5.5 X-ray properties of the clusters in the assembly

zone	M_{gas} [$10^{11}\,M_\odot$]	n_e [$10^{-4}\,\mathrm{cm}^{-3}$]	S [$\mathrm{keV\,cm}^2$]	p [$10^{-13}\,\mathrm{dyn\,cm}^{-2}$]	r_{min}, r_{max} [Mpc]	r_{500} [Mpc]	M_{500}^{tot} [$10^{13}\,M_\odot$]
1a	13.0 ± 3.2	4.6 ± 1.1	180.8 ± 52.8	7.9 ± 2.7	0.104, 0.460	0.490	5.8
1b	5.9 ± 1.1	6.7 ± 1.2	295.6 ± 103.4	24.0 ± 9.0	0.060, 0.315	0.490	5.8
1c	2.00 ± 0.25	23.7 ± 3.0	133.4 ± 27.5	90.0 ± 20.0	0.000, 0.115	-	-
2	2.7 ± 0.7	8.3 ± 2.3	158.4 ± 58.7	18.8 ± 7.9	0.000, 0.183	0.438	4.1
3a	8.5 ± 1.9	6.0 ± 1.3	204.2 ± 52.3	1.4 ± 0.4	0.071, 0.253	0.449	4.4
4a	7.0 ± 1.2	0.36 ± 0.06	287.8 ± 121.6	8.6 ± 3.8	0.000, 0.375	0.451	4.4

X-ray properties of the clusters. Column 1 lists the zones used for the spectral analysis (see Fig. 5.6). The following columns are the gas mass (2), gas density (3), entropy (4), pressure (5), the minimum and maximum radius of the extraction zone (6), the radius corresponding to matter overdensity of 500 times the critical density, r_{500}, (7) and the total mass within r_{500} (8).
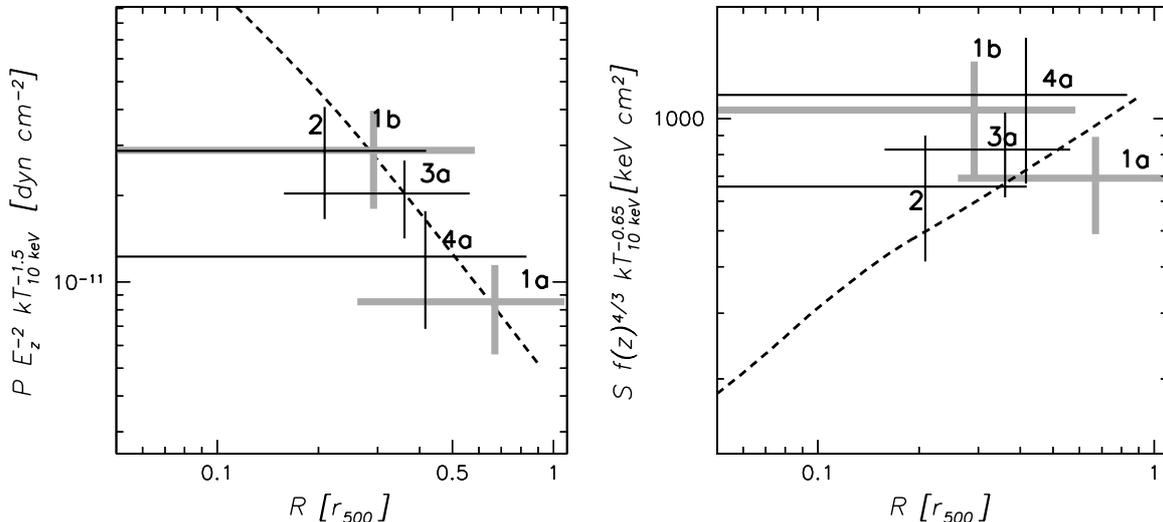
Figure 5.7 Pressure (left panel) and entropy (right panel) as a function of cluster radius for different spectral extraction zones (labeled in each panel, for comparison see Fig. 5.6). Thick crosses (zones *1a, 1b*) represent the CWAT-01 parent cluster. The length of the crosses indicates the 1σ errors. The dashed lines show the expected pressure and entropy behavior based on local cluster studies and scaled to the redshift of this system (see text for details).

relation from Finoguenov et al. (2001a). It is possible that the masses are up to 20% higher than the quoted values, according to recent XMM and Chandra results on the M-T relation (Arnaud et al. 2005; Vikhlinin et al. 2005). The uncertainty in the total mass estimate is primarily driven by the uncertainty in the measured temperature and is found to be on the level of 40% for the reported values. In Fig. 5.7 we compare the derived properties of the X-ray emission of the 4 clusters with the expectations based on local sample studies which we scale to the redshift of our cluster according to the expected evolution of shock heating (see Finoguenov et al. 2005 for details). The derived properties agree well with the prediction, which for shallow survey-type data, such as ours, is reassuring that the identification, background subtraction and point source confusion issues have been properly addressed.

The CWAT-01 parent cluster

The spectral properties of the CWAT-01 parent cluster are extracted from zones *1a, 1b* and *1c* (Fig. 5.6, bottom panel) as described in Sec. 5.4.1. The luminosity-weighted temperature of the CWAT-01 parent cluster (excluding zone *1c*) is ~ 1.7 keV and the total mass $\sim 5.8 \times 10^{13} M_{\odot}$ which makes it consistent with being a poor cluster (Finoguenov et al. 2001a). The spatial distribution of the diffuse X-ray emission of the cluster seems to be elongated and irregular. In order to obtain an estimate of its spatial characteristics (i.e. the core radius, r_c, and the β index), we obtain a 1-dimensional surface brightness profile using the $0.5 - 2.0$ keV background-subtracted image corrected for exposure time. We fit the radial profile with a two-component model: a) a Gaussian to describe the emission of the inner $\sim 20''$, and b) a traditional β-model (Cavaliere & Fusco-Femiano 1976) for the underlying cluster. The models are centered on the main peak of the X-ray emission. A

β-model with $\beta = 0.57 \pm 0.06$ and $r_c = 48.0^{+8.7}_{-18.0}\,'' = 170.5^{+30.9}_{-63.9}\,kpc$ is a good representation of the cluster X-ray emission. The extended cluster component yields a count rate in the (0.5-2.0) keV energy range out to r_{500} of 4.5×10^{-3} cnt/s. We find that the luminosity of the cluster that hosts CWAT-01 is 3.6×10^{42} erg/s, consistent with L-T relation of Markevitch (1998); Mulchaey (2000); Osmond & Ponman (2004).

Using the above derived values of β and r_c and a temperature of $kT \sim 2.26$ keV (zone *1b*) we compute the central number density (n_0) as described in Sakelliou et al. (1996). The central number density corresponds to $n_0 = 1.085^{+1.12}_{-0.08} \times 10^{-3}\,\mathrm{cm}^{-3}$ which is in agreement with the result of the spectral analysis (Tab. 5.5). In Sec. 5.5.2 we use the derived quantities (i.e. r_c and β) for hydrodynamical models explaining the bending of the jets of CWAT-01 and constraining the velocity of the host galaxy relative to the ICM.

5.4.2 Optical properties

Cluster identification using overdensities: Voronoi tessellations

To map the galaxy overdensity in the area of the X-ray cluster assembly we use the Voronoi tessellation-based approach (hereafter VTA; e.g. Ramella et al. 2001; Kim et al. 2002, Botzler et al. in prep). The VTA has several advantages over other overdensity estimators which make it favorable for the scope of this paper: First, no a-priori assumptions about cluster properties (e.g. density profile) are necessary making the technique sensitive to elongated, i.e. non-symmetrical structures (Botzler et al.in prep). Secondly, we are mainly interested in substructure which can efficiently be revealed with the VTA.

A *Voronoi tessellation* on a two-dimensional distribution of points (called nuclei) is a subdivision of the plane into polygonal regions (nuclei lying on the edge may have open polygons), where each of them contains one and only one nucleus. Each region consists of the set of points in the plane that are closer to that nucleus than to any other. The algorithm used here for the construction of the Voronoi tessellation and calculation of the local densities is the "varea" code written by Botzler et al.(in prep) which encompasses the "triangle" code by Shewchuk (1996). Our goal is to quantify the clustering in the area where CWAT-01 is located, thus the input for the Voronoi tessellation (nuclei) are galaxy positions drawn from the COSMOS photometric redshift catalog (Capak et al. 2007; Mobasher et al. 2007). The VTA then defines the effective area, A, that a galaxy occupies in the two dimensional space. Taking the inverse of the effective area gives the local density of the galaxy, $\rho_{local} = 1/A$.

The selection criteria we apply to the COSMOS photometric redshift catalog are the following: we select objects classified as galaxies ($STAR < 1$) in the redshift bin of width $\Delta z = 0.2$ centered at the CWAT-01 host galaxy's redshift reported in the catalog. The mean 2σ error of the selected galaxies is 0.11 ± 0.06 in photometric redshifts. Thus, 67% of our galaxies have 2σ errors in photometric redshifts better than 0.17 and 95% better than 0.23.

To robustly estimate the background density, we apply the VTA to a region ~ 10 times larger than the region of interest which is $10' \times 8'$ corresponding to $\sim (2.1 \times 1.7)$ Mpc^2

($z = 0.22$). In addition we run Monte Carlo simulations by randomly redistributing the total number of galaxies in the analyzed field. Then we apply the VTA to each generated field and calculate the mean density, resulting in a distribution of background densities with the corresponding standard deviation, $\overline{\rho_{bkg}} \pm \sigma_{bkg}$. We define overdense regions as regions that have local density values of $\rho_{local} > \overline{\rho_{bkg}} + 10\sigma_{bkg}$.
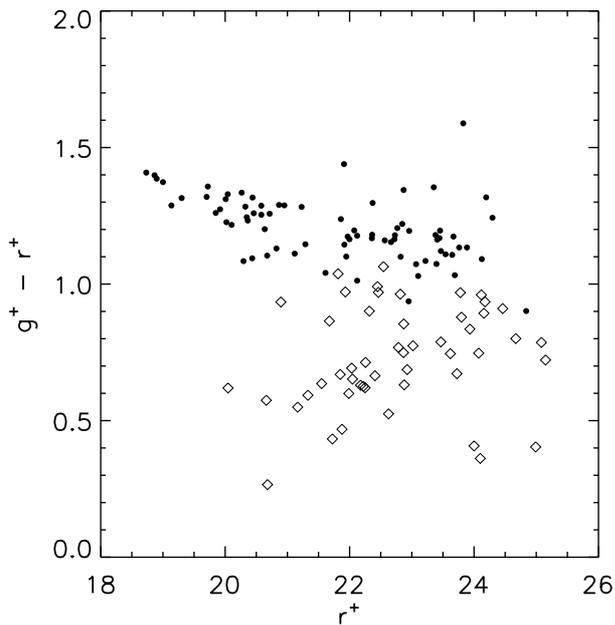

Figure 5.8 $g^+ - r^+$ vs. r^+ color magnitude diagram (CMD) using the COSMOS SUBARU g^+ and r^+ bands. The galaxies shown in the CMD are galaxies ($g^+ < 26.5$ and $Bj < 26.5$) within the cluster area of interest, corresponding to $\sim (2.1 \times 1.7)$ Mpc^2 ($z = 0.22$), which satisfy the overdensity criterion imposed in the VTA analysis: $\rho_{local} > \overline{\rho_{bkg}} + 10\sigma_{bkg}$ (see Sec. 5.4.2 for details). Galaxies in masked-out regions (around saturated objects) are excluded. Filled symbols represent early type galaxies (SED type < 2.5) while open symbols stand for late type galaxies (SED type > 2.5).

Utilizing the COSMOS SUBARU g^+ and r^+ bands, we show in Fig. 5.8 the $g^+ - r^+$ vs. r^+ color-magnitude diagram of galaxies with local density values $\rho_{local} > \overline{\rho_{bkg}} + 10\sigma_{bkg}$ and within the $\sim (2.1 \times 1.7)$ Mpc^2 area encompassing the cluster assembly. Galaxies in masked-out regions (around saturated objects) are excluded to reduce the number of artifacts (note that excluding the masked-out galaxies from the input sample for the VTA would only slightly lower the mean background density value). We also impose a magnitude cut of $Bj < 26.5$ and $g^+ < 26.5$ to exclude noise artifacts which are presumably due to the g^+ and Bj detection limits for extended sources. We therefore define the *final* sample of *"high-density" galaxies* as galaxies that satisfy the following criteria: a) $\rho_{local} > \overline{\rho_{bkg}} + 10\sigma_{bkg}$, b) $Bj < 26.5$ and $g^+ < 26.5$, and c) the galaxies are outside masked-out regions around saturated objects.

Cluster assembly structure

The Voronoi tessellation for the $\sim (2.1 \times 1.7)$ Mpc^2 area surrounding the cluster assembly with indicated "high-density" galaxies is shown in Fig. 5.9. The large-scale overdensity is elongated in NW-SE direction with several obvious subclumps. The spatial distribution of the galaxies seems not to be spherically-symmetric, but irregular, both, on large and small scales. In the areas around saturated stars (i.e. masked-out regions) we loose all information about clustering.
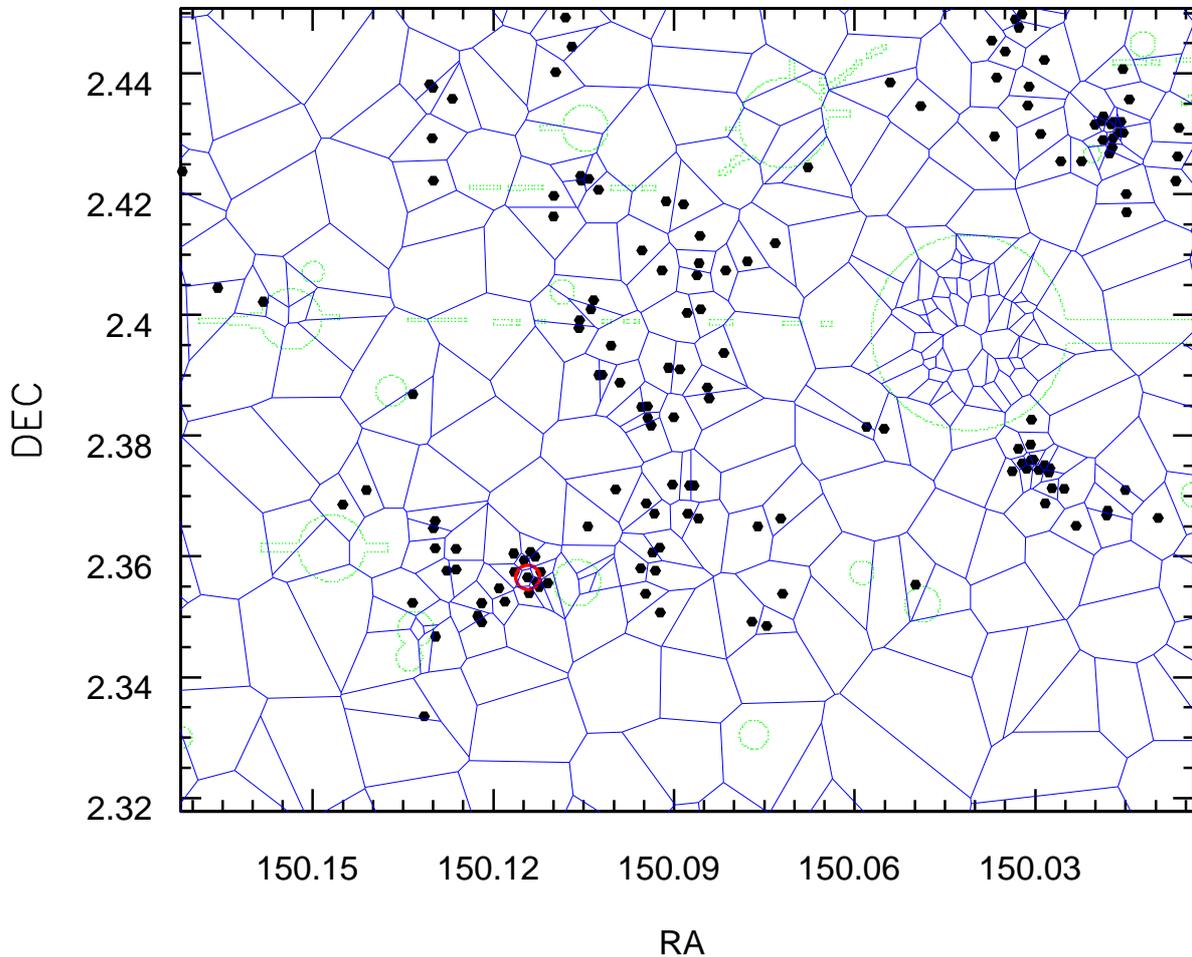
Figure 5.9 Voronoi tessellation analysis in the area of the cluster assembly (solid blue lines). The shown field is $\sim (2.1 \times 1.7)$ Mpc^2 (at $z = 0.22$) in size and ≈ 10 times smaller than the total area analyzed. Masked-out regions (around saturated objects) in the photometric redshift catalog are marked with dotted green lines (see text for details). The points represent "high-density" galaxies that a) satisfy our overdensity criterion of $\rho_{local} > \overline{\rho_{bkg}} + 10\sigma_{bkg}$, b) satisfy the magnitude criterion of $g^+ < 26.5$ and $B_j < 26.5$ and c) are not located in masked-out regions. CWAT-01 is marked with the open solid circle.

In Fig. 5.10 the "high-density" galaxies are overlaid on the SUBARU i^+ band image. For comparison, diffuse X-ray emission contours are also shown. It is evident that the "high-density" galaxies display a complex and irregular spatial distribution, consistent with the irregular and elongated distribution of the diffuse X-ray emission. Each X-ray identified poor cluster has a counterpart in optical overdensities approximately following the distribution of the X-ray emission. Note that the X-ray cluster corresponding to zone $4a$ is associated with an optical overdensity with a mean redshift of $z \approx 0.22$ like the other clusters. This is additionally confirmed by the SDSS J10006.65+022225.98 galaxy spectrum (see Tab. 5.2 for details).

The optical overdensities reveal, in addition, a clustering region north-west from the diffuse X-ray emission (LG-N in Fig. 5.10) not detected in the $0.5 - 2.0$ keV X-ray band.
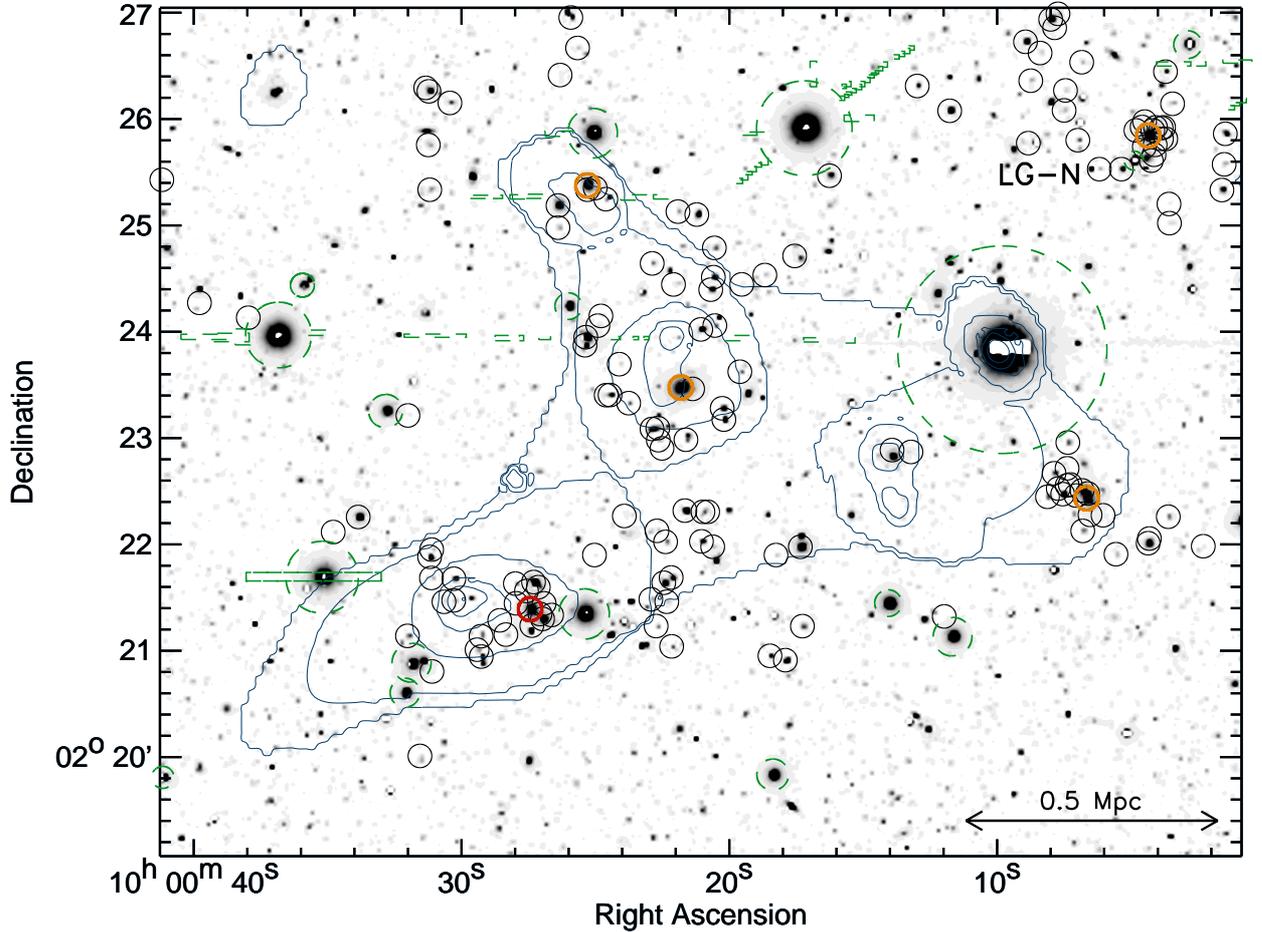
Figure 5.10 Grey scale SUBARU i^+ band image of the cluster area overlaid with X-ray contours (blue). The contour levels are the same as in Fig. 5.6. The shown area is $\sim (2.1 \times 1.7)$ Mpc^2 (at $z = 0.22$) with thin circles (black) denoting the "high-density" galaxies (same galaxies as in Fig. 5.9). Masked-out regions around saturated objects (drawn from the COSMOS photometric catalog) are indicated with dashed green lines. CWAT-01 is marked with the thick red circle. Orange circles indicate galaxies which have spectra (see Sec. 5.2.4 and Tabs. 5.1 and 5.2 for details). LG-N labels the overdensity evident from the Voronoi tessellation-based aproach (VTA) but not detected in X-rays (see text for details). The 0.5 Mpc projected distance is indicated for reference.

The SDSS J10004.35+022550.71 galaxy spectrum confirms that this structure is at the same redshift as the whole cluster system. We assume that LG-N is a loose group bound to the cluster assembly.

Substructure in the CWAT-01 parent cluster

The spatial distribution of the "high-density" galaxies (Fig. 5.11, top panel) in the CWAT-01 parent cluster is irregular and elongated with two dominant subclumps: a) a Western overdensity (including the CWAT-01 host galaxy) extended in NW-SE direction ($SC1$ in Fig. 5.11) and b) an Eastern overdensity elongated in NE-SW direction ($SC2$). There are three bright foreground stars contaminating the CWAT-01 parent cluster area. Nev-
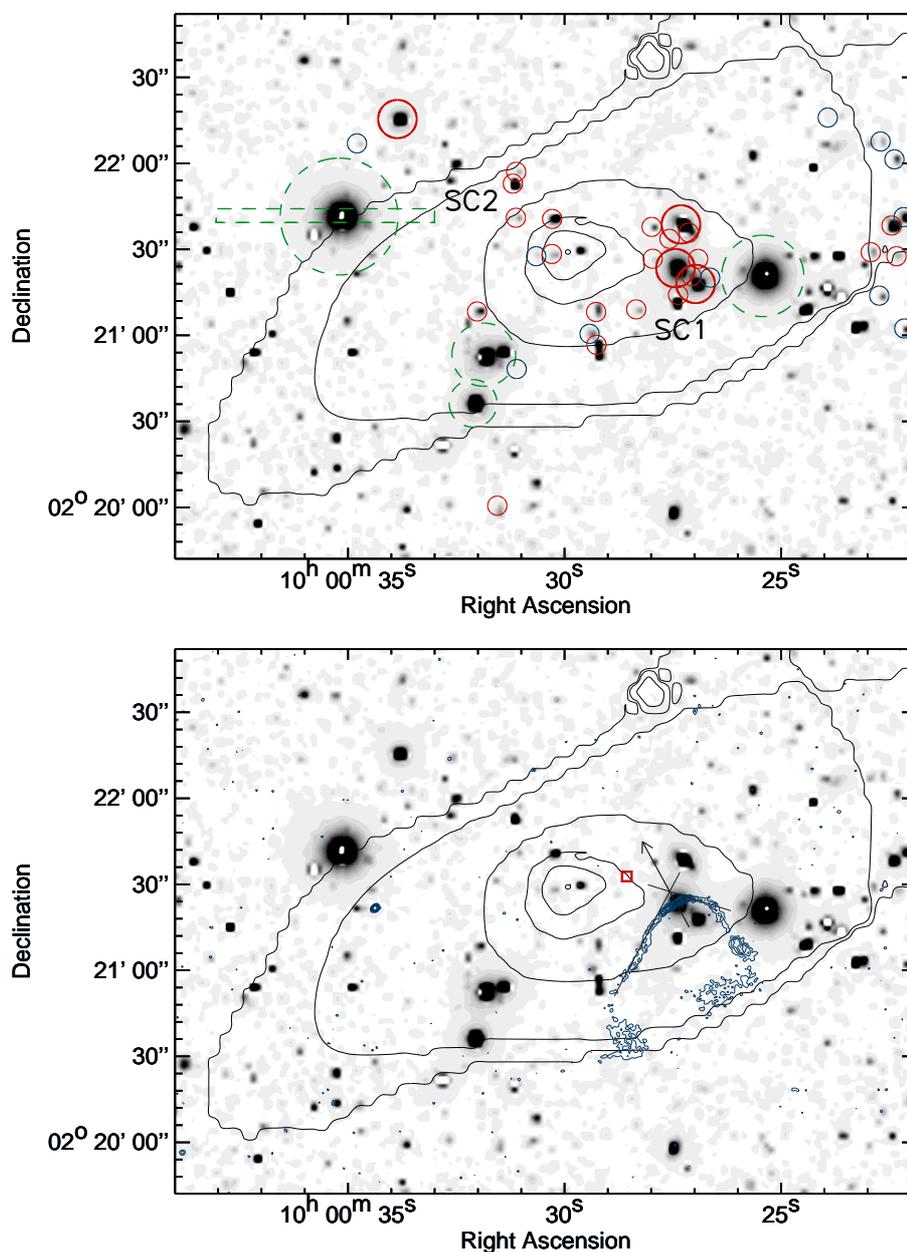
Figure 5.11 Top panel: SUBARU i^+ band image (grey scale) of the CWAT-01 parent cluster. Overlaid are X-ray contours with contour levels as in Fig. 5.6. Indicated are "high-density" galaxies. Red solid circles denote early type galaxies (SED type < 2.5) while blue solid circles indicate late type galaxies (SED type > 2.5). The brightest galaxies ($M_V < -20.5$) in this area are marked with thick red circles. Dashed green lines mark masked-out objects. $SC1$ and $SC2$ label the two subclumps evident in the cluster (see text for details). Bottom panel: SUBARU i^+ band image (grey scale) and X-ray contours as in top panel overlaid with 1.4 GHz radio contours. The radio contour levels start at the 3σ level and increase in steps of 1σ. The bending angle of CWAT-01 is indicated by thin lines while the arrow indicates the velocity direction of the galaxy. The open box marks the position of the center of mass of the cluster computed taking into account the stellar masses of the "high-density" galaxies in the CWAT-01 parent cluster (the stellar masses were drawn from the COSMOS photometric redshift catalog; Mobasher et al. 2007.

ertheless, those masked-out regions should not affect our results substantially since they are located at the outer parts of the parent cluster. Contrary to the expectation in relaxed systems where one would expect early type galaxies to be centrally concentrated around the bottom of the cluster potential well, the distribution of the early type galaxies (SED type < 2.5) in the CWAT-01 parent cluster is spatially elongated and coincident with subclumps SC1 and SC2 (see Fig. 5.11). Late type galaxies are preferentially at the outskirts of the cluster. The brightest galaxy in the cluster is the CWAT-01 host galaxy ($r^+ = 18.899 \pm 0.004$, $M_V = -22.9 \pm 0.1$). This is not surprising due to previous studies which have shown that WATs are generally associated with BCGs (e.g. Burns 1981). In addition, the brightest galaxies ($M_V < -20.5$) in the cluster are strongly clustered in the region around CWAT-01, while only one (i.e. the second brightest in absolute V magnitude) is located at the outskirts of the cluster (see Fig. 5.11, top panel).

Using the stellar masses reported in the COSMOS photometric redshift catalog Mobasher et al. (2007) of the "high-density" galaxies we compute the position of the center of mass (indicated in Fig. 5.11, bottom panel). The offset of the center of mass from the main peak in the diffuse X-ray emission is only $\sim 22''$. Note that because of the bias introduced by the masked-out regions in the cluster, the center of mass may be closer to the main X-ray peak than given above.

5.5   Discussion

The unified theory for the mechanism responsible for bending the jets of WAT radio galaxies is the dynamic pressure exerted on the jets by the ICM due to the relative motion between the galaxy and the ICM. In Sec. 5.5.1 we compare the minimum pressure present in the radio jets to the thermal ICM pressure in order to investigate the confinement of the jets. We have shown in previous sections that CWAT-01 is associated with the BCG in its parent cluster. Therefore it is expected to be at rest in the minimum of the gravitational potential (e.g. Bird 1994). In order to constrain the relative velocity between CWAT-01's host galaxy and the ICM we apply several hydrodynamical models explaining the bending of the jets of WATs (Sec. 5.5.2). In Sec. 5.5.3 we suggest possible merger and encounter scenarios responsible for the bending of the jets (Sec. 5.5.3). The environment of CWAT-01 on larger scales (i.e. the cluster assembly) is discussed in Sec. 5.5.4.

5.5.1   Pressure balance

It is often assumed that the radio jets are confined by the ICM (e.g. Miley 1980 and references therein) thus it is interesting to compare the minimum internal pressure in the radio jets with the thermal ICM pressure. The minimum internal pressure in the radio jets was calculated in the middle part of the Eastern tail (Sec. 5.3.1), $p_{min}^{jet} \cong 4.3 \times 10^{-13} \mathrm{dyn\,cm}^{-2}$, and it is lower than the ICM pressure in zone *1b*, which contains CWAT-01, $p_{ICM}^{zone\,1b} = (24 \pm 9) \times 10^{-13} \mathrm{dyn\,cm}^{-2}$ (see Sec. 5.4.1 for details). Such a pressure imbalance is not unusual for WATs (e.g. Hardcastle & Sakelliou 2004). It implies either some departure

from the minimum energy condition (which is almost equal to equipartition between the relativistic particles and the magnetic fields in the jets) or a contribution to the pressure from particles which do not participate in equipartition such as thermal protons. However, one should be careful in comparing the two pressure values due to the low resolution of the X-ray data and the numerous assumptions in the minimum pressure calculation. Nevertheless, the ram pressure models we apply to CWAT-01 in order to constrain the relative velocity between the galaxy and the ICM (next section) should not be affected by this pressure imbalance. The inherent assumption in these models is that the *dynamic* ram pressure of the ICM is comparable with the *pressure difference* across the jet.

5.5.2 Bending of the radio jets of CWAT-01: constraints on the galaxy velocity

In this section we apply several hydrodynamical models explaining the bending of the jets of CWAT-01 in order to constrain the velocity of CWAT-01's host galaxy relative to the ICM. The classical Euler equation describes the jets if the bulk plasma velocity in the jets is characterized by non-relativistic motions (e.g. Jaffe & Perola 1973; Begelman et al. 1979; Christiansen et al. 1981; Sakelliou et al. 1996). Sakelliou et al. (1996) developed a simple hydrodynamical model to describe the bending of the jets of 3C34.16. They assume that the forces acting on the jets are ram pressure and buoyancy and they model the jets in the plane of the sky assuming a steady plasma flow (Sakelliou et al. 1996, their equations [8]-[11]). The strength of this model is that it provides a constraint on the galaxy velocity relative to the ICM solely dependent on the jet density at the point where ram pressure and buoyancy balance. At the turn-over point the bending of the jet changes its direction. At this point the forces of ram pressure and buoyancy in the direction normal to the jet balance and the only unknowns are the galaxy velocity and the density of the jet at this point:

$$v_{gal}^2 = \frac{3\beta k T_{ICM} h}{\mu m_p r_c} \frac{\frac{r_{to}}{r_c}}{1 + \left(\frac{r_{to}}{r_c}\right)^2} \frac{\hat{\mathbf{r}} \cdot \hat{\mathbf{n}}}{\hat{\mathbf{V}}_{\mathbf{gal}} \cdot \hat{\mathbf{n}}} \left(1 - \frac{\rho_j}{\rho_{ICM}}\right) \tag{5.5}$$

Here r_{to} is the radial distance from the cluster center to the turn-over point (projected on the plane of the sky), r_c and β are the core radius and the standard hydrostatic-isothermal β model parameter, respectively (see Sec. 5.4.1), $\hat{\mathbf{n}}$ is the normal vector to the jet in the plane of the sky, v_{gal} is the component of the galaxy velocity in the plane of the sky, h is the scale height of the jet, ρ_j and ρ_{ICM} are the jet and ICM densities, respectively, kT_{ICM} is the ICM temperature in keV (~ 2.26 keV), μ is the mean molecular weight and m_p the proton mass.

The 1.4 GHz radio map (Fig. 5.1) clearly shows that the radio jets bend twice. Near the optical counterpart the jets turn to the south. The second bend of the jets is towards the south-west direction (points E1 and W1 in Fig. 5.1). The first bend can be attributed to ram pressure as a result of the relative motion of the galaxy through the ICM. At larger radii buoyancy takes over and the jets are pushed towards lower density regions in

the ICM. Fig. 5.12 shows the galaxy velocity as a function of the ratio of the jet density to the ICM density, ρ_j/ρ_{ICM}, calculated at the point W1 (thick solid line). The allowed range in velocities is indicated (broad hatched region). The limiting velocity of the galaxy relative to the ICM (in the limit $\rho_j/\rho_{ICM} \to 0$) is $v_{gal} \sim 400^{+150}_{-110}\, km\, s^{-1}$. Note that v_{gal} measures the projected velocity on the plane of the sky, thus any inclination of CWAT-01 to the line-of-sight would result in an additional line-of-sight component of velocity, thus increasing the total speed of the system. The upper and lower limits of the galaxy velocity were computed taking into account the errors of r_c, β, and kT. Additional uncertainties are introduced through the estimate of $\hat{\mathbf{n}}$ at the turn-over point and $\hat{\mathbf{r}} \cdot \hat{\mathbf{n}}$ which depends on the position of the center of the total mass of the cluster (discussed in Sec. 5.4.1). Thus, the derived velocity is a rough estimate of CWAT-01's velocity relative to the ICM as a function of ρ_j/ρ_{ICM}.
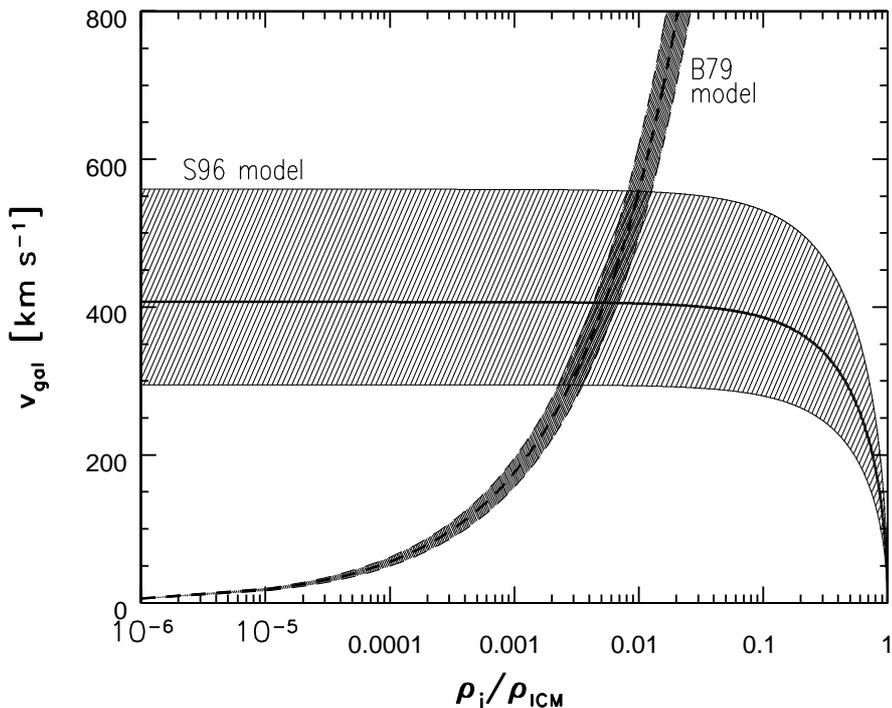

Figure 5.12   Mean galaxy velocity, v_{gal}, (thick lines) as a function of the ratio of the jet to ICM density, ρ_j/ρ_{ICM}, with the allowed ranges (hatched regions) corresponding to our error estimates. The broad hatched region shows the galaxy velocity calculated from eq. [5.5] using the model developed in Sakelliou et al. (1996, S96) which takes into account ram pressure and buoyancy as forces responsible for bending the jets (see text for details). The narrow hatched region shows the galaxy velocity calculated from eq. [5.6] (developed by Begelman, Rees, & Blandford 1979, B79) taking only ram pressure into account. If we require that the conditions of both models are satisfied, then the allowed ranges for v_{gal} and ρ_j are within the intersecting area.

Another hydrodynamical model, that we apply to CWAT-01 to estimate the galaxy velocity, was first proposed by Begelman, Rees, & Blandford (1979) to explain the jets in NGC1265. The curvature of the jets is again assumed to be produced by ram pressure exerted on the galaxy as it moves through the ICM. The ram pressure is balanced by the centrifugal force exerted by the jet as it curves:

$$\frac{\rho_{ICM}\,v_{gal}^2}{h} = \frac{\rho_j\,v_j^2}{R} \tag{5.6}$$

where v_j is the bulk jet velocity, h is the scale hight, R is the radius of curvature, v_{gal} is the galaxy velocity and ρ_{ICM} and ρ_j are the ICM and jet densities, respectively. Placing the mean jet velocity of the velocity range derived in Sec. 5.3.1, $v_j \sim 0.045c$, into eq. [5.6], using an estimate of the scale height (at point C0 in Fig. 5.1) of $h \sim 1.7''$ (~ 6 kpc) and the radius of curvature of $R \sim 10''$ (~ 35 kpc), we show the galaxy velocity as a function of the ρ_j/ρ_{ICM} ratio in Fig. 5.12 (dashed lines). Indicated is the galaxy velocity range corresponding to the jet velocity range, $0.04c \lesssim v_j \lesssim 0.05c$ (narrow hatched region).

Requiring that the conditions of both equations, eq. [5.5] and [5.6], are satisfied (as illustrated in Fig. 5.12), we obtain an estimate of both, the galaxy velocity, v_{gal}, and the jet density, ρ_j. v_{gal} is in the range of about $400^{+150}_{-100}\,km\,s^{-1}$ and ρ_j is $0.005^{+0.01}_{-0.003}\,\rho_{ICM}$, respectively. The ICM density is known from the spectral analysis, $\rho_{ICM} = (6.94 \pm 1.27) \times 10^{-4}\,cm^{-3}$, thus the estimated jet density with the corresponding errors is about $0.03^{+0.09}_{-0.02} \times 10^{-4}\,cm^{-3}$.

So far we have neglected possible *in situ* particle acceleration within the jets. If particle re-acceleration occurs then the bulk lifetime of the synchrotron electrons in the jets would be higher than the 13 Myr estimated in Sec. 5.3.1. A lower limit of the galaxy velocity can then be estimated by assuming efficient conversion of kinetic energy into internal energy in the plasma jet flow (e.g. Eilek 1979). If the observed luminosity, L, of the jets is supplied by conversion of the bulk kinetic energy with an efficiency, ϵ, then $L \sim \frac{\pi}{2}\rho_j h^2 v_j^3 \epsilon$ (e.g. Burns 1981; O'Donoghue et al. 1993). Substituting v_j in terms of the luminosity into eq. [5.6], one gets:

$$v_g \gtrsim \left(\frac{2L}{\pi}\right)^{1/3} \rho_j^{1/6} \rho_{ICM}^{-1/2} h^{-1/6} R^{-1/2} \epsilon^{-1/3} \tag{5.7}$$

which is only weakly dependent on the jet density, ρ_j. For an efficiency of $\sim 10\%$, assuming the above derived jet density, the galaxy velocity is roughly $v_g \gtrsim 350$ km s^{-1} which is consistent with the results from the previously applied models.

The models we applied to CWAT-01 in the above discussion thus suggest that the galaxy velocity relative to the ICM is in the range of about $300 - 550$ km s^{-1}.

5.5.3   Subcluster merging in the CWAT-01 parent cluster?

Beers et al. (1995) report a median velocity dispersion of 336 ± 40 km s^{-1} (which is in agreement with e.g. Ramella et al. 1994; Ledlow et al. 1996) for a sample of MKW/AWM poor clusters [3]. They find a velocity offset between the velocity of the central galaxy and the mean velocity of the rest of the galaxies of $\lesssim 150$ km s^{-1} for clusters with no

---

[3] A sample of 23 poor clusters of galaxies originally identified by Morgan, Kayser, & White (1975) and Albert, White, & Morgan (1977).

evidence for subclustering. The velocity range of $300 - 550$ km s^{-1} we found for CWAT-01's host galaxy, which is the dominant galaxy (BCG) in its parent cluster, is significantly higher than this limit which indicates recent merger events between less massive systems of galaxies (Bird 1994). High peculiar velocities are strongly correlated with the presence of substructure in the system (Bird 1994). Indeed, the VTA results indicate subclustering in the CWAT-01 parent cluster ($SC1$ and $SC2$ in Fig. 5.11). Furthermore, the brightest galaxies in the cluster are strongly concentrated around CWAT-01. We speculate that SC1 and SC2 interact and, furthermore, that SC2 may be infalling into the gravitational potential of SC1. This interaction may cause a dynamical state of the cluster violent enough to produce the inferred relative velocity of the CWAT-01 host galaxy to the ICM needed to bend the jets in the observed way. Moreover, the irregular assembly of early type galaxies in the CWAT-01 parent cluster (see Fig. 5.11) suggests that it is not a relaxed system. The elongated and irregular diffuse X-ray emission of this cluster indicates independently possible merger or accretion events in the cluster. Finoguenov et al. (2005) have shown that X-ray elongations are often seen at the outskirts of clusters and that their spectral characteristics correspond to a colder, dense gas in pressure equilibrium with the cluster. This gas is associated with accretion zones in clusters where dense parts of the filaments survive the accretion shock and penetrate the cluster outskirts.

Our results suggest that merger events within the CWAT-01 parent cluster caused such a dynamical state in the cluster which is needed for bending the radio jets of CWAT-01 in the observed way. Such a merging scenario is consistent with conclusions of previous studies which have suggested that the bent shape of WAT galaxies is caused by mergers (e.g. Gomez et al. 1997; Sakelliou et al. 1996; Sakelliou & Merrifield 2000).

Based on a sample of ~ 20 WAT galaxies which are located in Abell clusters and have ROSAT X-ray observations Sakelliou & Merrifield (2000) have shown that WATs travel predominantly radially towards or away from the center (as defined by the X-ray centroid) of their host cluster. CWAT-01 does not seem to be on a radial motion in the projected plane of the sky, as is evident in Fig. 5.11 (bottom panel). This may be a bias caused by projection effects. However, the gravitational influence of the neighboring clusters may have played a significant role in causing the inferred velocity modulus and direction of CWAT-01's host galaxy relative to the ICM.

Based on the above arguments we suggest that the radio jets of CWAT-01 were bent as a consequence of the motion of CWAT-01 relative to the ICM induced through interactions between subclusters (SC1 and SC2) and/or interactions between the CWAT-01 parent cluster and the other identified clusters.

5.5.4 Galaxy cluster assembly

Since CWAT-01 seems to be part of a very complex large-scale structure, the possible gravitational influence of the other clusters on the galaxy and its immediate environment cannot be neglected. Fig. 5.13 shows the distribution of emission from different parts of the electromagnetic spectrum within the cluster area. The diffuse X-ray emission has revealed that the CWAT-01 parent cluster is only one of the poor clusters encompassed in a
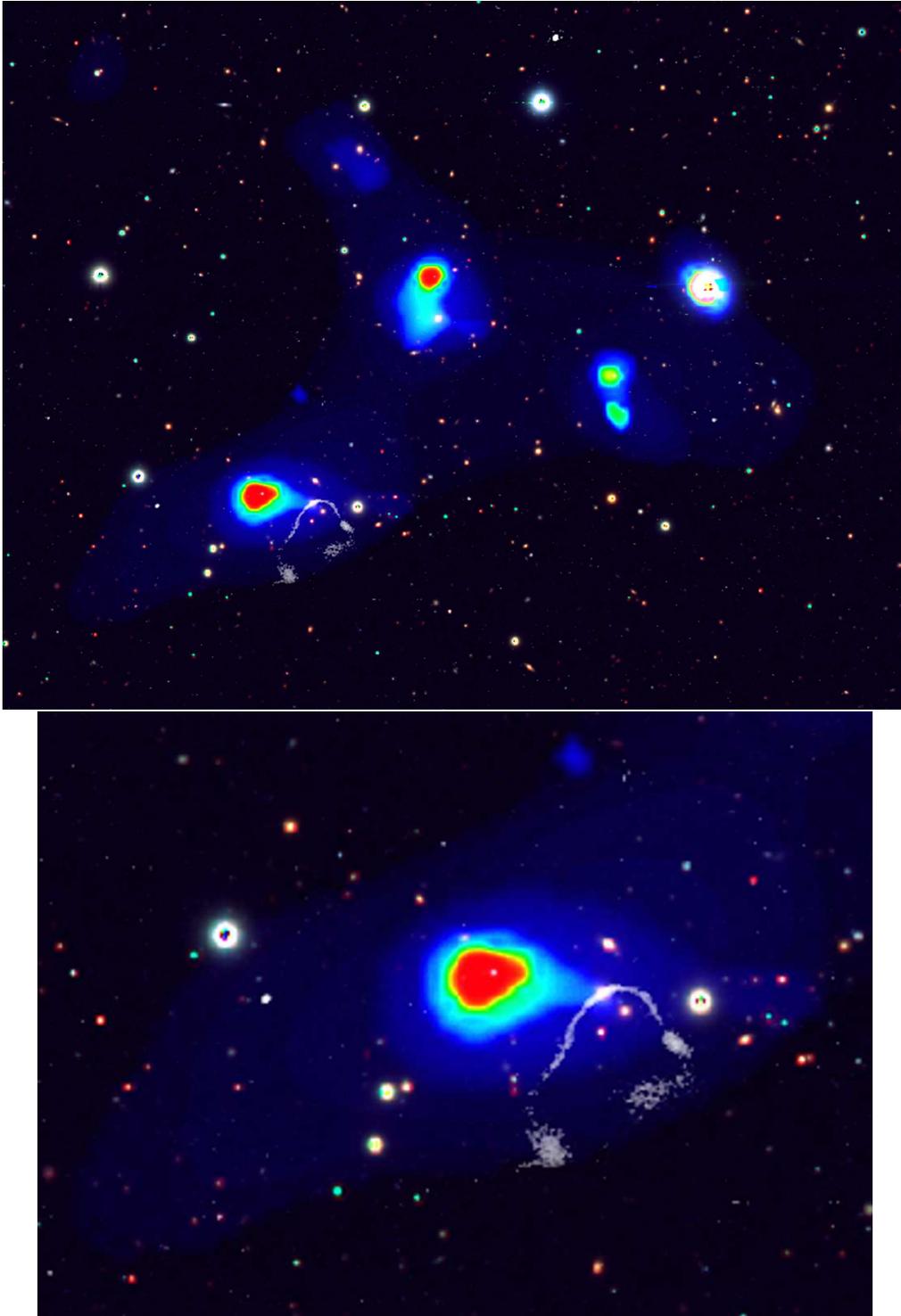
Figure 5.13 Color composite image of the cluster area (top) and the CWAT-01 parent cluster (bottom). The SUBARU B (blue), V (green), and i^+ (red) bands are displayed in the background. The diffuse X-ray emission is presented by rainbow colors and the 1.4 GHz map is shown in white. The top panel encompasses an area of $\sim (2.1 \times 1.7)$ Mpc^2 (analogous to Fig. 5.10). The size of the bottom panel is as in Fig. 5.11.

larger cluster structure. The cluster assembly contains a minimum of four X-ray luminous clusters within ~ 2 Mpc distance. In addition, the VTA indicates that there is at least one more loose group (LG-N; Fig. 5.10) on the outskirts of the X-ray cluster assembly but not detected in the X-rays. Furthermore, the whole cluster assembly is part of a large-scale structure component (LSS #17, Scoville et al. 2007b) extended over ~ 4 Mpc in NS direction.

The direction of the jets of CWAT-01 is almost perpendicular to the X-ray elongation of the CWAT-01 parent cluster as well as to the large-scale elongation of the X-ray emission. Although LSS #17 spatially extends ~ 4 Mpc in NS direction, the direction of its *long axis* (as defined in e.g. Novikov et al. 1999) is in the NW-SE direction (see Fig. 3 in Scoville et al. 2007b). Hence, the direction of the jets of CWAT-01 is almost perpendicular also to the long axis of LSS #17. This is in disagreement with the correlation of the alignment between the direction of the jets and a) the central X-ray emission elongation (Burns et al. 1994; Gomez et al. 1997) and b) the supercluster axis as defined by the distribution of the nearby Abell clusters (Novikov et al. 1999). Nevertheless, the misalignment seen in CWAT-01's orientation compared to the parent cluster and to LSS #17 elongations may not be unexpected if we assume an early stage of cluster formation. Rich clusters form at the intersection of large-scale filaments. Compared to numerical simulations (e.g. Burns et al. 2002; Springel et al. 2005) of cluster evolution at $z = 0.2$ the final cluster has not yet formed or relaxed at the intersection of filaments where matter is accreted from numerous filaments. Thus, in such an environment it would not be unexpected to observe a WAT galaxy with its jets not aligned with the cluster or large-scale structure elongations.

The X-ray and optical analysis indicate that each individual poor cluster within the cluster assembly is not spherically-symmetric, both in the diffuse X-ray emission and in the spatial distribution of galaxies in the optical (VTA). This strongly indicates that the poor clusters are not in a dynamically relaxed state. In addition, the overall, large-scale distribution of the cluster assembly is very complex and irregular. It is likely that the loose group LG-N is bound to the system. The lack of X-ray emission from this group suggests that the system is not very massive. The flux limit for the cluster search (see Sec. 5.2.2) allows a detection of an object at $z = 0.22$ with a limiting luminosity of $L_x^{limit} = 3 \times 10^{41}$ erg s^{-1}, which corresponds to a low-mass group (e.g. Mulchaey et al. 2003). Following the luminosity-temperature (L-T) relation for groups (Osmond & Ponman 2004) the limiting temperature then equals $T_x^{limit} \sim 0.4$ keV. Using the mass-temperature (M-T) relation from Finoguenov et al. (2001b) the minimum mass of a system to be detected in the diffuse $0.5 - 2$ keV band at $z = 0.22$ then corresponds to $M_{500}^{tot,limit} \sim 1.5 \times 10^{13} M_\odot$. Thus, the total mass of LG-N has to be less than this mass.

Although spectroscopic verification is needed for the physical connection of the clusters, we believe that we are witnessing a protocluster in the process of being built up of multiple galaxy clusters and groups. Adding up the estimated masses for the four clusters identified via diffuse X-ray emission (see Tab. 5.5) and the limiting mass inferred for LG-N the resulting combined mass is $M \sim 2.0 \times 10^{14} M_\odot$. This is a rough estimate of the total mass of the cluster system once it is formed since it does not include the material between the clusters nor other loose groups that may be bound to the cluster assembly (the cluster

assembly is only part of LSS #17). Thus, the estimated mass that the final cluster may have after the individual clusters merge would correspond to $\sim 20\%$ of the Coma cluster's total mass. This is the first time such a complex dynamically young cluster system in the process of formation is identified via a WAT radio galaxy.

5.6 Summary and conclusions

We have analyzed a wide angle tail (WAT) radio galaxy, CWAT-01, first resolved in the VLA-COSMOS survey. The multiwavelength data set of the COSMOS survey have enabled us to identify and analyze the environment of CWAT-01 in several independent ways. The cluster structure revealed via CWAT-01 seems to be more complex than any structure hosting WAT galaxies reported in the past. We summarize the basic findings of this analysis as follows:

- The lengths of the Eastern and Western radio jets of CWAT-01 are ~ 210 kpc and ~ 160 kpc, respectively, and the bending angle is $\sim 100°$ in the projected plane of the sky. It seems to be asymmetric and at this point we cannot rule out that the asymmetry is caused by projection effects. The 1.4 GHz radio power of $P_{1.4} = 2.0 \times 10^{24}\,\mathrm{W\,Hz^{-1}}$ puts CWAT-01 on the lower end of the FRI-II break region where WATs are usually found.

- The host galaxy of CWAT-01 is an elliptical galaxy with a shallower surface brightness profile than predicted by the de Vaucouleurs law. It is the brightest cluster galaxy (BCG) in the CWAT-01 parent cluster. The surface brightness profile is very well fit by the Sersic $r^{1/n}$ law with $n = 5$, $r_{\mathrm{eff}} = 8.2$ kpc and $\mu_{\mathrm{eff}} = 22.11\,\mathrm{mag\,arcsec^{-2}}$ consistent with values typical for brightest cluster galaxies (cD/D).

- Applying several hydrodynamical models, taking ram pressure and buoyancy forces into account, to explain the observed bending of the radio jets of CWAT-01, the allowed range of the galaxy velocity relative to the ICM is approximately $300 - 550$ km s^{-1}. Both, the upper and lower velocity are higher than is expected for dominant galaxies (i.e. BCGs) in relaxed systems.

- The cluster hosting CWAT-01 (CWAT-01 parent cluster) was detected in diffuse X-ray emission. The luminosity weighted temperature of the cluster is ~ 1.7 keV consistent with poor cluster temperatures. The total mass within the r_{500} radius is $\sim 5.8 \times 10^{13}\,M_\odot$. The cluster shows evidence for subclustering, both in diffuse X-ray emission and in the spatial distribution of galaxies found from the optical analysis applying the Voronoi tessellation-based approach (VTA). The distribution of early type galaxies is not centrally concentrated, it is irregular and partitioned into two apparently distinct subclumps.

- The CWAT-01 parent cluster itself is part of a larger cluster assembly consisting of a minimum of 4 clusters within ~ 2 Mpc distance identified via diffuse X-ray

emission. The ICM temperatures of the three clusters surrounding the CWAT-01 parent cluster are in the $1.4 - 1.5$ keV range consistent with temperatures of poor clusters. The total masses of the clusters within the r_{500} radius are in the range of about $(4.1 - 4.4) \times 10^{13} M_\odot$.

- The Voronoi tessellation-based approach (VTA) results indicate that there is at least one more loose group that is likely bound to the system. From the X-ray detection limit for diffuse sources we infer that the total mass of this group must be less than $1.5 \times 10^{13} M_\odot$.

The whole cluster structure described in this paper is encompassed in a large-scale structure component, LSS #17, reported in Scoville et al. (2007b). LSS #17 is elongated in NS direction and extends ~ 4 Mpc along the major axis. Our results strongly indicate that we are witnessing the formation of a large cluster from an assembly of multiple clusters, consistent with the scenario of hierarchical structure formation. If this is the case, then the estimated minimum total mass of the final single cluster after the poor clusters merge would correspond to $M \sim 2.0 \times 10^{14} M_\odot$ or $\sim 20\%$ of the Coma cluster mass. In this scenario, the large velocity of the CWAT-01 host galaxy relative to the ICM can easily be explained. The CWAT-01 parent cluster seems not to be relaxed, thus a plausible explanation of the motion of the galaxy relative to the ICM is interaction of the two identified subclumps (SC1 and SC2) within the cluster. On the other hand, we cannot rule out the gravitational influence of the other poor clusters as a cause for inducing such a velocity.

Resolving the detailed physics causing the bending of the radio jets of CWAT-01, the dynamical interplay between and within particular clusters as well as the spectroscopic confirmation of the physical connection of the clusters has to await the completion of the zCOSMOS program (Lilly et al. 2007). Nevertheless, our results support the idea that WAT galaxies are tracers of galaxy clusters, in particular dynamically young ones.

Chapter 6

Summary and outlook

The main aim of this thesis has been to expand our understanding of properties of radio-luminous sources, and place them into the general context of global properties of galaxies and their evolution. In this chapter a summary of the obtained results as well as future prospects are presented.

6.1 The faint radio population and its cosmic evolution

In the following section the major results of this thesis related to the faint radio population are summarized, and ongoing and future projects are discussed.

6.1.1 The submillijansky radio population

VLA-COSMOS Large Project

The VLA-COSMOS Large Project is state-of-the-art in current radio astronomy as it encompasses the widest area $(2\square^\circ)$ survey at 1.4 GHz (20 cm) with a resolution of only $1.5''$ and unprecedented sensitivity of $10.5\,(15)\,\mu$Jy beam^{-1} over the full $1\,(2)\square^\circ$. These observations have provided the basic data-set for the science presented in this thesis. Obtaining the 1.4 GHz mosaic has required a major effort of combining large amounts of telescope time (250 h with the VLA in A-array, and 25 h in C-array), computational power (it took more than two weeks of pure computation time only to image the 23 pointings), and human resources (about 2 years were required to observe, image, catalog, and thoroughly test the data). The pointing layout of the survey has been designed as a hexagonal pattern that consists of 23 individual overlapping pointings allowing to maximize a uniform noise coverage over the $2\square^\circ$. Exactly this uniform and low rms over the full large field makes the VLA-COSMOS mosaic exceptional compared to other deep radio surveys which usually observe smaller sky-areas with very non-uniform noise that substantially rises towards the edges of the field (e.g. Fomalont et al. 2006; see also Tab. 2.1).

The VLA-COSMOS source catalog has been carefully constructed using well tested automatic source-finding algorithms. Generally, in any survey sources that have intrinsically large angular sizes may be observed as multiple discrete components which is caused by the sources' surface brightness combined with the observational flux limit. It is extremely difficult to identify such objects and extract their flux densities in an automated way. This is in particular true in a radio survey as e.g. radio galaxy morphologies can be very complex. Therefore, special care was paid to identify such objects (mostly radio galaxies with (double-)jet radio morphologies). It is noteworthy that most other publically available catalogs at 20 cm (e.g. FIRST, NVSS) have not undertaken such an effort, and provide only component catalogs, implying that, when working with these tables, large extended sources first have to be identified (which is not trivial), and then combined either from the multiple entries in the catalog or from the images themselves.

The generated VLA-COSMOS source catalog contains an impressive number of $\sim 2,400$ radio sources with a signal to noise equal to, or greater than, 5 ($\sim 50\ \mu$Jy), providing to date the largest and most uniform statistical sample of radio sources down to such faint flux densities. About 90% of these sources have submillijansky flux densities, making the VLA-COSMOS 1.4 GHz radio sample the optimal data set to study the properties of the faint radio population that consists of two main populations: AGN and star forming galaxies. However, the relative contribution of AGN and star forming galaxies to the submillijansky radio population is not well understood, and has been hotly debated in the past (e.g. Condon 1984a; Windhorst et al. 1985a; Benn et al. 1993; Gruppioni et al. 1999; Seymour et al. 2004; Simpson et al. 2006; Fomalont et al. 2006). One of the major aims of this thesis has been to resolve this controversy about the composition of the faint radio population. This has been approached by an in-depth panchromatic statistical study of the VLA-COSMOS radio sources, in particular by developing a new method for disentangling AGN (both radio-quiet and radio-loud) from star forming galaxies.

New method for separating AGN from star forming galaxies

A new method has been developed to discriminate between AGN and star forming galaxies based purely on photometric – rest-frame color – data, thus eliminating the need for time-consuming spectroscopy. One major advantage of this method is that it separates well *low luminosity* AGN, such as Seyfert, LINER galaxies and absorption line AGN from star forming galaxies using a minimal number of parameters (the NUV – NIR SED). This makes it favorable for general purposes as it carries the potential to be efficiently applied to other data-sets where similarly to the VLA-COSMOS radio sources (see below) the two dominating sub-populations are star forming and AGN galaxies.

The separation is based on a rest-frame color – P1 – which is a linear superposition of colors in the Strömgren photometric system encompassing the wavelength range of 3500 – 5800 Å (Smolčić et al. 2006). The method has been well calibrated and thoroughly tested using a large local sample of galaxies representative of the VLA-COSMOS population at higher redshifts ($\sim 7,000$ sources in the SDSS "main" spectroscopic galaxy sample, NVSS and IRAS surveys). These local galaxies have been used to infer the statistical properties

of the photometrically selected samples of star forming and AGN galaxies, yielding a high completeness of the selected star forming ($\sim 85\%$) and AGN ($\sim 95\%$) galaxy samples, with a fairly modest contamination of $\sim 20\%$ of AGN in the first, and $\sim 5\%$ of star forming galaxies in the latter sample. Using the local optical - radio -IR galaxy sample (SDSS - NVSS - IRAS) it has been demonstrated that the rest-frame color based separation method is *not* biased against selecting dusty star forming galaxies. This is an especially important aspect for a radio-selected sample as radio emission is a valuable dust-unbiased star formation tracer.

The high angular resolution ($1.5''$), and the excellent astrometric accuracy (130 mas; see Chap. 2) of the VLA-COSMOS survey have allowed me to essentially unambiguously identify counterparts of VLA-COSMOS sources at other wavelengths (optical, MIR, X-ray; COSMOS Project; see Chap. 3). Galaxies in the VLA-COSMOS radio population (i.e. point sources – stars and QSOs – excluded) that have been securely associated with counterparts out to faint optical limits ($i \leq 26$) and $z \leq 1.3$ have been classified into star forming and AGN galaxies using the newly developed rest-frame color based method. The rest-frame color P1 has been computed by χ^2 fitting of the observed NUV – NIR SED of the VLA-COSMOS galaxies with a realization of 100,000 model spectra generated with the Bruzual & Charlot (2003) stellar population synthesis models, and its accuracy has been extensively tested (and shown to be ~ 0.1 mag). Further, in order to infer the effectiveness of the star forming/AGN galaxy discrimination of the VLA-COSMOS sources, the panchromatic properties of the identified star forming and AGN galaxies have been thoroughly studied, and compared with other independent diagnostic schemes that rely on mid-infrared colors and optical spectroscopy, demonstrating a remarkable agreement and confirming the validity of our classification method.

In summary, a new method that separates star forming from (low-luminosity) AGN galaxies, applicable out to high redshifts ($z \sim 1.3$), has been developed, robustly tested, and applied to the VLA-COSMOS 1.4 GHz radio – optical ($i \leq 26$) sources out to $z = 1.3$. Hence, well defined statistical radio – optical samples of star forming (340) and AGN (601) galaxies with submillijansky radio fluxes, located out to $z = 1.3$, have been constructed. This new method based on UV to NIR SEDs has the potential to become a standard tool also for other samples drawn from other wavelengths where the main populations are star forming and AGN galaxies.

The composition of the submillijansky radio population

In addition to the above described star formation/AGN galaxy discriminator, that has been applied to the VLA-COSMOS sources with secure optical counterparts ($i \leq 26; z \leq 1.3$), the panchromatic – optical/NIR, MIR and X-ray – properties of the *complete* VLA-COSMOS radio source sample ($\sim 2,000$ sources) have been used in order to put, for the first time, robust limits on the composition of the submillijansky radio sources ('population mix' hereafter). Inferring the 'population mix' has been subject of many studies for the past two decades that yielded controversial results estimating the fraction of star forming galaxies to range from about 20% to 80% (e.g. Fomalont et al. 2006; Padovani et al. 2007;

see Chap. 3 for more details). One of the major reasons for this discrepancy has been a conspiracy of good star formation/AGN classifiers usually ruling out statistically complete radio samples, and vise versa. The analyses presented in this thesis have overcome this problem by using various panchromatic diagnostic methods (see Chap. 3 for details) on a large statistical sample of ($\sim 2,000$) submillijansky radio sources, allowing a deep insight into the statistical composition of the faint radio population, not affected by any other (e.g. optical flux) limits. Our main finding is that star forming galaxies form only about $30 - 40\%$ of the submillijansky population, while the remainder is composed of AGN and QSOs.

6.1.2 The evolution of radio sources

The cosmic star formation history based on 1.4 GHz radio data

In Chap. 4 the luminosity evolution of star forming galaxies at 1.4 GHz has been constrained out to $z = 1.3$ by using the well constructed sample of VLA-COSMOS star forming galaxies (see Sec. 6.1.1). Given the large size ($2\square°$) of the VLA-COSMOS field, that samples a comoving volume at $z = 1$ comparable to the one observed locally with the SDSS (DR1), for the first time the evolution of the cosmic star formation rate in the rare, most intensely star forming galaxies ($\gtrsim 100\ M_\odot\ \mathrm{yr}^{-1}$) has been derived with high precision. Our results imply a slightly slower evolution for these massively star forming galaxies than previously predicted based on MIR data. Overall, we find that the radio-derived cosmic star formation history agrees well with other wavelength-based (Hα, [OII], UV, FIR) findings, when these are corrected for dust-obscuration where necessary. This verifies the necessary assumptions about the large (luminosity-dependent) corrections required at shorter wavelengths, especially in the UV regime.

Future prospects: The co-evolution of star formation and supermassive black hole accretion

The AGN luminosity function, and its evolution, constrain the cosmic formation history of supermassive black holes in centers of galaxies. As to date radio surveys allowed in-detail studies only of the evolution of radio-loud AGN (Dunlop & Peacock 1990; Willott et al. 2001; Snellen & Best 2001; Clewley & Jarvis 2004), which are genuinely rare – about 10 times less abundant than their radio-quiet counterparts (Goldschmidt et al. 1999; Ivezić et al. 2002) – optical and X-ray surveys have taken the lead in statistical AGN studies (e.g. Richards et al. 2002; Ueda et al. 2003). However, these short-wavelength windows are heavily biased against highly dust-obscured sources. Therefore, the radio – dust-unbiased – regime provides an essential, complementary view on the accretion history of the universe. Furthermore, the accretion history of supermassive black holes may be closely related to the star formation in their host galaxies. It has been demonstrated that the evolution of the luminosity density of star forming and AGN galaxies, where the first traces the cosmic star formation history and the latter the cosmic black hole accretion history,

exhibit a similar behavior out to $z \sim 2$ (e.g. Boyle & Terlevich 1998; Franceschini et al. 1999; Silverman et al. 2007).

The luminosity function for radio selected star forming galaxies, its evolution, and the radio-based cosmic star formation history have been presented in Chap. 4, and are summarized above. However, to date the 1.4 GHz luminosity function for (radio-quiet) AGN is known only in the local universe (Sadler et al. 1999; Best 2004), and its evolution is not well understood. In simulations the evolution of radio-quiet AGN is usually approximated using very indirect means, such as e.g. the evolved hard X-ray $(2-10 \text{ keV})$ AGN luminosity function (Ueda et al. 2003), converted to monochromatic 1 keV luminosity (known to correlate with 1.4 GHz luminosity; Brinkmann et al. 2000), and furthermore essentially 'guessing' the additional contribution of obscured (Compton thick) AGN (e.g. Jarvis & Rawlings 2004). Our large statistical samples of (~ 350) star forming and (~ 600) AGN from VLA-COSMOS will be used to address the co-evolution of the cosmic star formation rate and black hole accretion out to $z = 1.3$, from a dust un-biased perspective. For the first time, the pure radio evolution of the 1.4 GHz luminosity function for radio-quiet AGN will be robustly constrained. Our first results on the luminosity functions, derived separately for star forming and AGN galaxies out to $z = 1.3$, are shown in Fig. 6.1, implying a stronger luminosity evolution for star forming galaxies than for AGN.

It is noteworthy that constraining the luminosity function evolution for star forming and AGN galaxies at 1.4 GHz is of immediate relevance for the preparation of next generation radio interferometers (e.g. the Square Kilometre Array – SKA; commissioning scheduled for ~ 2020, and the Expanded VLA – EVLA; commissioning scheduled for 2009) that will reach orders of magnitudes deeper than current radio instruments. In particular, the star forming and AGN galaxy luminosity functions are planned to be constrained to fainter limits than currently by using the already existing deeper observations at 1.4 GHz of the inner 1□° of the COSMOS field (VLA-COSMOS Deep Project). The higher sensitivity of the VLA-COSMOS Deep, compared to the Large, Project allows one to probe a factor of ~ 2 fainter in luminosity, and these data will be combined with radio image stacking in order to probe even fainter levels of the luminosity functions. Reaching fainter luminosities will expand the parameter space allowing for more complex parameterizations of the luminosity function evolution, such as simultaneous density and luminosity evolution, or even luminosity-dependent density evolution.

6.2 Radio galaxies in galaxy clusters

Radio galaxies are important for many cosmological aspects. For example they can efficiently be used as tracers of dense environments (e.g. Zanichelli et al. 2001), such as high-redshift (e.g. Blanton et al. 2003; Miley et al. 2006) and/or dynamically young galaxy clusters (Chap. 5; Smolčić et al. 2007a). Furthermore, recently semi-analytical models have proposed that radio galaxies may be the main driver for cosmological processes related to galaxy formation (Croton et al. 2006; Bower et al. 2006). In the following the results presented in this thesis on the newly identified merging galaxy cluster assembly hosting the
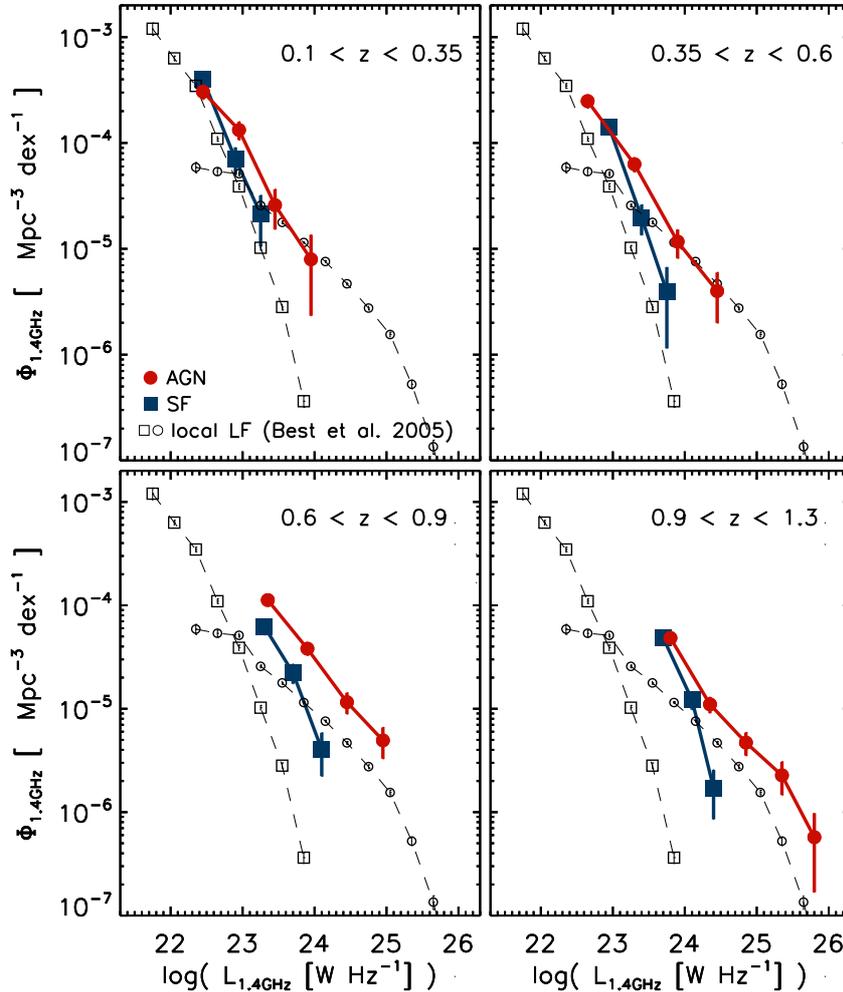
Figure 6.1   First results on the 1.4 GHz luminosity functions (LFs) for star forming (blue filled squares) and AGN (red filled squares) galaxies out to $z = 1.3$ derived using the well defined VLA-COSMOS SF and AGN samples (see Chap. 3 for details). The LFs were computed as described in Chap. 4, and the redshift range is indicated in each panel. For comparison the locally derived LFs (Best et al. 2005) for star forming (open squares) and AGN (open circles) galaxies are also shown in each panel. These results will for the first time allow to constrain the cosmic evolution of AGN at 1.4 GHz, shedding light on the co-evolution of the cosmic star formation rate (presented in Chap. 4) and black hole accretion from a dust unbiased perspective since ~ 5 Gyr after the Big Bang (see text for details).

peculiar radio galaxy CWAT-01 are summarized, and future scientific projects related to galaxy cluster evolution are discussed.

6.2.1   CWAT-01 galaxy cluster assembly

An in-depth case-study of a radio-luminous AGN, a wide angle tail radio galaxy named CWAT-01, found in the VLA-COSMOS survey has been presented in Chap. 5. CWAT-01 has been associated with a highly complex galaxy cluster assembly, consistent with the idea that such radio galaxies are efficient tracers of galaxy clusters. The assembly consists of at least one optically detected and four X-ray luminous clusters within ~ 2 Mpc distance at the same redshift ($z \cong 0.2$), and is most probably in the process of forming a large cluster, that will eventually contain a total mass of at least $\sim 20\%$ of the Coma cluster mass. Hence, a dynamically young, merging cluster environment in the process of forming a large cluster has been identified, consistent with the standard ΛCDM cosmological model that suggests a hierarchical, bottom-up, structure formation scenario. The complexity of this cluster assembly implies that it may become a proto-typical example for merger of

multiple cluster constituents at intermediate redshift. Therefore, detailed studies of this cluster assembly, especially accurately mapping its internal kinematics and structure, will shed light on processes deemed important for cosmological structure growth.

It is noteworthy that the 5 identified clusters have recently been spectroscopically verified to be exactly at $z = 0.22$ via 31 galaxy spectra (see Fig. 6.2) obtained by the zCOSMOS survey (Lilly et al. 2007) which samples spectroscopy for bright objects ($i < 22.4$) in the COSMOS field at low spectral resolution ($R = 300 - 500$). In order to map the precise internal kinematics, structure, and properties of the clusters, higher resolution spectroscopy (R $\sim$ 1000) out to faint levels ($r = 24$) for $\sim$ 250 potential cluster members using the ESO/VLT (FORS2 instrument) has already been proposed.
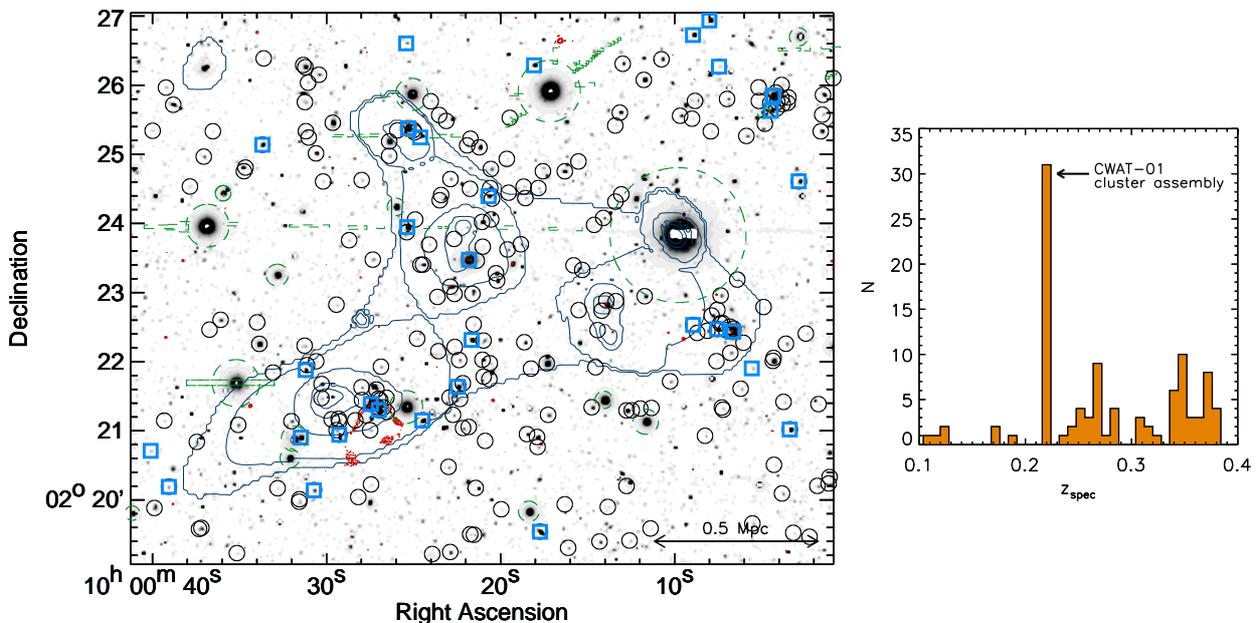

Figure 6.2 *Left panel:* Grey scale SUBARU i^+ band image of the CWAT-01 galaxy cluster assembly overlaid with X-ray contours (thin dark-blue contours on large scales). The shown area is $\sim (2.1 \times 1.7)$ Mpc^2 (at $z = 0.22$) with thin black circles denoting the photometrically selected potential cluster member galaxies. CWAT-01 is part of the cluster at the lower-left in the panel, and shown in red contours. Regions outlined with green lines are flagged areas in the photometric catalog. Bold blue squares indicate the galaxies with available spectroscopy that puts them exactly at $z = 0.22$ (see right panel). *Right panel:* The distribution of the *spectroscopic* redshifts for galaxies with $i < 22.4$ obtained by the zCOSMOS survey in the area $10' \times 7'$ around the cluster assembly, shown in the left panel. The overdense structure at $z = 0.22$ is clearly identified (blue squares in the left panel).

6.2.2   Future prospects

Galaxy clusters consist of two major components: i) individual member galaxies emitting in the UV-optical through IR regime and ii) a hot plasma encompassing them (i.e. the intra-cluster medium – ICM), most prominent in the X-rays. Clusters containing

moderate-power radio galaxies provide even more information with cosmological implications (e.g. Fabian et al. 2003; Forman et al. 2005): radio galaxies are now thought to be the main drivers of the so-called 'AGN energy feedback' process, which was recently invoked in cosmological models (Croton et al. 2006; Bower et al. 2006). In order to explain the observed galaxy properties, in particular the truncation at the upper end of the galaxy mass function, cosmological models have introduced energy feedback from AGN as the most relevant mechanism for the suppression of mass growth (Croton et al. 2006; Bower et al. 2006). It is believed that the 'radio mode', i.e. the energy outflows from radio galaxies (as these are energetically most favorable), heats the surrounding gas, and thereby truncates star formation in the host galaxy disabling it to grow too high in mass. However, it is debated both theoretically and observationally, exactly how (and if) the AGN feedback works. Observationally, particular cases have been found where AGN energy outflows have been demonstrated to directly impact the AGN's environment. Namely, in galaxy clusters which contain central *cooling flows*, AGN feedback may account for the observed *lack* of cooler gas in the cluster core. However, direct evidence of such a radio – thermal gas interplay has been seen in only a few local examples (e.g. Fabian et al. 2003; Forman et al. 2005), and it is unclear whether this is common behavior.

The above theoretical suggestions and observational results invoke interesting cosmological aspects that require further investigations. With about 50 X-ray identified galaxy clusters hosting a radio galaxy, detected out to redshifts of ~ 1.2, the COSMOS survey is optimally suited for in-depth studies of clusters that contain a radio galaxy at both intermediate ($0.2 \leq z \leq 0.6$) and high redshifts ($z > 0.6$). Both redshift ranges are similarly important, as previous detailed studies were limited to small and heterogeneous samples at these cosmic times (e.g. Zhang et al. 2005; Popesso et al. 2007, and AGN feedback processes were studied in detail only in a few local examples (e.g. McNamara et al. 2000; Blanton et al. 2001; Dunn & Fabian 2006). A project exploiting the COSMOS data, and performing spectroscopic follow-up to advance the topic of galaxy cluster evolution with a particular focus on the impact of AGN feedback on galaxy formation is underway.

6.3   Further radio observations of the COSMOS field

Three further directions need to, and will, be taken for increasing our knowledge of galaxy properties and their evolution from a radio perspective. These are observations of the COSMOS field at i) higher angular resolution, ii) higher sensitivity and iii) additional radio frequencies.

The e-Merlin radio interferometer provides the largest potential to improve on the first point. Using this instrument, observations at 1.4 GHz over the entire $2\square°$ field can (and are being planned to) be performed at comparable sensitivity to the Large Project, but with an angular resolution higher by *one order of magnitude*. This sub-arcsecond ($\sim 0.15''$) angular resolution would enable radio morphology studies i) in star forming galaxies, discriminating from the radio perspective alone between radiation arising from the nuclear (most probably AGN) vs. disk (star formation) galaxy component, and ii) in

radio galaxies, allowing better constraints on the structure and physics of radio jets and lobes with the immediate application in galaxy cluster studies (see previous section). Such high angular resolution would enable reaching closer to understanding an important aspect of galaxy properties, namely the properties, fraction, and evolution of *composite objects*, where star formation and black hole accretion co-exist and -evolve, possibly also inducing each other (e.g. Boyle & Terlevich 1998; Franceschini et al. 1999; Silverman et al. 2007).

Higher sensitivity observations have already been performed in the inner $1\square°$ of the COSMOS field (VLA-COSMOS Deep Project) reaching an rms of $\sim 7\ \mu$Jy beam^{-1}. These observations have been taken in 2006; the data reduction, imaging, and mosaicing have been performed by VS and ES as described in Chap. 2. The final catalog contains 3,744 sources down to a 4σ limit at $2.5''$ resolution, and was generated by A. Datta and CC. As described in Sec. 6.1.2 these data will be important to better constrain the faint end of our 1.4 GHz radio luminosity functions for star forming and AGN galaxies out to $z = 1.3$.

Additional observations of the entire COSMOS field at other radio frequencies are essential for statistical studies of the radio synchrotron spectrum emitted from different radio populations posing the question: Is the hardness of the synchrotron spectrum different for star forming and AGN galaxies? Further, constraining the synchrotron spectrum for radio galaxies allows detailed studies of the physics, and energy losses, of the synchrotron radiation in radio galaxies, providing important implications on AGN feedback studies. In particular, the EVLA (Expanded VLA) is planned on being used for observations of the COSMOS field at both lower and higher frequencies than 1.4 GHz (320 MHz, 4.8 GHz).

Appendix A

Summary of all-sky surveys

A.1 The Sloan Digital Sky Survey

The Sloan Digital Sky Survey (SDSS; York et al. 2000; Stoughton et al. 2002; Abazajian et al. 2003, 2004, 2005; Adelman-McCarthy et al. 2006, 2007) is a spectroscopic and photometric survey that aims at mapping one-quarter of the entire sky ($\sim 10,000\square°$) and perform a comprehensive redshift survey of galaxies, quasars and stars. To date the SDSS has made publically available photometry for ~ 215 million objects observed over 8,000$\square°$ (DR5) in five NUV – NIR broad photometric bands (u, g, r, i, z) with effective wavelengths of (3551, 4686, 6165, 7481, 8931) Å, and a median angular resolution of $1.4''$. Spectroscopy at a resolution of $R = \lambda/d\lambda = 1800$ is systematically obtained in the wavelength range of 3800Å to 9200Å with targeting magnitude limits of $r_{\mathrm{Pet}} < 17.7$ for galaxies and $i < 19.1$ for quasars. In total, to date ~ 1 million spectra, observed over 5740$\square°$, have been made publically available. The spectroscopy of extragalactic sources is divided into three main samples: the 'main' galaxy sample (Strauss et al. 2002), the luminous red galaxy sample (Eisenstein et al. 2001), and quasars (Richards et al. 2002). Details about the survey, and its extension (SDSS-II; DR6) can be found at *www.sdss.org*.

A.2 The NRAO VLA Sky Survey (NVSS)

The National Radio Astronomy Observatory VLA Sky Survey (NVSS; Condon et al. 1998) has observed the entire sky north of $-40°$ declination at 1.4 GHz (20 cm) continuum with the Very Large Array (VLA). The major product is a catalog of ~ 1.8 million discrete sources. Note that extended sources, that consist of several discrete components, have not been matched in the catalog, but are reported separately. The angular resolution of the survey is $45''$, and the positional uncertainties vary from less than $1''$ for relatively strong (> 15 mJy) point sources to $7''$ for the faintest (~ 2.3 mJy) sources. More details can be found at *www.cv.nrao.edu/nvss*

A.3   The Faint Images of the Radio Sky at 20 cm

The Faint Images of the Radio Sky at Twenty-centimetres (FIRST; Becker et al. 1995) has mapped over $10,000\square°$ of the North Galactic Cap at 1.4 GHz (20 cm) continuum with the Very Large Array. The angular resolution is $5''$, and the positional accuracy varies from less than 0.5" at the 3 mJy to 1" at the survey detection threshold of 1 mJy. A discrete source catalog with $\sim 811,000$ sources has been made publically available. Components of extended sources are reported separately in the catalog, and it needs to be cautioned that sources with angular sizes larger than $10''$ are out-resolved by the survey, and therefore their integrated fluxes are underestimated. More details can be found at *sundog.stsci.edu*.

A.4   The Infrared Astronomical Satellite (IRAS) All-sky Survey

IRAS is the abbreviation for the Infrared Astronomical Satellite (Neugebauer et al. 1984) that conducted an almost all-sky survey ($\sim 98\%$ of the sky) in four broadband IR photometric channels at 12, 25, 60 and 100 μm. The angular resolution varied between $\sim 0.5'$ at 12 μm to $\sim 2'$ at 100 μm. The positional accuracy is about $20''$, or better. Two main catalogs have been generated: The IRAS Point Source Catalog (IRAS PSC) containing $\sim 250,000$ sources with angular sizes less than approximately $0.5'$, $0.5'$, $1.0'$, and $2.0'$ at 12, 25, 60 and 100 μm, respectively; and the IRAS Faint Source Catalog (IRAS FSC). The sensitivity of the FSC exceeds that of the PSC by about a factor of 2.5. The FSC contains data for $\sim 173,000$ point sources with flux densities typically greater than 0.2 Jy at 12, 25, and 60 μm and greater than 1 Jy at 100 μm. Although the angular resolution is of the order of one arcminute, and the faint limits reach only 1 Jy, IRAS remains a highly valuable resource due to its important wavelength range and nearly full sky coverage. More details can be found at *lambda.gsfc.nasa.gov/product/iras*

A.5   2MASS

The Two Micron All Sky Survey used two telescopes located in the northern and southern hemispheres (Mt. Hopkins, Arizona and Cerro Tololo/CTIO Chile, respectively) to observe the entire sky in three near IR photometric bands around 2 μm: J (1.25 μm), H (1.65 μm), and Ks (2.17 μm). The survey's 10σ point source sensitivity is about 1 mJy. The main 2MASS catalogs contain ~ 471 million point sources (2MASS PSC) and ~ 1.65 million extended sources (2MASS XSC). Details about 2MASS photometry is given in Jarrett et al. (2000).

A.6   The 2dF Galaxy Redshift Survey

The 2dF Galaxy Redshift Survey (2dFGRS), integrated with the 2dF QSO survey, is a major spectroscopic survey performed using the 2dF (Two Degree Field) facility built by the Anglo-Australian Observatory. About 220,000 spectra for objects brighter than $b_J = 19.45$ (extinction-corrected) over $\sim 1500\square°$ have been obtained yielding reliable redshifts. More details can be found here: *magnum.anu.edu.au/ TDFgg.*

A.7   GALEX

The Galaxy Evolution Explorer (GALEX) satellite was launched in 2003 and will eventually map the entire sky in two photometric ultraviolet bands: NUV (1750 - 2800Å) and FUV (1350 - 1750Å) down to AB magnitudes of 20 to 25. Further details can be found at *www.galex.caltech.edu.*

Appendix B

Relevant equations

B.1 The computation of radio luminosity

The rest-frame 1.4 GHz luminosity is calculated in the following way:

$$L_{1.4\text{GHz}} = \frac{4\pi D_L^2}{(1+z)^{1-\alpha}} F_{1.4\text{GHz}} \tag{B.1}$$

where $F_{1.4\text{GHz}}$ is the total flux density observed at 1.4 GHz frequency, D_L is the luminosity distance, z is the redshift and α is the spectral index (assuming a synchrotron spectrum $\propto \nu^{-\alpha}$).

B.2 Conversions of 1.4 GHz radio luminosity to star formation rate

The star formation rate for an individual galaxy is directly proportional to its 1.4 GHz radio luminosity. There are two commonly adopted calibrations. The first was initially developed by Condon (1992) based on the Milky Way supernovae rate, and later modified by Haarsma et al. (2000). The second was derived by Bell (2003), based on the total IR – radio correlation. These two calibrations agree within a factor of ~ 2.

Condon (1992) used an extended Miller-Scalo (1979) initial mass function (IMF), $\psi(M) \propto M^{-2.5}$, and modeled the average formation rate of stars more massive than 5 $M_\odot$ (with an upper cut-off mass of 100 $M_\odot$). This model was modified by Haarsma et al. (2000) to account for the formation of lower mass stars ($0.1 - 100\ M_\odot$), as well as for a different (Salpeter) IMF, $\psi(M) \propto M^{-2.35}$. The correlation between 1.4 GHz luminosity and star formation rate given by Haarsma et al. (2000) yields:

$$\text{SFR } [M_\odot\ \text{yr}^{-1}] = 1.20 \times 10^{-21}\ L_{1.4\text{GHz}} \tag{B.2}$$

where $L_{1.4\text{GHz}}$ is the 1.4 GHz radio luminosity in units of W Hz^{-1} (see Appendix B.1), and a typical synchrotron spectral index of 0.8 is assumed. Assuming a synchrotron spectral index of 0.7 instead would yield a conversion factor of 1.16×10^{-21}.

The conversion of 1.4GHz luminosity to star formation rate proposed by Bell (2003) is given as follows:

$$
\text{SFR } [\text{M}_\odot \, \text{yr}^{-1}] = \begin{cases} 5.52 \times 10^{-22} \, \text{L}_{1.4\text{GHz}} \, , & \text{L}_{1.4\text{GHz}} > \text{L}_\text{c} \\ \frac{5.52 \times 10^{-22}}{0.1 + 0.9(\text{L}_{1.4\text{GHz}}/L_c)^{0.3}} \, \text{L}_{1.4\text{GHz}} \, , & \text{L}_{1.4\text{GHz}} \leq \text{L}_\text{c} \end{cases}
\tag{B.3}
$$

where $\text{L}_\text{c} = 6.4 \times 10^{21}$ W Hz^{-1}, and $\text{L}_{1.4\text{GHz}}$ is the 1.4 GHz radio luminosity in units of W Hz^{-1}.

The difference in the derived star formation rates using the two calibrations is shown in Fig. B.1 as a function of 1.4 GHz luminosity. This calibration given by Bell (2003) gives star formation rates lower by a factor of ~ 2 for $\text{L}_{1.4\text{GHz}} \gtrsim 6 \times 10^{21}$ W Hz^{-1} compared to Haarsma et al. (2000). As the luminosity decreases the Bell (2003) star formation rates approach those above, and become higher for luminosities of $\text{L}_{1.4\text{GHz}} \lesssim 2 \times 10^{20}$ W Hz^{-1}.
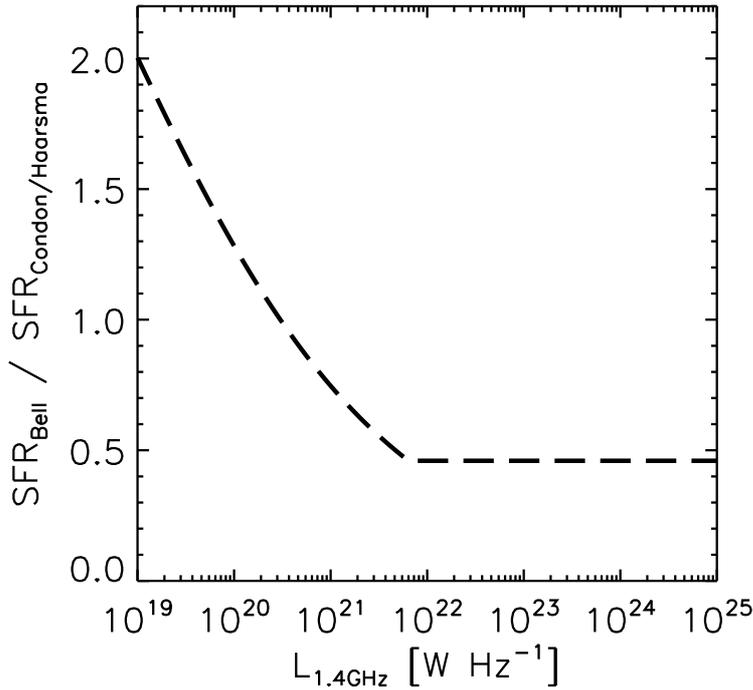
Figure B.1   The ratio of star formation rates obtained using the 1.4 GHz luminosity to star formation rate calibration from Bell (2003, eq B.3) and Haarsma et al. (2000, eq B.2) as a function of 1.4 GHz radio luminosity. There is a factor of ~ 2 discrepancy changing with luminosity.

> "It was the best of times, it was the worst of times"
> Charles Dickens, A Tale of Two Cities (1859)

> ”Bilo je to najbolje vrijeme, bilo je to najgore vrijeme”
> Charles Dickens, Priča o dva grada (1859)

Mnogi su ljudi, kojima sam beskrajno zahvalna, doprinjeli ovom putu. Najprije bih htjela zahvaliti Koradu Korleviću što mi je pokazao da granice ne postoje; svaki individualac je jednako važan u pokretanju svijeta. Zahvaljujem Krešimiru Pavlovskom što mi je osobnim trudom stvorio prilike za moj pčetni znanstvani rad i što me tretirao s ogromnim poštovanjem još za vrijeme dodiplomskog studija. Vječno sam zahvalna Željku Iveziću što mi je omogućio ući u svjetsku ligu astronomije i cijelo vrijeme bio snažan stup oslonac. Hvala Hans-Walter Rixu što mi je, još u Vatikanskoj ljetnoj školi 2003, stvorio mogućnost za poslijediplomski studij u Heidelbergu.

Htjela bih zahvaliti Chris Carilliu na podršci i pomoći vezanoj uz moj pslijediplomski rad te Irini Sakelliou i Alexis Finoguenovu što su mi učinili visoko energetsko zračenje iz skupova galaksija vrlo jasnim. Posebno hvala ide Eric Bellu na mnogim diskusijama vezanim uz znanstvene projekte na kojima sam radila te pomoći oko tehničkih procedura i detalja; zahvaljujući Ericu Monte Carlo simulacije su mi danas sitnica. Također zahvaljujem Gianni Zamoraniu na mnogim diskusijama te detaljnom i temeljitom poimanju znanosti koje je mnogo doprinjelo mojem znanstvenom nadograđivanju; te Nick Scovilleu što mi je otvorio put u Caltech. Posebno zahvaljujem Evi Schinnerer što mi je omogućila da radim na odličnom novom projektu – COSMOS – i na strpljivosti za vrijeme mojih početaka u radio astronomiji te uvijek odličnim komentarima vezanim uz clanke koje sam pripremala.

Mojim prijateljima u Heidelbergu i Zagrebu – Dominiku, Florianu, Isabel, Marie-Helene, Anji, Dinku, Idi, Maji-Lauri i Kristini – puno hvala što su mi ispunjavali i uljepšali vrijeme provedeno u Heidelbergu. Posebno zahvaljujem Dominiku što je uvijek strpljivo slušao moje probleme i uvijek bio voljan otići na pivu nakon (vrlo) dugog radnog dana.

Veliko hvala mojoj cijeloj obitelji na podršci i pomoći. Uvijek ste bili, i uvijek će mi biti, najveći oslonac u mom životu. Posebno bih istaknula klince – Borisa, Marka, Martina, Tomislava i Patriciu – koji su me uvijek znali oraspoložiti u djeliću sekunde. Teta Hana i Željka, hvala na ekspeditivnoj pomoći oko pravog prijevoda gornjeg citata.

Monika, uvijek ću ti biti zahvalna što si bila uz mene u najtežim trenucima, tješila me i oraspoloživala kad je trebalo ...a najviše od svega što si ostala uz mene. Uz tebe je sve lakše.

Iznad svega, moje najveće zahvale idu mami Vesni i teti Zlati. Mama i teta, hvala Vam na konstantnoj podršci i potpori u svakom pogledu. Bez Vas ne bih bila ovdje gdje jesam. Vi ste razlog zbog kojeg sam to sto jesam.

Curriculum Vitae

Vernesa Smolčić
Max-Planck-Institut für Astronomie
Königstuhl 17
69117 Heidelberg
Germany

Phone: +49-(0)6221-528258
Fax: +49-(0)6221-528246
smolcic@mpia.de
http://www.mpia.de/homes/smolcic/

Basic information

Nationality: Croatian

Date of Birth, Sex: February 23rd 1980, Female

Languages: Native Croatian, fluent English and German, good Italian, school knowledge of Latin

Present Position: PhD student, MPIA, Heidelberg, Germany

Future Position: California Institute of Technology, Pasadena, CA, USA; CARMA Postdoctoral Scholar (2008 − 2011)

Education

Research: 2003 − Present (2007)
− Max-Planck Institut für Astronomie, Heidelberg, Germany
− Princeton University Observatory, Peyton Hall, Princeton, USA
− Department of Physics, Faculty of Science, University of Zagreb, Croatia

PhD Studies and Thesis: 2004 − 2007 (submitted)
− University of Heidelberg
− International Max Planck Research School for Astronomy and Cosmic Physics
− Max-Planck Institut für Astronomie, Heidelberg, Germany
− PhD thesis title: *The Faint Radio Population in the VLA-COSMOS Survey: Star Forming Galaxies and Active Galactic Nuclei*
− Supervisors: Dr. Eva Schinnerer, Prof. Dr. H.-W. Rix

Diploma Studies and Thesis: 1998 − 2004
− Department of Physics, Faculty of Science, University of Zagreb, Croatia, graduated April 16th 2004
− Princeton University Observatory, Peyton Hall, Princeton, USA
− Diploma Thesis: *Rest-frame Properties of 99,000 Sloan Digital Sky Survey Galaxies*
− Supervisors: Prof. Dr. Ž. Ivezić, Prof. Dr. K. Pavlovski

Research Interests
- Extragalactic Star Formation
- AGN, Radio Galaxies
- Galaxy Clusters, Large Scale Structure
- Survey Science: (VLA-)COSMOS, SDSS, multi-wavelength follow-up

I. T. Skills
Programming: IDL, SM, Fortran, AIPS, Latex, HTML, PHP
Operating systems: Linux, Windows
Data reduction: optical imaging (DoPhot), radio synthesis imaging (AIPS)

Membership in Scientific Collaborations and Societies
Cosmic Evolution Survey (COSMOS)
Sloan Digital Sky Survey (SDSS)
Sloan Extension for Galactic Understanding and Exploration (SEGUE)
American Astronomical Society (AAS)
Croatian Physical Society (HFD)

Awards and Honors
2006: Ernst Patzer Award (for best refereed publications by young MPIA scientists)
2006: IAU (International Astronomical Union) grant for the XXVI General Assembly, Prague
2003: University of Zagreb Rector's Award (for best research projects by undergraduate students)

Selected Conferences, Workshops and Summer Schools
2007: Legacy of Multi-wavelength Surveys; International Workshop in Xining, China; invited talk
2006: IAU Symposium 235 : "Galaxy Evolution across the Hubble Time"
2005: Workshop on Multi-wavelength Surveys, Ringberg, Germany
2004: IRAM Summer School: "mm Observing Techniques and Applications", Grenoble, France
2003: Vatican Observatory Summer School in Astronomy and Astrophysics: "Observations and Theoretical Understanding of Galaxy Evolution: From the Local Universe to the Distant Universe", Castel Gandolfo, Rome, Italy;
"Spectroscopically and Spatially Resolving the Components of Close Binary Stars workshop", Dubrovnik, Croatia, I also helped organizing this workshop

Teaching
2007: Astronomy - astrophysics Lab Course at the University of Heidleberg
2003: Primary school physics replacement teacher (7th and 8th grades) for several weeks
1995–2004: Mathematics, physics and English tutor of primary and high school students

List of publications

Refereed Publications

a) **Submitted**

20 **Smolčić, V.**, et al., "A new method to separate star forming from AGN galaxies at intermediate redshift: The submillijansky radio population in the VLA-COSMOS survey", submitted to ApJ; Chap. 3 in this thesis

19 **Smolčić, V.**, et al., "The dust un-biased cosmic star formation history derived using 1.4 GHz data from the VLA-COSMOS survey", about to be submitted to ApJ; Chap. 4 in this thesis

18 Sakelliou, I., **Smolčić, V.**, et al., submitted to MNRAS, "The Hot Gas and Galaxies in Abell 2151"

b) **Accepted**

17 Younger, J. D., inter alios **Smolčić, V.**, et al., accepted for publication in ApJ, "Evidence for a Population of High-Redshift Submillimeter Galaxies from Interferometric Imaging"

16 **Smolčić, V.**, Zucker, D., et al., 2007, AJ, 134, 1901, "Improved Photometry of Sloan Digital Sky Survey Crowded-Field Images: Structure and Dark Matter Content in the Dwarf Spheroidal Galaxy Leo I"

15 Adelman-McCarthy, J. K., inter alios **Smolčić, V.**, et al. 2007, ApJS, 172, 634, "The Fifth Data Release of the Sloan Digital Sky Survey"

14 T. Murayama, Y.Taniguchi, N. Z. Scoville, inter alios **Smolčić, V.**, et al., 2007, ApJS, 172, 523, COSMOS special issue, "Lyman alpha Emitters at Redshift 5.7 in the COSMOS Field"

13 C. L. Carilli, M. Ajiki, R. Wang, inter alios **Smolčić, V.**, et al., 2007, ApJS, 172, 518, COSMOS special issue, "Radio and Millimeter Properties of $z \sim 5.7$ Ly alpha Emitters in the COSMOS Field: Limits on Radio AGN, Submm Galaxies, and Dust Obscuration"

12 M. I. Takahashi, Y. Shioya, Y. Taniguchi, inter alios **Smolčić, V.**, et al., 2007, ApJS, 172, 456, COSMOS special issue, "The [O II] λ 3727 Luminosity Function and Star Formation Rate at $z \approx 1.2$ in the COSMOS 2 Square-Degree Field and the Subaru Deep Field"

11 **Smolčić, V.**, Schinnerer. E., et al., 2007, ApJS, 2007, 172, 295, COSMOS special issue, "A Wide Angle Tail Radio Galaxy in the COSMOS field: Evidence for Cluster Formation"; Chap. 5 in this thesis

10 A. Finoguenov, inter alios **Smolčić, V.**,et al., 2007, ApJS, 172, 182, COSMOS special issue, "The XMM-Newton Wide-Field Survey in the COSMOS Field: Statistical Properties of Clusters of Galaxies"

9 Bertoldi, F., inter alios **Smolčić, V.**, et al., 2007, ApJS, 172, 132, COSMOS special issue, "COSBO: The MAMBO 1.2 mm Imaging Survey of the COSMOS Fiels"

8 Schinnerer. E., **Smolčić, V.**, et al. 2007, ApJS, 172, 46, COSMOS special issue, "The VLA-COSMOS Survey: II. Source Catalog of the Large Project"; Chap. 2 in this thesis

7 **Smolčić, V.**, Ivezić, Ž., et al. 2006, MNRAS, 371, 121, "The Rest-frame Optical Colours of 99,000 Sloan Digital Sky Survey Galaxies"

6 Obric, M., Ivezić, Ž., inter alios **Smolčić, V.**, et al. 2006, MNRAS, 370, 1677, "Panchromatic Properties of 99,000 Galaxies Detected by SDSS, and (some by) ROSAT, GALEX, 2MASS, IRAS, GB6, FIRST, NVSS and WENSS Surveys"

5 Adelman-McCarthy, J. K., inter alios **Smolčić, V.**, et al. 2006, ApJS, 162, 38, "The Fourth Data Release of the Sloan Digital Sky Survey"

4 Abazajian, K., inter alios **Smolčić, V.**, et al. 2005, AJ, 129, 1755, "The Third Data Release of the Sloan Digital Sky Survey"

3 Abazajian, K., inter alios **Smolčić, V.**, et al. 2004, AJ, 128, 502, "The Second Data Release of the Sloan Digital Sky Survey"

2 **Smolčić, V.**, Ivezić, Ž., et al. 2004, ApJ, 615, 141, "A Second Stellar Color Locus: a Bridge from White Dwarfs to M stars"

1 Abazajian, K., inter alios **Smolčić, V.**, et al. 2003, AJ, 126, 2081, "The First Data Release of the Sloan Digital Sky Survey"

<u>Non-refereed Publications</u>

a) **Proceedings**

11 **Smolčić, V.**, et al., 2007, IAUS, 235, 428, "Obtaining the (dust-obscured) star formation history using the VLA-COSMOS survey"

10 Ivezić, Ž., Lupton, R., Schlegel, D., **Smolčić, V.**, et al., 2004, ASPC, 327, 104, "Halo Structure Traced by SDSS RR Lyrae"

9 **Smolčić, V.**, Ivezić, Ž. et al., 2004, ASPC, 318, 396, "Second Stellar Color Locus: a Bridge from White Dwarfs to M stars"

8 Ivezić, Ž., inter alios **Smolčić, V.**, et al., 2004, ASPC, 317, 179, "Reaching to the Edge of the Milky Way Halo with SDSS"

7 Obrić, M., inter alios **Smolčić, V.**, et al., 2004, IAUS, 222, 533, "Multiwavelength view of SDSS galaxies"

6 Ivezić, Ž., inter alios **Smolčić, V.**, et al., 2004, mas, conf, 53, "The Distribution of Quasars and Galaxies in Radio Color-Color and Morphology Diagrams"

b) **Abstracts**

5 **Smolčić, V.**, et al. 2006, AAS, 209, 8005, "The VLA-COSMOS 1.4 GHz Survey: The Properties of the Faint Radio Population and Star Formation Rates"

4 Paglione, T., **Smolčić, V.**, et al. 2006, AAS, 209, 8001, "The Luminosity Function of COSMOS Radio Sources"

3 Carilli, C. L., Bertoldi, F., Schinnerer, E., Voss, H., **Smolčić, V.**, et al., 2005, AAS, 207, 8305, "MAMBO Observations of the COSMOS Field: Probing High Redshift, Dusty Starburst Galaxies"

2 Schinnerer, E., **Smolčić, V.**, Carilli, C. L., et al., AAS, 2005, 270, 8303, "Radio Sources in the COSMOS Field",

1 **Smolčić, V.**, Schinnerer et al., 2005, AAS, 207, 621, "A Wide Angle Tail Galaxy in the COSMOS Field: Evidence for Cluster Formation"

PhD Thesis

- "The Faint Radio Population in the VLA-COSMOS Survey: Star Forming Galaxies and Active Galactic Nuclei", 2007, submitted to the University of Heidelberg, Germany; this manuscript

Diploma Thesis

- "Fotometrijska svojstva galaksija iz SDSS DR1 baze podataka", 2004, Department of Physics, Faculty of Science, University of Zagreb, Croatia

Bibliography

Abazajian, K., Adelman-McCarthy, J. K., Agüeros, M. A., et al. 2004, AJ **128**, 502–512, *The Second Data Release of the Sloan Digital Sky Survey.*

Abazajian, K., Adelman-McCarthy, J. K., Agüeros, M. A., et al. 2005, AJ **129**, 1755–1759, *The Third Data Release of the Sloan Digital Sky Survey.*

Abazajian, K., Adelman-McCarthy, J. K., Agüeros, M. A., et al. 2003, AJ **126**, 2081–2086, *The First Data Release of the Sloan Digital Sky Survey.*

Adelman-McCarthy, J. K., Agüeros, M. A., Allam, S. S., et al. 2007, ApJS **172**, 634–644, *The Fifth Data Release of the Sloan Digital Sky Survey.*

Adelman-McCarthy, J. K., Agüeros, M. A., Allam, S. S., et al. 2006, ApJS **162**, 38–48, *The Fourth Data Release of the Sloan Digital Sky Survey.*

Afonso, J., Georgakakis, A., Almeida, C., et al. 2005, ApJ **624**, 135–154, *The Phoenix Deep Survey: Spectroscopic Catalog.*

Afonso, J., Mobasher, B., Koekemoer, A., Norris, R. P., & Cram, L. 2006, AJ **131**, 1216–1230, *Optical and X-Ray Identification of Faint Radio Sources in the GOODS CDF-S Advanced Camera for Surveys Field.*

Aguirre, J. E., Schlaerth, J. A., Glenn, J., et al. 2007, ApJS, *The Bolocam 1.1 mm Survey in the COSMOS Field. I. First Results.*

Albert, C. E., White, R. A., & Morgan, W. W. 1977, ApJ **211**, 309–310, *cD galaxies in poor clusters. II.*

Alexander, D. M., Brandt, W. N., Hornschemeier, A. E., et al. 2001, AJ **122**, 2156–2176, *The Chandra Deep Field North Survey. VI. The Nature of the Optically Faint X-Ray Source Population.*

Appleton, P. N., Fadda, D. T., Marleau, F. R., et al. 2004, ApJS **154**, 147–150, *The Far- and Mid-Infrared/Radio Correlations in the Spitzer Extragalactic First Look Survey.*

Aretxaga, I., Hughes, D. H., & Dunlop, J. S. 2005, MNRAS **358**, 1240–1246, *Confirmation of the effectiveness of submm source redshift estimation based on rest-frame radio-FIR photometry.*

Arnaud, M., Pointecouteau, E., & Pratt, G. W. 2005, A&A **441**, 893–903, *The structural and scaling properties of nearby galaxy clusters. II. The M-T relation.*

Arnouts, S., Moscardini, L., Vanzella, E., et al. 2002, MNRAS **329**, 355–366, *Measuring the redshift evolution of clustering: the Hubble Deep Field South.*

Baldry, I. K., Glazebrook, K., Brinkmann, J., et al. 2004, ApJ **600**, 681–694, *Quantifying the Bimodal Color-Magnitude Distribution of Galaxies.*

Baldwin, J. A., Phillips, M. M., & Terlevich, R. 1981, PASP **93**, 5–19, *Classification parameters for the emission-line spectra of extragalactic objects.*

Balogh, M. L., Baldry, I. K., Nichol, R., et al. 2004, ApJL **615**, L101–L104, *The Bimodal Galaxy Color Distribution: Dependence on Luminosity and Environment.*

Balogh, M. L., Schade, D., Morris, S. L., et al. 1998, ApJL **504**, L75+, *The Dependence of Cluster Galaxy Star Formation Rates on the Global Environment.*

Barthel, P. D. & Arnaud, K. A. 1996, MNRAS **283**, L45–L49, *Anomalous radio-loudness of Cygnus A and other powerful radio galaxies.*

Becker, R. H., White, R. L., & Helfand, D. J. 1995, ApJ **450**, 559–+, *The FIRST Survey: Faint Images of the Radio Sky at Twenty Centimeters.*

Beckwith, S. V. W., Stiavelli, M., Koekemoer, A. M., et al. 2006, AJ **132**, 1729–1755, *The Hubble Ultra Deep Field.*

Beers, T. C. & Geller, M. J. 1983, ApJ **274**, 491–501, *The environment of D and cD galaxies.*

Beers, T. C., Kriessler, J. R., Bird, C. M., & Huchra, J. P. 1995, AJ **109**, 874–919, *Kinematics and dynamics of the MKW/AWM poor clusters.*

Begelman, M. C., Rees, M. J., & Blandford, R. D. 1979, Nature **279**, 770–773, *A twin-jet model for radio trails.*

Bell, E. F. 2003, ApJ **586**, 794–813, *Estimating Star Formation Rates from Infrared and Radio Luminosities: The Origin of the Radio-Infrared Correlation.*

Bell, E. F., McIntosh, D. H., Barden, M., et al. 2004, ApJL **600**, L11–L14, *GEMS Imaging of Red-Sequence Galaxies at $z \sim 0.7$: Dusty or Old?*

Bell, E. F., Wolf, C., Meisenheimer, K., et al. 2004, ApJ **608**, 752–767, *Nearly 5000 Distant Early-Type Galaxies in COMBO-17: A Red Sequence and Its Evolution since $z \sim 1$.*

Benn, C. R., Rowan-Robinson, M., McMahon, R. G., Broadhurst, T. J., & Lawrence, A. 1993, MNRAS **263**, 98–122, *Spectroscopy of faint radio sources - The nature of the sub-mJy radio-source population.*

Bennett, A. S. & Smith, F. G. 1961, MNRAS **122**, 71–+, *A comparison of three surveys of radio stars.*

Bertin, E. & Arnouts, S. 1996, A&AS **117**, 393–404, *SExtractor: Software for source extraction.*

Bertoldi, F., Carilli, C., Aravena, M., et al. 2007, ApJS **172**, 132–149, *COSBO: The MAMBO 1.2 Millimeter Imaging Survey of the COSMOS Field.*

Best, P. N. 2004, MNRAS **351**, 70–82, *The environmental dependence of radio-loud AGN activity and star formation in the 2dFGRS.*

Best, P. N., Kauffmann, G., Heckman, T. M., & Ivezić, Ž. 2005, MNRAS **362**, 9–24, *A sample of radio-loud active galactic nuclei in the Sloan Digital Sky Survey.*

Bird, C. M. 1994, AJ **107**, 1637–1648, *Substructure in clusters and central galaxy peculiar velocities.*

Blandford, R. D. & Cowie, L. L. 1982, ApJ **260**, 625–634, *Radio emission from supernova remnants in a cloudy interstellar medium.*

Blanton, E. L., Gregg, M. D., Helfand, D. J., Becker, R. H., & White, R. L. 2000, ApJ **531**, 118–136, *FIRST Bent-Double Radio Sources: Tracers of High-Redshift Clusters.*

Blanton, E. L., Gregg, M. D., Helfand, D. J., Becker, R. H., & White, R. L. 2003, AJ **125**, 1635–1641, *Discovery of a High-Redshift (z=0.96) Cluster of Galaxies Using a FIRST Survey Wide-Angle-Tailed Radio Source.*

Blanton, E. L., Sarazin, C. L., McNamara, B. R., & Wise, M. W. 2001, ApJL **558**, L15–L18, *Chandra Observation of the Radio Source/X-Ray Gas Interaction in the Cooling Flow Cluster Abell 2052.*

Blanton, M. R., Dalcanton, J., Eisenstein, D., et al. 2001, AJ **121**, 2358–2380, *The Luminosity Function of Galaxies in SDSS Commissioning Data.*

Blanton, M. R., Eisenstein, D., Hogg, D. W., Schlegel, D. J., & Brinkmann, J. 2005, ApJ **629**, 143–157, *Relationship between Environment and the Broadband Optical Properties of Galaxies in the Sloan Digital Sky Survey.*

Blanton, M. R., Hogg, D. W., Bahcall, N. A., et al. 2003, ApJ **592**, 819–838, *The Galaxy Luminosity Function and Luminosity Density at Redshift z = 0.1.*

Blundell, K. M. & Rawlings, S. 2001, ApJL **562**, L5–L8, *The Optically Powerful Quasar E1821+643 is Associated with a 300 Kiloparsec-Scale FR I Radio Structure.*

Bondi, M., Ciliegi, P., Schinnerer, E., et al. 2007, in prep, *The VLA-COSMOS Survey: III Further Catalog Analysis and the Radio Source Counts.*

Bondi, M., Ciliegi, P., Zamorani, G., et al. 2003, A&A **403**, 857–867, *The VLA-VIRMOS Deep Field. I. Radio observations probing the mu Jy source population.*

Borch, A., Meisenheimer, K., Bell, E. F., et al. 2006, A&A **453**, 869–881, *The stellar masses of 25 000 galaxies at $0.2 < z < 1.0$ estimated by the COMBO-17 survey.*

Bower, R. G., Benson, A. J., Malbon, R., et al. 2006, MNRAS **370**, 645–655, *Breaking the hierarchy of galaxy formation.*

Boyle, B. J. & Terlevich, R. J. 1998, MNRAS **293**, L49–L51, *The cosmological evolution of the QSO luminosity density and of the star formation rate.*

Bridle, A. H. & Perley, R. A. 1984, ARA&A **22**, 319–358, *Extragalactic Radio Jets.*

Brinchmann, J., Charlot, S., White, S. D. M., et al. 2004, MNRAS **351**, 1151–1179, *The physical properties of star-forming galaxies in the low-redshift Universe.*

Brinkmann, W., Laurent-Muehleisen, S. A., Voges, W., et al. 2000, A&A **356**, 445–462, *Radio and X-ray bright AGN: the ROSAT - FIRST correlation.*

Brown, M. J. I., Dey, A., Jannuzi, B. T., et al. 2007, ApJ **654**, 858–877, *The Evolving Luminosity Function of Red Galaxies.*

Brusa, M., Zamorani, G., Comastri, A., et al. 2007, ApJS **172**, 353–367, *The XMM-Newton Wide-Field Survey in the COSMOS Field. III. Optical Identification and Multiwavelength Properties of a Large Sample of X-Ray-Selected Sources.*

Bruzual, G. & Charlot, S. 2003, MNRAS **344**, 1000–1028, *Stellar population synthesis at the resolution of 2003.*

Burns, J. O. 1981, MNRAS **195**, 523–533, *The structure and environment of the wide-angle tailed radio galaxy 1919 + 479.*

Burns, J. O., Loken, C., Roettiger, K., et al. 2002, New Astronomy Review **46**, 135–140, *Stormy weather and cluster radio galaxies.*

Burns, J. O., Rhee, G., Owen, F. N., & Pinkney, J. 1994, ApJ **423**, 94–115, *Clumped X-ray emission around radio galaxies in Abell clusters.*

Calzetti, D. 2001, PASP **113**, 1449–1485, *The Dust Opacity of Star-forming Galaxies.*

Capak, P., Aussel, H., Ajiki, M., et al. 2007, ApJS **172**, 99–116, *The First Release COSMOS Optical and Near-IR Data and Catalog.*

Cappelluti, N., Hasinger, G., Brusa, M., et al. 2007, ApJS **172**, 341–352, *The XMM-Newton Wide-Field Survey in the COSMOS Field. II. X-Ray Data and the logN-logS Relations.*

Caputi, K. I., Lagache, G., Yan, L., et al. 2007, ApJ **660**, 97–116, *The Infrared Luminosity Function of Galaxies at Redshifts $z = 1$ and $z \sim 2$ in the GOODS Fields.*

Carilli, C. L. & Barthel, P. D. 1996, A&AR **7**, 1–54, *Cygnus A.*

Carilli, C. L. & Yun, M. S. 2000, ApJ **530**, 618–624, *The Scatter in the Relationship between Redshift and the Radio-to-Submillimeter Spectral Index.*

Carter, B. J., Fabricant, D. G., Geller, M. J., Kurtz, M. J., & McLean, B. 2001, ApJ **559**, 606–619, *Star Formation in a Complete Spectroscopic Survey of Galaxies.*

Cavaliere, A. & Fusco-Femiano, R. 1976, A&A **49**, 137–144, *X-rays from hot plasma in clusters of galaxies.*

Chan, B. H. P., Cram, L. E., Sadler, E. M., et al. 2004, MNRAS **352**, 1245–1254, *Faint 1.4-GHz radio sources in the 2dF Galaxy Redshift Survey.*

Charlot, S. & Fall, S. M. 2000, ApJ **539**, 718–731, *A Simple Model for the Absorption of Starlight by Dust in Galaxies.*

Christiansen, W. A., Pacholczyk, A. G., & Scott, J. S. 1981, ApJ **251**, 518–522, *On the energetics and morphology of radio tail galaxies.*

Ciliegi, P., McMahon, R. G., Miley, G., et al. 1999, MNRAS **302**, 222–244, *A deep VLA survey at 20 CM of the ISO ELAIS survey regions.*

Clewley, L. & Jarvis, M. J. 2004, MNRAS **352**, 909–914, *The cosmic evolution of low-luminosity radio sources from the Sloan Digital Sky Survey Data Release 1.*

Coleman, G. D., Wu, C.-C., & Weedman, D. W. 1980, ApJS **43**, 393–416, *Colors and magnitudes predicted for high redshift galaxies.*

Colless, M., Dalton, G., Maddox, S., et al. 2001, MNRAS **328**, 1039–1063, *The 2dF Galaxy Redshift Survey: spectra and redshifts.*

Condon, J. J. 1984a, ApJ **287**, 461–474, *Cosmological evolution of radio sources.*

Condon, J. J. 1984b, ApJ **284**, 44–53, *Cosmological evolution of radio sources found at 1.4 GHz.*

Condon, J. J. 1992, ARA&A **30**, 575–611, *Radio emission from normal galaxies.*

Condon, J. J. 1997, PASP **109**, 166–172, *Errors in Elliptical Gaussian FITS.*

Condon, J. J., Cotton, W. D., & Broderick, J. J. 2002, AJ **124**, 675–689, *Radio Sources and Star Formation in the Local Universe.*

Condon, J. J., Cotton, W. D., Greisen, E. W., et al. 1998, AJ **115**, 1693–1716, *The NRAO VLA Sky Survey.*

Croton, D. J., Springel, V., White, S. D. M., et al. 2006, MNRAS **365**, 11–28, *The many lives of active galactic nuclei: cooling flows, black holes and the luminosities and colours of galaxies.*

Daddi, E., Alexander, D. M., Dickinson, M., et al. 2007, ArXiv e-prints, *Multiwavelength study of massive galaxies at z ∼ 2. II. Widespread Compton thick AGN and the concurrent growth of black holes and bulges.*

Daddi, E., Cimatti, A., Renzini, A., et al. 2004, ApJ **617**, 746–764, *A New Photometric Technique for the Joint Selection of Star-forming and Passive Galaxies at 1.4 < z < 2.5.*

Dressler, A., Thompson, I. B., & Shectman, S. A. 1985, ApJ **288**, 481–486, *Statistics of emission-line galaxies in rich clusters.*

Dunlop, J. S. & Peacock, J. A. 1990, MNRAS **247**, 19–+, *The Redshift Cut-Off in the Luminosity Function of Radio Galaxies and Quasars.*

Dunn, R. J. H. & Fabian, A. C. 2006, MNRAS **373**, 959–971, *Investigating AGN heating in a sample of nearby clusters.*

Edge, D. O., Shakeshaft, J. R., McAdam, W. B., Baldwin, J. E., & Archer, S. 1959, Memoirs of the Royal Astronomical Society **68**, 37–60, *A survey of radio sources at a frequency of 159 Mc/s.*

Eilek, J. A. 1979, ApJ **230**, 373–385, *Particle reacceleration in radio galaxies.*

Eisenstein, D. J., Annis, J., Gunn, J. E., et al. 2001, AJ **122**, 2267–2280, *Spectroscopic Target Selection for the Sloan Digital Sky Survey: The Luminous Red Galaxy Sample.*

Evrard, A. E. 1990, ApJ **363**, 349–366, *Formation and evolution of X-ray clusters - A hydrodynamic simulation of the intracluster medium.*

Faber, S. M. & Jackson, R. E. 1976, ApJ **204**, 668–683, *Velocity dispersions and mass-to-light ratios for elliptical galaxies.*

Faber, S. M., Willmer, C. N. A., Wolf, C., et al. 2007, ApJ **665**, 265–294, *Galaxy Luminosity Functions to z ∼ 1 from DEEP2 and COMBO-17: Implications for Red Galaxy Formation.*

Fabian, A. C., Sanders, J. S., Allen, S. W., et al. 2003, MNRAS **344**, L43–L47, *A deep Chandra observation of the Perseus cluster: shocks and ripples.*

Fanaroff, B. L. & Riley, J. M. 1974, MNRAS **167**, 31P–36P, *The morphology of extragalactic radio sources of high and low luminosity.*

Ferguson, H. C., Dickinson, M., & Williams, R. 2000, ARA&A **38**, 667–715, *The Hubble Deep Fields.*

Fey, A. L., Ma, C., Arias, E. F., et al. 2004, AJ **127**, 3587–3608, *The Second Extension of the International Celestial Reference Frame: ICRF-EXT.1.*

Finoguenov, A., Arnaud, M., & David, L. P. 2001a, ApJ **555**, 191–204, *Temperature and Heavy-Element Abundance Profiles of Cool Clusters of Galaxies from ASCA.*

Finoguenov, A., Böhringer, H., & Zhang, Y.-Y. 2005, A&A **442**, 827–839, *XMM-Newton study of the two-dimensional structure of the REFLEX-DXL galaxy clusters.*

Finoguenov, A., Guzzo, L., Hasinger, G., et al. 2007, ApJS **172**, 182–195, *The XMM-Newton Wide-Field Survey in the COSMOS Field: Statistical Properties of Clusters of Galaxies.*

Finoguenov, A., Pietsch, W., Aschenbach, B., & Miniati, F. 2004, A&A **415**, 415–424, *XMM-Newton witness of M 86 X-ray metamorphosis.*

Finoguenov, A., Reiprich, T. H., & Böhringer, H. 2001b, A&A **368**, 749–759, *Details of the mass-temperature relation for clusters of galaxies.*

Fischera, J., Dopita, M. A., & Sutherland, R. S. 2003, ApJL **599**, L21–L24, *Starburst Galaxies: Why the Calzetti Dust Extinction Law?*

Flores, H., Hammer, F., Thuan, T. X., et al. 1999, ApJ **517**, 148–167, *15 Micron Infrared Space Observatory Observations of the 1415+52 Canada-France Redshift Survey Field: The Cosmic Star Formation Rate as Derived from Deep Ultraviolet, Optical, Mid-Infrared, and Radio Photometry.*

Fomalont, E. B. 1999, *Astrometry and Geodesy*, In G. B. Taylor, C. L. Carilli, and R. A. Perley (Eds.), *Synthesis Imaging in Radio Astronomy II*, Volume 180 of *Astronomical Society of the Pacific Conference Series*, pp. 463–+.

Fomalont, E. B., Kellermann, K. I., Cowie, L. L., et al. 2006, ApJS **167**, 103–160, *The Radio/Optical Catalog of the SSA 13 Field.*

Forman, W., Nulsen, P., Heinz, S., et al. 2005, ApJ **635**, 894–906, *Reflections of Active Galactic Nucleus Outbursts in the Gaseous Atmosphere of M87.*

Franceschini, A., Hasinger, G., Miyaji, T., & Malquori, D. 1999, MNRAS **310**, L5–L9, *On the relationship between galaxy formation and quasar evolution.*

Frenk, C. S., Evrard, A. E., White, S. D. M., & Summers, F. J. 1996, ApJ **472**, 460–+, *Galaxy Dynamics in Clusters.*

Garrett, M. A. 2002, A&A **384**, L19–L22, *The FIR/Radio correlation of high redshift galaxies in the region of the HDF-N.*

Giallongo, E., Salimbeni, S., Menci, N., et al. 2005, ApJ **622**, 116–128, *The B-Band Luminosity Function of Red and Blue Galaxies up to z = 3.5.*

Giavalisco, M., Ferguson, H. C., Koekemoer, A. M., et al. 2004, ApJL **600**, L93–L98, *The Great Observatories Origins Deep Survey: Initial Results from Optical and Near-Infrared Imaging.*

Goldschmidt, P., Kukula, M. J., Miller, L., & Dunlop, J. S. 1999, ApJ **511**, 612–624, *A Comparison of the Optical Properties of Radio-loud and Radio-quiet Quasars.*

Gomez, P. L., Ledlow, M. J., Burns, J. O., Pinkey, J., & Hill, J. M. 1997, AJ **114**, 1711–+, *The Cluster Dynamics, X-Ray Emission, and Radio Galaxies in Abell 578 = Abell 1569.*

Gower, J. F. R., Scott, P. F., & Wills, D. 1967, Memoirs of the Royal Astronomical Society **71**, 49–+, *A survey of radio sources in the declination ranges -07deg to 20deg and 40deg to 80deg.*

Graham, A., Lauer, T. R., Colless, M., & Postman, M. 1996, ApJ **465**, 534–+, *Brightest Cluster Galaxy Profile Shapes.*

Greisen, E. W. 2003, *AIPS, the VLA, and the VLBA*, In A. Heck (Ed.), *Astrophysics and Space Science Library*, Volume 285 of *Astrophysics and Space Science Library*, pp. 109–+.

Gruppioni, C., Mignoli, M., & Zamorani, G. 1999, MNRAS **304**, 199–217, *Optical identifications and spectroscopy of a faint radio source sample: the nature of the sub-mJy population.*

Gull, S. F. 1973, MNRAS **161**, 47–+, *A numerical model of the structure and evolution of young supernovaremnants.*

Gull, S. F. & Northover, K. J. E. 1973, Nature **244**, 80–+, *Bubble Model of Extragalactic Radio Sources.*

Haarsma, D. B., Partridge, R. B., Windhorst, R. A., & Richards, E. A. 2000, ApJ **544**, 641–658, *Faint Radio Sources and Star Formation History.*

Hardcastle, M. J. & Sakelliou, I. 2004, MNRAS **349**, 560–575, *Jet termination in wide-angle tail radio sources.*

Hashimoto, Y., Oemler, A. J., Lin, H., & Tucker, D. L. 1998, ApJ **499**, 589–+, *The Influence of Environment on the Star Formation Rates of Galaxies.*

Hasinger, G., Cappelluti, N., Brunner, H., et al. 2007, ApJS **172**, 29–37, *The XMM-Newton Wide-Field Survey in the COSMOS Field. I. Survey Description.*

Hauschildt, P. H., Baron, E., & Allard, F. 1997, ApJ **483**, 390–+, *Parallel Implementation of the PHOENIX Generalized Stellar Atmosphere Program.*

Helou, G., Soifer, B. T., & Rowan-Robinson, M. 1985, ApJL **298**, L7–L11, *Thermal infrared and nonthermal radio - Remarkable correlation in disks of galaxies.*

Henry, J. P., Finoguenov, A., & Briel, U. G. 2004, ApJ **615**, 181–195, *Wide-Field X-Ray Temperature, Pressure, and Entropy Maps of A754.*

Hogg, D. W., Blanton, M. R., Eisenstein, D. J., et al. 2003, ApJL **585**, L5–L9, *The Overdensities of Galaxy Environments as a Function of Luminosity and Color.*

Hopkins, A. M. 2004, ApJ **615**, 209–221, *On the Evolution of Star-forming Galaxies.*

Hopkins, A. M., Afonso, J., Chan, B., et al. 2003, AJ **125**, 465–477, *The Phoenix Deep Survey: The 1.4 GHz Microjansky Catalog.*

Hopkins, A. M., Miller, C. J., Nichol, R. C., et al. 2003, ApJ **599**, 971–991, *Star Formation Rate Indicators in the Sloan Digital Sky Survey.*

Hopkins, A. M., Mobasher, B., Cram, L., & Rowan-Robinson, M. 1998, MNRAS **296**, 839–846, *The PHOENIX Deep Survey: 1.4-GHz source counts.*

Hopkins, P. F., Bundy, K., Hernquist, L., & Ellis, R. S. 2007, ApJ **659**, 976–996, *Observational Evidence for the Coevolution of Galaxy Mergers, Quasars, and the Blue/Red Galaxy Transition.*

Hubble, E. 1929, Proceedings of the National Academy of Science **15**, 168–173, *A Relation between Distance and Radial Velocity among Extra-Galactic Nebulae.*

Hubble, E. 1936, Science **84**, 509–510, *Astronomy. (Scientific Books: The Realm of the Nebulae; Theoretical Astrophysics).*

Humason, M. L. 1936, ApJ **83**, 10–+, *The Apparent Radial Velocities of 100 Extra-Galactic Nebulae.*

Huynh, M. T., Jackson, C. A., Norris, R. P., & Prandoni, I. 2005, AJ **130**, 1373–1388, *Radio Observations of the Hubble Deep Field-South Region. II. The 1.4 GHz Catalog and Source Counts.*

Ilbert, O., Arnouts, S., McCracken, H. J., et al. 2006, A&A **457**, 841–856, *Accurate photometric redshifts for the CFHT legacy survey calibrated using the VIMOS VLT deep survey.*

Im, M., Simard, L., Faber, S. M., et al. 2002, ApJ **571**, 136–171, *The DEEP Groth Strip Survey. X. Number Density and Luminosity Function of Field E/S0 Galaxies at z < 1.*

Impey, C. D., Trump, J. R., McCarthy, P. J., et al. 2007, *A survey of AGN and supermassive black holes in the COSMOS Survey*, In V. Karas and G. Matt (Eds.), *IAU Symposium*, Volume 238 of *IAU Symposium*, pp. 287–290.

Ivezić, Ž., Menou, K., Knapp, G. R., et al. 2002, AJ **124**, 2364–2400, *Optical and Radio Properties of Extragalactic Sources Observed by the FIRST Survey and the Sloan Digital Sky Survey.*

Jackson, C. A. & Londish, D. M. 2000, Publications of the Astronomical Society of Australia **17**, 234–240, *Spectral characteristics of the 2dFGRS-NVSS galaxies.*

Jaffe, W. J. & Perola, G. C. 1973, A&A **26**, 423–+, *Dynamical Models of Tailed Radio Sources in Clusters of Galaxies.*

Jansen, F., Lumb, D., Altieri, B., et al. 2001, A&A **365**, L1–L6, *XMM-Newton observatory. I. The spacecraft and operations.*

Jarrett, T. H., Chester, T., Cutri, R., et al. 2000, AJ **119**, 2498–2531, *2MASS Extended Source Catalog: Overview and Algorithms.*

Jarvis, M. J. & Rawlings, S. 2004, New Astronomy Review **48**, 1173–1185, *The accretion history of the universe with the SKA.*

Jing, Y. P., Borner, G., & Valdarnini, R. 1995, MNRAS **277**, 630–+, *Three-Point Correlation Function of Galaxy Clusters in Cosmological Models - a Strong Dependence on Triangle Shapes.*

Kauffmann, G., Heckman, T. M., Tremonti, C., et al. 2003c, MNRAS **346**, 1055–1077, *The host galaxies of active galactic nuclei.*

Kauffmann, G., Heckman, T. M., White, S. D. M., et al. 2003a, MNRAS **341**, 33–53, *Stellar masses and star formation histories for 10^5 galaxies from the Sloan Digital Sky Survey.*

Kauffmann, G., Heckman, T. M., White, S. D. M., et al. 2003b, MNRAS **341**, 54–69, *The dependence of star formation history and internal structure on stellar mass for 10^5 low-redshift galaxies.*

Kennicutt, Jr., R. C. 1998, ARA&A **36**, 189–232, *Star Formation in Galaxies Along the Hubble Sequence.*

Kewley, L. J., Dopita, M. A., Sutherland, R. S., Heisler, C. A., & Trevena, J. 2001, ApJ **556**, 121–140, *Theoretical Modeling of Starburst Galaxies.*

Kim, D.-C., Veilleux, S., & Sanders, D. B. 2002, ApJS **143**, 277–314, *Optical and Near-Infrared Imaging of the IRAS 1 Jy Sample of Ultraluminous Infrared Galaxies. I. The Atlas.*

Kinney, A. L., Calzetti, D., Bohlin, R. C., et al. 1996, ApJ **467**, 38–+, *Template Ultraviolet to Near-Infrared Spectra of Star-forming Galaxies and Their Application to K-Corrections.*

Koekemoer, A. M., Aussel, H., Calzetti, D., et al. 2007, ApJS **172**, 196–202, *The COSMOS Survey: Hubble Space Telescope Advanced Camera for Surveys Observations and Data Processing.*

Kong, X., Charlot, S., Brinchmann, J., & Fall, S. M. 2004, MNRAS **349**, 769–778, *Star formation history and dust content of galaxies drawn from ultraviolet surveys.*

Kukula, M. J., Dunlop, J. S., Hughes, D. H., & Rawlings, S. 1998, MNRAS **297**, 366–382, *The radio properties of radio-quiet quasars.*

Lacy, M., Storrie-Lombardi, L. J., Sajina, A., et al. 2004, ApJS **154**, 166–169, *Obscured and Unobscured Active Galactic Nuclei in the Spitzer Space Telescope First Look Survey.*

Le Floc'h, E., Papovich, C., Dole, H., et al. 2005, ApJ **632**, 169–190, *Infrared Luminosity Functions from the Chandra Deep Field-South: The Spitzer View on the History of Dusty Star Formation at $0 < z < 1$.*

Leauthaud, A., Massey, R., Kneib, J.-P., et al. 2007, ApJS **172**, 219–238, *Weak Gravitational Lensing with COSMOS: Galaxy Selection and Shape Measurements.*

Ledlow, M. J., Loken, C., Burns, J. O., Hill, J. M., & White, R. A. 1996, AJ **112**, 388–+, *Redshift and Optical Properties for S Statistically Complete Sample of Poor Galaxy Clusters.*

Lewis, I., Balogh, M., De Propris, R., et al. 2002, MNRAS **334**, 673–683, *The 2dF Galaxy Redshift Survey: the environmental dependence of galaxy star formation rates near clusters.*

Lilly, S. J., Fèvre, O. L., Renzini, A., et al. 2007, ApJS **172**, 70–85, *zCOSMOS: A Large VLT/VIMOS Redshift Survey Covering $0 < z < 3$ in the COSMOS Field.*

Lilly, S. J., Le Fevre, O., Hammer, F., & Crampton, D. 1996, ApJL **460**, L1+, *The Canada-France Redshift Survey: The Luminosity Density and Star Formation History of the Universe to Z approximately 1.*

Lin, H., Yee, H. K. C., Carlberg, R. G., et al. 1999, ApJ **518**, 533–561, *The CNOC2 Field Galaxy Luminosity Function. I. A Description of Luminosity Function Evolution.*

Loken, C., Roettiger, K., Burns, J. O., & Norman, M. 1995, ApJ **445**, 80–97, *Radio jet propagation and wide-angle tailed radio sources in merging galaxy cluster environments.*

Maccacaro, T., Gioia, I. M., Wolter, A., Zamorani, G., & Stocke, J. T. 1988, ApJ **326**, 680–690, *The X-ray spectra of the extragalactic sources in the Einstein extended medium sensitivity survey.*

Machalski, J. & Godlowski, W. 2000, A&A **360**, 463–471, *1.4 GHz luminosity function of galaxies in the Las Campanas redshift survey and its evolution.*

Madau, P., Ferguson, H. C., Dickinson, M. E., et al. 1996, MNRAS **283**, 1388–1404, *High-redshift galaxies in the Hubble Deep Field: colour selection and star formation history to $z \sim 4$.*

Mahdavi, A., Finoguenov, A., Böhringer, H., Geller, M. J., & Henry, J. P. 2005, ApJ **622**, 187–204, *XMM-Newton and Gemini Observations of Eight RASSCALS Galaxy Groups.*

Malumuth, E. M., Kriss, G. A., Dixon, W. V. D., Ferguson, H. C., & Ritchie, C. 1992, AJ **104**, 495–530, *Dynamics of clusters of galaxies with central dominant galaxies. I - Galaxy redshifts.*

Markevitch, M. 1998, ApJ **504**, 27–+, *The L X-T Relation and Temperature Function for Nearby Clusters Revisited.*

Martini, P., Kelson, D. D., Mulchaey, J. S., & Trager, S. C. 2002, ApJL **576**, L109–L112, *An Unexpectedly High Fraction of Active Galactic Nuclei in Red Cluster Galaxies.*

Mathis, J. S., Rumpl, W., & Nordsieck, K. H. 1977, ApJ **217**, 425–433, *The size distribution of interstellar grains.*

McNamara, B. R., Wise, M., Nulsen, P. E. J., et al. 2000, ApJL **534**, L135–L138, *Chandra X-Ray Observations of the Hydra A Cluster: An Interaction between the Radio Source and the X-Ray-emitting Gas.*

Merritt, D. 1984, ApJ **276**, 26–37, *Relaxation and tidal stripping in rich clusters of galaxies. II - Evolution of the luminosity distribution.*

Miley, G. 1980, ARA&A **18**, 165–218, *The structure of extended extragalactic radio sources.*

Miley, G. K., Overzier, R. A., Zirm, A. W., et al. 2006, ApJL **650**, L29–L32, *The Spiderweb Galaxy: A Forming Massive Cluster Galaxy at $z \sim 2$.*

Mobasher, B., Capak, P., Scoville, N. Z., et al. 2007, ApJS, *Photometric redshifts of galaxies in cosmos.*

Morgan, W. W., Kayser, S., & White, R. A. 1975, ApJ **199**, 545–548, *cD galaxies in poor clusters.*

Mulchaey, J. S. 2000, ARA&A **38**, 289–335, *X-ray Properties of Groups of Galaxies.*

Mulchaey, J. S., Davis, D. S., Mushotzky, R. F., & Burstein, D. 2003, ApJS **145**, 39–64, *An X-Ray Atlas of Groups of Galaxies.*

Neugebauer, G., Habing, H. J., van Duinen, R., et al. 1984, ApJL **278**, L1–L6, *The Infrared Astronomical Satellite (IRAS) mission.*

Novikov, D. I., Melott, A. L., Wilhite, B. C., et al. 1999, MNRAS **304**, L5–L9, *Cluster winds blow along supercluster axes.*

Obrić, M., Ivezić, Ž., Best, P. N., et al. 2006, MNRAS **370**, 1677–1698, *Panchromatic properties of 99000 galaxies detected by SDSS, and (some by) ROSAT, GALEX, 2MASS, IRAS, GB6, FIRST, NVSS and WENSS surveys.*

O'Dea, C. P. & Owen, F. N. 1987, ApJ **316**, 95–112, *Astrophysical implications of the multifrequency VLA observations of NGC 1265.*

Odell, A. P., Schombert, J., & Rakos, K. 2002, AJ **124**, 3061–3072, *The Color-Magnitude Relation in Coma: Clues to the Age and Metallicity of Cluster Populations.*

O'Donoghue, A. A., Eilek, J. A., & Owen, F. N. 1993, ApJ **408**, 428–445, *Flow dynamics and bending of wide-angle tailed radio sources.*

Oegerle, W. R. & Hill, J. M. 2001, AJ **122**, 2858–2873, *Dynamics of cD Clusters of Galaxies. IV. Conclusion of a Survey of 25 Abell Clusters.*

Osmond, J. P. F. & Ponman, T. J. 2004, MNRAS **350**, 1511–1535, *The GEMS project: X-ray analysis and statistical properties of the group sample.*

Pacholczyk, A. G. 1970, *Radio astrophysics. Nonthermal processes in galactic and extragalactic sources.* Series of Books in Astronomy and Astrophysics, San Francisco: Freeman, 1970.

Padovani, P., Mainieri, V., Tozzi, P., et al. 2007, ArXiv Astrophysics e-prints, *The micro-Jy Radio Source Population: the VLA-CDFS View.*

Padovani, P. & Urry, C. M. 1992, ApJ **387**, 449–457, *Luminosity functions, relativistic beaming, and unified theories of high-luminosity radio sources.*

Peacock, J. A., Cole, S., Norberg, P., et al. 2001, Nature **410**, 169–173, *A measurement of the cosmological mass density from clustering in the 2dF Galaxy Redshift Survey.*

Pen, U.-L. 1999, ApJS **120**, 49–50, *Analytical Fit to the Luminosity Distance for Flat Cosmologies with a Cosmological Constant.*

Peterson, B. M. 1997, The Observatory **117**, 314–+, *An introduction to active galactic nuclei / Cambridge U Press, 1997.*

Pilkington, J. D. H. & Scott, P. F. 1965, Memoirs of the Royal Astronomical Society **69**, 183–+, *A survey of radio sources between declinations 20deg and 40deg.*

Pinkney, J., Burns, J. O., & Hill, J. M. 1994, AJ **108**, 2031–2045, *1919+479: Big WAT in a poor cluster.*

Polletta, M. d. C., Wilkes, B. J., Siana, B., et al. 2006, ApJ **642**, 673–693, *Chandra and Spitzer Unveil Heavily Obscured Quasars in the Chandra/SWIRE Survey.*

Popesso, P., Biviano, A., Romaniello, M., & Böhringer, H. 2007, A&A **461**, 411–421, *RASS-SDSS galaxy cluster survey. VI. The dependence of the cluster SFR on the cluster global properties.*

Prandoni, I., Gregorini, L., Parma, P., et al. 2001, A&A **365**, 392–399, *The ATESP radio survey. III. Source counts.*

Prescott, M. K. M., Impey, C. D., Cool, R. J., & Scoville, N. Z. 2006, ApJ **644**, 100–115, *Quasars in the COSMOS Field.*

Quintana, H. & Lawrie, D. G. 1982, AJ **87**, 1–+, *On the Determination of Velocity Dispersions for CD Clusters of Galaxies.*

Ramella, M., Boschin, W., Fadda, D., & Nonino, M. 2001, A&A **368**, 776–786, *Finding galaxy clusters using Voronoi tessellations.*

Ramella, M., Diaferio, A., Geller, M. J., & Huchra, J. P. 1994, AJ **107**, 1623–1628, *The birthplace of compact groups of galaxies.*

Ranalli, P., Comastri, A., & Setti, G. 2003, A&A **399**, 39–50, *The 2-10 keV luminosity as a Star Formation Rate indicator.*

Rawlings, S. & Saunders, R. 1991, Nature **349**, 138–140, *Evidence for a common central-engine mechanism in all extragalactic radio sources.*

Richards, E. A. 2000, ApJ **533**, 611–630, *The Nature of Radio Emission from Distant Galaxies: The 1.4 GHz Observations.*

Richards, G. T., Fan, X., Newberg, H. J., et al. 2002, AJ **123**, 2945–2975, *Spectroscopic Target Selection in the Sloan Digital Sky Survey: The Quasar Sample.*

Rix, H.-W., Barden, M., Beckwith, S. V. W., et al. 2004, ApJS **152**, 163–173, *GEMS: Galaxy Evolution from Morphologies and SEDs.*

Roche, N. D., Lowenthal, J. D., & Koo, D. C. 2002, MNRAS **330**, 307–328, *Keck spectroscopy and imaging of faint galaxies identified as microjansky radio sources.*

Rola, C. S., Terlevich, E., & Terlevich, R. J. 1997, MNRAS **289**, 419–427, *New diagnostic methods for emission-line galaxies in deep surveys.*

Ryle, M. & Clarke, R. W. 1961, MNRAS **122**, 349–+, *An examination of the steady-state model in the light of some recent observations of radio sources.*

Sadler, E. M., Jackson, C. A., Cannon, R. D., et al. 2002a, MNRAS **329**, 227–245, *Radio sources in the 2dF Galaxy Redshift Survey - II. Local radio luminosity functions for AGN and star-forming galaxies at 1.4 GHz.*

Sadler, E. M., Jackson, C. A., Cannon, R. D., et al. 2002b, MNRAS **329**, 227–245, *Radio sources in the 2dF Galaxy Redshift Survey - II. Local radio luminosity functions for AGN and star-forming galaxies at 1.4 GHz.*

Sadler, E. M., McIntyre, V. J., Jackson, C. A., & Cannon, R. D. 1999, Publications of the Astronomical Society of Australia **16**, 247–56, *Radio sources in the 2dF Galaxy Redshift Survey. I. Radio source populations.*

Sakelliou, I. & Merrifield, M. R. 2000, MNRAS **311**, 649–656, *The origin of wide-angle tailed radio galaxies.*

Sakelliou, I., Merrifield, M. R., & McHardy, I. M. 1996, MNRAS **283**, 673–682, *What bent the jets in 4C 34.16?*

Salim, S., Rich, R. M., Charlot, S., et al. 2007, ArXiv e-prints, *UV Star Formation Rates in the Local Universe.*

Sanders, D. B. 2003, Journal of Korean Astronomical Society **36**, 149–158, *The Cosmic Evolution of Luminous Infrared Galaxies: Strong Interactions/Mergers of Gas-Rich Disks.*

Sanders, D. B. & Mirabel, I. F. 1996, ARA&A **34**, 749–+, *Luminous Infrared Galaxies.*

Sanders, D. B., Salvato, M., Aussel, H., et al. 2007, ApJS **172**, 86–98, *S-COSMOS: The Spitzer Legacy Survey of the Hubble Space Telescope ACS 2 deg² COSMOS Field I: Survey Strategy and First Analysis.*

Sanders, D. B., Soifer, B. T., Elias, J. H., et al. 1988a, ApJ **325**, 74–91, *Ultraluminous infrared galaxies and the origin of quasars.*

Sanders, D. B., Soifer, B. T., Elias, J. H., Neugebauer, G., & Matthews, K. 1988b, ApJL **328**, L35–L39, *Warm ultraluminous galaxies in the IRAS survey - The transition from galaxy to quasar?*

Schinnerer, E., Carilli, C. L., Scoville, N. Z., et al. 2004, AJ **128**, 1974–1989, *The VLA-COSMOS Survey. I. Radio Identifications from the Pilot Project.*

Schinnerer, E., Smolčić, V., Carilli, C. L., et al. 2007, ApJS **172**, 46–69, *The VLA-COSMOS Survey. II. Source Catalog of the Large Project.*

Schmidt, M. 1968, ApJ **151**, 393–+, *Space Distribution and Luminosity Functions of Quasi-Stellar Radio Sources.*

Schneider, D. P., Hall, P. B., Richards, G. T., et al. 2005, AJ **130**, 367–380, *The Sloan Digital Sky Survey Quasar Catalog. III. Third Data Release.*

Schombert, J. M. 1987, ApJS **64**, 643–666, *The structure of brightest cluster members. II - Mergers.*

Scoville, N., Abraham, R. G., Aussel, H., et al. 2007c, ApJS **172**, 38–45, *COSMOS: Hubble Space Telescope Observations.*

Scoville, N., Aussel, H., Benson, A., et al. 2007b, ApJS **172**, 150–181, *Large Structures and Galaxy Evolution in COSMOS at $z < 1.1$.*

Scoville, N., Aussel, H., Brusa, M., et al. 2007a, ApJS **172**, 1–8, *The Cosmic Evolution Survey (COSMOS): Overview.*

Serjeant, S., Gruppioni, C., & Oliver, S. 2002, MNRAS **330**, 621–624, *The local star formation rate and radio luminosity density.*

Sersic, J. L. 1968, *Atlas de galaxias australes.* Cordoba, Argentina: Observatorio Astronomico, 1968.

Seymour, N., McHardy, I. M., & Gunn, K. F. 2004, MNRAS **352**, 131–141, *Radio observations of the 13^h XMM-Newton/ROSAT Deep X-ray Survey Area.*

Shewchuk, R. J. 1996, Workshop on Applied Computational Geormetry, Towards Geometric Engineering, 203–222, *Triangle: Engineering a 2D Quality Mesh Generator and Delaunay Triangulator.*

Shu, F. 1991, *Physics of Astrophysics: Volume I Radiation.* Published by University Science Books, 648 Broadway, Suite 902, New York, NY 10012, 1991.

Silva, L., Granato, G. L., Bressan, A., & Danese, L. 1998, ApJ **509**, 103–117, *Modeling the Effects of Dust on Galactic Spectral Energy Distributions from the Ultraviolet to the Millimeter Band.*

Silverman, J. D., Green, P. J., Barkhouse, W. A., et al. 2007, ArXiv e-prints, *The Luminosity Function of X-ray Selected Active Galactic Nuclei: Evolution of Supermassive Black Holes at High Redshift.*

Simpson, C., Martínez-Sansigre, A., Rawlings, S., et al. 2006, MNRAS **372**, 741–757, *Radio imaging of the Subaru/XMM-Newton Deep Field - I. The 100-μJy catalogue, optical identifications, and the nature of the faint radio source population.*

Smith, R. K., Brickhouse, N. S., Liedahl, D. A., & Raymond, J. C. 2001, ApJL **556**, L91–L95, *Collisional Plasma Models with APEC/APED: Emission-Line Diagnostics of Hydrogen-like and Helium-like Ions.*

Smolčić, V., Ivezić, Ž., Gaćeša, M., et al. 2006, MNRAS **371**, 121–137, *The rest-frame optical colours of 99000 Sloan Digital Sky Survey galaxies.*

Smolčić, V., Ivezić, Ž., Knapp, G. R., et al. 2004, ApJL **615**, L141–L144, *A Second Stellar Color Locus: a Bridge from White Dwarfs to M stars.*

Smolčić, V., Schinnerer, E., Finoguenov, A., et al. 2007a, ApJS **172**, 295–313, *A Wide-Angle Tail Radio Galaxy in the COSMOS Field: Evidence for Cluster Formation.*

Smolčić, V., Zucker, D. B., Bell, E. F., et al. 2007b, AJ **134**, 1901–1915, *Improved Photometry of Sloan Digital Sky Survey Crowded-Field Images: Structure and Dark Matter Content in the Dwarf Spheroidal Galaxy Leo I.*

Snellen, I. A. G. & Best, P. N. 2001, MNRAS **328**, 897–902, *Distant FR I radio galaxies in the Hubble Deep Field: implications for the cosmological evolution of radio-loud AGN.*

Soifer, B. T., Neugebauer, G., Helou, G., et al. 1984, ApJL **283**, L1–L4, *The remarkable infrared galaxy ARP 220 = IC 4553.*

Spergel, D. N., Bean, R., Doré, O., et al. 2007, ApJS **170**, 377–408, *Three-Year Wilkinson Microwave Anisotropy Probe (WMAP) Observations: Implications for Cosmology.*

Springel, V., White, S. D. M., Jenkins, A., et al. 2005, Nature **435**, 629–636, *Simulations of the formation, evolution and clustering of galaxies and quasars.*

Steidel, C. C., Adelberger, K. L., Giavalisco, M., Dickinson, M., & Pettini, M. 1999a, ApJ **519**, 1–17, *Lyman-Break Galaxies at $z > 4$ and the Evolution of the Ultraviolet Luminosity Density at High Redshift.*

Steidel, C. C., Adelberger, K. L., Giavalisco, M., Dickinson, M., & Pettini, M. 1999b, ApJ **519**, 1–17, *Lyman-Break Galaxies at $z > 4$ and the Evolution of the Ultraviolet Luminosity Density at High Redshift.*

Stern, D., Eisenhardt, P., Gorjian, V., et al. 2005, ApJ **631**, 163–168, *Mid-Infrared Selection of Active Galaxies.*

Stoughton, C., Lupton, R. H., Bernardi, M., et al. 2002, AJ **123**, 485–548, *Sloan Digital Sky Survey: Early Data Release.*

Strateva, I., Ivezić, Ž., Knapp, G. R., et al. 2001, AJ **122**, 1861–1874, *Color Separation of Galaxy Types in the Sloan Digital Sky Survey Imaging Data.*

Strauss, M. A., Weinberg, D. H., Lupton, R. H., et al. 2002, AJ **124**, 1810–1824, *Spectroscopic Target Selection in the Sloan Digital Sky Survey: The Main Galaxy Sample.*

Szkody, P., Anderson, S. F., Agüeros, M., et al. 2002, AJ **123**, 430–442, *Cataclysmic Variables from The Sloan Digital Sky Survey. I. The First Results.*

Szkody, P., Fraser, O., Silvestri, N., et al. 2003, AJ **126**, 1499–1514, *Cataclysmic Variables from the Sloan Digital Sky Survey. II. The Second Year.*

Takeuchi, T. T., Yoshikawa, K., & Ishii, T. T. 2003, ApJL **587**, L89–L92, *The Luminosity Function of IRAS Point Source Catalog Redshift Survey Galaxies.*

Taniguchi, Y., Scoville, N., Murayama, T., et al. 2007, ApJS **172**, 9–28, *The Cosmic Evolution Survey (COSMOS): Subaru Observations of the HST Cosmos Field.*

Tran, Q. D., Lutz, D., Genzel, R., et al. 2001, ApJ **552**, 527–543, *ISOCAM-CVF 5-12 micron spectroscopy of ultraluminous infrared galaxies.*

Trump, J. R., Impey, C. D., McCarthy, P. J., et al. 2007, ApJS **172**, 383–395, *Magellan Spectroscopy of AGN Candidates in the COSMOS Field.*

Tully, R. B. & Fisher, J. R. 1977, A&A **54**, 661–673, *A new method of determining distances to galaxies.*

Ueda, Y., Akiyama, M., Ohta, K., & Miyaji, T. 2003, ApJ **598**, 886–908, *Cosmological Evolution of the Hard X-Ray Active Galactic Nucleus Luminosity Function and the Origin of the Hard X-Ray Background.*

van der Laan, H. & Perola, G. C. 1969, A&A **3**, 468–+, *Aspects of Radio Galaxy Evolution.*

Veilleux, S., Kim, D.-C., & Sanders, D. B. 2002, ApJS **143**, 315–376, *Optical and Near-Infrared Imaging of the IRAS 1 Jy Sample of Ultraluminous Infrared Galaxies. II. The Analysis.*

Veilleux, S. & Osterbrock, D. E. 1987, ApJS **63**, 295–310, *Spectral classification of emission-line galaxies.*

Veilleux, S., Sanders, D. B., & Kim, D.-C. 1999, ApJ **522**, 139–156, *New Results from a Near-Infrared Search for Hidden Broad-Line Regions in Ultraluminous Infrared Galaxies.*

Vikhlinin, A., Markevitch, M., Murray, S. S., et al. 2005, ApJ **628**, 655–672, *Chandra Temperature Profiles for a Sample of Nearby Relaxed Galaxy Clusters.*

Waddington, I., Dunlop, J. S., Peacock, J. A., & Windhorst, R. A. 2001, MNRAS **328**, 882–896, *The LBDS Hercules sample of mJy radio sources at 1.4 GHz - II. Redshift distribution, radio luminosity function, and the high-redshift cut-off.*

Watson, M. G., Auguères, J.-L., Ballet, J., et al. 2001, A&A **365**, L51–L59, *The XMM-Newton Serendipitous Survey. I. The role of XMM-Newton Survey Science Centre.*

Weiler, K. W., Sramek, R. A., Panagia, N., van der Hulst, J. M., & Salvati, M. 1986, ApJ **301**, 790–812, *Radio supernovae.*

Weinberg, D. H., Davé, R., Katz, N., & Hernquist, L. 2004, ApJ **601**, 1–21, *Galaxy Clustering and Galaxy Bias in a ΛCDM Universe.*

Weiner, B. J., Phillips, A. C., Faber, S. M., et al. 2005, ApJ **620**, 595–617, *The DEEP Groth Strip Galaxy Redshift Survey. III. Redshift Catalog and Properties of Galaxies.*

White, R. L., Becker, R. H., Helfand, D. J., & Gregg, M. D. 1997, ApJ **475**, 479–+, *A Catalog of 1.4 GHz Radio Sources from the FIRST Survey.*

White, S. D. M. & Rees, M. J. 1978, MNRAS **183**, 341–358, *Core condensation in heavy halos - A two-stage theory for galaxy formation and clustering.*

Williams, R. E., Blacker, B., Dickinson, M., et al. 1996, AJ **112**, 1335–+, *The Hubble Deep Field: Observations, Data Reduction, and Galaxy Photometry.*

Willmer, C. N. A., Faber, S. M., Koo, D. C., et al. 2006, ApJ **647**, 853–873, *The Deep Evolutionary Exploratory Probe 2 Galaxy Redshift Survey: The Galaxy Luminosity Function to z ∼ 1.*

Willott, C. J., Rawlings, S., Blundell, K. M., Lacy, M., & Eales, S. A. 2001, MNRAS **322**, 536–552, *The radio luminosity function from the low-frequency 3CRR, 6CE and 7CRS complete samples.*

Willott, C. J., Rawlings, S., Blundell, K. M., et al. 2002, MNRAS **335**, 1120–1132, *Optical spectroscopy of radio galaxies in the 7C Redshift Survey.*

Windhorst, R. A., Fomalont, E. B., Partridge, R. B., & Lowenthal, J. D. 1993, ApJ **405**, 498–517, *Microjansky source counts and spectral indices at 8.44 GHz.*

Windhorst, R. A., Miley, G. K., Owen, F. N., Kron, R. G., & Koo, D. C. 1985a, ApJ **289**, 494–513, *Sub-millijansky 1.4 GHz source counts and multicolor studies of weak radio galaxy populations.*

Windhorst, R. A., Miley, G. K., Owen, F. N., Kron, R. G., & Koo, D. C. 1985b, ApJ **289**, 494–513, *Sub-millijansky 1.4 GHz source counts and multicolor studies of weak radio galaxy populations.*

Yip, C. W., Connolly, A. J., Szalay, A. S., et al. 2004, AJ **128**, 585–609, *Distributions of Galaxy Spectral Types in the Sloan Digital Sky Survey.*

York, D. G., Adelman, J., Anderson, Jr., J. E., et al. 2000, AJ **120**, 1579–1587, *The Sloan Digital Sky Survey: Technical Summary.*

Yun, M. S., Reddy, N. A., & Condon, J. J. 2001, ApJ **554**, 803–822, *Radio Properties of Infrared-selected Galaxies in the IRAS 2 Jy Sample.*

Zanichelli, A., Scaramella, R., Vettolani, G., et al. 2001, A&A **379**, 35–45, *Radio-optically selected clusters of galaxies. II The cluster sample.*

Zhang, Y.-Y., Böhringer, H., Finoguenov, A., et al. 2005, Advances in Space Research **36**, 667–671, *Exploring the structure of galaxy clusters: XMM-Newton observations of the REFLEX-DXL clusters at z ∼ 0.3.*

Zheng, X. Z., Bell, E. F., Rix, H.-W., et al. 2006, ApJ **640**, 784–800, *Detecting Faint Galaxies by Stacking at 24 μm.*